Self-Assembly of Block Copolymers in External Fields

DISSERTATION

zur Erlangung des akademischen Grades eines
Doktors der Naturwissenschaften (Dr. rer. nat.)
im Fach Chemie der Fakultät für Biologie, Chemie und Geowissenschaften
der Universität Bayreuth

vorgelegt von

Alexander Böker

geboren in Frankfurt/Main

Bayreuth, 2002

Die vorliegende Arbeit wurde in der Zeit von März 1999 bis Juli 2002 in Bayreuth an den Lehrstühlen für Physikalische Chemie II und Makromolekulare Chemie II unter der Betreuung von Herrn Prof. Dr. Georg Krausch und Herrn Prof. Dr. Axel H.E. Müller angefertigt.

Promotionsgesuch eingereicht am: 18.7.2002

Prüfungsausschuß:

Prof. Dr. G. Krausch (Erstgutachter)

Meiner Familie

There are more things in heaven and earth,

Than are dreamt of in your philosophy.

W. Shakespeare

Table of Contents

1.   Introduction

In this thesis the potential of *external fields* for guided self-assembly of block copolymer microdomains is investigated. Microphase-separated block copolymers usually exhibit well-ordered structures on the mesoscale. However, in the absence of external fields typically an isotropic grain structure is obtained characterized by a random distribution of microdomain orientations. In the present work both *surface fields* and *electric fields* are used to overcome this drawback and macroscopically align the block copolymer mesostructures.

Some studies on thin films have shown that external interfaces can align the block copolymer morphology, given that the interface selectively attracts one of the constituent blocks[1,2]. In these cases, the geometry of thin film morphologies does not lead to lateral surface patterns as the lower surface tension component typically assembles at the film surface and covers the whole film. In the first part of this work, we demonstrate how *surface fields* can be used to generate stable two-dimensional surface patters via adsorption of ultrathin block copolymer layers onto a polar substrate.

In order to achieve large scale alignment throughout a macroscopically large thin film or bulk sample, several techniques have been used in the last decades. In the bulk, an external *mechanical field*, i.e. shear, has been proven to be a successful technique[3 - 7].

Alignment of microdomains by application of *electric fields* has also been investigated in the recent past[8,9]. So far, all these experiments have been conducted in the melt. Here, however, large electric fields ($10 - 30$ kV/mm) are required. We therefore focused on the investigation of electric field alignment of block copolymer solutions, aiming to establish a new method for large scale microdomain alignment in thin films and in bulk. The electric field strengths needed are about one order of magnitude smaller than required for melt processing. The kinetics of microdomain alignment in concentrated block copolymer solutions, the temperature and electric field strength dependence, and the threshold field strengths for different systems were investigated. Finally, the competing interaction between surface and electric fields was studied.

1.1. Microphase separation of block copolymers

Block copolymers composed of immiscible components microphase-separate to generate structures on a mesoscopic scale, e.g. on a length scale of several tens of nanometers. Typically grains of such microdomains are formed which exhibit a regular order[10]. Macroscopic phase separation cannot occur since the blocks of the copolymer are chemically connected at a junction point. The emerging microdomains of A-rich and B-rich regions of a diblock copolymer maintain their own characteristics, e.g. they stay in the amorphous state, behave as a glass or an elastomer or exhibit a liquid crystalline phase.

The tendency to form microphase-separated domains is governed by two counteracting driving forces: One is the tendency to minimize the unfavorable interaction energy between the different segments via the formation of A- and B-rich regions. Thereby, the smallest possible interface to volume ratio is achieved, thus minimizing the unfavorable interfacial free energy per unit volume. On the other hand, as microphase separation is associated with a significant stretching of the respective block copolymer chains, i.e. loss of translational and configurational entropy, an entropic energy penalty has to be balanced by the gain in energy from the reduction of the interfacial area.

In the past, theoretical models for the microphase separation of block copolymers have been developed for AB diblock copolymers[11-13].

In the following, we will consider the relevant parameters, which influence the phase behavior of AB diblock copolymers: The overall degree of polymerization, N, the volume fractions of the individual blocks (ϕ_A, $\phi_B = 1-\phi_A$), the individual segment lengths of the monomers, and the A-B segment-segment interaction, described by the Flory-Huggins parameter, χ. The product χN is used to express the enthalpic-entropic balance and it parameterizes the block copolymer phase along with the volume fraction, ϕ, of the copolymer segments. In principle, the latter parameter determines which morphology is obtained as long as the block copolymer remains in the range of an ordered phase.

Besides the volume fraction of the block copolymer components, the Flory-Huggins interaction parameter, χ, plays an important role for the description of the phase separation of block copolymers. Especially in the theory of the formation of complex morphologies in ABC triblock copolymers, the surface tension, γ, which is proportional to $\sqrt{\chi}$, is used as a parameter for the miscibility of the different segments (Equation 1-1). Both parameters are readily derived in good approximation from the cohesive energy density.

$$\gamma_{ij} \propto \sqrt{\chi_{ij}}$$

Equation 1-1

γij: *surface tension between the segments i and j of a block copolymer*
χij: *Flory-Huggins-interaction parameter between the segments i and j of a block copolymer*

The Flory-Huggins interaction parameter is derived from experiments or can be calculated from the solubility parameters of both components, i and j, using the van-Laar-Hildebrand-Equation (Equation 1-2):

$$\chi_{ij} = \frac{V}{RT} \cdot \left(\delta_i - \delta_j \right)^2$$

Equation 1-2

$\delta_{i,j}$:   *solubility parameter for the segments i and j of a block copolymer [(cal/cm³)]$^{1/2}$*
V: *molar segment volume, calculated by the mean value of the molar volume of both segments (i and j), which are derived from the molar mass of the repeating unit and the density [cm³/mol]*
R: *universal gas constant 2 [cal/(K·mol)]*
T: *temperature [K]*

1.1.1.   Theoretical models for phase separation in AB diblock copolymers

As described above, χ and N play an important role for the formation of phase-separated structures in block copolymers. Depending on the degree of incompatibility, the product χN defines regimes of weak segregation (weak segregation limit, WSL, $\chi N \leq 10$), intermediate segregation, and strong segregation (SSL, $\chi N \gg 10$). Based on the classical division of AB diblock copolymers into the WSL and SSL, different models for the phase behavior have been developed:

In the case that χN is significantly smaller than unity, entropic effects dominate over the tendency of the block copolymer to minimize the unfavorable interfacial energy of two different segments. Consequently, the formation of a mixed, isotropic phase is observed and the chain segments of both components penetrate into each other.

With an increase of the product χN by either a higher incompatibility or a larger degree of polymerization, a correlation hole occurs in the polymer melt with a fluctuation length scale, D, proportional to the radius of gyration (Equation 1-3).

$$D \propto R_G \propto N^{1/2}$$

Equation 1-3

    D: *fluctuation length scale [nm]*
    R_G: *radius of gyration of the block copolymer [nm]*
    N: *degree of polymerization*

These fluctuations can be regarded as the origin of the formation of a microphase-separated structure,[14] and result from the tendency of the connected polymer chains to minimize the amount of unfavorable interactions.
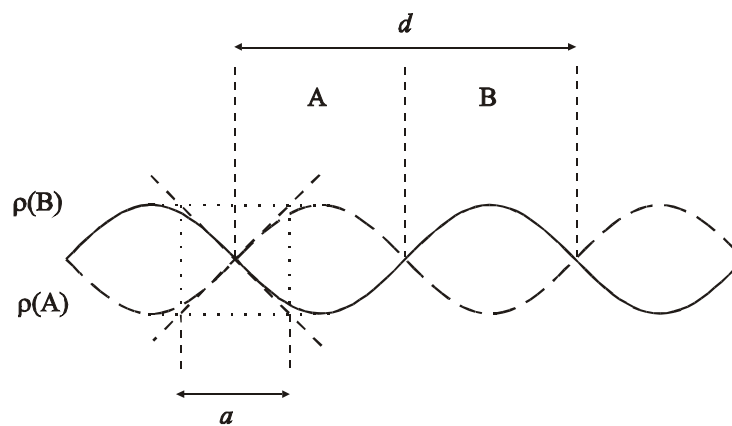
Figure 1-1: Sinusoidal composition profile for phase-separated AB diblock copolymers in the weak segregation limit (WSL)[11]
    d: length of repeating unit in the composition profile
    a: thickness of the shared interface of the two components
    $\rho(A)$, $\rho(B)$: density profile of the components A and B in the different phases

With further increase of the product χN, the weak segregation limit (WSL) is reached where the 'disorder to order' phase transition (ODT) is observed. The individual domains in the ordered microstructures are enriched with one component, indicated by an approximately sinusoidal composition profile for both components (Figure 1-1).

Similar to the length scale fluctuation of the mixed block copolymer, the dimensions of the microphase-separated structure are expected to scale with the square root of the overall degree of polymerization (Equation 1-4). This fact results from the Gaussian conformation assumed for the chains.[11]

$$D \propto R_G \propto N^{1/2}$$

Equation 1-4

    D: *domain size [nm]*

A phase diagram for weakly segregated diblock copolymers was first calculated by Leibler using Landau's mean-field approximation[14]. He compared the free energy of different ordered phases with respect to the disordered phase. His theory predicts that for all diblock copolymers with asymmetric composition $(\phi_A \neq 0.5)$, a microphase separation from the disordered into the metastable body-centered cubic structure (BCC) occurs. According to the phase diagram in Figure 1-2, a transition to the thermodynamically stable hexagonal and lamellar phases is expected upon further increase of the product χN. Only for symmetrical diblock copolymers $(\phi_A = 0.5)$, a direct first-order transition from the disordered to the lamellar phase is expected.
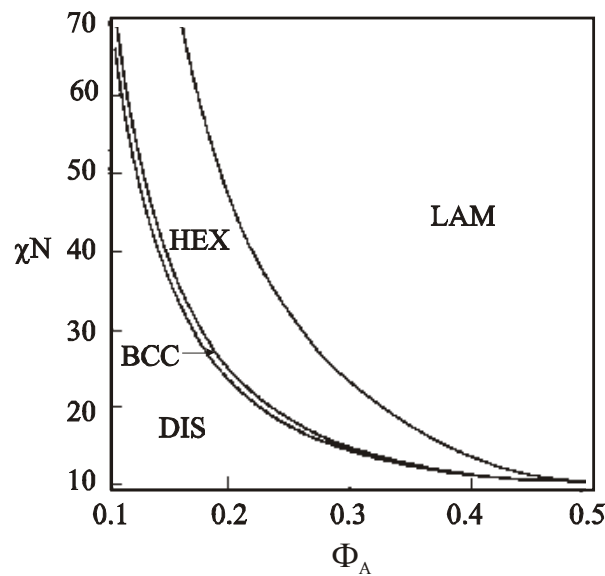
Figure 1-2: Phase diagram for diblock copolymers in the weak segregation (WSL) limit calculated by Leibler[14]
LAM: lamellar microphase
HEX: hexagonal microphase (cylinders)
BCC: body-centered cubic microphase (spheres)
DIS: disordered phase
ϕ_A: volume fraction of component A in the diblock copolymer

Diblock copolymers belonging to the regime of the strong segregation limit (SSL, $\chi N \gg 10$) show a strong incompatibility of the two segments, which is indicated by a large value for χ. Even for small N, phase separation occurs, the interphases between the domains are narrow and well separated, and nearly pure A and B microdomains are obtained as illustrated in Figure 1-3. The function, which describes the composition profile over the regime of phase separation, resembles a step function with values of one and zero, corresponding to the two regions of the particular pure component.
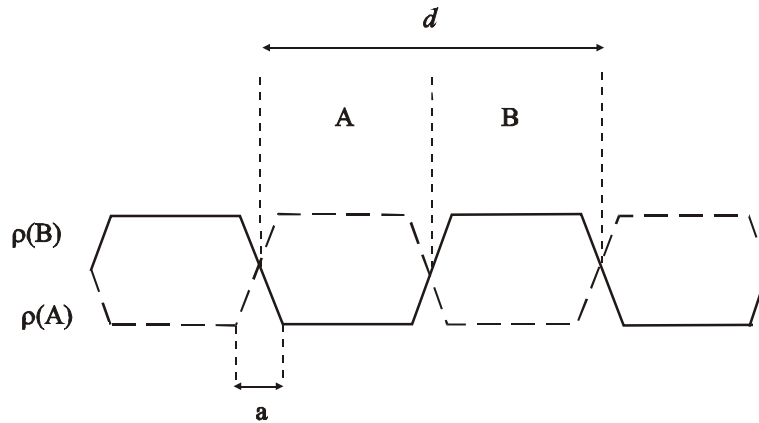
Figure 1-3:   Characteristic composition profile in the case of strong segregation limits (SSL)[11]
d: length of repeating unit in the composition profile
a: thickness of the shared interface of the two components
ρ(A), ρ(B): density profile of the components A and B in the different phases

The interaction energy associated with the contacts between A and B segments is localized in these interfacial regions. In order to maintain a homogenous segment density, the tendency of the system to minimize the total area of such an interface has to be accompanied by an extended chain configuration near the interface. These opposing forces in the minimization of enthalpic energy and entropic penalty lead to perturbed chain configurations and microdomain periods D:[12,15]

$$D \propto N^{\frac{2}{3}} \chi^{\frac{1}{6}}$$

Equation 1-5

A comparison of Equation 1-5 and Equation 1-4 leads to the conclusion that the effect of extended chain configuration in the SSL accounts for the $N^{2/3}$ dependence of the domain size on the degree of polymerization.

Matsen and Bates[16] successfully combined the two limiting cases of WSL and SSL using the self-consistent field theory developed by Helfand and Wasserman[17]. Their calculations established a phase diagram for microphase-separation of diblock copolymers including the formation of the lately discovered gyroid structure and the corresponding order-order transitions (Figure 1-4).

The structures of the different thermodynamically stable microphases for AB diblock copolymers are presented in Figure 1-5. While the lamellar, body-centered cubic, and hexagonal microphases have been known for a long time, the 'gyroid' phase was discovered independently by two groups in 1994.[18,19] Recently, it turned out that the gyroid phase is the only thermodynamically stable phase between lamellae and cylinders. Other morphologies,

such as OBDD (ordered bicontinuous double diamond) or hexagonal perforated layer (HPL), are meanwhile considered as transient or 'long-lived' metastable phases.[20,21]
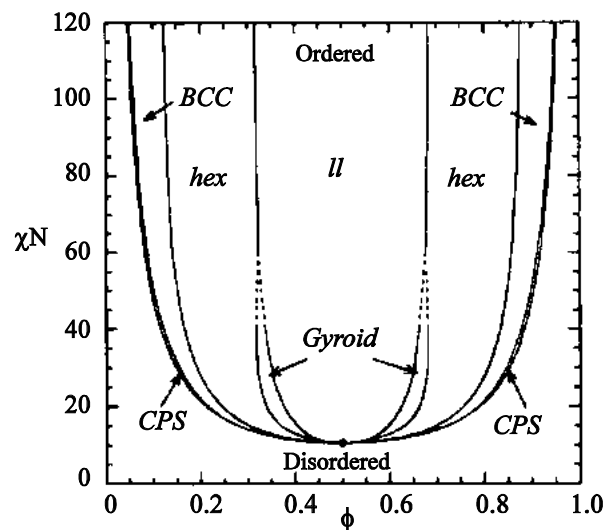
Figure 1-4: Phase diagram for diblock copolymers in the strong segregation limit (SSL) as calculated by Matsen et al.[16]
ll: lamellar microphase
hex: hexagonal microphase
BCC: body-centered cubic microphase
CPS: centered packed spheres
DIS: disordered phase
ϕ_A: volume fraction of component A in the diblock copolymer
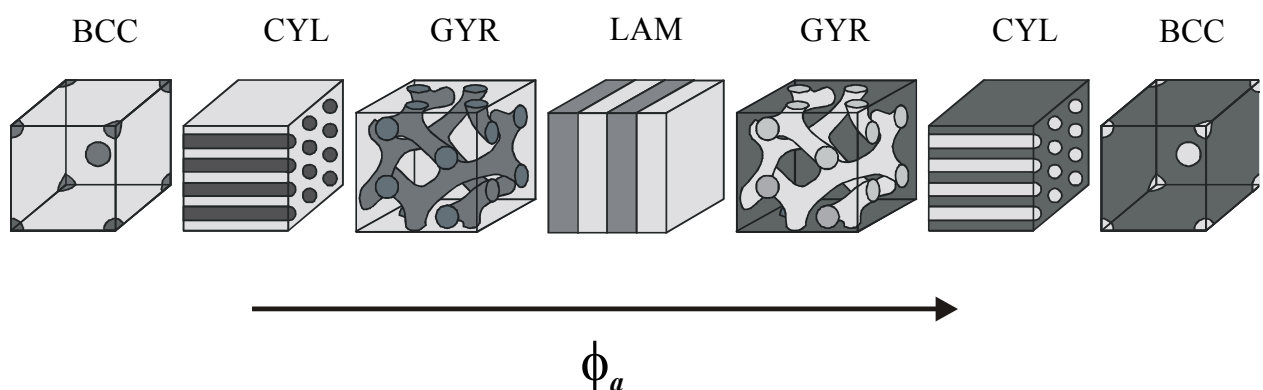
Figure 1-5: Thermodynamic equilibrium morphologies in AB diblock copolymers depending on the volume fraction of component A.
BCC: spheres, arranged on a body centered cubic lattice
HEX: cylinders, arranged on a hexagonal lattice
GYR: gyroid, biscontinuous phase
LAM: lamellar structure

Symmetric diblock copolymers ($\phi_A = 0.5$) arrange into a lamellar phase (LAM), with alternating layers of the constituent blocks. The increase of the volume fraction of one component leads to more asymmetrical copolymers, for which a bicontinuous cubic 'gyroid' phase (GYR) is observed. A phase of hexagonal-packed cylinders (HEX) and a body-centered (BCC) cubic phase occur with a further increase of the volume fraction of the matrix component. Simultaneously, the interfacial curvature increases on changing the morphology from the LAM to the BCC phase.
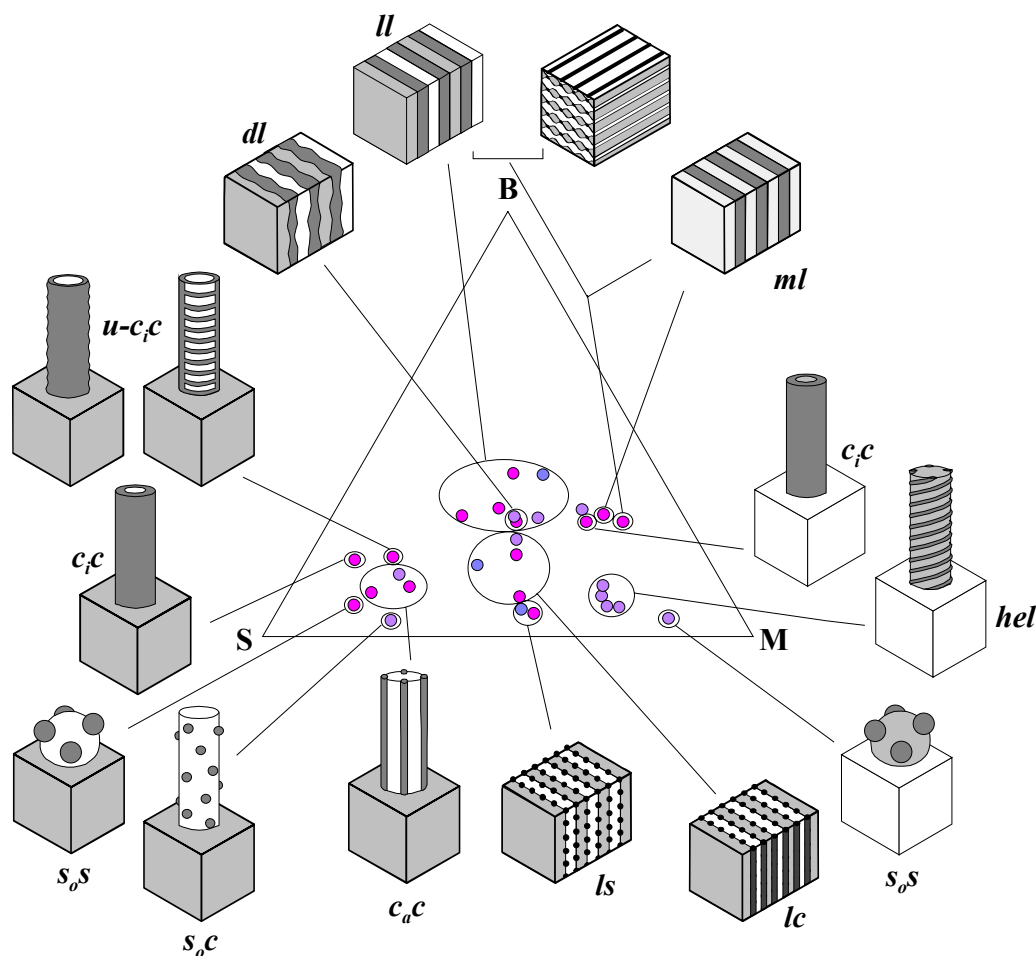
Figure 1-6:   Ternary phase diagramm of SBM triblock copolymers, color according to staining witht OsO$_4$. PS: grey, PB: black, PMMA: white.

With ABC triblock copolymers the situation is even more complex, as not only AB contacts play a role but also AC and BC interactions. As a result there is a rich variety of triblock copolymer structures. Pioneering work on ABC triblock copolymers was done by Arai *et al.*[22], Mogi *et al.*[23 - 25] and Stadler *et al.* [26 - 28] (Figure 1-6). Other types of block copolymers (e.g. star-, brush-like or dendritic) also can increase the variety of morphologies[29]. A detailed discussion of this field is, however, far beyond the scope of this introduction.

1.2.   Surface Induced Microdomain Structures in Thin Block Copolymer Films

Ultrathin films of polystyrene-*b*-poly(2-vinyl pyridine) block copolymers can self-assemble into surface induced nanopatterns due to strongly different affinities of the polymer blocks towards a substrate[30,31]. A very characteristic aspect of these patterns is the fact that the anchoring block adsorbs so strongly on the substrate that its conformation is transformed to a two dimensional coil. This, from the entropic point of view very unfavorable state can be realized because of an enthalpic gain due to the interactions between polymer and substrate. The adsorbing block is stretched in its lateral dimensions to such a degree that the non adsorbing cannot follow. The gain in enthalpy that would result from wetting the surface formed by the polar block is not sufficient to allow for chain stretching. Therefore, the non adsorbing block dewets the adsorbed layer and forms small isolated clusters. From this description it becomes clear that these surface patterns are only formed, if the adsorbing blocks form a large number of contacts with the substrate[32]. This is only the case for ultrathin films, in thicker block copolymer films, the surface is in contact with more polymer chains and the number of contacts per chain and the stretching of the adsorbing blocks is reduced, so the block copolymers can adopt a layered structure parallel to the substrate[33].

The approach presented in this work relies on ABC triblock copolymers with a selectively adsorbing short middle block (e.g. poly(2-vinyl pyridine) or poly(2-hydroxyethyl methacrylate)) and polystyrene and poly(methyl methacrylate) end blocks. Based on recent mean field calculations by Pickett and Balasz, we expect this middle block to facilitate the generation of well-defined lateral morphologies[34]. In chapter 3 a detailed investigation of the surface structures and their size scaling will be presented, describing the parameters that can be used to control the domain spacing of different morphologies. These parameters are the polymer composition, the film thickness and the concentration of the polymer solution from which the film is prepared. The influence of these parameters is demonstrated in chapter 3.

1.3.   Alignment of Block Copolymer Microstructures

Control of the orientation of a block copolymer microstructure allows the development of polymeric materials with novel and interesting properties. Anisotropic mechanical, optical,

electrical or mass transport properties can be tailored by proper orientation of the block copolymer microstructure. Alignment of glassy microphase-separated cylinders in a rubbery matrix gives a material with a glassy modulus along the cylindrical axis and a rubbery modulus along the transverse directions[35]. If the cylinders are made conductive, the material becomes a directional conductor[36 - 39]. Quantum dots or wires could be made from block copolymers with a spherical or cylindrical microstructure. The birefringence inherent in lamellar or cylindrical block copolymers could be useful for optical applications. Alignment of microstructures also is desirable for scientific investigations because interpretation of experiments, e.g. transmission electron microscopy, is simplified when the microstructure is uniformly oriented.

1.3.1.   Shear Alignment

Commonly, the long-range order of the microdomains of a block copolymer is perturbed by defects. If the microphase-separated state is formed from a disordered state in the absence of a strong aligning field, the resulting grains nucleating at different centers will exhibit various randomly distributed orientations. This finally leads to defects at the grain boundaries like wall and line defects and curvature. In the past, many research groups have shown that macroscopic alignment of lamellar and cylindrical microstructures can be achieved by flow[40 - 42]. Most studies have focused on shear which is easily applied. The variety of observed alignments has been explained by several mechanisms, including rotation of ordered regions (grains), disordering of regions that are destabilized by flow-induced deformation, followed by reordering in a preferred alignment direction[43 - 47].

In oscillatory shear experiments, the direction of alignment depends on the amplitude and frequency of shear and on temperature[48,49]. Under certain conditions, the normal vector of lamellar microdomains aligns in the flow gradient direction („parallel" alignment), other conditions lead to alignment along the vorticity direction („perpendicular" alignment). Patel *et al.*[45] proposed that the mechanical contrast between the two microdomains is a primary consideration in choice of alignment direction. Koppi *et al.*[47] suggested that the vorticity in shear induces instabilities in the parallel lamellae and thus favors perpendicular alignment. All these considerations indicate, that the behavior of block copolymer microstructures under flow is quite complex.

From a practical point of view, the most prominent procedures devised in the past are, for example, Large Amplitude Oscillatory Shear (LAOS)[50-52] and roll-casting[53].

1.3.2. Electric Field Alignment

Flow provides a strong aligning force. However, because of boundary constraints and conditions of continuity, the potential for flow-induced orientation is limited. Electric fields provide a weaker aligning force but offer the advantage of local alignment control by application of spatially specific electric fields. For these reasons, electric fields may provide a unique pathway to new applications for block copolymers. In addition, electric field alignment is scientifically interesting because the driving force for alignment is much simpler than that induced by flow. Studies of field alignment can be used to learn about materials properties like defect mobilities and give straightforward insight into alignment mechanisms. Investigations on solvent-based systems of different block copolymers will be described in chapters 5 to 8.

1.3.2.1. Electrothermodynamics of Microphase-Separated Block Copolymers

As an example we consider a block copolymer filling the gap between parallel, planar electrodes. The electrodes are held at a constant potential by a voltage source. Therefore, the free energy of the system contains an electrostatic contribution[54]:

$$F = F_0 - \frac{1}{8\pi} \int_{V} \varepsilon(r) |E(r)|^2 d^3 r \qquad\qquad Equation\ 1\text{-}6$$

F_0:   *free energy in the absence of an electric field*
$\varepsilon(r)$:   *local dielectric constant*
$E(r)$:   *electric field*
The integration is over the volume of the material, V.

According to this expression, materials with a high dielectric constant are attracted to regions of high field strength, in order to maximize the magnitude of the negative electrostatic contribution to the free energy. Different composition patterns within a block copolymer material and the associated spatially varying local dielectric constant produce different patterns of electric field. The consequence is a composition-pattern dependent electrostatic

contribution to the free energy. Certain orientations of the composition pattern are thermodynamically favored over others. The forces that give rise to preferred orientations arise from field-induced polarization charges resulting from gradients in the dielectric constants. Using Maxwell´s equation for dielectric materials, we find that polarization charges exist wherever the gradient in the dielectric constant has a component in the direction of the applied field.

We will now consider the two different microdomain orientations of a lamellar AB diblock copolymer parallel and perpendicular to the electrodes. For the parallel orientation, symmetry in the transverse direction dictates a vertical electric field everywhere with the continuity condition at the AB interface:

$$\varepsilon_A E_A = \varepsilon_B E_B \,,$$

Equation 1-7

where ε_A and ε_B are the dielectric constants of the materials A and B, and E_A and E_B are the electric field strengths in regions of the materials A and B. The discontinuity in the field strength at the phase boundaries arises from excess polarization charges. The total voltage drop across the lamellae must equal the applied voltage, V:

$$E_A \phi_A d + E_B \phi_B d = V \,,$$

Equation 1-8

Where ϕ_A and ϕ_B are the volume fractions of components A and B and d is the electrode spacing. Equations 1-7 and 1-8 yield the field strengths:

$$E_A = \frac{V}{d}\frac{1}{\phi_A + \dfrac{\phi_B \varepsilon_A}{\varepsilon_B}}\,, \qquad E_B = \frac{V}{d}\frac{1}{\phi_B + \dfrac{\phi_A \varepsilon_B}{\varepsilon_A}}$$

Equation 1-9

Knowing the field strength, the electrostatic contribution to the free energy can be derived from Equation 1-6:

$$F - F_0 = -\frac{1}{8\pi}\int_{v}\varepsilon(r)\left|E(r)\right|^2 d^3 r = -\frac{1}{8\pi}\varepsilon_h\left(\frac{V}{d}\right)^2 \boldsymbol{v}$$

Equation 1-10

where ε_h is the harmonic average of the dielectric constants:

$$\frac{1}{\varepsilon_h} = \frac{\phi_A}{\varepsilon_A} + \frac{\phi_B}{\varepsilon_B}$$

Equation 1-11

This gives the effective dielectric constant of the material in the parallel orientation.

If the lamellae are perpendicular to the electrode surfaces, all the interfaces are parallel to the electric field and thus there will be no excess polarization charges. The field will be a constant V/d throughout the material. The electrostatic contribution to the free energy can be calculated as

$$F - F_0 = -\frac{1}{8\pi}\left(\frac{V}{d}\right)^2 \int_v \varepsilon(r)d^3r = -\frac{1}{8\pi}\varepsilon_a\left(\frac{V}{d}\right)^2 \mathbf{v}$$

Equation 1-12

where ε_a is the arithmetic average of the dielectric constants:

$$\varepsilon_a = \phi_A\varepsilon_A + \phi_B\varepsilon_B$$

Equation 1-13

This is the effective dielectric constant of the material in the perpendicular orientation.

As the arithmetic mean of the dielectric constant always matches or exceeds the harmonic mean, the perpendicular orientation always represents the lower energy state:

$$\varepsilon_a - \varepsilon_h = (\varepsilon_A - \varepsilon_B)^2 \frac{\phi_A\phi_B}{\phi_B\varepsilon_A + \phi_A\varepsilon_B} \geq 0$$

Equation 1-14

The effective dielectric constant for an arbitrary orientation where the lamellar normal vector forms a tilt angle, θ, with respect to the vertical can be expressed as follows:

$$\varepsilon_{eff}(\theta) = \varepsilon_a + (\varepsilon_h - \varepsilon_a)cos^2\theta$$

Equation 1-15

The material experiences a torque whenever the lamellae are not perpendicular to the electrodes. The torque arises from the forces of attraction between the excess polarization charges at the interfaces and the charges on the electrodes.

In the above considerations, the anisotropic behavior of the block copolymer microstructure arises from shape and not from molecular anisotropy. In contrast to work by Gurovich[55 - 57], contributions to the electrostatic free energy from the alignment and stretching

of chains and their difference in polarizability in the direction along and perpendicular to the bonds has been neglected.

In the following, we will briefly describe the calculation of the electrostatic contributions to the free energy, based on Equation 1-6, as derived by Amundson *et al.*[58]:

The local dielectric constant in a block copolymer sample is a function of local composition and can be expressed as an expansion in the composition pattern, $\overline{\psi}$, associated with the ordered state:

$$\varepsilon(r) = \varepsilon_D(r) + \beta\overline{\psi}(r) + \frac{1}{2}\frac{\partial^2\varepsilon}{\partial^2\psi}\left[\overline{\psi}(r)\right]^2 \qquad\qquad \textit{Equation 1-16}$$

Here, β characterizes the sensitivity of the dielectric constant to compositional change: $\beta = \delta\varepsilon/\delta\psi$, ε_D is the dielectric constant in the limit of vanishing stationary composition pattern and includes a contribution from dynamic composition fluctuations. The effect of dynamic fluctuations is separated from the effect of the composition pattern, $\overline{\psi}$, associated with the ordered phase. Since the dynamic fluctuations have short correlation lengths, they will not significantly couple to an electric field. The stationary composition pattern can have a much larger correlation length and can couple more effectively to an electric field.

Using Maxwell′s equation, $\nabla\left[\varepsilon(r)\,E(r)\right] = 0$, and Equation 1-6, the electrostatic contribution to the free energy density for lamellar microstructure can be written as:

$$\frac{F - F_0}{V} = \frac{1}{8\pi}\varepsilon_D|E_0|^2\left[\left(\frac{\beta}{\varepsilon_D}\right)^2\langle\overline{\psi}^2\rangle\left(\hat{e}_q\hat{e}_z\right)^2 - \frac{\langle\varepsilon\rangle}{\varepsilon_D}\right], \qquad\qquad \textit{Equation 1-17}$$

with $\hat{e}_q$ as the unit vector of the lamellar pattern and $\hat{e}_z$ as the unit vector in the direction of the applied electric field E_0. $\langle\varepsilon\rangle$ denotes the space-averaged dielectric constant.

Only the first term in the brackets is anisotropic and contributes towards alignment. The free energy is minimized, when the wave vectors are in the plane perpendicular to E, i.e. the lamellar planes contain E. The alignment force is proportional to the square of the applied field strength $E_0{}^2$, the mean square of the composition pattern, $\langle\overline{\psi}^2\rangle$, and the material parameter β^2/ε_D.

The size of the anisotropic component of the electric energy is rather small, i.e. for the energy difference between aligned and misaligned orientations of a region to equal k_BT, the

region must be of order of some hundred nanometers for a PS-*b*-PMMA block copolymer. The electric field can only affect the microdomains if it is acting on an organized state with long-range order.

1.4.   Structure of this Thesis

The following chapters in this thesis describe in detail:

➢   Fundamentals of the most commonly used characterization and synthetic methods (Chapter 2)

➢   Synthesis and characterization of functional ABC triblock copolymers for controlled surface patterns on nanometer scale (Chapter 3)

➢   Investigation of homopolymer wetting behavior on chemically nanopatterned Surfaces (Chapter 4)

➢   Introduction of a solvent-based method to generate highly anisotropic block copolymer bulk samples using electric fields (Chapter 5)

➢   Elucidation of governing mechanisms responsible for electric field-induced alignment of block copolymer microdomains in a PS-*b*-PI block copolymer in concentrated toluene solutions (Chapter 6)

➢   Investigation of kinetics and mechanism of the electric field-induced alignment of a PS-*b*-PHEMA-*b*-PMMA block copolymer in concentrated tetrahydrofuran solutions, determining the influence of phase separation and dielectric contrast (Chapter 7)

➢   Application of electric field-induced alignment of block copolymer microdomains to high molecular weight AB and ABC block copolymers with high dielectric contrast (PS-*b*-P2VP, PS-*b*-PtBMA, PS-*b*-P2VP-*b*-P*t*BMA) (Chapter 8)

References

[1] Anastasiadis, S.H.; Russell, T.P.; Satija, S.K.; Majkrzak, C.F. *Phys. Rev. Lett.* **1989**, *62*, 1852.

[2] Annighöfer, F.; Gronski, W. *Makromol. Chem., Rapid Commun.* **1983**, *4*, 123.

[3] Wiesner, U. *Macromol. Chem. Phys.* **1997**, *198*, 3319.

[4] Chen, Z.-R.; Kornfield, J.A.; Smith, S.D.; Grothaus, J.T.; Satkowski, M.M. *Science* **1997**, *277*, 1248.

[5] Chen, Z.-R.; Kornfield, J.A. *Polymer* **1998**, *39*, 4679.

[6] Keller, A.; Pedemonte, E.; Willmouth, F.M. *Nature* **1970**, *225*, 538.

[7] Albalak, R.J.; Thomas, E.L. *J. Polym. Sci., Polym. Phys. Ed.* **1993**, *31*, 37.

[8] Thurn-Albrecht, T.; Schotter, J.; Kastle, G.A.; Emley, N.; Shibauchi, T.; Krusin-Elbaum, L.; Guarini, K.; Black, C.T.; Tuominen, M.T.; Russell, T.P. *Science* **2000**, *290*, 2126.

[9] Amundson, K.; Helfand, E.; Davis, D.D.; Quan, X.; Patel, S.S.; Smith, S.D.; *Macromolecules* **1991**, *24*, 6546.

[10] Bates, F.S.; Frederickson, G.H. *Physics Today* **1999**, *52*, 32.

[11] Bates, F. S.; Fredrickson, G. H. *Annu. Rev. Phys. Chem.* **1990**, *41*, 525.

[12] Semenov, A.N. *Sov. Phys. JETP* **1985**, *61*, 733.

[13] Ohta, T.; Kawasaki, K. *Macromolecules* **1986**, *19*, 2621.

[14] Leibler, L. *Macromolecules* **1980**, *13*, 1602.

[15] Helfand, E.; Wassermann, Z.R. *Macromolecules* **1976**, *9*, 879.

[16] Matsen, M.W.; Bates, F.S. *Macromolecules* **1996**, *13*, 1091.

[17] Helfand, E.; Wasserman, Z.R. *Macromolecules* **1980**, *13*, 994.

[18] Schulz, M.F.; Bates, F.S.; Almdal, K.; Mortensen, K.; Hajduk, D.A. *Phys. Rev. Lett.* **1994**, *77*, 3153.

[19] Hadjuk, D.A.; Harper, P.E.; Gruner, S.M.; Honeker, C.C.; Kim, G.; Thomas, E.L.; Fetters, L.J. *Macromolecules* **1993**, *27*, 4063.

[20] Hadjuk, D.A.; Harper, P.E.; Gruner, S.M.; Honeker, C.C.; Thomas, E.L.; Fetters, L.J. *Macromolecules* **1995**, *28*, 2570.

[21] Vigild, M.E.; Almdal, K.; Mortensen, K.; Hamley, I.W.; Fairclough, J.P.A.; Ryan, A.J. *Macromolecules* **1998**, *31*, 5702.

[22] Arai, K.; Kotaka, T.; Kitano, Y.; Yoshimura, K. *Macromolecules* **1980**, *13*, 455.

[23] Mogi, Y.; Kotsuji, H.; Kaneko, Y.; Mori, K.; Matsushita, Y.; Noda, I. *Macromolecules* **1992**, *25*, 5408.

[24] Mogi, Y.; Mori, K.; Kotsuji, H.; Matsushita, Y.; Noda, I.; Han, C.C. *Macromolecules* **1993**, *26*, 5169.

[25] Mogi, Y.; Nomura, M.; Kotsuji, H.; Ohnishi, K.; Matsushita, Y.; Noda, I. *Macromolecules* **1994**, *27*, 6755.

[26] Stadler, R.; Auschra, C.; Beckmann, J.; Krappe, U.; Voigt-Martin, I.; Leibler, L. *Macromolecules* **1995**, *28*, 3080.

[27] Breiner, U.; Krappe, U.; Abetz, V.; Stadler, R. *Macromol. Chem. Phys.*, **1997**, *198*, 1051.

[28] Breiner, U.; Krappe, U.; Thomas, E. L.; Stadler, R. *Macromolecules,* **1998**, *31*, 135.

[29] Hückstädt, H.; Göpfert, A.; Abetz, V. *Polymer*, **2000**, *41*, 9089.

[30] Spatz, J.P.; Sheiko, S.S.; Möller, M. *Adv. Mate*r. **1996**, *8*, 513.

[31] Spatz, J.P.; Möller, M.; Noeske, M.; Behm, R.J.; Pietralla, M. *Macromolecule*s, **1997**, *30*, 3874.

[32] In ref. 31 Spatz *et al.* found that every third to second 2VP unit is in contact with the substrate. This is sufficient to prevent a significant expansion of the adsorbing block into the third dimension (perpendicular to the substrate surface).

[33] Russell, T.P.; Coulou, G.; Deline, V.R.; Miller, D.C. *Macromolecules* **1989**, *22*, 4600.

[34] Pickett, G. T.; Balazs, A. C. *Macromol. Theory Simul.* **1998**, *7*, 249.

[35] Albalk, R.J.; Thomas, E.L. *Polymer* **1995**, *35*, 4115.

[36] Tassoni, R.; Schrock, R.R. *Chem. Mater.* **1994**, *6*, 744.

[37] Saunders, R.S.; Cohen, R.E.; Schrock, R.R. *Macromolecules* **1991**, *24*, 5599.

[38] Ishizu, K.; Yamada, Y.; Saito, R.; Kanbara, T.; Yamamoto, T. *Polymer* **1993**, *34*, 2256.

[39] Morkved, T.L.; Wiltzius, P.; Jaeger, H.M.; Grier, D.G.; Witten, T.A. *Appl. Phys. Lett.* **1994**, *64*, 422.

[40] Barclay, G.G.; Ober, C.K. *Prog. Polym. Sci.* **1993**, *18*, 899.

[41] Heilmeir, G.H.; Goldmacher, J.E. *Appl. Phys. Lett.* **1969**, *13*, 132.

[42] Lavrentovich, O.D.; Kléman, M. *Phys. Rev. E* **1993**, *48*, R39.

[43] Hadziioannou, G.; Mathis, A.; Skoulios, A. *Colloid Polym. Sci.* **1979**, *257*, 136.

[44] Larson, R.G.; Winey, K.I.; Patel, S.S.; Watanabe, H.; Bruinsma, R. *Rheol. Acta* **1993**, *32*, 245.

[45] Patel, S.S.; Larson, R.G.; Winey, K.I.; Watanabe, H. *Macromolecules* **1995**, *28*, 4313.

[46] Winey, K.I.; Patel, S.S.; Larson, R.G.; Watanabe, H. *Macromolecules* **1993**, *26*, 4373.

[47] Koppi, K.A.; Tirrell, M.; Bates, F.S.; Almdal, K.; Colby, R.H. *J. Phys. (Paris)* **1993**, *2*, 1941.

[48] Gupta, V.; Krishnamoorti, R.; Kornfiled, J.A.; Smith, S.D. *Macromolecules* **1996**, *29*, 1359.

[49] Gupta, V.; Krishnamoorti, R.; Chen, Z.R.; Kornfiled, J.A.; Smith, S.D.; Satkowski, M.M.; Grothaus, J.T. *Macromolecules* **1996**, *29*, 875.

[50] Wiesner, U.; *Macromol. Chem. Phys.* **1997**, *198*, 3319.

[51] Chen, Z.-R.; Kornfield, J.A.; Smith, S.D.; Grothaus, J.T.; Satkowski, M.M.; *Science* **1997**, *277*, 1248.

[52] Chen, Z.-R.; Kornfield, J.A.; *Polymer* **1998**, *39*, 4679.

[53] Albalak, R.J.; Thomas, E.L.; *J. Polym. Sci., Polym. Phys. Ed.* **1993**, *31*, 37.

[54] Landau, L.D.; Lifshitz, E.M.; Pitaevskii, L.P. *Landau and Lifshitz Course of Theoretical Physics,* Vol. 8: *Electrodynamics of Continuous Media*, 2nd ed., Pergamon Press, New York, **1984**, pp. 44-51.

[55] Gurovich, E. *Macromolecules* **1994**, *27*, 7063.

[56] Gurovich, E. *Macromolecules* **1994**, *27*, 7339.

[57] Gurovich, E. *Phys. Rev. Lett.* **1995**, *74*, 482.

[58] Amundson, K.; Helfand, E.; Quan, X.; Smith, S.D. *Macromolecules* **1993**, *26*, 2698.

2.   Methods

2.1.   Synthesis

2.1.1.   Anionic Polymerization

Anionic polymerization of styrene[1] and dienes[2,3] initiated by alkali metals has been well-known since the early 1900´s. The interest in these reactions has increased continuously over the last decades since Szwarc first reported the "living" nature of the anionic polymerization of styrene and diene monomers in 1956.[4,5] One important aspect of the term living polymerization refers to the fact that the reaction occurs in the absence of irreversible termination and chain transfer.[4-6] Therefore, the molecular weight in a living polymerization is controlled by the stoichiometry of the reaction and the degree of conversion. The living nature of the propagating chain allows the synthesis of block copolymers by sequential addition of different monomers. Due to the complex, reaction condition dependent, mechanism the properties of the polymer can be adjusted to specific requirements. By variation of composition and architecture the following properties can be controlled:

➢ *Molecular weight and molecular weight distribution*

➢ *Topology of the polymers*
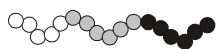
multiblock copolymer   star block copolymer [7-9]   comb shaped polymer [10-12]
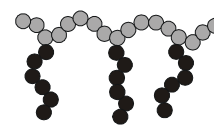
➢ *Sequence of the monomer units* [4,5,13]

block copolymer   statistical copolymer   alternating copolymer

➢ *End-functionalized polymers by a functionalized initiator or end capping of the living chain end* [14-16]

➢ *Tacticity for monomers of the type CH₂=CHR or CH₂=CR₁R₂*

isotactic   syndiotactic   atactic
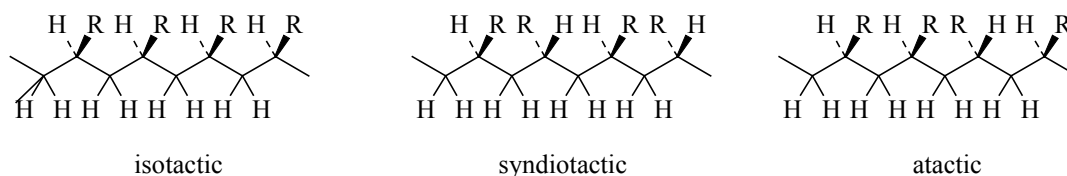
➢ *Microstructure of diene-based polymers (Regiochemistry)*

1,2-polybutadiene   1,4-cis polybutadiene   1,4-trans polybutadiene
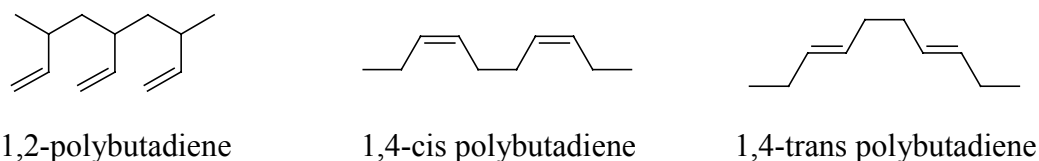
In the last 50 years, new polymerization techniques such as cationic polymerization,[17] Ziegler-Natta,[18] ring-opening metathesis[19] or group transfer polymerization[20,21] have been developed in order to control the architecture of polymers. Recently, "living"/ controlled radical polymerization (e.g., atom transfer radical polymerization, ATRP) has become a major topic of research [22,23].

2.1.2. Fundamentals of Anionic Polymerization

2.1.2.1. Molecular Weight Distribution and Mechanism

As described above, the molecular weight in a living polymerization is controlled by the stoichiometry of the reaction and the degree of conversion. Therefore, a living anionic polymerization only consists of initiation and propagation steps in the absence of termination and chain transfer. As a consequence, the concentration of propagating chains, c^*, is constant during the course of the reaction and the number-average molecular weight depends linearly on the conversion, p. This yields for the number-average degree of polymerization, $\overline{X}_n$, at full conversion[24]:

$$\overline{X}_n = \frac{[M]_0}{[I]_0},$$
<div align="right">*Equation 2-1*</div>

[M]₀: initial concentration of monomer
[I]₀: initial concentration of monofunctional initiator

A consequence of the absence of termination and chain transfer in a polymerization is that the resulting polymer should be nearly monodisperse ($\overline{M}_w \cong \overline{M}_n$), when the following conditions are fulfilled: Initiation must be fast compared to propagation so that all propagations centers begin to grow simultaneously. Efficient mixing ($t_{mix} \ll t_{1/2}$) throughout the polymerization is required and depropagation must be slow relative to propagation. Moreover, there must be a fast equilibrium between propagating species of different reactivity. Under these circumstances, the size distribution will be given by a Poisson distribution [25,26]. The polydispersity index (*PDI*) can be expressed as

$$\frac{\overline{X}_w}{\overline{X}_n} = 1 + \frac{\overline{X}_n - 1}{\overline{X}_n^{\;2}} \cong 1 + \frac{1}{\overline{X}_n} \qquad\qquad\qquad Equation\ 2\text{-}2$$

$\overline{X}_n$ *: number-average degree of polymerization*

$\overline{X}_w$ *: weight-average degree of polymerization*

Equation 2-2 shows that for sufficiently high degrees of polymerization, the size distribution will be narrow with *PDI* being close to unity. Practically, living anionic systems under ideal conditions yield $\overline{X}_w / \overline{X}_n < 1.1$ [27,28].

In general, anionic polymerizations can be described by the following three reaction schemes, where the reaction is terminated deliberately by addition of a hydrogen transfer agent (e.g. methanol or water).

$$I^* + M \xrightarrow{\;\;k_i\;\;} P_i^* \qquad\qquad Initiation$$

I^*:   *initiator*
M: *monomer*
P_i^*:   *active polymer chain with i monomer units*
k_i: *rate constant of initiation*

$$R-Li \;+\; \overset{Y}{=\!\!/} \;\xrightarrow{\;\;k_i\;\;}\; R\overset{Y}{\underset{|}{\curvearrowright C^- Li^+}}$$
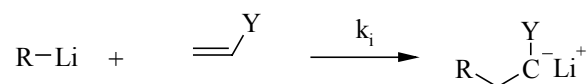
Y: electron withdrawing group

Figure 2-1:   Reaction scheme for the initiation step of an anionic polymerization

The initiator required to polymerize a monomer depends on the reactivity of the monomer towards nucleophilic attack. The monomer reactivity increases with increasing ability to

stabilize the carbanion charge. Very strong nucleophiles such as amide anions[29] or alkyl carbanions are needed to polymerize monomers, such as styrene and butadiene, with relatively weak electron-withdrawing substituents. Weaker nucleophiles, such as alkoxide[30] or hydroxide ions, can initiate the polymerization of monomers with strongly electron-withdrawing substituents, such as acrylonitrile, methyl methacrylate and methyl vinyl ketone, although the efficiency is lower than that of stronger nucleophiles[31-35].

$$P_i^* + M \xrightarrow{\ k_p\ } P_{i+1}^* \qquad\qquad Propagation$$
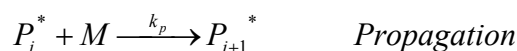
k_P: rate constant of propagation
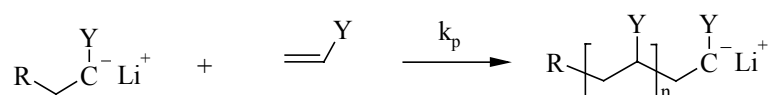
Figure 2-2:   Reaction scheme of the propagation step of an anionic polymerization

The rate constant of propagation and rate of propagation for an anionic polymerization are strongly affected by the nature of both the solvent and the counterion. If we consider for example the polymerization of styrene with sodium counterion, the apparent rate constant of propagation is increased by two orders of magnitude when the reaction is conducted in tetrahydrofuran ($\varepsilon = 7.6$) rather than in benzene ($\varepsilon = 2.2$), i.e. the polymerization is much faster in a more polar solvent[36]. The stronger solvating power of the reaction medium increases the fraction of solvent separated ion pairs relative to contact ion pairs and thus increases their reactivity. On the other hand also the counterion itself influences the fraction solvent separated ion pairs: the smaller Li^+ is solvated to a much greater extend than the larger Cs^+.

$$P_i^* + X - Y \xrightarrow{\ k_t\ } P_i - Y + X^- \qquad\qquad\qquad Termination$$

k_t: rate constant of termination
X-Y: quenching agent for termination of the polymerization
X^-: anion of the terminating agent

Figure 2-3:   Termination of an anionic chain end by water

2.1.2.2. Kinetics

Under the condition that initiation is faster than propagation (i.e. the concentration of active polymer chains in the system, c^*, is constant), the rate of propagation can be described by a pseudo-first-order rate equation.

$$R_p = -\frac{d[M]}{dt} = k_p c^* [M] = k_{app}[M]$$
Equation 2-3

R_p: *rate of propagation*
[M]: monomer concentration
c^*: *concentration of active polymer chains in the system*
k_{app}: *pseudo-first-order rate constant*

Integration of Equation 2-3 yields:

$$\ln\frac{[M]_0}{[M]_t} = k_p c^* t = k_{app}t$$
Equation 2-4

[M]$_o$: initial monomer concentration
[M]$_t$: monomer concentration at time t

A time-conversion plot results in a straight line through the origin in the case of instantaneous initiation and absence of termination. The slope of the curve is equal to the apparent rate constant of propagation, k_{app}.

2.2.   Characterization

2.2.1.   Scanning Force Microscopy (SFM)

Scanning force microscopy (SFM) is becoming increasingly important in polymer characterization with regard to both surface topography and surface mechanical properties. The instrument used in this work is a Digital Instruments Dimension 3100 SFM with a Nanoscope III Controller. Of particular interest in determining topography and phase morphology in polymer films is Tapping Mode SFM.

Tapping Mode imaging is implemented in ambient air by oscillating the cantilever at or near its resonance frequency using a piezoelectric crystal. The piezo motion causes the cantilever to oscillate with a high amplitude (typically equal or greater than 20nm) when the tip is not in contact with the surface. The oscillating tip is then moved toward the surface until it begins to slightly touch, or "tap" the surface. During scanning, the vertically oscillating tip alternately contacts the surface and lifts off, generally at a frequency of 250 - 350 kHz. As the oscillating cantilever begins to intermittently contact the surface, the cantilever oscillation amplitude is reduced due to energy loss caused by the tip contacting the surface. The oscillation amplitude of the tip is measured. A digital feedback loop then adjusts the tip-sample separation to maintain a constant amplitude. The reduction in oscillation amplitude is used to identify and measure surface features.

Below we give a summary of the various types of images that can be collected in Tapping Mode:

Height Data: The vertical position of the probe tip is monitored by noting changes in the length of the z-axis on the xyz scanning piezo tube. The input voltage to the scanning piezo tube is proportional to the length of the tube. The change in the z-axis is plotted as a topographical map of the sample surface. Height data is a good measure of the height of surface features but does not show distinct edges of these features.

Phase Data: This type of imaging monitors the change in phase offset, or phase angle, of the oscillating cantilever with respect to the phase offset of the input drive signal (to the drive piezo). The phase of the drive signal is compared to the phase of the cantilever response signal on the photo diode detector. The phase offset between the two signals is defined as zero for the cantilever oscillating freely in air. As the probe tip engages the sample surface, the phase offset of the oscillating cantilever changes by a certain angle with respect to the phase offset of the input drive signal. As regions of differing elasticity are encountered on the sample surface, the phase angle between the two signals changes. These changes in phase

offset are due to differing amounts of damping experienced by the probe tip as it rasters across the sample surface. This phase shift is very sensitive to variations in material properties such as adhesion and viscoelasticity.

Amplitude Data: The amplitude of the cantilever is monitored by the photo diode detector. The RMS value of the laser signal on the y-axis of the detector is recorded for each of the 512 segments on a given raster of the probe tip. These values are plotted as an amplitude map of the sample surface. Amplitude images tend to highlight edges of surface features.

2.2.2.   Transmission Electron Microscopy (TEM)[37,38]

2.2.2.1. Fundamentals of Transmission Electron Microscopy

Transmission electron microscopy (TEM) is one of the most versatile analytical tools for the investigation of polymer microstructures, especially when studying multiphase polymer morphologies and polymer blends. In the 1930´s, it provided the first insight into structural features on a sub-micrometer scale. The transmission electron microscope overcomes the limitation of the optical microscope the spatial resolution of which is limited to about half the wavelength of the visible light.

Presently, the resolution limit in transmission electron microscopy is in the order of about 0.1 nm using an acceleration voltage of about 10^4-10^5 V. Figure 2-4 shows a schematic cross-section of a transmission electron microscope that can be divided into two parts, the illumination and the imaging system.

The former consists of the electron gun and the first and second condenser lenses. Electrons are emitted from a V-shaped heated tungsten filament whereas the emitted electron density is controlled by the voltage applied at the filament. A grid cap fading out parts of the electron emitting cathode allows the generation of a spot-shaped electron beam. A high voltage field accelerates the emitted electrons which reach the system of condenser lenses in the illumination system after crossing the ring anode. These lenses regulate the intensity and refocus the electron beam. The specimen is then hit by an intense, parallel beam of mono-energetic electrons.

The imaging system is build up by the objective lens, the intermediate lens and their corresponding apertures, the projector lens, a phosphor viewing screen, and the photographic film. The most important parts of the imaging system are the objective lens and objective aperture which can either generate a bright-field or a dark-field image of the specimen. The

apertures act as filters mainly for elastically or inelastically scattered or transmitted electrons and are necessary to create a phase contrast in the sample. Specimens of low-density hydrocarbon materials like polymers must be less than 100 nm thick while high-density metals should be less than 20 nm thick. Bright field is the most widely used mode of transmission electron microscopy imaging, selecting the weakly scattered and transmitted electrons by location of the objective aperture on the optic axis. Dark areas on the image correspond to strongly scattering areas in the specimen.
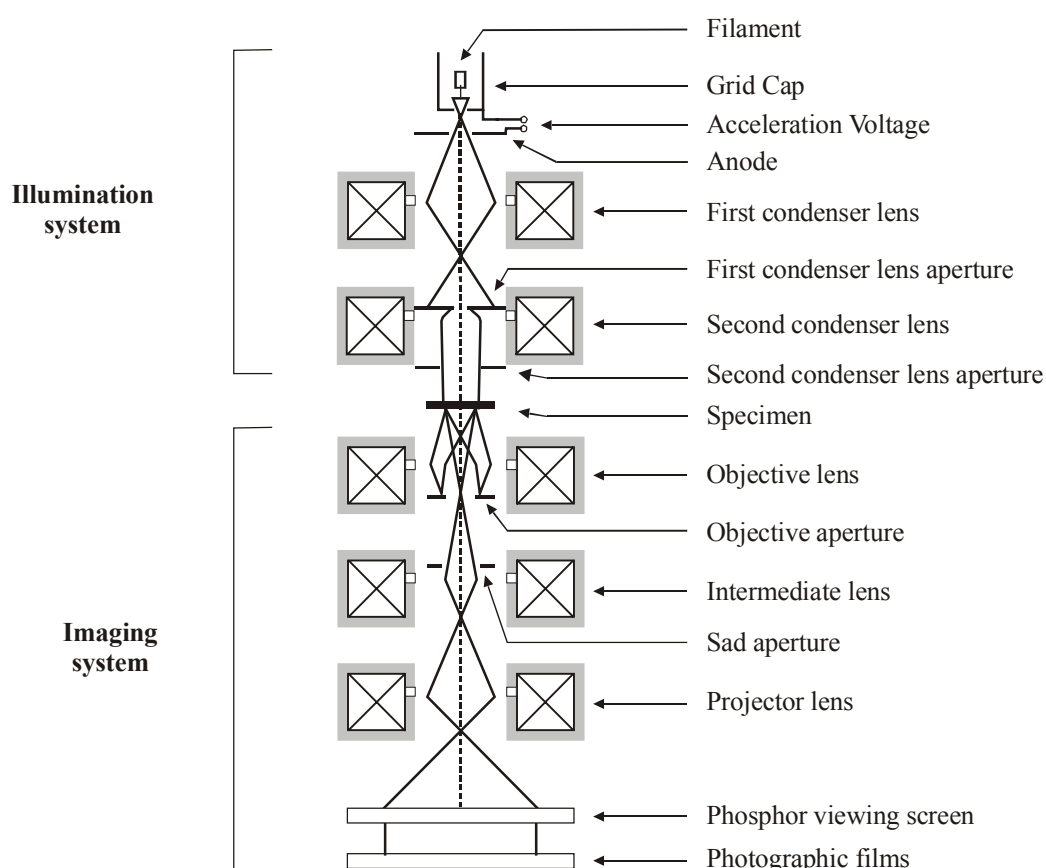
Figure 2-4:   Schematic cross section of a transmission electron microscope[37]

For dark-field imaging the objective aperture is set to collect a portion of the scattered electrons, while the non-scattered or weakly scattered electrons are filtered out by the aperture.

Usually, due to relatively similar electron densities, the contrast between most organic polymers is rather limited and too low for a direct microphase investigation by bright-field or dark-field imaging.[39] A variety of methods is available to impose contrast in the TEM images. Any substance that selectively reacts with or diffuses into one phase of the microstructure can

be used as staining agent. Hereby, the contrast increases with the mass of the staining atom and number of staining sites occupied per volume.

2.2.2.2. Staining of Polymer Samples

Ruthenium tetroxide (RuO_4) is a strong oxidizing agent and reacts with both aromatic and olefinic double bonds.[40-42] The reaction of the staining agent with aromatic double bonds is shown in Figure 2-5.
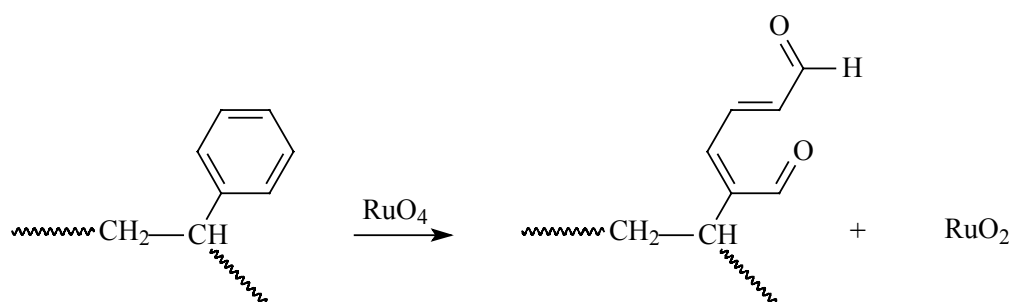
Figure 2-5:   Reaction of RuO$_4$ with aromatic double bonds

The selectivity of RuO_4 strongly depends on the staining time and on the concentration of the vapor. RuO_4 does not react with ester groups present in polymers, like poly(methyl methacrylate). The interfaces in strongly segregated microphase-separated polymers are often stained more strongly by RuO_4 than expected from the corresponding homogenous phase. This observation is explained by an enhanced reactivity of the functional groups due to mechanical tension of the polymer chain at phase interfaces.[43,44]

Typically, RuO_4 vapor is generated by the reaction of hydrated ruthenium trichloride ($RuCl_3 \cdot 3H_2O$) and a 15-20 wt.-% aqueous solution of sodium hypochlorite (NaOCl, Figure 2-6).

$$2\ RuCl_3 \cdot 3\ H_2O\ +\ 8\ NaOCl\ \longrightarrow\ 2\ RuO_4\uparrow +\ 8\ NaCl\ +\ 3\ Cl_2\ +\ 3\ H_2O$$

Figure 2-6:   Generation of ruthenium tetroxide from ruthenium chloride

In order to selectively stain poly(2-vinyl pyridine), iodine is used frequently. Samples are exposed to iodine vapor at room temperature which diffuses into the microstructure and forms a charge-transfer complex with the amino function of the 2-vinyl pyridine moieties. The reaction is shown in Figure 2-7.
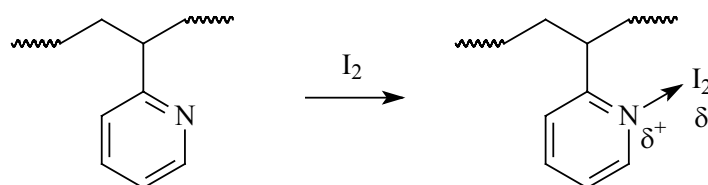
Figure 2-7:   Formation of a charge-transfer complex between iodine and 2-vinyl pyridine.

2.2.2.3. Radiation Damage

For the interpretation of TEM micrographs, one has always to take into account possible structural changes by radiation damage[45].

When the high-energy electrons of the beam pass through the sample, they transfer energy to an electron at the site of interaction. In some cases, the irradiated organic molecules respond by a disruption of specific bonds. If radiation breaks a bond in a polymer that is part of the main chain the material will undergo degradation. This process can continue until the fragments are small enough to volatilize in the vacuum of the microscope. Aromatic compounds are much less sensitive to radiation damage than aliphatic ones due to delocalized excitations.[46] It was shown that in block copolymers containing poly(methyl methacrylate) as one phase, the apparent micrograph does not reflect the real dimensions in the specimen, e.g. the thickness of the lamellae is underestimated from the micrograph[47,48].

2.2.3. Small-Angle X-Ray Scattering (SAXS)

2.2.3.1. Fundamentals of Scattering

Depending on the system being studied and the desired resolution, light, X-ray, or neutron scattering can be used. The basic concepts governing the scattering of different types of electromagnetic waves are very similar although the mode of interaction between waves and particles varies with the wavelength. Therefore, the choice of the radiation strongly depends on the polymer structure. Figure 2-8 presents the general experimental setup of a scattering experiment.
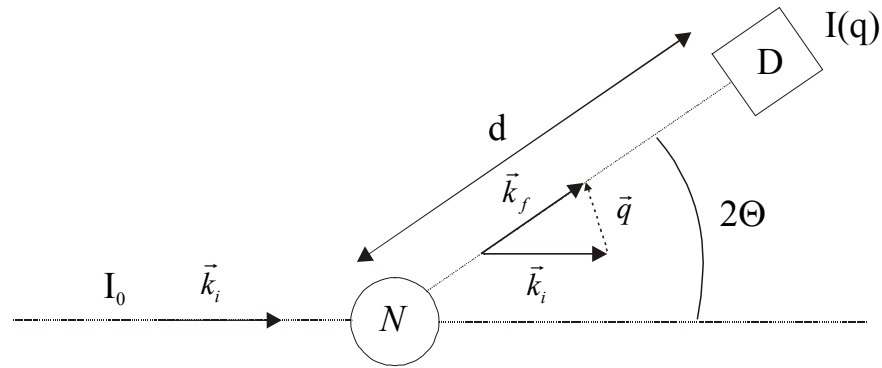
Figure 2-8:   General setup of a scattering experiment

   I_0:   *intensity of the incident beam*
   I(q): *intensity of the scattered beam as a function of q*
   $\vec{k}$: *wave vector [nm⁻¹]*
   d: *distance between scattering object and detector [nm]*
   $\vec{q}$: *scattering vector [nm⁻¹]*
   D: *detector*
   N: *total number of particles*
   Θ: *Bragg scattering angle [°]*

An incident beam of monochromatic radiation with a wavelength λ and an intensity I_0 is partly absorbed or scattered by a sample while the rest is transmitted unchanged. The intensity of the scattered, $I(q)$, waves is registered by a detector D at a distance d while the direction of observation is varied. The scattering vector, $\vec{q}$, is equal to the difference between the wave vectors of the incident, $\vec{k}_i$, and the scattered, $\vec{k}_f$, plane waves. Coherent scattering occurs primarily in the experiments on polymers. The radiation is scattered elastically and, hence, the wave vectors are equal in their magnitude (Equation 2-5).

$$\left|\vec{k}_f\right| \approx \left|\vec{k}_i\right| = \frac{2\pi}{\lambda} \qquad\qquad\qquad \textit{Equation 2-5}$$

  k_f: *wave vector of the scattered beam [nm⁻¹]*
  k_i: *wave vector of the incident beam [nm⁻¹]*
  λ: *wavelength [nm]*

The vector $\vec{q}$ can be defined as the difference $\vec{k}_f$ - $\vec{k}_i$. Isotropic materials are described with the norm of the scattering vector, $\vec{q}$, being a function of the Bragg angle, Θ, as shown in Equation 2-6.

$$\sin \Theta = \frac{|\vec{q}|/2}{|\vec{k}_i|} = \frac{|\vec{q}|/2}{2\pi/\lambda} \qquad with \qquad q = |\vec{q}| = \frac{4\pi \sin \Theta}{\lambda} \qquad\qquad \textit{Equation 2-6}$$

Θ: Bragg angle [°]
$\vec{q}$: scattering vector

In contrast to the coherently scattered X-rays, the incoherently scattered ones result in scattered waves of longer wavelengths. No coherence between the incident and the scattered beam is preserved. This behavior is predominantly observed in wide-angle X-ray scattering (WAXS) experiments.

For coherent elastic scattering of radiation at an angle 2Θ with respect to the incident beam, the intensity, $I(q)$, of the scattered beam is proportional to the square norm of the amplitude, $A(q)$, (Equation 2-7).

$$I(q) \approx |A(q)|^2 \qquad\qquad \textit{Equation 2-7}$$

$I(q)$ intensity of the scattered beam
$A(q)$: amplitude of the scattered beam

As shown in Equation 2-8, the amplitude itself derives from the electron density distribution within the sample.

$$A(q) = \int_V \rho(r) \exp(iqr) dr \qquad\qquad \textit{Equation 2-8}$$

$A(q)$: amplitude of the scattered beam
V: scattering volume of the sample [cm^3]
$\rho(r)$: electron density [C/cm^3]

For materials exhibiting a long-range and periodic order, the amplitude can be defined as the product of the so called lattice factor, $L(q)$, and the structure factor, $F(q)$, (Equation 2-9).

$$A(q) \approx |L(q)| \cdot |F(q)| \qquad\qquad \textit{Equation 2-9}$$

$A(q)$: amplitude of the scattered beam
$L(q)$: lattice factor
$F(q)$: structure factor

2.2.3.2. Small-Angle X-Ray Scattering on Microphase Separated Block Copolymers

Small-angle X-ray scattering (SAXS) is one of the most widely used techniques available to study polymer structures on a scale of 2-200 nm. While transmission electron microscopy allows the investigation of the microphase in local areas of a few micrometers, SAXS provides average information about bulk properties of the segregated microdomains within the sample. The X-rays scattered from different electrons interfere with each other and generate a diffraction pattern. Due to the interaction of the beam with the electrons, segments of the block copolymers need to be different in their electron density in order to allow a monitoring of the morphology by SAXS. Otherwise, the regularity of the morphology cannot be detected in form of well-defined intensity maxima in the scattering profile. In a first approximation, the electron density can be calculated using Equation 2-10.

$$\rho_{ei} = \frac{N_A \rho_i Z_{ei}}{m_i}$$

Equation 2-10

ρ_{ei}:   *electron density of component I [C/cm^3]*
N_A: *Avogadro's number [mol^{-1}]*
ρ_I: *density of component I [g/cm^3]*
Z_{ei}:   *number of electrons of component I [C]*
m_i: *molar mass of component I [g/mol]*

The scattered intensity pattern arising from a microphase-separated block copolymer is similar to the diffraction pattern obtained from a crystalline solid. However, the Bragg diffraction peaks occur at smaller scattering angles and show a broadening of the peaks due to the diminished regularity as compared to a regular crystalline lattice.[49] Both factors in Equation 2-9 must be defined in relation to the specific characteristics of block copolymers compared to crystals.

When the lattice has long-range periodicity, the lattice factor, $L(q)$, provides information about the spatial distribution of the scattering objects (spheres, cylinders, lamellae) and can be described as a linear array of delta functions for a particular set of lattice planes. The spacing of the delta functions is related to the distance of the lattice by an inverse proportionality.[50] Depending on the type of lattice, only certain peaks can be found corresponding to allowed reflexes of the particular structure. Bragg's Equation (Equation 2-11) describes the condition for the interference of the beam scattered at two different planes in the crystal.

$$n\lambda = 2d_{hkl} \sin \Theta \qquad\qquad\qquad\qquad \text{\textit{Equation 2-11}}$$

Θ: *Bragg angle [°]*
n: order of the reflex
d_{hkl}: *distance between two planes (hkl) [nm]*

Equation 2-11 together with the definition of the size of the scattering vector (Equation 2-6) determines the spacing d_{hkl} (Equation 2-12) from the diffraction pattern of the crystal.

$$d_{hkl} = \frac{2\pi n}{q} \qquad\qquad\qquad\qquad \text{\textit{Equation 2-12}}$$

The observed values for the spacing can be compared to the characteristic sequences of model lattices and the ratio of the characteristic peaks, d_{hkl}, with the first peak, d_{100}. Table 2-1 presents the ratios of Bragg spacings for different spatial arrangements, such as lamellae, hexagonally packed cylinders and body centered cubic (bcc) spheres.
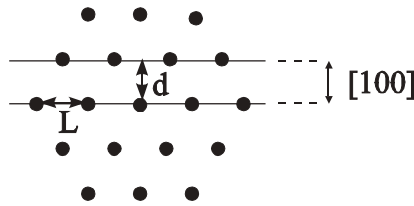
Figure 2-9:   Cylindrical long period L and distance d in a hexagonal lattice.

L: cylindrical long period determined by TEM, shortest distance between two related cylinders [nm]
d: distance between parallel planes obtained by the reflex q_{100} for a hexagonal lattice [nm]

Morphology		Scattering Maxima					
		1	2	3	4	5	6
Spheres	d_{hkl}/d_{100}	1	0.707	0.577	0.5	0.447	0.408
bcc	q_{hkl}/q_{100}	1	$\sqrt{2}$	$\sqrt{3}$	$\sqrt{4}$	$\sqrt{5}$	$\sqrt{6}$
	hkl	110	200	211	220	310	222
Cylinders hexagonal	d_{hkl}/d_{100}	1	0.577	0.5	0.378	0.333	0.289
	q_{hkl}/q_{100}	1	$\sqrt{3}$	$\sqrt{4}$	$\sqrt{7}$	$\sqrt{9}$	$\sqrt{12}$
	hkl	100	110	200	210	300	320
Lamellae	d_{hkl}/d_{100}	1	0.5	0.333	0.25	0.20	0.167
	q_{hkl}/q_{100}	1	2	3	4	5	6
	hkl	100	200	300	400	500	600

Table 2-1:   Ratios of consecutive Bragg spacings for different model morphologies:
*   Body centered cubic spheres (bcc), hexagonally packed cylinder*
*   and lamellae*

In a hexagonally packed lattice, the distance d_{100} resulting from the scattering peak q_{100} corresponds directly to the shortest distance between two parallel neighboring lattice planes (Figure 2-9).

While TEM also provides the shortest distance between two cylinders, L, SAXS only yields information about the distance between two neighboring planes. For a hexagonal symmetry of the structure, both values are correlated by Equation 2-13.

$$d_{100} = \frac{\sqrt{3}}{2} L$$

Equation 2-13

d_{100}: *distance between two parallel planes [nm] (Figure 2-9)*

The structure factor (Equation 2-9) depends on the geometric shape of an object and derives from a Fourier transformation of an individual domain structure. For solid spheres, cylinders, and lamellae, the structure factors are rapidly oscillating functions.[51] Spheres can be described by trigonometric functions (Equation 2-14).[52]

$$F_s(q) \propto \frac{\sin qr - \sin qr \cos qr}{(qr)^3}$$

Equation 2-14

$F_S(q)$:   *structure factor of a homogenous sphere*
r: *radius of the sphere [nm]*
q: *scattering vector*

A Bessel function of first order is used to describe the structure factor for cylinders, which have negligible diameters compared to their lengths (Equation 2-15).

$$F_C(q) \propto \frac{J_1(qr)}{qr}$$

Equation 2-15

with

$$J_1(qr) = \sum_{v=0}^{\infty} \frac{(-1)^v}{v!\,\Gamma(v+2)} \left(\frac{qr}{2}\right)^{1+2v}$$

F_C: *structure factor of a homogenous cylinder*
r: *radius of the cylinder [nm]*
J_1:   *Bessel function of first order*

Both functions strongly depend on the product of the scattering vector, q, and the radius, r, of the spheres or cylinders. If the minimum in the function is equal to zero, no diffraction peak will be observed even if it corresponds to a scattering vector which represents a solution

for the delta function of the lattice vector. Thus, the absence of a diffraction peak in an expected sequence may be the result of a weak structure factor.

2.2.3.3. Setup of Synchrotron-SAXS Beamline (ID02A, ESRF, Grenoble)

The in-situ Synchrotron-SAXS measurements in this work were carried out at the ID02A beamline at the European Synchrotron Radiation Facility (ESRF, Grenoble, France). A schematic depiction of the beamline is shown in Figure 2-10. The typical photon flux routinely obtained at the ID02 sample position is 10^{13} photons/sec, corresponding to twice the full width at half maximum beam size $(0.2 \text{ mm})^2$ and energy bandwidth $\Delta E/E = 2\text{x}10^{-4}$. The operating energy range was 12.5 keV, corresponding to a wavelength of 0.1 nm , at which the highest photon flux is obtained. The direction of the X-ray beam (cross section: 200 μm) was perpendicular to the vector of the applied electric field.

The detector system with a standard 2-dimensional SAXS camera is housed in a 10 m evacuated flight tube. For most experiments an image intensified CCD detector is used, which can handle the full X-ray flux. The CCD is capable of acquiring up to 10 frames of 1024x1024 pixels per second and a sequence of 125 frames can be acquired with this time resolution. Prior to data analysis, background scattering was subtracted from the data and corrections were made for spatial distortions and for the detector efficiency.
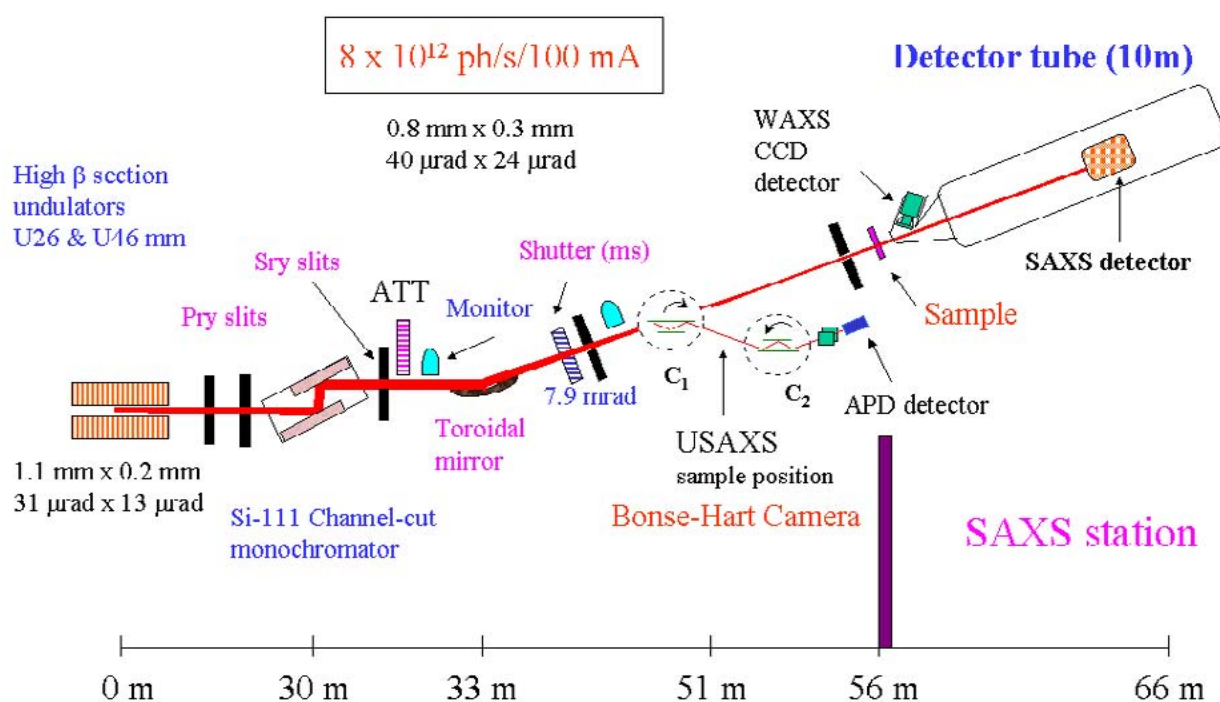

Figure 2-10: Setup of ID02A High-Brilliance Beamline at the ESRF, Grenoble (France)

References

[1] Schlenk, W.; Appenrodt, J.; Michael, A.; Thal, A. *Chem. Ber.* **1914**, *47*, 473.

[2] Matthews, F.E.; Strange, E.H. *British Patent* **1910**, *24*, 790.

[3] Harries, C. *Justus Liebigs Ann. Chem.* **1911**, *383*, 213.

[4] Szwarc, M. *Nature*, **1956**, *178*, 1168.

[5] Szwarc, M.; Levy, M.; Milkovich, R. *J. Am. Chem. Soc.,* **1958**, *78*, 2656.

[6] Szwarc, M.; *Carbanions, Living, Polymers and Electron Transfer Processes, Interscience, New York*, **1968**.

[7] Bywater,S.; *Adv. Polym. Sci.* **1979**, *30*, 89.

[8] Rempp, P.; Volkov; V. I.; Parrod, J.; Sadron, C. *Bull. Soc. Chim. Fr.* **1960**, 919.

[9] Quirk, R.P.; Yoo, T.; Lee, B. *J. Macromol. Sci. Pure Appl. Chem.* **1994**, *A31*, 911.

[10] Ceresa, R. J.(ed.); *Block and Graft Copolymerization, Vol. 1+2*, Wiley-Intersience, New York **1973**.

[11] Dreyfuss, P.; Quirk, R.P.; *Encyclopedia of Polymer Science and Engineering, Vol. 7*, p.551, Wiley-Intersience, New York, **1985**.

[12] Rempp, P. F.; Lutz, P. J.; *Comprehensive Polymer Sience, Vol. 6*, p.403, Pergamon Press, Elmsford, **1989**.

[13] Quirk, R.P.; Kinning, D.J.; Fetters, L.J.; *Comprehensive Polymer Science, Vol. 7*, Pergamon Press, Elmsford, **1989**.

[14] Quirk, R.P.; Yin, J.; Guo, S.-H.; Hu, X.-W.; Summers, G.; Kim, J.; Zhu, L.-F.; Schock, L.E. *Makromol. Chem. Macromol. Symp.* **1990**, *32*, 47.

[15] Morton M.; Fetters, L. J. *Macromol. Rev.* **1967**, *2*, 71.

[16] Fontanille, M.; *Comprehensive Polymer Science, Vol. 3*, p.425, Pergamon Press, Elmsford, **1989**.

[17] Miyamato, M.; Sawamoto, M.; Higashimura, T. *Macromolecules* **1984**, *17*, 265.

[18] Doi, Y.; Keii, T. *Adv. Polym. Sci.* **1986**, *73/74*, 201.

[19] Amass, A.J.; Beevers, M.S.; Farren, T.R.; Stowell, J.A. *Makromol. Chem.* **1987**, *188*, 2535.

[20] Webster, O.W.; Hertler, W.; Sogah, D.Y.; Farnham, W.B.; Rajen-Babu, T.V. *J. Am. Chem. Soc.* **1983**, *105*, 5706.

[21] Müller, A.H.E. *Makromol. Chem., Macromol. Symp.* **1990**, *32*, 87.

[22] Georges, M.K.; Veregin, R.P.N.; Kazmaier, P.M.; Hamer, G.K. *Macromolecules* **1993**, *26*, 2987.

[23] Matyjaszewski, K.; Wang, J.-L.; Grimaud, T.; Shipp, D.A. *Macromolecules* **1998**, *31*, 1528.

[24] Waack, R.; Rembaum, A.; Coombes, J. D.; Szwarc, M. *J. Am. Chem. Soc.* **1957**, *79*, 2026.

[25] Flory, P. J. *J. Am. Chem. Soc.* **1940**, *62*, 1561.

[26] Schulz, G.V. *Z. Elektrochem.* **1956**, *60*, 199.

[27] Fetters, L.J.; *Encyclopedia of Polymer Science and Engineering, Vol. 10*, p.19 Wiley-

Intersience, New York, **1985**.

[28] Billingham, N.C.; *Comprehensive Polymer Science*, *Vol. 3*, p.43, Pergamon Press, Elmsford, **1989**.

[29] Antoun, S.; Teyssie, Ph.; Jerome, R. *J. Polym. Sci., Part A: Polym. Chem.* **1997**, *35*, 3637.

[30] Nagasaki, Y. *Recent Res. Dev. Macromol. Res.* **1997**, *2*, 11.

[31] Bywater, S.; „Anionic Polymerization", Chap.2 in: *Progress in Polymer Science*, *Vol. 4*, Jenkins, A D. (ed.), Pergammon Press, New York, **1975**.

[32] Fontanille, M.; *Comprehensive Polymer Science*, *Vol. 3*, p.365, Pergamon Press, Elmsford, **1989**.

[33] Bywater, S.; *Encyclopedia of Polymer Science and Engineering*, 2nd ed., *Vol. 2*, p.1, John Wiley and Sons, New York, **1986**.

[34] Morton, M.; „*Anionic Polymerizations: Prinziples and Practice*", Academic Press, New York, **1983**.

[35] Young, R.N.; Quirk, R.P.; Fetters, L.J. *Adv. Polym. Sci.* **1984**, *56*, 1.

[36] Swarc, M.; Smid, J.; "*The Kinetics of Propagation of Anionic Polymerization and Copolymerization*", Chap. 5 in "*Progress in Reaction Kinetics*", *Vol. 2*, G. Porter (ed.), Pergamon Press, Oxford, **1964**.

[37] Thomas, E.L.; *Electron micrsocopy*, Chap. 5 in *Encyclopedia of Polymer Science & Engineering*, p. 644, **1985**.

[38] Tsuji, M.; *Comprehensive Polymer Science* **1989**, *V1*, 785.

[39] Sawyer, L.C.; Grubb, D.T.; *Fundamentals of microscopy*, Chap. 2 in *Polymer Microscopy*, Chapman & Hall, London, **1996**.

[40] Trent, J.S.; Scheinbein, J.I.; Couchman, P.R. *J. Polym. Sci., Polym. Lett. Ed.* **1981**, *19*, 315.

[41] Trent, J.S.; Scheinbein, J.I.; Couchman, P.R. *Macromolecules* **1983**, *16*, 589.

[42] Vitali, R.; Montani, E. *Polymer* **1980**, *21*, 1220.

[43] Auschra, C.; Stadler, R. *Macromolecules* **1993**, *26*, 2171.

[44] Auschra, C.; Stadler, R. *Macromolecules* **1993**, *26*, 6364.

[45] Grubb, D. T. *J. Mat. Sci.* **1974**, *9*, 1715.

[46] Pullman, B.; Pullman, A.; *Quantum Biochemistry,* Interscience, New York, **1963**.

[47] Breiner, U.; Krappe, U.; Thomas, E.L.; Stadler, R. *Macromolecules* **1998**, *31*, 135.

[48] Abetz, V.; Goldacker, T. *Macromol. Rapid Commun.* **2000**, *21*, 16.

[49] Christ, B. *J. Polym. Sci. Polym. Phys. Ed.* **1973**, *11*, 635.

[50] Tadakoro, H.; *Structures of Crystalline Polymers*, Wiley-Interscience, New York, **1979**.

[51] Oster, G.; Riley, D. P.; *Acta Crystallogr.* **1952**, *5*, 272.

[52] Glatter, O.; Kratky, O.; *Small Angle X-ray Scattering*, Academic Press, **1981**.

Chapter 3

Nanoscopic Surface Patterns
from Functional ABC Triblock Copolymers[1]

Abstract

We synthesized analogous series of monodisperse ABC triblock copolymers with symmetrical end blocks A/C and different short middle blocks B (5-10 wt.-%) with varying polarities by sequential anionic polymerization; i.e. polystyrene-*b*-poly(2-vinylpyridine)-*b*-poly(methyl methacrylate) (PS-*b*-P2VP-*b*-PMMA) and polystyrene-*b*-poly(2-hydroxyethyl methacrylate)-*b*-poly(methyl methacrylate) (PS-*b*-PHEMA-*b*-PMMA). Thin (thickness ~ 20 nm) and ultrathin films (thickness ≤ 7 nm) were prepared by either dip-coating or adsorption from solution onto silicon wafers. The copolymer films were investigated by scanning force microscopy. In thin films, the polar middle block adsorbs preferentially to the polar substrate, resulting in a polymer film surface that exclusively consists of PS and PMMA microdomains. In ultrathin films the two polar B and C blocks behave like a single B block resulting in structures which can be described by recent scaling laws. The lateral spacing and the morphology of the structures can be controlled by film thickness and A/C block length.

3.1. Introduction

In recent years, the use of block copolymers for surface patterning has attracted increasing attention[2,3,4,5,6]. Well-defined laterally patterned surfaces are important for a variety of technological applications, e.g. as compatibilizers for polymer blends or as templates for growing biological cells with controlled shapes and sizes[7]. In addition, patterned polymer substrates can also be used as templates in fabrication of optoelectronic devices through the selective adsorption of a conducting material[8], which results in a system of alternating polymeric and metallic stripes with domain spacings in the tens of nanometers scale, an order of magnitude smaller than typically achieved through photolithography. The high potential of polymer-patterned substrates for lithographic purposes has recently been demonstrated by Spatz *et al.*, who deposited   polystyrene-*b*-poly(2-vinylpyridine) (PS-*b*-P2VP) block copolymers on mica and created highly ordered hexagonal arrays of PS dots on the surface. These were used as templates for lithographic masks[9,10]. Aside from these practical applications, laterally patterned polymer surfaces can be of use as model systems for the study of wetting and dewetting phenomena on heterogeneous substrates[11].

To this point, most of the experiments described in the literature involved diblock copolymers only, disregarding the potential advantage of ABC triblock copolymers for the generation of lateral structures in thin films. The latter was recently pointed out by Pickett and Balazs in the context of self-consistent-field calculations for the case of symmetric ABC triblock copolymers[12]. The authors showed that a perpendicular alignment of the lamellae with respect to the plane of the films is expected, when the boundary surfaces preferentially attract the middle block B. In case of a sufficiently strong interaction between the walls and the adsorbing block B, the A and C end blocks may even be expelled from the walls, resulting in homogeneous layers of B next to the walls and a laterally microphase-separated layer of A and C in the film center. Given that the end blocks have a lower surface energy than the middle block B, these results suggest that one may remove one of the walls and expect that the film structure consists of a homogeneous B layer adsorbed at the substrate covered with a laterally microphase-separated A/C striped surface layer. First experiments along these lines were recently reported[13].

The aim of the present work is to generate striped surfaces of controlled size and domain spacing in the nanometer range by use of suitably chosen ABC triblock copolymers. Control over the lateral dimensions is gained by variation of film thickness and A/C block length. Thin and ultrathin films of two series of block copolymers are investigated by Tapping

Mode™ SFM. The experimental results are discussed in view of recent scaling considerations developed in the context of pattern formation in diblock copolymer thin films[14,15].

3.2. Experimental Section

The block copolymers were synthesized by sequential anionic polymerization (see Scheme 3-1). The deprotection of the hydroxyl group of the PHEMA block was accomplished by precipitating the polymer into technical grade methanol. Gel permeation chromatography (GPC) proved that the polymerization yielded monodisperse triblock copolymers (Figure 3-1). The functional block copolymers were synthesized to give two series of polymers with constant relative amounts of polystyrene, poly(methyl methacrylate) ($\sim$ 45 wt-%) and the functional middle block (consisting of 5-10 wt-% poly(2-hydroxyethyl methacrylate) or poly(2-vinylpyridine), respectively). In each series only the overall molecular weight of the whole block copolymer was varied as shown in Table 3-1. The composition was calculated from ^{1}H-NMR of the block copolymer using GPC results for the corresponding PS precursor, calibrated with narrowly distributed PS standards.
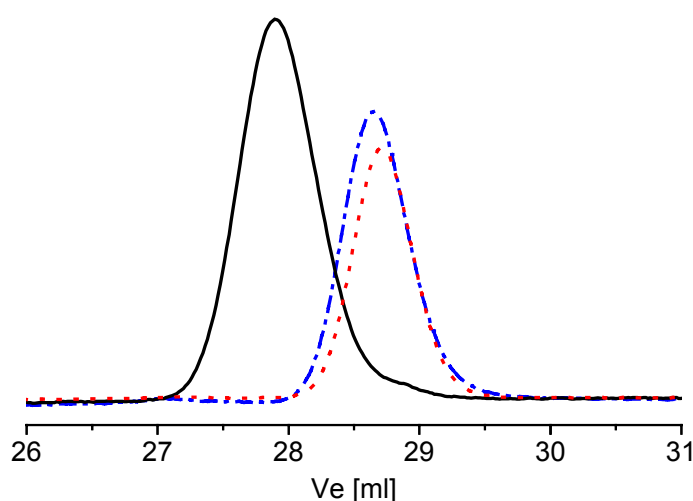
Figure 3-1: GPC trace (RI signal) of triblock copolymer $S_{47} H_{10} M_{43}{}^{82}$ (━) and its precursors PS (.....) and PS-b-PHEMA (.-.-.). M_n = 82300 g/mol, M_w/M_n = 1.04

3.2.1. Solvents and Materials

Unless noted, all chemicals were purchased from Aldrich and used without further purification.

Styrene was stirred twice over calcium hydride for 24 h and finally, after overnight treatment with MgBu$_2$ (bright yellowish color), it has been condensed into an ampoule and set under nitrogen for storage.

Trimethylsilyl protected 2-hydroxyethyl methacrylate (TMS-HEMA) was stirred twice over calcium hydride for 24 h and purified by reduced pressure distillation. Prior to use it was filtered over a 1 cm column filled with neutral alumina.

2-Vinylpyridine was treated with triethyl aluminium for 3 h and condensed into a Schlenk flask, from which it was taken directly for the polymerization procedure.

Methyl methacrylate was stirred with triethyl aluminium for 2 h, condensed into a glass ampoule and finally stored under nitrogen.

The solvent tetrahydrofuran (THF) was distilled over calcium hydride for 48 h and finally refluxed over potassium under nitrogen for another 2 days.

3.2.2. Synthesis of 2-[(Trimethylsilyl)oxy]ethyl methacrylate (TMS-HEMA)

The trimethylsilyl protecting group was introduced as previously reported by Hirao *et al.*[16] using hexamethyldisilazane and trimethylsilyl chloride.

3.2.3. Block Copolymerizations

1 l freshly distilled THF was cooled down to $-78\,°C$. 0.36 ml *sec*-BuLi (1.55 molar solution in *n*-hexane/cyclohexane) were injected, before 23.4 g styrene were added. After 60 minutes of polymerization the styryl anions were capped with 0.17 ml 1,1-diphenylethylene (DPE), which results in a deep red colour of the reaction mixture. One hour later, the polymerization was resumed by injection of 7.9 ml (7.3 g) TMS-HEMA, which leads to immediate disappearance of the red colour. After additional 2 hours, 24 g MMA were added quickly and polymerized for another 45 minutes. Finally, the reaction was terminated with 1 ml degassed methanol.

The polymer was precipitated in 5 l methanol, which also leads to deprotection of the PHEMA block. Then the product was redissolved in THF and reprecipitated two more times into *iso*-propanol and dried under vacuum at room temperature.

A similar procedure was chosen for the preparation of the polystyrene-*b*-poly(2-vinylpyridine)-*b*-poly(methyl methacrylate) block copolymers. After capping the styryl anions with DPE, the 2-vinylpyridine was allowed to polymerize for 1 h. Before addition of MMA, DPE was added again and reacted overnight in order to achieve a complete capping reaction.

The block ratio was determined by ^{1}H-NMR spectra using the integrated aromatic signals of the polystyrene block in combination with the GPC results of the styrene precursor.
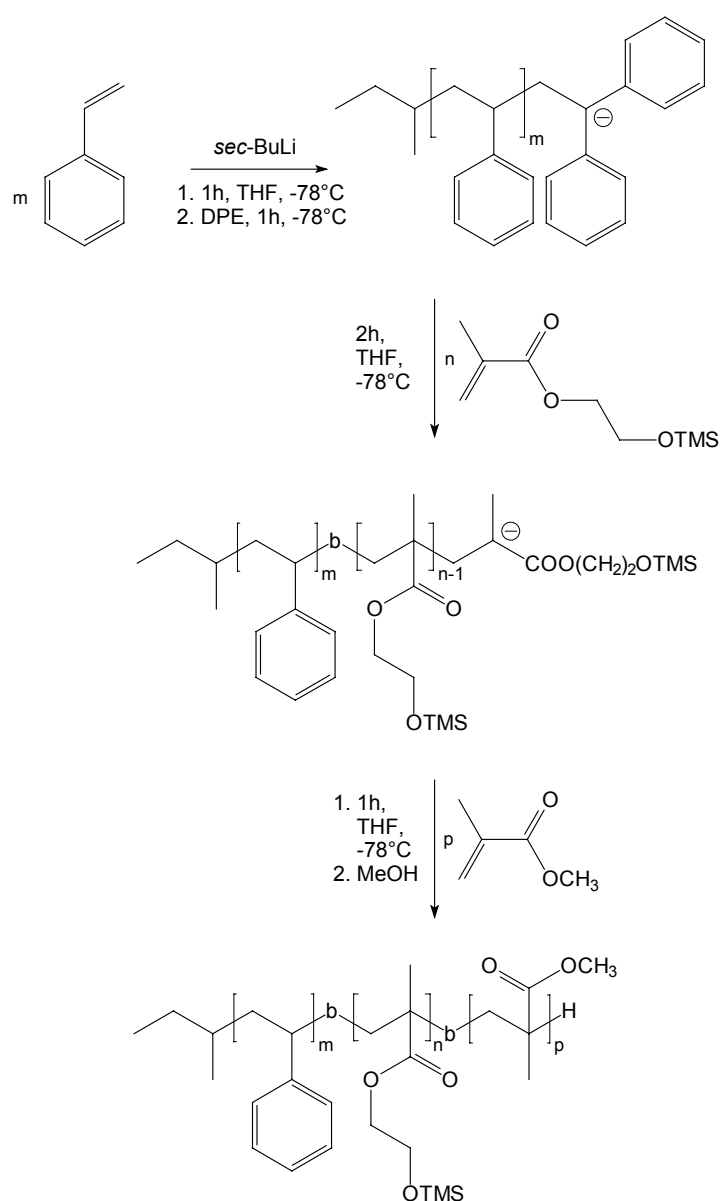
Scheme 3-1:   *Synthesis of PS-b-PHEMA-b-PMMA (SHM) triblock copolymers.*

3.3. Methods

Polymer Analysis: GPC measurements were performed using a set of 30 cm SDV-gel columns of 5 µm particle size having 10^5, 10^4, 10^3 and 10^2 Å pore size and dual detectors (RI and UV [$\lambda = 254$ nm]). The solvent was THF at room temperature with an elution rate of 1 ml/min. Narrowly distributed polystyrene samples were used as calibration standards.

^{1}H-NMR spectra were acquired on a 250 MHz Bruker AC 250 instrument using CDCl$_3$ or THF-d$_8$ as solvents and tetramethylsilane (TMS) as internal standard. The molecular weights of the B and C blocks were calculated using the block copolymer composition determined by

NMR and the polystyrene molecular weights obtained from GPC.

Polymer	M_n (S) [kg/mol]	M_n (H/2VP) [kg/mol]	M_n (M) [kg/mol]	M_w/M_n (GPC)	ΣM_n (total) [kg/mol]
$S_{47}H_{10}M_{43}{}^{82}$	38.7	8.4	35.2	1.04	82.3
$S_{46}H_4M_{50}{}^{134}$	61.5	5.2	67.7	1.06	134.4
$S_{67}H_6M_{27}{}^{129}$	86.4	8.0	34.1	1.02	128.5
$S_{51}2VP_5M_{44}{}^{110}$	56.2	5.9	48.2	1.06	110.3
$S_{48}2VP_5M_{47}{}^{180}$	85.8	8.6	85.5	1.05	179.9
$S_{56}2VP_6M_{38}{}^{299}$	168.4	16.6	113.6	1.05	298.6

Table 3-1:   GPC data of the synthesized block copolymers.
The subscript indicates the weight fraction of the corresponding blocks. The superscript denotes the total M_n in kg/mol.

Sample Preparation: Thin polymer films were prepared on polished silicon wafers by dip-coating from 1 mg/ml solutions of the block copolymers in THF. To study ultrathin films, the silicon wafers were exposed to 1 mg/ml solutions of the polymers for 3-4 days, which led to adsorption of the block copolymer onto the polar substrate. Subsequently, the wafers were rinsed 4 times with 5 ml THF.

Prior to use, the Si wafers were rinsed in organic solvents (THF, chloroform and acetone) and subsequently treated with a beam of CO_2 crystals ("snow jet™") to remove any organic residues from the surface.

Scanning Force Microscopy: SFM images were taken on a Digital Instruments Dimension 3100 microscope operated in Tapping Mode™ (free amplitude of the cantilever ≈ 20 nm, amplitude set point ≈ 0.98). The standard silicon nitride probes were driven at 3 % offset below their resonance frequencies in the range of 250-350 kHz. Height and phase images were taken at scanning speeds of around 6 μm/sec.

Transmission Electron Microscopy: The bulk morphology of the block copolymers was examined using TEM. Films (around 1 mm thick) were cast from 5 wt.% solutions in THF and allowed to evaporate slowly for 5 days. The as-cast films were dried for one day in a vacuum oven at room temperature followed by annealing at 140 °C for at least one week under vacuum. Thin sections were cut at room temperature using a Reichert-Jung Ultracut E microtome equipped with a diamond knife. In order to enhance the electron density contrast

between polystyrene and the methacrylic blocks, the sections were exposed to RuO_4 vapor for 45 minutes, which leads to a preferential staining of the polystyrene block. Bright field TEM was performed using a Zeiss electron microscope (CEM 902) operated at 80 kV.

Small Angle X-Ray Scattering: SAXS measurements were performed using a Bruker-AXS Nanostar instrument with a Siemens Kristalloflex 760 X-ray source (Cu K_α radiation: 1.541 Å) operated at 40 mA and 40 kV and a 2D Histar detector.

Scanning Electron Microscopy: SEM was performed using a LEO 1530 Gemini instrument equipped with a field emission cathode with a lateral resolution of approximately 2 nm. The acceleration voltage was 1 kV. Prior to the measurements the films were stained with RuO_4 vapor for 45 minutes.

Evaluation of characteristic length scales and estimation of experimental errors:

The lateral spacing of the thin film structures was determined from the reciprocal of the maximum intensity position of the Fourier transform of a 3 x 3 μm^2 SFM image. The Fourier transform was calculated using the software supplied with the microscope (version 4.42r4). The uncertainty of the lateral dimensions was estimated from the half-width of the peak in the Fourier transform. The film thickness was determined by SFM scans in a region where the polymer film had been partially removed by a scratch. At least 20 single cross sections were taken at different locations at the step.

The lateral patterns in the ultrathin films were evaluated with respect to the mean stripe-to-stripe or island-to-island half-distance D, the mean height H, the mean island radius or stripe half-width R and the number of aggregated PS chains n_{PS} in an island or defined section of a stripe (see Scheme 3-2). The mean half-distance D was determined using Fourier transform as described above for the thin film structures. In the case of the uniform stripe morphology, the average of at least 15 single stripe height values obtained from the SFM height images was taken as the mean stripe height H. For the island morphology, the tool *Particle Analysis* of the above mentioned commercial software was used to determine the mean height H from a 3 x 3 μm^2 SFM height image. In both cases, the experimental uncertainty was estimated from the statistical scattering of the single island/stripe height values.

PS

PMMA

R

D

H
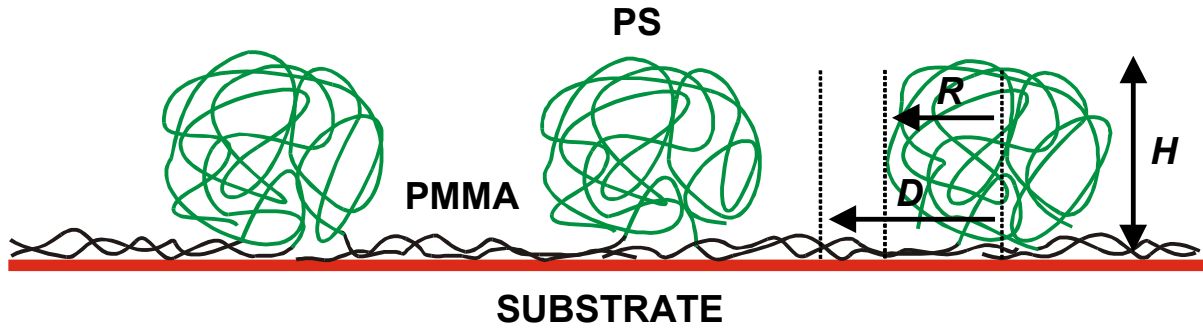
SUBSTRATE

Scheme 3-2:   *Schematic representation of a cross-section through an ultrathin film of PS-b-PMMA diblock copolymers adsorbed onto a silicon substrate.*

The mean radius R of the islands was determined applying *Particle Analysis* of the Nanoscope III software 4.42r4 to a 3 x 3 µm^2 SFM height image with a constant threshold height of 1 nm. The average of at least 15 single stripe half-widths values was taken as the mean stripe half-width R. In both cases, the error ΔR was estimated from the statistical scattering of the single island/stripe R values. For a correct evaluation of the mean radii or half-widths R, one has to take into account the convolution with the curvature of the tip apex, which causes a systematic error by enlarging the lateral dimensions of elevated objects by roughly the tip apex, which itself varies by at least 10 % between different tips. In this study tips were changed regularly to avoid artifacts due to tip contamination. We assume that all tips had a tip radius of $t = 10$ nm by which the imaged objects are enlarged. This value was subtracted from the measured radii and half-width values R.

H

$2R$

R
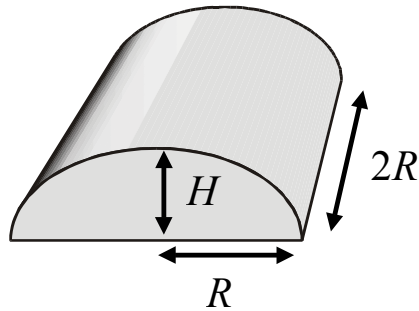
Scheme 3-3:   *Schematic representation of a stripe section with a base of 2R x 2R.*

The number of aggregated PS chains n_{PS} in an island or defined section of a stripe was calculated using the following expressions, assuming a spherical cap-like shape of the islands. The volume of a stripe section was modelled as a cylindrical cap with a rectangular base of *2R x 2R* and a height H (see Scheme 3-3). For the density of PS we assume $\rho = 1.1$ g/cm^3.

(a) Islands:

$$n_{PS,Island} = \frac{\frac{\pi}{6}H\left(3R^2 + H^2\right)\rho N_A}{M_n(PS)} \quad (1)$$

(b) Stripes:

$$n_{PS,Stripes} \approx \frac{\left[\frac{(R^2+H^2)}{H}\left(\sqrt{R^2+\frac{4}{3}H^2}-R\right)+2RH\right]R\rho N_A}{M_n(PS)} \quad (2)$$

with N_A and $M_n(PS)$ being the Avogadro number and the molecular weight of the PS block, respectively. We note that the estimate for the aggregation number of the stripe pattern $n_{PS,Stripes}$ is based on an approximation for the volume of the cylindrical cap, which leads to an error of less than 3 %.

3.4. Results and Discussion

3.4.1. Bulk Morphology of ABC Block Copolymers

The bulk morphology of the block copolymers was investigated using TEM and SAXS as described above. All polymers except $S_{67} H_6 M_{27}^{129}$ (which shows a cylindrical microdomain structure) exhibit a lamellar morphology with a characteristic lamellar spacing L_0 ranging between 40 and 100 nm. The L_0 values determined by the two independent methods are shown in Table 3-2.

3.4.2. Thin Films of ABC Block Copolymers

Thin films were produced on polished silicon wafers by dip-coating from dilute (1 mg/ml) solutions of the block copolymers in tetrahydrofuran (THF). Subsequently, the films were dried at room temperature.

Figure 3-2a-d shows typical SFM topography and phase images of PS-b-PHEMA-b-PMMA and PS-b-P2VP-b-PMMA triblock copolymers. All dip-coated samples exhibit a well defined worm-like surface structure both in the height and in the phase images. Vacuum annealing (5d at 140 °C) does not lead to significant changes in surface morphology. The characteristic lateral spacings of all samples were obtained from Fourier transforms of the SFM images as described above. Film thicknesses as determined by SFM

scans range between 14 and 30 nm which is well below L_0 for each individual sample (Table 3-2).
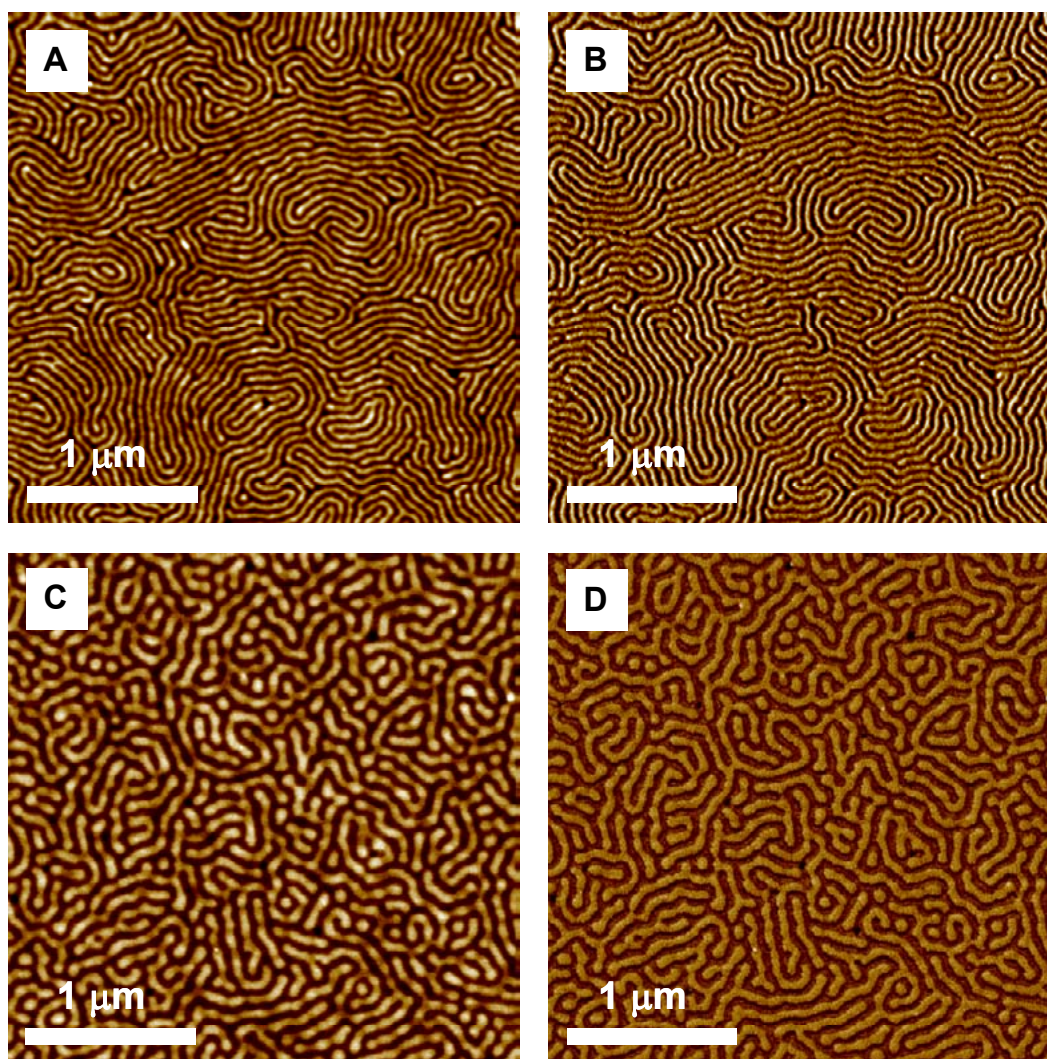
Figure 3-2:   *SFM topography (a,c) and phase images (b,d) of thin films dip-coated from 1 mg/ml THF solutions onto a polished silicon wafer: (a, b) 15 nm thick film of $S_{46} H_4 M_{50}^{134}$;*
(c, d) 25 nm thick film of $S_{56} 2VP_6 M_{38}^{299}$. Topography: 8 nm, Phase: 8 °.

In the following, we shall try to establish a microscopic model of the thin film morphology responsible for the observed surface structures. We expect the polar middle block B (either PHEMA or P2VP) to strongly interact with the native oxide layer on top of the silicon substrate. Therefore we may assume that only polystyrene (PS) and poly(methyl methacrylate) (PMMA) microdomains are present at the film surface. This notion is supported by the following considerations.

Differences in the solubility of the different components of a block copolymer lead to well-defined topographical features at the film surface[13,17]. It was found that after spin- or dip-coating domains rich in the polymer with the lower solubility tend to protrude over the ones rich in the polymer with the higher solubility. As THF is a slightly better solvent for PS than

for PMMA, we expect the PMMA microdomains to protrude over the PS phase. We may therefore identify the protruding features in Figure 3-2 as PMMA microdomains. The mean height difference between the protrusions (PMMA) and the depressions (PS) ranges between 2 ... 4 nm depending on the size of the PS and PMMA blocks of the respective polymer.
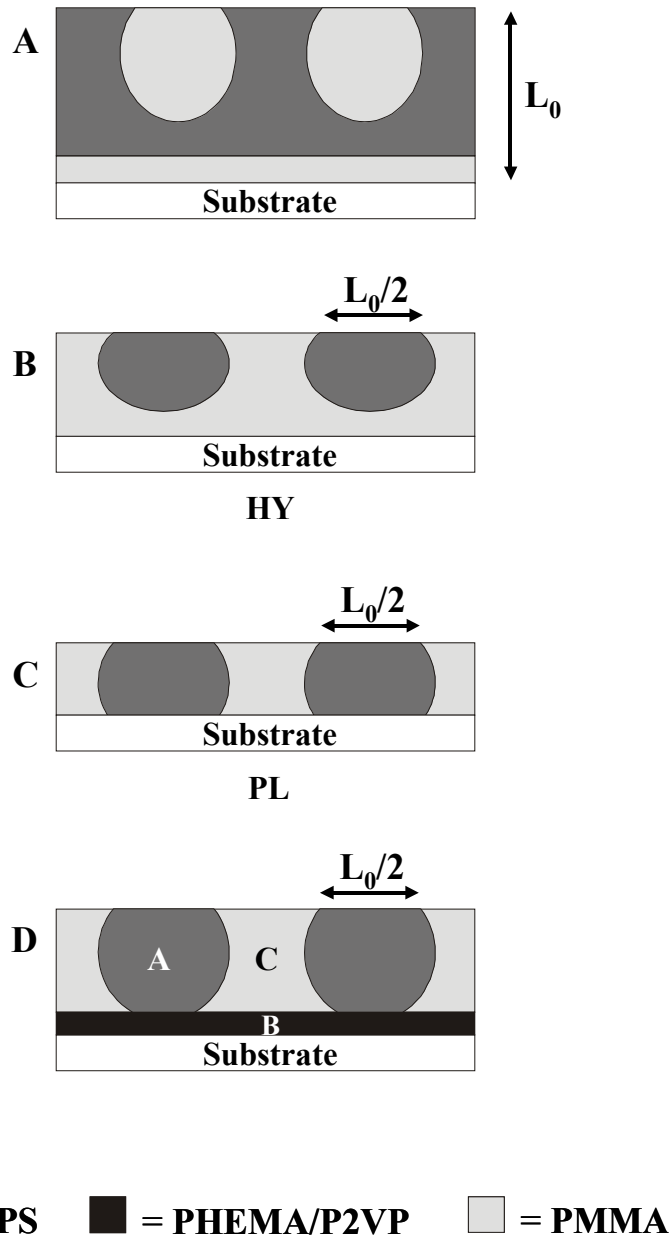
Scheme 3-4:   *Schematic depiction of proposed surface perpendicular morphologies for AB and ABC block copolymers.*

This assignment is corroborated by the fact that the protruding domains show a slightly larger phase shift compared to the depressed domains. The average difference in the phase shift between neighboring domains amounts to about 4° (with small variations depending on

the tip characteristics and therefore on the measurement conditions). As the harder material commonly exhibits a larger phase shift than a softer material in Tapping Mode SFM images taken in the repulsive regime, this observation confirms our statement that the protruding phase consists of PMMA.

This finding is in agreement with experiments on thin films of PS-*b*-PMMA on silicon nitride[18]. In these experiments, SFM and TEM measurements were performed at the same spot of the sample. The authors showed that, in fact, the PMMA phase protrudes over the PS domains when the samples were prepared from common solvents exhibiting a higher solubility for PS.

Polymer	$N_S/N_{H/2VP}/N_M$	Film thickness [nm]	Domain spacings [nm]		
			SFM	TEM [a]	SAXS
$S_{47}H_{10}M_{43}^{82}$	370/65/350	14 ± 2	44 ± 4	40 ± 4	49 ± 6
$S_{46}H_4M_{50}^{134}$	590/40/680	15 ± 2	53 ± 4	50 ± 5	61 ± 7
$S_{67}H_6M_{27}^{129}$	830/60/340	12 ± 2	58 ± 5	49 ± 5 [b]	59 ± 7 [b]
$S_{51}2VP_5M_{44}^{110}$	540/55/480	18 ± 2	47 ± 5	45 ± 5	49 ± 6
$S_{48}2VP_5M_{47}^{180}$	825/80/855	30 ± 4	73 ± 8	60 ± 6	63 ± 8
$S_{56}2VP_6M_{38}^{299}$	1620/160/1140	25 ± 4	92 ± 9	80 ± 8	80 ± 9

Table 3-2:   *Characteristic spacings of phase separated block copolymers in bulk and thin films as determined by SFM, TEM and SAXS.*
[a] bulk values, all films cast from THF solution, [b] cylinders

Moreover, we observe that the lateral spacings of the thin PS-*b*-PHEMA-*b*-PMMA and PS-*b*-P2VP-*b*-PMMA triblock copolymer films are nearly identical to the ones determined for bulk samples using TEM and SAXS (Table 3-2). Deviations tend to occur in films of block copolymers with a large amount of PMMA and may be due to degradation of the poly(methacrylates) in the electron beam during the TEM measurements.

Our experiments indicate that the formation of a laterally phase-separated and therefore patterned surface can be accomplished by simple dip-coating from 1 mg/ml THF solutions onto a polished silicon wafer. The patterned regions extend over large areas the size of which mainly depends on the uniformity of film thickness. Aiming towards a model for the microdomain morphology of our samples in the thin film regime, we briefly review related work on diblock copolymers. Morkved *et al.*[6] observed a kinetically stable perpendicular lamellar structure for symmetric PS-*b*-PMMA diblock copolymers at film thicknesses around one lamellar spacing L_0. The authors take into account a possible "capping" of the PS sheets

by PMMA at the (polar) substrate (see Scheme 3-4a). Recent self-consistent-field calculations by Fasolka *et al.*[19] suggest two types of perpendicular morphologies in the thin film regime for thicknesses below about 1/3 L_0, which are depicted in Scheme 3-4b/c. The authors describe a "hybrid structure" (HY), which consists of a PMMA layer at the substrate/polymer interface with protrusions extending to the polymer/air interface, perforating a PS top layer (Scheme 3-4b). Alternatively, a so-called "perpendicular lamellae" (PL) morphology is discussed, which consists of full lamellae aligned perpendicular to the plane of the film (Scheme 3-4c). The calculations predict both (HY and PL) morphologies to exhibit an equilibrium lateral spacing equal to L_0.

The latter prediction is also fulfilled by the observations made in the case of the thin PS-*b*-PHEMA-*b*-PMMA and PS-*b*-P2VP-*b*-PMMA triblock copolymer films discussed in the present work. Compared to the situation faced in the above studies, the P2VP / PHEMA middle blocks are expected to exhibit an even stronger interaction with the SiO$_x$ substrate. We therefore assume that the substrate is covered with the polar middle blocks, resulting in a thin film structure that consists of a homogeneous B layer adsorbed at the substrate, covered with a laterally microphase-separated PS/PMMA surface layer. This notion is in agreement with the SFM results and follows the prediction based on SCF calculations of Pickett and Balazs[12] (see Scheme 3-4d). Given the rather short length of the middle blocks, however, we cannot exclude that part of the substrate is covered with PMMA as well. This would then lead to a compromise between the morphologies depicted in Scheme 3-4b and d. In comparing experiment and theoretical prediction one has to realize that the structures observed experimentally were formed during the dip-coating and subsequent drying process and did not change significantly on further annealing. It remains unclear though, whether they represent the thermodynamic equilibrium structure of the film. In contrast, the SCF calculations predict the equilibrium morphology based on the minimum of the free energy of the system.

3.4.3. Ultrathin Films

Ultrathin films were prepared by adsorption of the block copolymers from dilute (1 mg/ml) solutions in tetrahydrofuran (THF) onto polished silicon wafers. In order to ensure that only strongly physisorbed polymer molecules are present at the surface, the silicon wafer was rinsed thoroughly in pure THF after being removed from solution. Subsequently, the samples were dried at room temperature. THF was chosen because it dissolves the outer blocks of the different block copolymers well and therefore we do not expect micelle formation in solution. Detailed investigations on the solution properties are presently under way in order to

illuminate the structure forming process and will be described elsewhere. Thus, so far we can assume that the surface structures are formed by adsorption of individual block copolymer molecules. The dried films were investigated with SFM operated in Tapping Mode™.
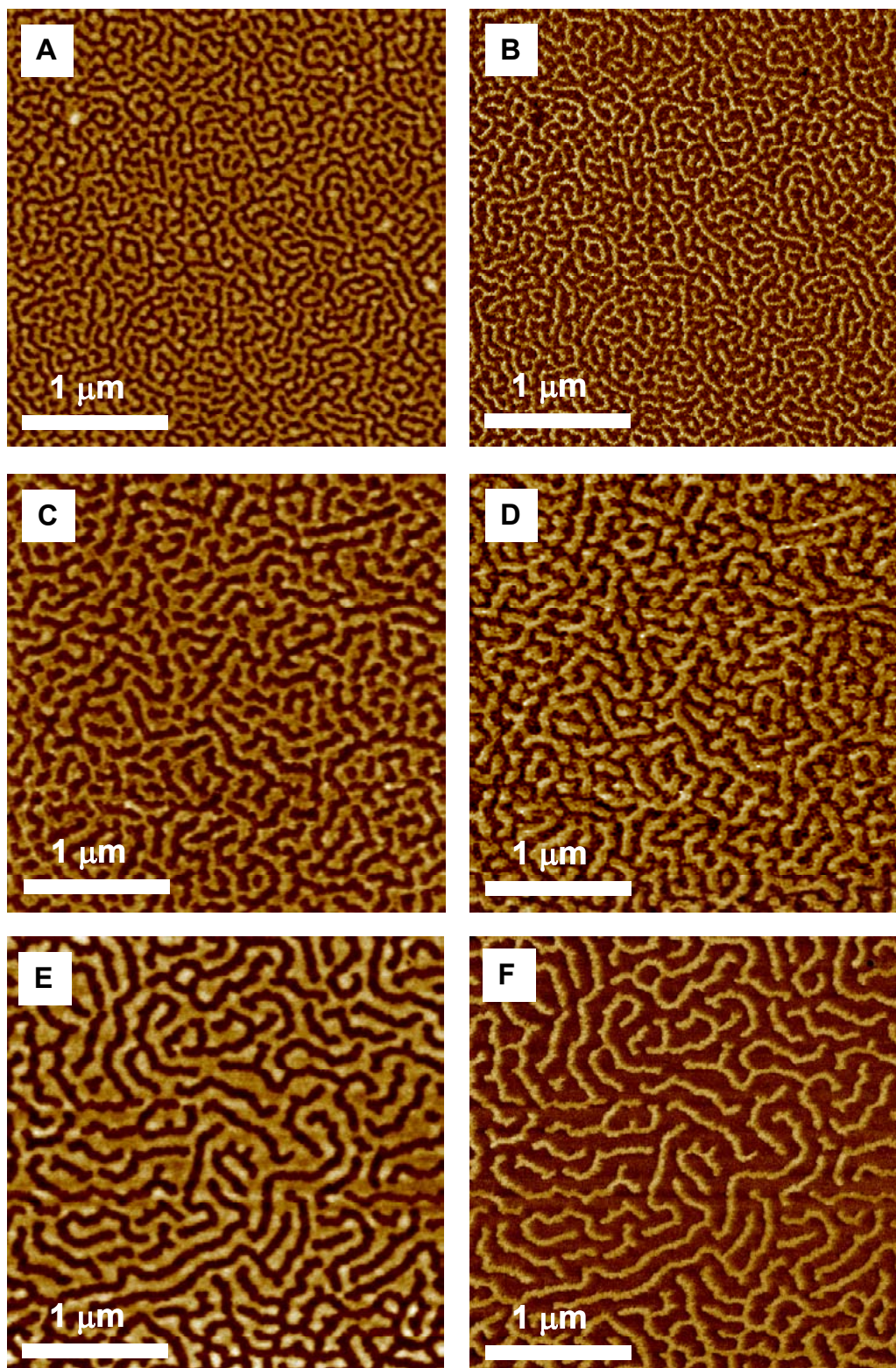
*Figure 3-3:*   *SFM micrographs and phase images of ultrathin films of PS-b-PHEMA-b-PMMA adsorbed from 1 mg/ml THF solutions onto a polished silicon wafer.*
(a, b) $S_{47} H_{10} M_{43}{}^{82}$; (c, d) $S_{46} H_4 M_{50}{}^{134}$; (e, f) $S_{67} H_6 M_{27}{}^{129}$. Topography: 8 nm, Phase: 15 °.

51

Figures 3-3 and 3-4 show a series of ultrathin block copolymer films from PS-*b*-PHEMA-*b*-PMMA and PS-*b*-P2VP-*b*-PMMA, respectively. All samples exhibit a striped surface morphology with characteristic values of half-width *R*, height *H* and half-distance *D* of the stripes. The molecular parameters as well as the *R*, *H* and *D* values are summarized in Table 3-3. The SFM phase images in Figure 3-3 demonstrate that at least two clearly distinguishable materials are found on the surface. The regions that appear brighter in the phase image correspond to materials which induce a higher phase shift ($\Delta\varphi$: 4-6 °). As mentioned above, the larger phase shift is expected to occur on the harder material (PMMA). Height profiles over a surface area where the polymer has partially been removed by scratching with a needle confirm that the valleys are covered by an ultrathin polymer layer of thickness around 1-2 nm.

Therefore, according to previous work on ultrathin films[15,20,24], we assume a surface structure as depicted in Scheme 3-2 where the B and C blocks (PHEMA/P2VP-*b*-PMMA) are adsorbed to the polar substrate and PS protrusions form the characteristic stripes. Details of the morphology will be discussed later.

Polymer	$N_S/N_{H/2VP}/N_M$	*R* [nm]	*H* [nm]	*D* [nm]	n_{PS}
$S_{47}H_{10}M_{43}{}^{82}$	370/65/350	29 ± 5	3.8 ± 0.6	50 ± 8	140
$S_{46}H_4M_{50}{}^{134}$	590/40/680	44 ± 6	4.0 ± 0.8	73 ± 9	220
$S_{67}H_6M_{27}{}^{129}$	830/60/340	53 ± 7	4.3 ± 0.8	90 ± 10	250
$S_{51}2VP_5M_{44}{}^{110}$	540/55/480	38 ± 5	3.9 ± 0.8	64 ± 7	180
$S_{48}2VP_5M_{47}{}^{180}$	825/80/855	50 ± 5	4.4 ± 0.6	80 ± 7	230
$S_{56}2VP_6M_{38}{}^{299}$	1620/160/1140	73 ± 9	5.2 ± 1.2	125 ± 15	290

Table 3-3:   Characteristic lateral spacings of phase separated block copolymers in ultrathin films adsorbed from 1 mg/ml THF solution showing stripe morphology.
n_{PS} = average number of aggregated PS chains in a segment of a circle in cross-section with a basis of 2R x 2R and a height H (error range ± 40%)

Figure 3-3a shows an ultrathin film of $S_{47}H_{10}M_{43}{}^{82}$ (degrees of polymerization: 370/65/350). The sample exhibits a continuous stripe-like surface pattern characterized by $H = 3.8 \pm 0.6$ nm, $D = 50 \pm 8$ nm, and $R = 29 \pm 5$ nm. The average half-width *R* of a stripe has been estimated taking into account the convolution of the topographic profile with the curvature of the tip apex. If we picture the PS stripes as composed of many cylindrical caps of contact area $(2R)^2$ and height *H* (see Scheme 3-3) with a density $\rho = 1.1$ g/cm^3, the aggregation number n_{PS} is estimated to be 140 ± 50. (The large uncertainty in n_{PS} is caused by the difficulties involved in a precise determination of the stripe half-width *R*.)

The SFM topography image in Figure 3-3c shows an ultrathin film of $S_{46} H_4 M_{50}^{134}$ (590/40/680). The sample exhibits the same typical characteristics as described for $S_{47} H_{10} M_{43}^{82}$. The pattern is very regular in height, half-distance and half-width of the stripes which surround isolated valleys of PHEMA-*b*-PMMA. The respective values of D, R, H, and n_{PS} are included in Table 3-3.

Figure 3-3e shows the topography image of $S_{67} H_6 M_{27}^{129}$ (830/60/340) which again exhibits the regular and continuous stripe pattern. In addition, the film shows a tendency to break-up into an island-like structure (lower right corner). We shall return to this issue below. Furthermore, a comparison with $S_{47} H_{10} M_{43}^{82}$ (Figure 3-3a) demonstrates the significant influence of the PS block on the half-distance D of the stripes.
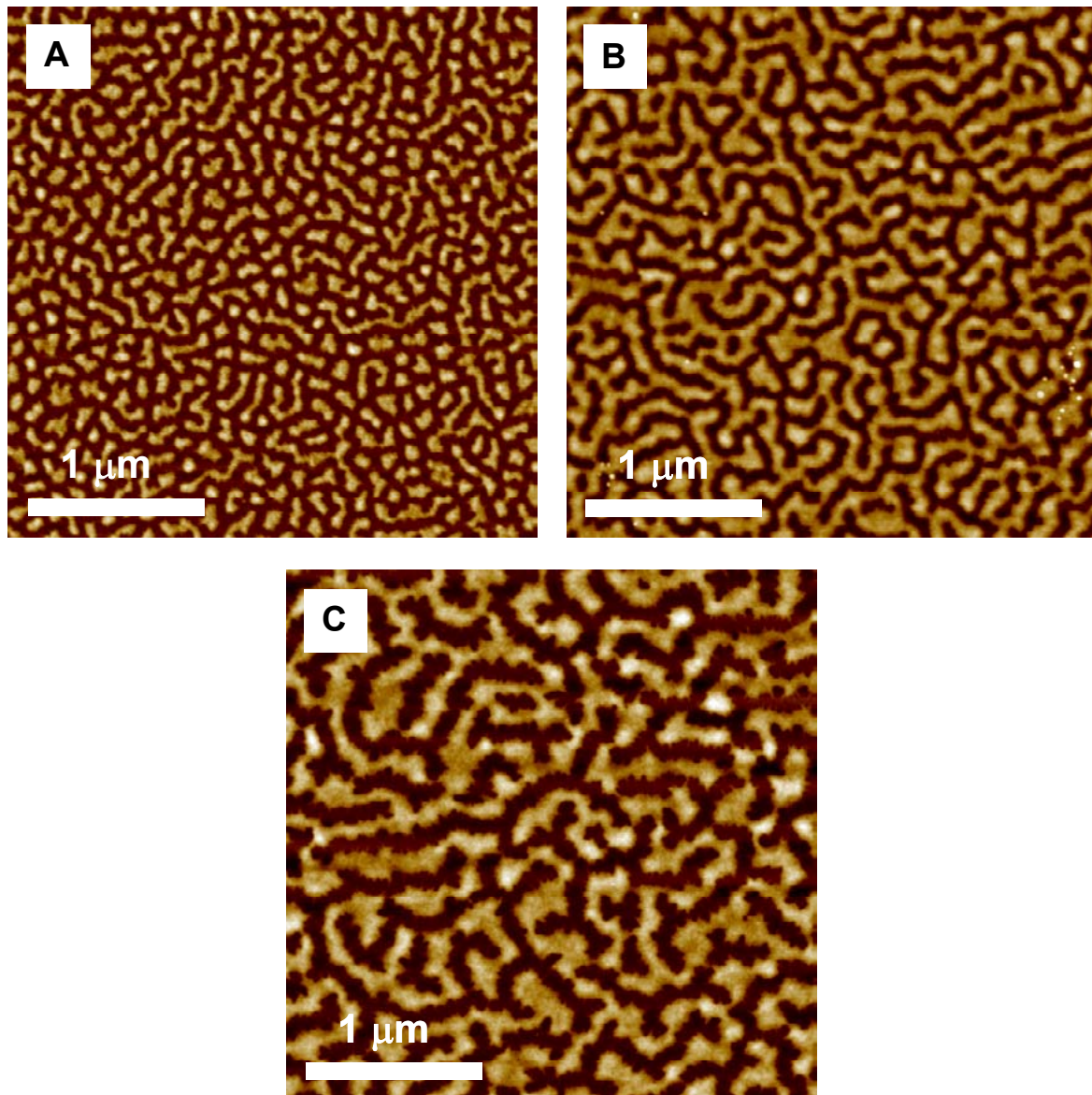

Figure 3-4:   *SFM micrographs of ultrathin films of PS-b-P2VP-b-PMMA adsorbed from 1 mg/ml THF solutions onto a polished silicon wafer.*
(a) $S_{51} 2VP_5 M_{44}^{110}$; (b) $S_{48} 2VP_5 M_{47}^{180}$; (c) $S_{56} 2VP_6 M_{38}^{299}$. Z-range: 8 nm.

Figure 3-4a shows an ultrathin film of S_{51} $2VP_5$ M_{44}^{110} (540/55/480). Compared to all other samples the stripes in this case are not continuous but broken up into long and short islands that still exhibit the characteristics of a stripe pattern. Half-width, half-distance and height are still uniform and correlate well with spacings found in the other samples as will be discussed further below. ($R = 38 \pm 5$ nm, $D = 64 \pm 7$ nm, $H = 3.9 \pm 0.8$ nm). The aggregation number n_{PS} can be estimated to some 180 agglomerated PS chains.

The ultrathin film morphology of S_{48} $2VP_5$ M_{47}^{180} (825/80/855) is shown in Figure 3-4b. According to the expected behavior, the characteristic scales increase so that $R = 50 \pm 5$ nm and $D = 80 \pm 7$ nm. Besides the stripes some island-like features are also detected that fit well to the overall scaling. The number of aggregated PS chains as defined above rises to $n_{PS} = 230$.
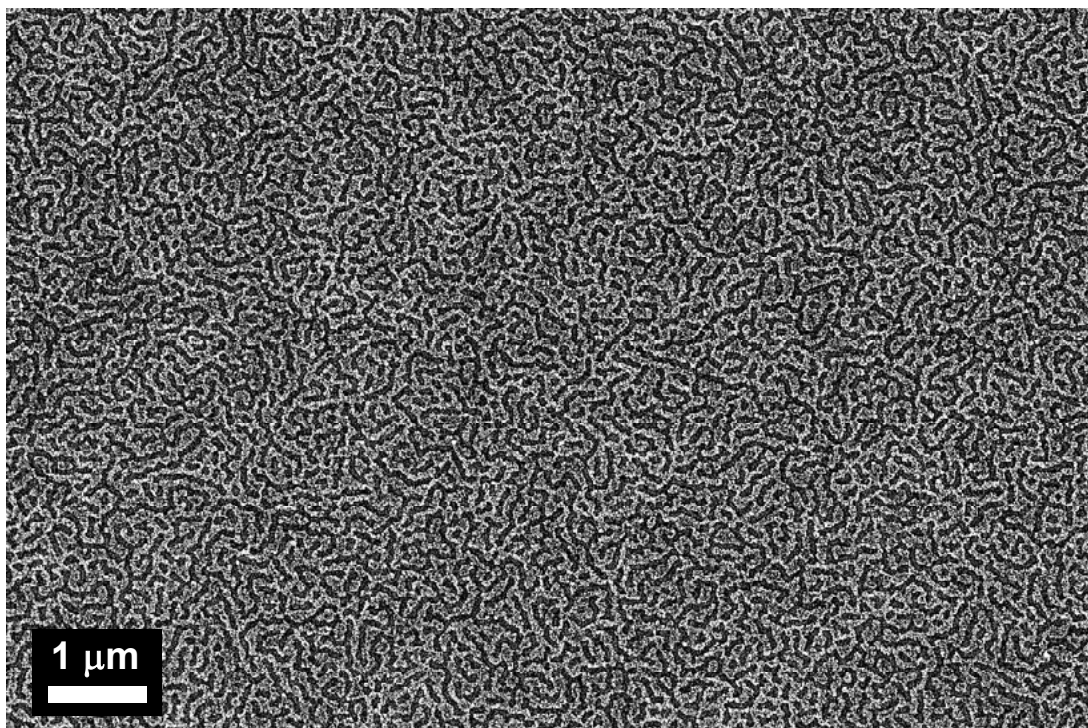
Figure 3-5:   *Large area SEM micrograph of an ultrathin film of S_{48} $2VP_5$ M_{47}^{180} adsorbed from 1 mg/ml THF solution onto a polished silicon wafer*

In order to show that the surface patterns indeed extend over large areas over the whole substrate, SEM pictures were taken. In Figure 3-5 an image of an ultrathin film of S_{48} $2VP_5$ M_{47}^{180} is shown. SEM has been chosen instead of a large area SFM image because high resolution images can be obtained easily capturing large areas. As the PS block has been stained with RuO_4 vapour prior to the measurement, the PS stripes appear brighter than the P2VP and PMMA sublayer. The haziness in the PS parts may be due to electron emission

from the edges of the slightly rough PS stripes. The structure shown in Figure 3-5 demonstrates the large scale quality common to all surface structures reported on in this work.

The topographic SFM image of the polymer with the largest overall molecular weight $S_{56} 2VP_6 M_{38}^{299}$ (1620/160/1140) is shown in Figure 3-4c. As expected, the characteristic spacings are larger than in any other block copolymer investigated in this work. In addition, also the average aggregation number of a PS stripe increases considerably. The average R, H, D and n_{PS} values are given in Table 3-3. The SFM image shows that the half-width R of the PS stripes is not very uniform and the edges of the stripes appear to be rather rough. Another feature which appears more or less pronounced in all ultrathin films is a partial undulation of the stripes. This undulation and the partial break-up of the stripes lead to the conclusion that the observed patterns may be metastable and may undergo a significant rearrangement under certain conditions (e.g. annealing or solvent vapour treatment).

As can be seen in Figures 3-3 and 4, the half-width R of the PS stripes increases with increasing molecular weight of the PS block. The half-distance D, on the other hand, is controlled by the molecular weight of the PHEMA-b-PMMA and P2VP-b-PMMA blocks, respectively. Yet, at constant molecular weight of the PHEMA-b-PMMA blocks an increase of the degree of polymerization of the PS block also leads to a significantly larger value of D (compare, e.g. $S_{47} H_{10} M_{43}^{82}$ (370/65/350), $D = 50 \pm 8$ nm, and $S_{67} H_6 M_{27}^{129}$ (830/60/340), $D = 90 \pm 10$ nm). In addition, the aggregation number n_{PS} nearly doubles from 140 to 250 agglomerated chains per stripe section.

Finally we note that the stripe to stripe distances ($2D$) in the ultrathin films are considerably larger than the respective bulk values. This widening of the structure indicates a significant stretching of the adsorbed blocks resulting in a quasi 2-dimensional surface layer, as will be discussed further below.

3.4.3.1. Annealed Ultrathin Films

As indicated by the undulations of the surface stripes found in the ultrathin film samples, the observed patterns may not represent the thermodynamically stable surface morphology. Consequently, the ultrathin films were annealed for 8 days at 170 °C in a vacuum oven. This temperature is 40-50 °C higher than the highest glass transition temperature (T_g) of the block copolymer components in the ultrathin films. The relatively high temperature was chosen with respect to the fact that the T_g´s in thin films can be significantly increased compared to the bulk values due to interactions between polar monomers and the substrate surface, whereas the reverse effect is expected for non-polar monomers[21,22,23].
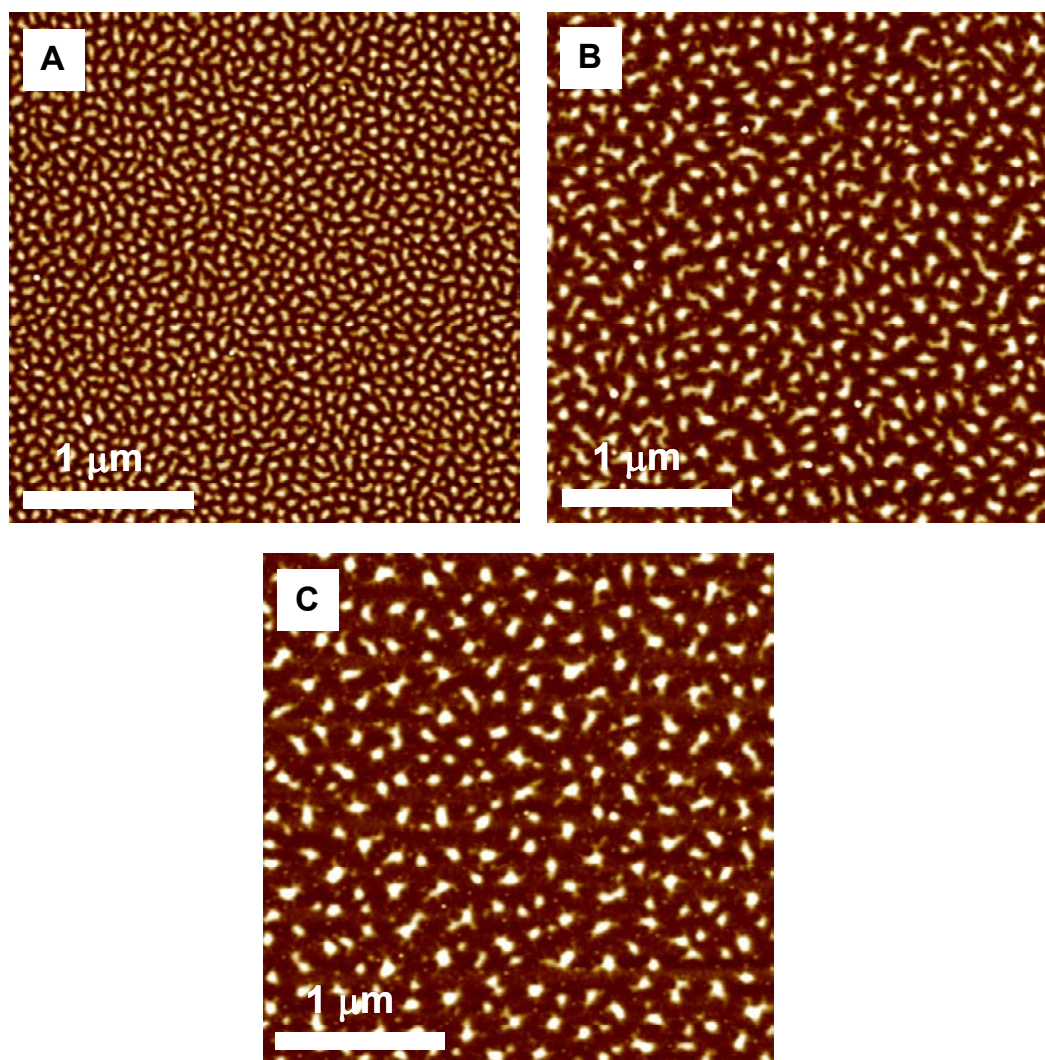
Figure 3-6:   *SFM micrographs of ultrathin films adsorbed from 1 mg/ml THF solutions onto a polished silicon wafer after annealing for 8 days at 170 °C in vacuum.*
(a) $S_{47} H_{10} M_{43}^{82}$ (Z-range: 6 nm); (b) $S_{67} H_6 M_{27}^{129}$; (c) $S_{56} 2VP_6 M_{38}^{299}$, Z-range: 10 nm (b/c).

In fact, on annealing we observe a clear transition from PS stripes to more or less round shaped PS islands as shown in Figure 3-6. The level of ordering is not very high and additional annealing at the same temperature does not change the surface pattern any more. The characteristic spacings are listed in Table 3-4. The half-width R of the round shaped PS aggregates was estimated assuming a circular basis with radius R. This estimate and the broad distribution of the size of the aggregates leads to the large error in R. Nevertheless, the SFM micrographs in Figure 3-6 exhibit a clear correlation of the radius R and the height H with the molecular weight of the PS block. Furthermore, it can be seen that the overall spacings between the agglomerates increase with increasing PHEMA/P2VP-*b*-PMMA block length. Compared to the surface patterns observed prior to annealing, the lateral spacing (i.e. the half-distance D) remains constant within the experimental error. Accordingly, the height values coincide with previous height data obtained from the stripe morphologies of the

unannealed samples. In contrast, the average mean radii R decreased significantly after annealing, especially for the formerly broad stripes. The overall impression is dominated by the observation that the radii of the clusters generated from stripes with large half-width are less uniform than for clusters resulting from smaller stripes (see Figure 3-6a/c). In addition, the average number of aggregated chains per cluster ranges between 50 and 90 with an estimated error of ± 60 %.

We note in passing that a 7 day treatment in saturated THF vapor results in a morphological transition nearly identical to the one observed after annealing.

Polymer	$N_S/N_{H/2VP}/N_M$	R [nm] [a]	H [nm]	D [nm]
$S_{47}H_{10}M_{43}^{82}$	370/65/350	23 ± 5	3.5 ± 0.5	42 ± 6
$S_{46}H_4M_{50}^{134}$	590/40/680	32 ± 10	4.3 ± 0.8	63 ± 10
$S_{67}H_6M_{27}^{129}$	830/60/340	34 ± 14	5.9 ± 1.1	81 ± 15
$S_{51}2VP_5M_{44}^{110}$	540/55/480	27 ± 9	4.9 ± 1.0	55 ± 10
$S_{48}2VP_5M_{47}^{180}$	825/80/855	30 ± 12	5.8 ± 1.0	78 ± 19
$S_{56}2VP_6M_{38}^{299}$	1620/160/1140	36 ± 14	6.6 ± 1.0	104 ± 20

Table 3-4:   Characteristic lateral spacings of phase separated block copolymers in ultrathin films adsorbed from 1 mg/ml THF solution after annealing at 170 °C for 8 days showing island morphology.
[a] estimated from Nanoscope Particle Analysis assuming a circular basis of the aggregates

3.4.3.2. Concentration Dependence of Pattern Formation

When ultrathin films are prepared by dip-coating from 0.1 mg/ml solutions in THF onto polished silicon wafers, the surface patterns are very similar to the stripe-like morphologies as prepared by adsorption from 1 mg/ml solutions in THF. In fact, the scaling of the lateral spacings is identical to the one found for the adsorbed films whereas the height values appear to be slightly larger. This may be due to a higher overall coverage. In addition, the as-prepared films exhibited a smooth and structureless surface. This finding may be attributed to a nearly complete PS coverage, which only partially dewetts the adsorbed sublayer. A few irregular holes are formed as shown in Figure 3-7. After exposue to saturated THF vapor for a few hours, the PS surface layer completely brakes up to form the well-known stripe-like patterns. Similarly, annealing also leads to a morphological transition resulting in an island-like morphology.
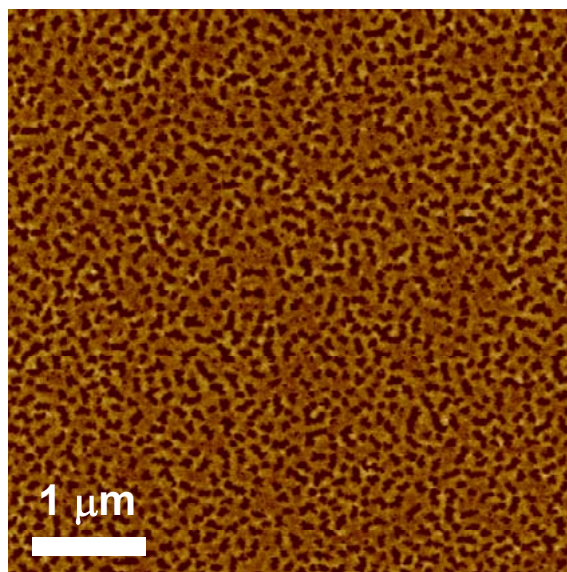
Figure 3-7:   SFM micrograph of ultrathin film of S_{48} $2VP_5$ M_{47}^{180} dip-coated from 0.1 mg/ml THF solution onto a polished silicon wafer. Z-range: 8 nm.

When samples were prepared by dip-coating from 0.01 mg/ml solutions in THF onto polished silicon wafers, an irregular pattern of small elongated or oval islands was observed. Two samples (S_{46} H_4 M_{50}^{134} (590/40/680) and S_{48} $2VP_5$ M_{47}^{180} (825/80/855)) were used for these studies. The islands had a diffuse shape at their base, which may be attributed to bundles of polymer chains (Figure 3-8a/b). Apparently, the substrate is not covered completely by the polymer but very small aggregates of polymer chains are spread all over the wafer. The mean height of the main clusters for S_{46} H_4 M_{50}^{134} was determined to be 2 ± 1 nm, excluding all objects with $H < 0.5$ nm. A similar result was obtained for the as-prepared adsorbates of S_{48} $2VP_5$ M_{47}^{180} (see Table 3-5).

Polymer	$N_S/N_{H/2VP}/N_M$	R [nm]	H [nm]	D [nm]	Number of Clusters [3×3 μm^2]
$S_{46}H_4M_{50}^{134}$	590/40/680	19 ± 14	2 ± 1	56 ± 14	≈ 1200
after annealing		20 ± 6	4 ± 1	50 ± 12	≈ 1100
$S_{48}2VP_5M_{47}^{180}$	825/80/855	20 ± 12	2 ± 1	74 ± 15	≈ 850
after annealing		25 ± 8	5 ± 2	75 ± 18	≈ 700

Table 3-5:   Characteristic lateral spacings of phase separated block copolymers in ultrathin films adsorbed from 0.01 mg/ml THF solution showing island morphology before and after annealing at 190 °C for 5 days.
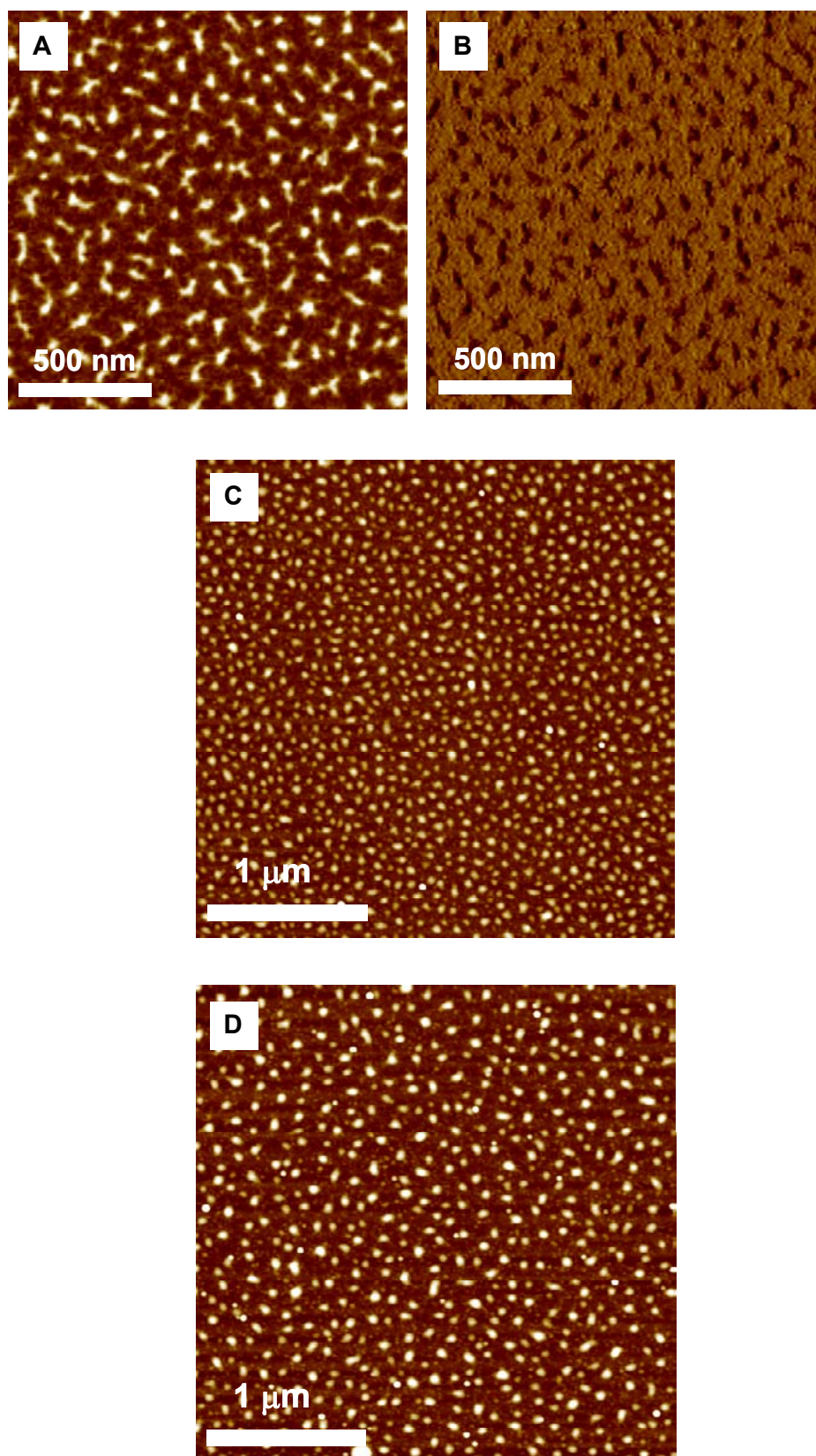
Figure 3-8:   *SFM micrographs of ultrathin films dip-coated from 0.01 mg/ml THF solutions onto a polished silicon wafer: $S_{46} H_4 M_{50}^{134}$ (a) topography (5 nm) and (b) phase (15 degrees) as-prepared and (c) after annealing for 5 days at 190 °C; (d) $S_{48} 2VP_5 M_{47}^{180}$ after annealing for 5 days at 190 °C. Z-range: 10 nm (c/d).*

After annealing for 5 days at 190 °C an array of more regularly round shaped polymer clusters is formed (Figure 3-8c/d). The mean radii R were determined to 20 ± 6 nm and 25 ± 8 nm for $S_{46} H_4 M_{50}{}^{134}$ and $S_{48} 2VP_5 M_{47}{}^{180}$, respectively. No significant change in the lateral spacing was found on further annealing. However, the height of the clusters changed significantly which may be attributed to an incorporation of the small molecule bundles spread on the surface, thus increasing the cluster height and volume. This is also supported by the small decrease in the overall number of clusters higher than 0.5 nm which changes from ~1200 to ~1100 and from ~850 to ~700 for $S_{46} H_4 M_{50}{}^{134}$ and $S_{48} 2VP_5 M_{47}{}^{180}$, respectively (see Table 3-5). The calculation of the aggregation number n_{PS} gives a value of 25 and 40 chains per cluster with an error range of ± 65 %.

These findings underline the fact that the amount of polymer deposited during dip-coating is not sufficient to cover the surface completely. Due to the lack of polymeric material, the most favourable form for the aggregates on the surface is given by a drop- or island-like agglomeration.

3.4.4.   Scaling Analysis

Recently, Potemkin *et al.* developed a theory predicting the scaling parameters of surface patterns observed in ultrathin films of PS-*b*-P2VP and PS-*b*-P4VP diblock copolymers[14,15]. In this system the PVP blocks adsorb to the substrate and the PS blocks dewet from the PVP sublayer. The degree of polymerization and the surface energies (with $\gamma_{PVP} > \gamma_{PS}$) of both blocks were found to affect the size and shape of the observed structures, i.e. island or stripe morphologies of different spacings. Their calculations resulted in the following dependences:

$$R, H \propto \left(N_A^{d-3} N_B^{d+1} \right)^{\frac{1}{3d-1}} \quad \text{(3a)}$$

$$D \propto \left(N_A^{d+1} N_B^{d-1} \right)^{\frac{1}{3d-1}} \quad \text{(3b)}$$

with $d = 3$ for island and $d = 2$ for stripe morphologies, where N_A is the degree of polymerization (DP) of the adsorbing block (in their case PVP) and N_B the DP of the protruding block (PS), which leads to:

$$R, H \propto N_A^{-0.2} N_B^{0.6} \quad \text{(4a)}$$

$$D \propto N_A^{0.6} N_B^{0.2} \qquad (4b)$$

for a stripe morphology and

$$R, H \propto N_B^{0.5} \qquad (5a)$$

$$D \propto N_A^{0.5} N_B^{0.25} \qquad (5b)$$

for an island morphology.

Given the rather short length of the middle blocks in our study and the fact that the PMMA end blocks are expected to adsorb onto a polar substrate as well, we shall try to model our system by treating blocks B and C as a single adsorbing unit and use the above theoretical approach. This choice is further corroborated by the surface energy differences between the blocks, which fullfil the assumption of the above model, i.e. $\gamma_{PHEMA,PMMA} > \gamma_{PS}$ and $\gamma_{P2VP,PMMA} > \gamma_{PS}$.

3.4.4.1. Striped Patterns

In Figure 3-9 the scaling behavior of half-width R, half-distance D and height H are compared to the above theory. The axes of the graphs are scaled in a way that the experimental points should fall onto straight lines. As can be seen in Figure 3-9a the scaling of the half-width R of the stripes is well described by the theory. The line drawn in the plot is calculated by linear regression. Stripe heights H (Figure 3-9c), which are expected to scale identically to the half-width R, also agree quite well with theory even though the accuracy is not as good as for the R values or the half-distance D. Obviously, the nature of the middle block B (PHEMA or P2VP) does not seem to have a strong influence on the scaling behaviour of R and H as especially $S_{46} H_4 M_{50}^{134}$ (590/40/680) and $S_{51} 2VP_5 M_{44}^{110}$ (540/55/480) as well as $S_{67} H_6 M_{27}^{129}$ (830/60/340) and $S_{48} 2VP_5 M_{47}^{180}$ (825/80/855) exhibit an interesting similarity in half-width and height. They only differ significantly in the length of the PMMA block which contributes to a different scaling behaviour with regard to D. In Figure 3-9b the strong influence of the PS molecular weight on the stripe to stripe distance D can be seen. The asymmetrical polymer $S_{67} H_6 M_{27}^{129}$ (830/60/340) shows a very large stripe-to-stripe half-distance D which is about 1.6 times larger than expected according to the line calculated using linear regression disregarding $S_{67} H_6 M_{27}^{129}$ (hollow square). Compared to the sample $S_{47} H_{10} M_{43}^{82}$ (370/65/350) the molecular weight of the adsorbing blocks B/C is nearly

constant so that the only difference is given by the PS block which is 2.25 times larger. This phenomenon has been observed earlier in the case of asymmetric PS-*b*-P2VP diblock copolymers with a ratio N(PS) : N(P2VP) of approximately 3 : 1 which is similar to the ratio N(PS) : N(PHEMA/PMMA) in $S_{67} H_6 M_{27}^{129}$ (830/60/340)[15]. A possible explanation for the above observation could be that in this case, there is not a homogeneous PHEMA-*b*-PMMA sublayer below the PS stripes but a certain area where PS is in direct contact with the silicon substrate[15]. If the linear regression is carried out without the D value of polymer $S_{67} H_6 M_{27}^{129}$, one finds very good qualitative agreement with the scaling prediction.

3.4.4.2. Island-like Patterns

In the following we compare the measured R, H and D values of the island-like surface patterns with the theory by Potemkin *et al.*[14] using equations 5a/b. Figure 3-10 shows a series of graphs where the radii R, half-distances D and heights H are plotted such that the data points should fall onto straight lines. The black line drawn in the plots is calculated according to linear regression. Both the radius R and the height H (Figure 3-10a/c) are expected to depend on the PS molecular weight only and should scale as $N_{PS}^{0.5}$. This is indeed observed. The large error bars reflect the broad distribution of the cluster radii and the difficulties in the correct determination of R as described earlier. The height values are more reliable and have a much smaller error range. Besides, like in the case of the stripe morphology, we find similarities in the characteristic spacings especially for $S_{46} H_4 M_{50}^{134}$ (590/40/680) and $S_{51} 2VP_5 M_{44}^{110}$ (540/55/480) as well as $S_{67} H_6 M_{27}^{129}$ (830/60/340) and $S_{48} 2VP_5 M_{47}^{180}$ (825/80/855) which both have PS blocks of similar length. As expected, the radius R and the height H are nearly identical without any influence induced by the different B/C block composition. As our results show a qualitatively good agreement between the scaling predictions for the observed structures ($R, H \propto N_{PS}^{0.5}$) and the actual radius and height of the clusters, we may conclude that the conformation of the PS chains in an aggregate is nearly Gaussian.

The half-distance D of the PS aggregates scales nearly perfectly according to the theoretical predictions (Figure 3-10b). If one compares the ultrathin annealed film of $S_{47} H_{10} M_{43}^{82}$ (370/65/350) to $S_{67} H_6 M_{27}^{129}$ (830/60/340) as shown in Figure 3-6a/b it turns out that an increase of the degree of polymerization of the PS block at a constant molecular weight of the PHEMA-*b*-PMMA blocks leads to a significantly larger value of D which increases from $D = 42 \pm 6$ nm to 81 ± 15 nm. The lateral spacing in the latter case is 1.6 times larger than expected according to the black line given by the linear fit. This is a very similar

deviation as measured for the stripe-like morphology. A possible explanation for this phenomenon has already been given for the same observation made in films with stripe morphology and therefore will not be discussed further.
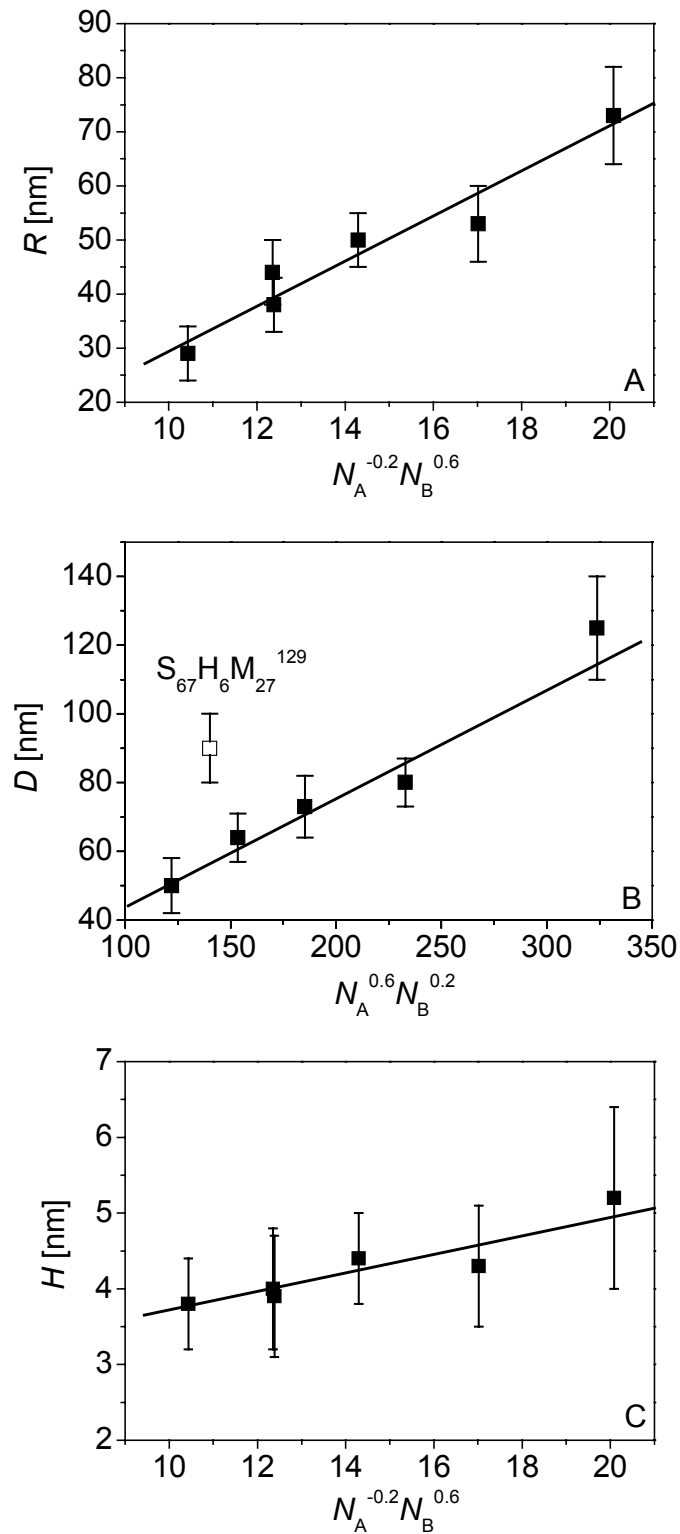

Figure 3-9:   *Scaling of PS-b-PHEMA-b-PMMA and PS-b-P2VP-b-PMMA stripe morphology.*
                   (A) half-width R, (B) half-distance D, (C) height H of PS stripes.
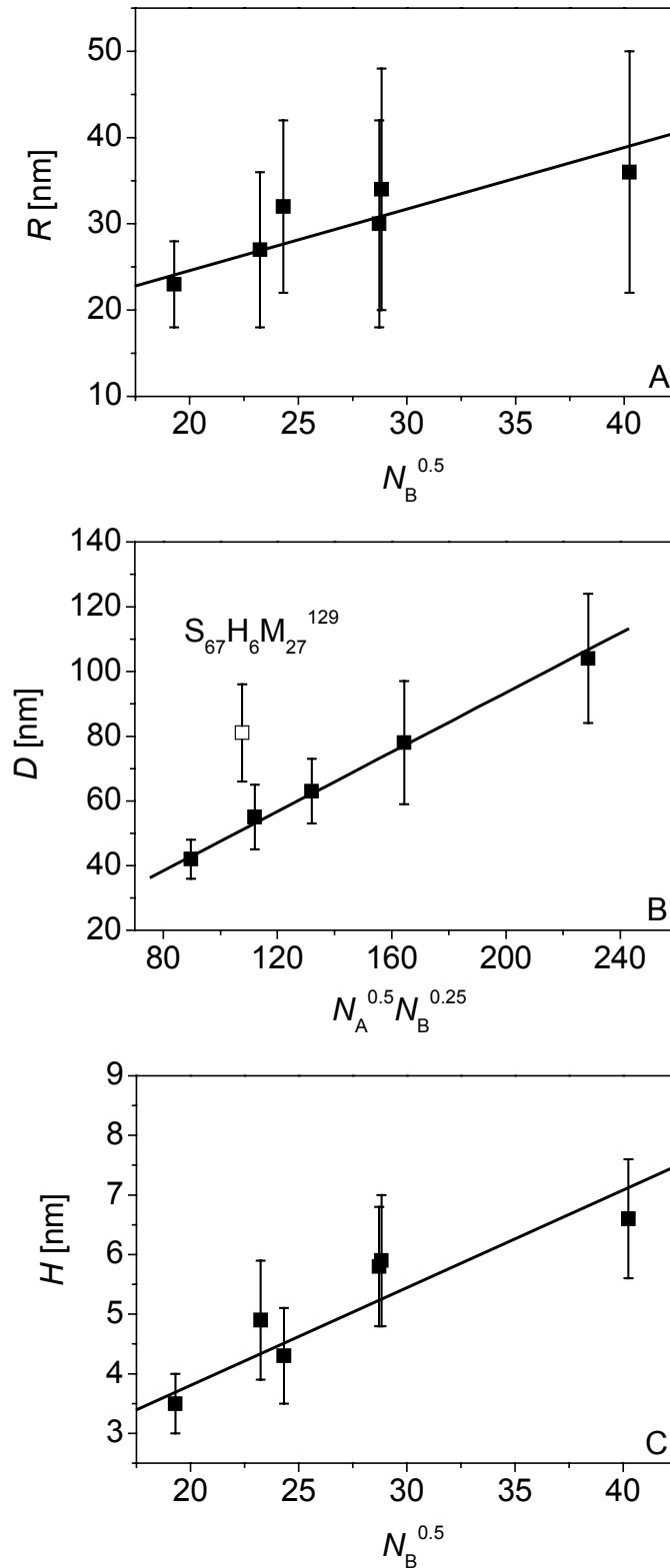
Figure 3-10:   *Scaling of PS-b-PHEMA-b-PMMA and PS-b-P2VP-b-PMMA island morphology.*
                   (A) half-width R, (B) half-distance D, (C) height H of PS islands.

In the following we shall discuss the scaling behavior of the above described ultrathin film morphologies. Based on previous investigations on ultrathin films of PS-*b*-P2VP and

PS-*b*-P4VP [15,20,24] we expect the observed structures to consist of PS stripes with a mixed sublayer of PMMA and PHEMA or P2VP, respectively. The good agreement of our results to the scaling analysis developed for diblock copolymers corroborates this notion. Obviously, once in contact with the silicon wafer, the polarity of both the middle blocks and the PMMA end block leads to co-adsorption to the substrate surface, resulting in a quasi 2-dimensional layer of the PHEMA-*b*-PMMA and P2VP-*b*-PMMA portion of the block copolymers. Due to the unfavourable interaction and elastic contributions to the free energy (see below), the PS blocks do not cover this layer completely but rather dewet the sublayer. During this process, the PS chains form aggregates of different size and spacing resulting in the three-dimensional structures observed in the SFM images. The size, height and half-distance of the resulting structures clearly depend on the PS/PMMA block length as shown in Table 3-3. The definition of the parameters used for scaling analysis and a cross-section of the morphology are depicted in Scheme 3-2 which summarizes schematically the above descriptions.

So far only the dimensions associated with the PS stripes were considered. One can easily calculate the half-width of the valleys between adjacent stripes, which should consist mainly of PMMA, from the difference of the D and R values summarised in Table 3-3. It is interesting to compare these values to the radii of gyration of the PMMA block. As an example, for $S_{48} 2VP_5 M_{47}^{180}$ (825/80/855) the radius of gyration of the PMMA block is about 8 nm, whereas the half-width of the valleys found in the corresponding ultrathin film amounts to some 30 nm. This result indicates significant streching of the PMMA chains in the adsorbed layer. The free energy cost due to stretching must therefore be balanced by maximizing the number of contacts to the substrate and the corresponding adhesion energy. In order to cover the PMMA layer in the valleys completely, the PS chains ($R_g \sim 8$ nm) would have to stretch approximately 4 times as well. Since no enthalpic gain of comparable magnitude is expected at the PS/PMMA interface, complete coverage of PMMA by PS is not observed. From the D and R data for the other block copolymers we consistently find a streching of the adsorbing blocks by about 4-5 times compared to an unperturbed Gaussian chain. The half-width of the observed valleys is 6 times smaller compared to the respective PMMA contour length. Together with the average thickness of the adsorbed polymer layer of approximately 1-2 nm, we may conclude that the adsorbed coils form trains and loops on the substrate surface as shown in Scheme 3-2.

In the case of $S_{67} H_6 M_{27}^{129}$ (830/60/340) the picture is quite different. As indicated earlier the unusually large spacing of the PS stripes could be due to an incomplete coverage of the substrate by a PHEMA-*b*-PMMA sublayer. This assumption is further supported by the fact

that the adsorbed blocks would have to be stretched more than 8 times (which is half the contour length) in order to form a complete sublayer. It is questionable whether the corresponding entropic energy cost can be compensated for by the adhesion energy. Therefore, partial coverage of the substrate by the PS chains and a reduced stretching of the PMMA coils seems to be a more favourable condition.

After annealing, the ultrathin films show significant morphological changes with the striped surface pattern turning into an island-like surface structure. This behavior indicates that the striped patterns do not correspond to the thermodynamically stable morphology. In contrast to other investigations on ultrathin block copolymer films[25] the size of the clusters is not very uniform and only a poor long range order develops. We may assume that this observation is related to the properties of the substrate, following the results of Spatz *et al.*, who found a pronounced influence of the substrate on the size and uniformity of PS-*b*-P2VP clusters on mica and GaAs surfaces, respectively.
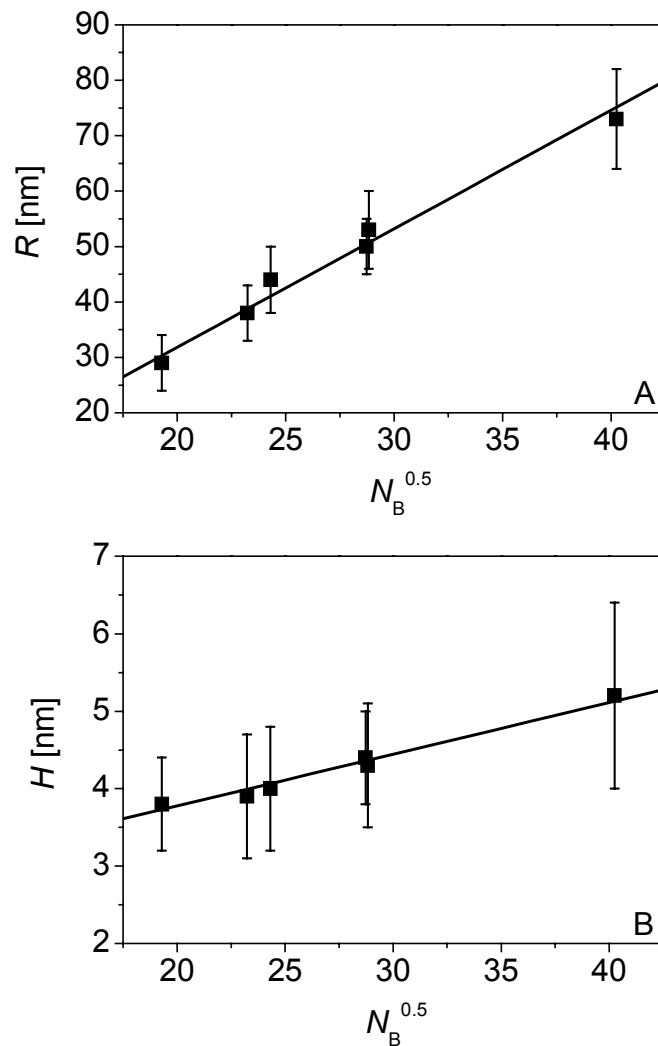

Figure 3-11:   *Scaling of PS-b-PHEMA-b-PMMA and PS-b-P2VP-b-PMMA stripe morphology according to Gaussian behaviour: (A) half-width R, (B) height H of PS stripes.*

Furthermore, according to recent calculations by Potemkin *et al.*[14] on the stability of islands and stripes and the transition between both phases, we expect that our system is located close to the phase transition between stripes and islands. One important factor that accounts for the stability of one phase is given by the difference in surface tension of the dominant blocks. Compared to the system PS-*b*-P2VP ($\Delta\gamma \approx 50$ mN/m[26]) the difference in surface tension between PS and PMMA only amounts to $\Delta\gamma \approx 0.4 - 20.2$ mN/m depending on the amount of moisture absorbed by PMMA $(0 - 3\ \%)$[26]. According to the predictions of Potemkin *et al.*[14], stripes are more stable for γ(adsorbing block/air) $> \gamma$(dewetting block/air) which would result in a smaller surface area to be covered by the adsorbing block. The larger the difference in surface tension, the more energetically favourable is the striped structure. On the other hand, the island-like pattern would be more stable if the surface tension ratio was reverse. A difference in surface tension as small as described above does not provide a thermodynamic argument to decide in favour of one or the other morphology.

Another hint pointing towards an instability of the observed stripe morphology is given by the scaling behavior of the stripe dimensions H and R, respectively. For a state close to the transition regime a Gaussian behaviour of H and R is expected ($R, H \propto N_{PS}^{0.5}$)[14]. As is shown in Figure 3-11, this is indeed observed. The fit for the island-like morphology obtained after annealing the striped samples (see Figure 3-10) does not show such a good agreement with theory, which can be explained by the large errors due to the non-uniformity of the clusters.

A transition from stripes to islands has already been observed earlier by changing the overall molecular weight ratios[14], but in the present study the transition is induced by instabilities resulting from the fact that the corresponding block copolymers are located in a region near the phase boundary between the two phases.

3.5. Conclusions

We have shown that thin and ultrathin films of polystyrene-*b*-poly(2-vinyl-pyridine)-*b*-poly(methyl methacrylate) and polystyrene-*b*-poly(2-hydroxyethyl methacrylate)-*b*-poly(methyl methacrylate) block copolymers reveal regular surface patterns with worm-, stripe- and island-like morphologies. The characteristic spacings can be controlled via the molecular weight of the different blocks of the respective copolymers.

Thin films prepared by dip-coating from a polymer solution were found to exhibit a phase-separated worm-like surface morphology that presumably only consists of PS and PMMA microdomains with a characteristic lateral length scale similar to the bulk period L_0. We

assume that the generation of such a striped surface pattern can be explained by complete coverage of the silicon oxide surface by PHEMA or P2VP, resulting in a thin film structure that consists of a homogeneous layer of the middle block adsorbed at the substrate covered with a laterally microphase-separated surface layer of PS and PMMA microcomains. The proposed model for this morphology is in agreement with previous SCF calculations by Pickett and Balazs[12].

In the case of the *ultrathin films*, our results demonstrate that adsorption of a block copolymer as an ultrathin film leads to a periodic surface domain structure (stripes), where both polar blocks (B and C) adsorb to the surface. Due to significant stretching of the adsorbed blocks the spacings between the domains are large for the rather low molecular weight block copolymers. The lateral dimensions correlate well with the molecular dimensions of the A and B/C blocks according to previously derived scaling laws[14].

It could be shown that the striped structure observed in the as-prepared samples exhibits the tendency to rearrange into a thermodynamically more stable island-like structure on annealing. These patterns show a lower uniformity in size and long-range order, presumably due to the influence of the silicon substrate.

Especially for ultrathin films our results show that the size of the PS domains is dominated by the molecular weight of PS whereas the spacing of the PS stripes or clusters can be controlled by the length of the PHEMA-*b*-PMMA and P2VP-*b*-PMMA blocks. The understanding of domain formation by self-assembly of block copolymers into certain surface morphologies by tailoring the polymer architecture is an important aspect for future investigations on generation of polymeric templates for a large variety of applications.

Acknowledgement

References

[1] The results of this chapter have already been pubilshed: A. Böker, A.H.E. Müller, G. Krausch *Macromolecules* **2001**, *34*, 7477-7488.

[2] Kellogg, G. J.; Walton, D. G.; Mayes, A. M.; Lambooy, P.; Russel, T. P.; Gallagher, P. D.; Satija, S. K. *Phys. Rev. Lett.* **1996**, *76*, 2503.

[3] Morkved, T. L.; Lu, M.; Urbas, A. M.; Ehrichs, E. E.; Jaeger, H. M.; Mansky, P.; Russell, T. P. *Science* **1996**, *273*, 931.

[4] Walton, D. G.; Kellogg, G. J.; Mayes, A. M.; Lambooy, P.; Russell, T. P. *Macromolecules* **1994**, *27*, 6225.

[5] Henkee, C. S.; Thomas, E. L.; Fetters, L. J. *J. Mat. Sci.* **1988**, *23*, 1685.

[6] Morkved, T. L.; Jaeger, H. M. *Europhys. Lett.* **1997**, *40*, 643.

[7] Singhvi, R.; Kumar, A.; Lopez, G. P.; Stephanopoulos, G. N.; Wang, D. I. C.; Whitesides, G. M.; Ingber, D. E. *Science* **1994**, *264*, 696.

[8] Morkved, T. L.; Wiltzius, P.; Jaeger, H. M.; Grier, D.; Witten, T. *Appl. Phys. Lett.* **1994**, *64*, 422.

[9] Spatz, J. P.; Roescher, A.; Möller, M. *Adv. Mater.* **1996**, *8*, 337.

[10] Spatz, J. P.; Eibeck, P.; Mößmer, S.; Möller, M.; Herzog, T.; Ziemann, P. *Adv. Mater.* **1998**, *10*, 849.

[11] Fukunaga, K.; Elbs, H.; Krausch, G. *Langmuir* **2000**, *16*, 3774.

[12] Pickett, G. T.; Balazs, A. C. *Macromol. Theory Simul.* **1998**, *7*, 249.

[13] Elbs, H.; Fukunaga, K.; Stadler, R.; Sauer, G.; Magerle, R.; Krausch, G. *Macromolecules* **1999**, *32*, 1204.

[14] Potemkin, I. I.; Kramarenko, E. Y.; Khokhlov, A. R.; Winkler, R. G.; Reineker, P.; Eibeck, P.; Spatz, J. P.; Möller, M. *Langmuir* **1999**, *15*, 7290.

[15] Eibeck, P.; Spatz, J. P.; Potemkin, I. I.; Kramarenko, E. Y.; Khokhlov, A. R.; Möller, M. *Polymer Prepr.* **1999**, *40*, 990.

[16] Hirao, A.; Kato, H.; Yamaguchi, K.; Nakahama, S. *Macromolecules* **1986**, *19*, 1294.

[17] Walheim, S.; Böltau, M.; Mlynek, J.; Krausch, G.; Steiner, U. *Macromolecules* **1997**, *30*, 4995.

[18] Morkved, T. L.; Lopes, W. A.; Hahm, J.; Sibener, S. J.; Jaeger, H. M. *Polymer* **1998**, *39*, 3871.

[19] Fasolka, M. J.; Banerjee, P.; Mayes, A. C.; Pickett, G.; Balazs, A. C. *Macromolecules* **2000**, *33*, 5702.

[20] Spatz, J. P.; Möller, M.; Noeske, M.; Behm, R. J.; Pietralla, M. *Macromolecules* **1997**, *30*, 3874.

[21] Keddie, J. L.; Jones, R. A. L. *Isr. J. Chem.* **1995**, *35*, 21.

[22] Keddie, J. L.; Jones, R. A. L.; Cory, R. A. *Faraday Disc.* **1994**, *98*, 219.

[23] Fryer, D. S.; Nealey, P. F.; de Pablo, J. J. *Macromolecules* **2000**, *33*, 6439.

[24] Spatz, J. P.; Sheiko, S.; Möller, M. *Adv. Mater.* **1996**, *8*, 513.

[25] Spatz, J. P.; Eibeck, P.; Mössmer, S.; Möller, M.; Kramarenko, E. Y.; Khalatur, P. G.; Potemkin, I. I.; Winkler, R. G.; Reineker, P. *Macromolecules* **2000**, *33*, 150.

[26] Brandrup, J.; Immergut, E. H. *Polymer Handbook*; 3rd ed.; Wiley Publisher: New York, **1991**.

Chapter 4

Wetting of Chemically Nanopatterned
Model Surfaces

Abstract

We investigate the wetting behavior of thin ~ 20 nm polystyrene films floated onto chemically nanopatterned (heterogeneous) substrates, formed by adsorption of a polystyrene-*b*-poly(2-vinyl pyridine)-*b*-poly(methyl methacrylate) block copolymer onto a polished silicon wafer. These substrates exhibit a surface morphology mainly consisting of PS brushes on a PMMA sublayer. Upon annealing, we observe partial dewetting of the PS film from the substrate, resulting in an undulated meander-like PS pattern. In contrast, treatment in saturated chloroform vapor leads to complete dewetting of the PS film induced by growth of large holes.

4.1.   Introduction

In recent years, the use of block copolymers for surface patterning has attracted increasing attention[1-5]. Well-defined laterally patterned surfaces are important for a variety of applications, e.g. as compatibilizers for polymer blends[6] or as templates for growing biological cells with controlled shapes and sizes[7]. Furthermore, laterally patterned polymer surfaces can be used as model systems for the study of wetting and dewetting phenomena on heterogeneous substrates[8-10]. This field recently received a great amount of attention, because the wetting behavior of thin polymer films on different types of substrates is of considerable importance in practical applications such as paints, adhesives, lubricants, dielectrics, biomedical devices, and nonlinear optics. The study of basic wetting phenomena in polymeric systems is even more important as it has been demonstrated that the wetting dynamics and dewetting instability of polymer molecules can be very different from those of simple liquids[11-14].

The wetting behavior of thin PS films on homogeneous silicon substrates has been studied extensively over the last years. The initiation of the dewetting process, the underlying mechanisms as well as its kinetics have been investigated in detail[14-22]. More recent experiments focus on the wetting behavior of chemically and topographically nanostructured surfaces[23,24].

Following recent results by Eibeck et al.[25,26] and our own studies[27], we use the adsorption of a polystyrene-b-poly(2-vinyl pyridine)-b-poly(methyl methacrylate) triblock copolymer onto a polished silicon wafer to generate well-defined dot- or stripe-like PS/PMMA patterns of characteristic lateral spacing on the surface.

The aim of the present work is to study the wetting behavior of thin PS films on these chemically patterned (heterogeneous) model substrates.

The use of polymers for this purpose has several advantages compared to common low molecular weight liquids. The vapor pressure of polymers is negligible and thus the mass of the film is conserved and the low mobility of polymer melts favors time-resolved experiments.

4.2.   Experimental Section

4.2.1.   Materials and Methods

The block copolymer used in this study was synthesized by sequential anionic polymerization as described in detail elsewhere[27]. The composition as calculated from ^{1}H-NMR of the block copolymer using GPC results for the corresponding PS precursor, calibrated with narrowly distributed PS standards, yields 48 wt.-% PS, 5 wt.-% P2VP, and 47 wt.-% PMMA with an overall number-average molecular weight M_n of 180,000 g/mol (in the following, we will denote the polymer as $S_{48}2VP_5M_{47}^{180}$, for chemical structure see Figure 4-1). The polystyrene (PS) homopolymer samples were purchased from PSS, Mainz, Germany. PS 14, PS 54 and PS 104 denote homopolymer samples with M_n of 14 kg/mol, 54 kg/mol and 104 kg/mol, respectively.
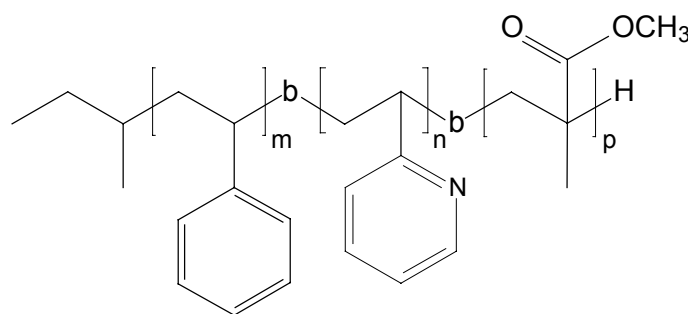

Figure 4-1:   *Chemical structure of PS-b-P2VP-b-PMMA triblock copolymer (N_{PS} = 825, N_{P2VP} = 80, N_{PMMA} = 855).*

4.2.2.   Sample Preparation

In order to laterally pattern the silicon wafers, they were exposed to 1 mg/ml solutions of the block copolymer in THF for 3-4 days, which led to adsorption of the polymer onto the polar substrate. Subsequently, the wafers were rinsed 4 times with 5 ml THF.

Prior to use, the Si wafers were rinsed in organic solvents (THF, chloroform and acetone) and subsequently treated with a beam of CO_2 crystals ("snow jet™") to remove any organic residues from the surface.

The thin PS films were prepared by spin coating a toluene solution of the respective polymer onto silicon wafers. After drying, they were floated from the silicon support and transferred via the surface of deionized water onto the patterned model substrates.

4.2.3.   Scanning Force Microscopy

SFM images were taken on a Digital Instruments Dimension 3100 microscope operated in Tapping Mode^{TM} (free amplitude of the cantilever $\approx$ 20 nm, amplitude set point $\approx$ 0.98). The standard silicon nitride probes were driven at 3 % offset below their resonance frequencies in the range of 250-350 kHz. Height and phase images were taken at scanning speeds of around 6 μm/sec.

4.3.   Results

Before we start the description of the wetting behavior of PS films on chemically structured surfaces, we briefly recall the surface morphology of ultrathin block copolymers adsorbed onto silicon wafers. As has been reported earlier[27], the adsorption of an ABC triblock copolymer with a short anchoring middle block (in this case P2VP, which enhances the adsorption from solution) leads to a surface structure as described in Scheme 3-2 in chapter 3, where the B and C blocks (P2VP-*b*-PMMA) are adsorbed to the polar substrate and PS protrusions form a island- or stripe-like pattern. For the $S_{48}2VP_5M_{47}^{180}$ block copolymer used in this study, we find a characteristic half-spacing of $D = 80 \pm 7$ nm, which does not change significantly upon annealing (height H of the protrusions: 4.4 ± 0.6 nm, for details see chapter 3).
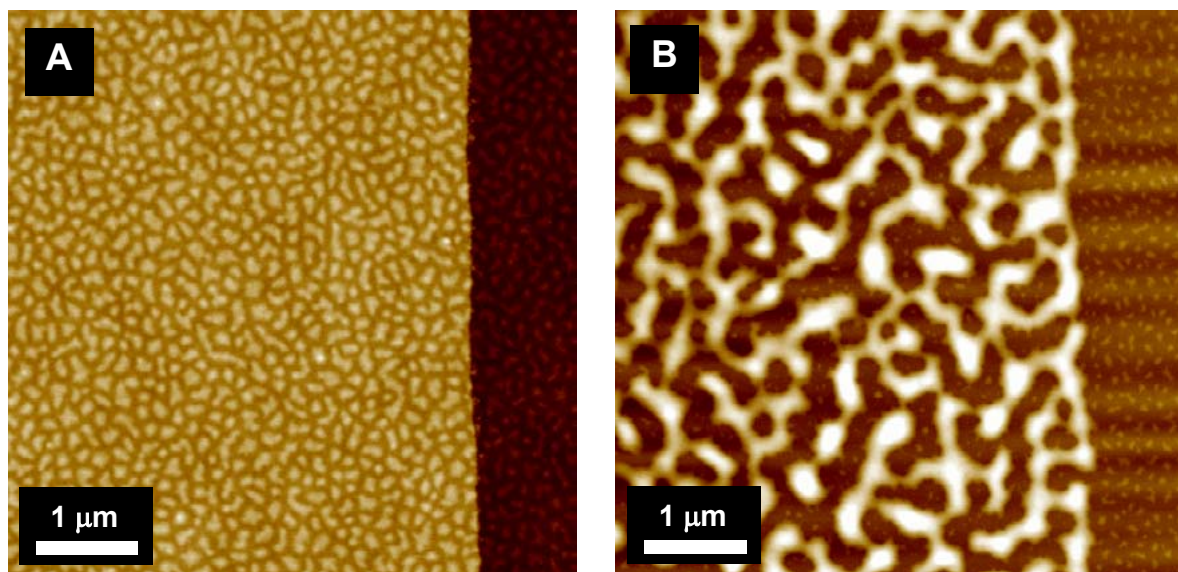

Figure 4-2:   *SFM topography image of PS 54 on $S_{48}2VP_5M_{47}^{180}$: (A) as prepared (z-range: 30 nm) and (B) after 5 min at 130 °C (z-range: 60 nm). The right side of each image shows the pure triblock copolymer substrate.*

74

When a thin PS film (thickness ~ 20 nm) is floated onto the above described model surface, we partially observe rupture of the film, leading to sharp edges between regions covered with the homopolymer film (on the left in Figure 4-2A) and the free block copolymer surface (on the right in Figure 4-2B). This allows us to investigate the changes in morphology for the PS film as well as for the free block copolymer surface. In addition, we can see in Figure 4-2A that the PS protrusions of the adsorbed block copolymer layer even slightly deform the PS sheet covering the sublayer. Thus, the topography of the sublayer can also be seen on the left side of Figure 4-2A.
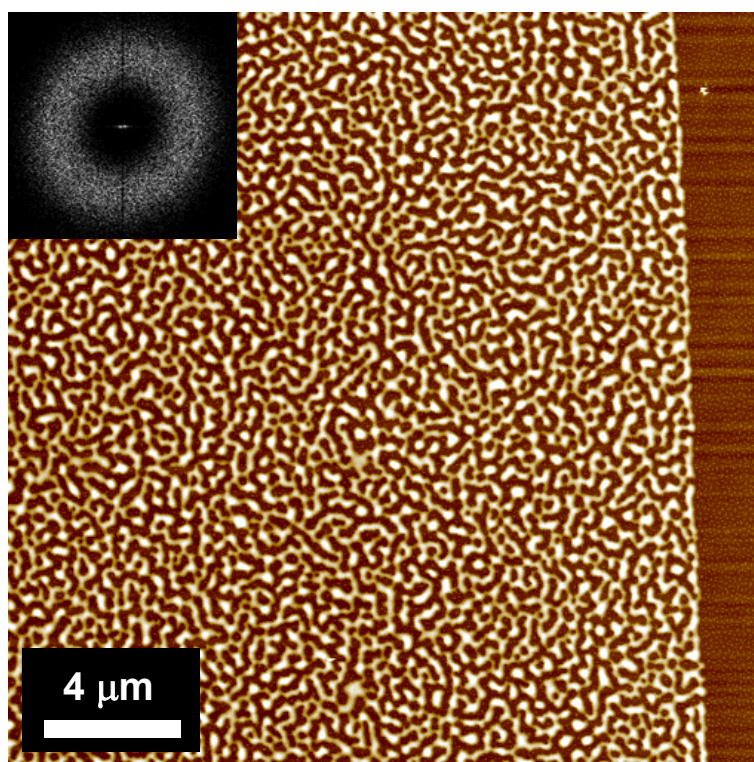

Figure 4-3:   *SFM topography image of PS 54 on $S_{48}2VP_5M_{47}^{180}$ after 5 min at 130 °C (z-range: 60 nm). Fourier-transform of the PS pattern (inset) yields d ~ 420 nm.*

4.3.1.   Stability of polystyrene films on a triblock copolymer model surface

4.3.1.1.   Annealing

In order to check the stability of the homopolymer film on our patterned substrates, the samples were annealed on a hotstage at 130°C, which is well above the glass transition temperature of polystyrene (T_g ~ 100°C). Here, we report the observations made with a 20 nm thick PS 54 film on $S_{48}2VP_5M_{47}^{180}$. After 5 minutes, we observe a characteristic dewetting pattern as shown in Figure 4-2B. The previously homogeneous film has broken up into an

undulated meander-like pattern. Between the dewetted PS stripes, parts of the triblock copolymer sublayer become visible. In the region of the homopolymer film the distance between the PS protrusions of the sublayer seems to be larger than in the areas of the pure triblock copolymer sublayer. It appears as if the triblock has been incorporated partially with its PS block into the homopolymer film, acting as a compatibilizer and thus preventing a complete, large scale dewetting process as found for pure silicon wafers[15]. A Fourier-transform analysis of the dewetting pattern as shown in the inset in Figure 4-3 reveals a mean distance, d, between the PS meanders of approximately 420 nm. This is about 2.5 times larger than the mean spacing between the PS protrusions of the underlying ultrathin block copolymer film. We note that these surface features are still too small to be visualized optically, so that the wafer does not turn opaque due to large dewetting structures. We anticipate that longer annealing times may eventually lead to an amplification of the undulations and finally result in a break-up of the meander-like stripes into small droplets.
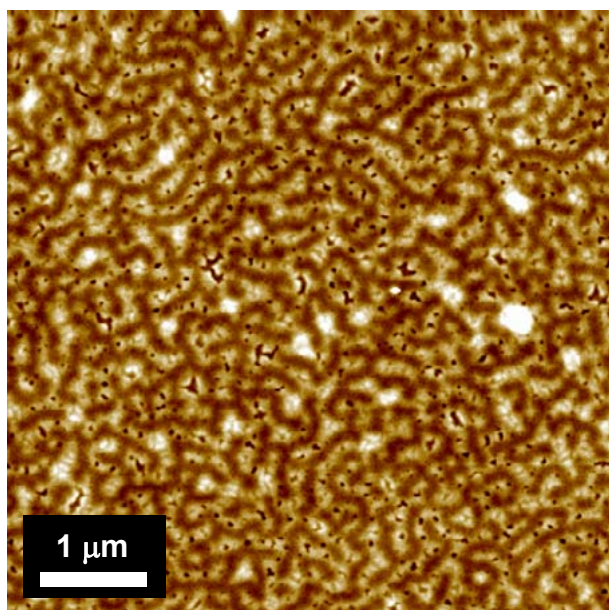

Figure 4-4:   *SFM topography image of PS 14 on $S_{48}2VP_5M_{47}^{180}$ after 1 min of exposure to saturated $CHCl_3$ vapor (z-range: 15 nm).*

4.3.1.2.   Solvent Vapor Treatment

For the experiments using saturated chloroform vapor, we start with a sample morphology identical to the one depicted in Figure 4-2A. At the very early stages of the vapor treatment, we observe rupture of the thin homopolymer films at the spots where the PS sheet covers the PS protrusions formed by the triblock copolymer sublayer as can be seen in Figure 4-4 for a PS 14 on $S_{48}2VP_5M_{47}^{180}$ after one minute of treatment with saturated chloroform vapor. This is also observed for PS 104. We note that except for the dewetting kinetics, we did not detect

any difference in the wetting behavior depending on the molecular weight during solvent vapor treatment. Therefore, in the following, we will focus on data of PS 104 on $S_{48}2VP_5M_{47}^{180}$ as the slower kinetics allows a better time resolution of the experiment.
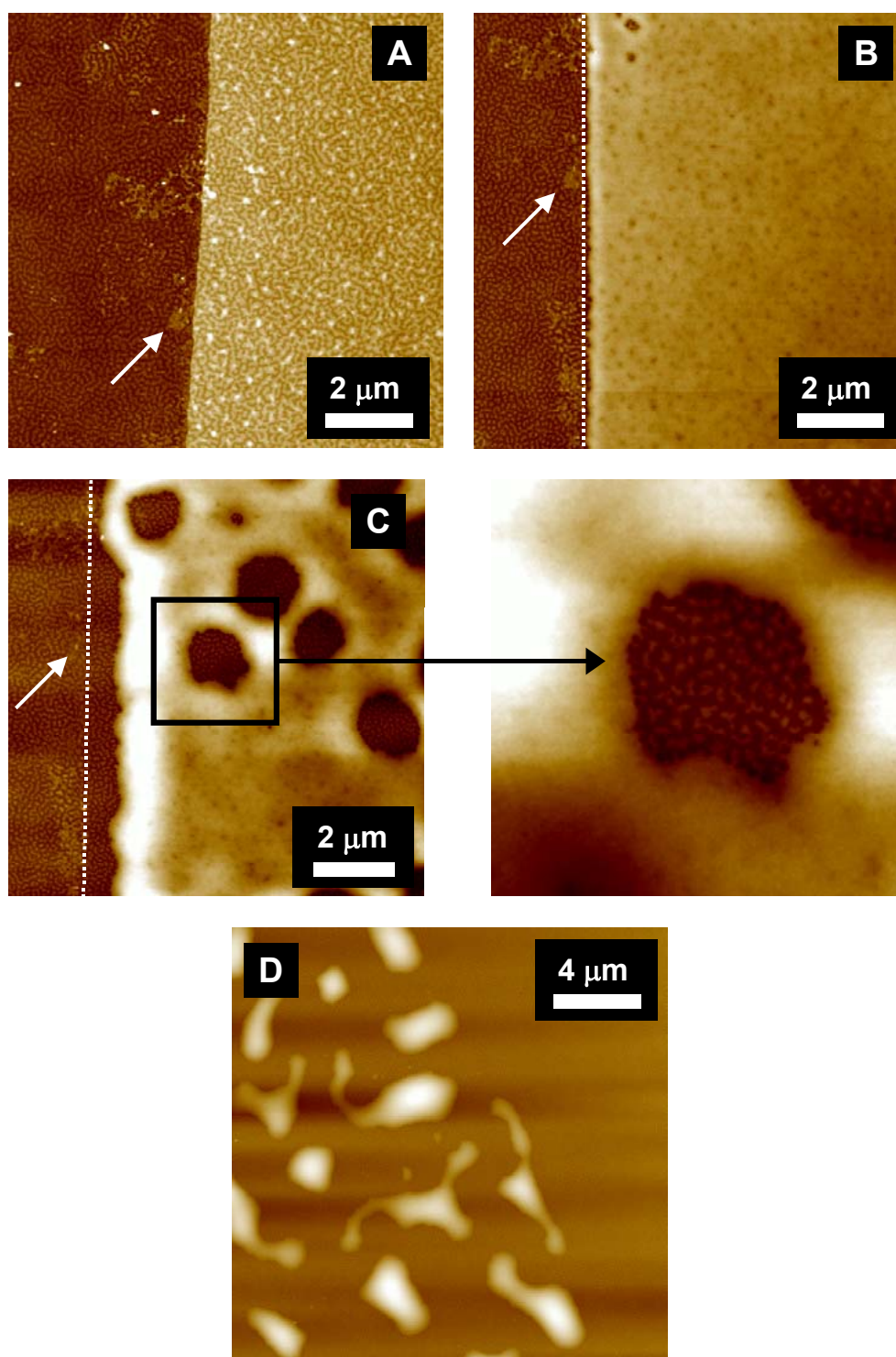

Figure 4-5:   *SFM topography images of PS 104 on $S_{48}2VP_5M_{47}^{180}$ (A) as prepared, (B) after 3 min (C) 9.5 min (z-range: 50 nm) and (D) 15 min saturated CHCl$_3$ vapor (z-range: 250 nm). The dotted lines show the original position of the rim. The arrow points to a defect in the sublayer.*

In Figure 4-5 we show a series of SFM images taken at different stages of solvent vapor treatment at the same spot of the sample (see arrow in Figure 4-5A-C). After the above

described rupture, the film seems to relax to form a more homogeneous surface, where the PS protrusions of the sublayer do not influence the surface topography of the homopolymer film any more. Nevertheless, in Figure 4-5B we observe a large number of widely distributed indents and even first holes in the PS film. As can be seen in Figure 4-5C, the film forms a large rim (original position indicated by dotted line) which slowly retracts while more holes are created which grow with time. The magnification of a large hole in Figure 4-5C reveals that the block copolymer sublayer seems to be unperturbed by the whole dewetting process.

Finally, as depicted in Figure 4-5D, the holes connect to each other and PS droplets are formed. Compared to the dewetting pattern observed after annealing, the distance between the droplets is much larger. Additionally, there are at least two orders of magnitude between the average spacing and size of the PS protrusions of the underlying block copolymer layer and the droplets formed during solvent vapor annealing.

These dewetting patterns are now large enough to be visualized optically, i.e. the sample turns opaque. An optical micrograph of a completely dewetted film is shown in Figure 4-6. These structures are very similar to "classical" dewetting patterns formed by PS on pure silicon wafers as described in detail by G. Reiter[15].
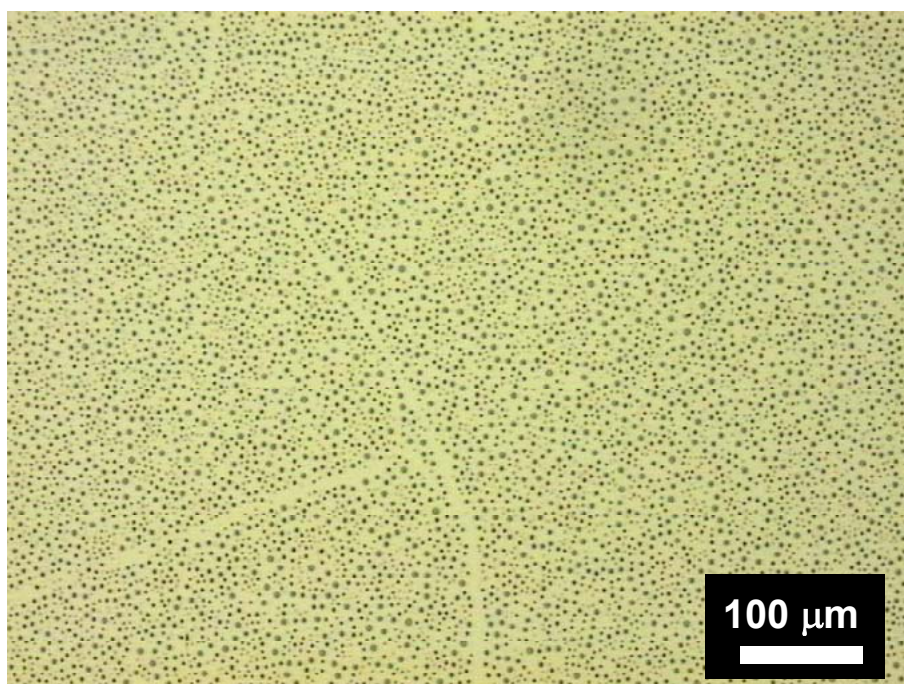

Figure 4-6:   *Optical micrograph of PS 14 on $S_{48}2VP_5M_{47}^{180}$ after CHCl$_3$ vapor treatment for 5.5 min.*

78

4.4.   Discussion

From the above described experiments, we cannot draw any definite conclusions about the wetting behavior of PS homopolymer films on a PS/PMMA nanopatterned surface. From surface tension considerations we may have expected a significant stabilization of the homopolymer films compared to the behavior on pure silicon wafers. This has only been observed for the annealed film, where undulated PS meanders are formed. Their spacings are larger than the dimensions of the sublayer but do not exhibit a difference in size of several orders of magnitude as found for the vapor treated films.

In the case of the PS homopolymer films annealed in solvent vapor, the sublayer does not seem to be influenced by the dewetting PS film. Even though we expect the mobility of chains in a vapor swollen film to be much higher than during thermal annealing, interpenetration of the homopolymer and the PS blocks of the sublayer does not seem to occur. Here, it could well be that "autodewetting" is observed. It is well-known that an entropic barrier can be established when polymer molecules are confined in specific configurations (e.g. end-grafted to a solid substrate forming a dense brush[28], ordered in lamellae in a block copolymer at an interface[29] or interconnected in a network/gel type matrix[30]). In these cases the entropic gain in free energy associated with interpenetration of the homopolymer chains and the chains at the substrate surface is more than compensated for by the loss in conformational entropy due to distortion of the substrate chains and a well defined interface is formed. The excess energy associated with this interface can then destabilize the film and induce dewetting.

4.5.   Conclusions

We have presented first studies on the wetting behavior of thin PS homopolymer films on chemically nanopatterned substrates which already show that a partial stabilization of a PS film can be achieved by an ultrathin sublayer of a polystyrene-*b*-poly(2-vinyl pyridine)-*b*-poly(methyl methacrylate) block copolymer. So far, the experiments only allow a very qualitative description of the results. Further work will have to concentrate on a systematic variation of the PS domain spacing D of the sublayer in order to elucidate any correlation with the mean spacing of the dewetting pattern. Furthermore, the influence of the molecular weight of the homopolymer and the film thickness on the wetting behavior and kinetics should be investigated systematically.

Acknowledgement

References

[1] Kellogg, G.J.; Walton, D G.; Mayes, A.M.; Lambooy, P.; Russel, T. P.; Gallagher, P.D.; Satija, S. K. *Phys. Rev. Lett.* **1996**, *76*, 2503.

[2] Morkved, T.L.; Lu, M.; Urbas, A.M.; Ehrichs, E.E.; Jaeger, H.M.; Mansky, P.; Russell, T.P. *Science* **1996**, *273*, 931.

[3] Walton, D.G.; Kellogg, G.J.; Mayes, A.M.; Lambooy, P.; Russell, T.P. *Macromolecules* **1994**, *27*, 6225.

[4] Henkee, C.S.; Thomas, E.L.; Fetters, L.J. *J. Mat. Sci.* **1988**, *23*, 1685.

[5] Morkved, T.L.; Jaeger, H.M. *Europhys. Lett.* **1997**, *40*, 643.

[6] Fukunaga, K.; Elbs, H.; Krausch, G. *Langmuir* **2000**, *16*, 3474.

[7] Singhvi, R.; Kumar, A.; Lopez, G.P.; Stephanopoulos, G.N.; Wang, D.I.C.; Whitesides, G.M.; Ingber, D.E. *Science* **1994**, *264*, 696.

[8] Konnur, R.; Kargupta, K.; Sharma, A. *Phys. Rev. Lett.* **2000**, *84*, 931.

[9] Kargupta, K.; Konnur, R.; Sharma, A. *Langmuir* **2000**, *16*, 10243.

[10] Kargupta, K.; Sharma, A. *J. Chem. Phys.* **2002**, *116*, 3042.

[11] Silberzan, P.; Léger, L. *Macromolecules* **1992**, *25*, 1267.

[12] Bruinsma, R. *Macromolecules* **1990**, *23*, 276.

[13] Zhao, W.; Rafailovich, M.H.; Sokolov, J.; Fetters, L.J.; Plano, R.; Sanyal, M.K.; Sinha, S.K.; Sauer, B.B. *Phys. Rev. Lett.* **1993**, *70*, 2659.

[14] Reiter, G. *Langmuir* **1993**, *9*, 1344.

[15] Reiter, G. *Phys. Rev. Lett.* **1992**, *68*, 75.

[16] Brochard, F.; di Meglio, J.M.; Quéré, D. *C. R. Acad. Sci., Ser. II* **1987**, *304*, 553.

[17] Brochard, F.; de Gennes, P.G. *Langmuir* **1992**, *8*, 3033.

[18] Brochard-Wyart, F.; Redon, C.; Sykes, C. *C. R. Acad. Sci., Ser. II* **1992**, *314*, 10.

[19] Brochard-Wyart, F.; de Gennes, P. G.; Hervet, H.; Redon, C. *Langmuir* **1994**, *10*, 1566.

[20] Reiter, G. *Macromolecules* **1994**, *27*, 3046.

[21] Seemann, R.; Herminghaus, S.; Jacobs, K. *J. Phys.: Condens. Matter* **2001**, *13*, 4925.

[22] Seemann, R.; Herminghaus, S.; Jacobs, K. *Phys. Rev. Lett.* **2001**, *86*, 5534.

[23] Rockford, L.; Liu, Y.; Mansky, P.;Russell, T.P.; Yoon, M.; Mochrie, S.G.J. *Phys. Rev. Lett.* **1999**, *82*, 2602.

[24] Rehse, N.; Krausch, G. *Eur. Phys. J. E* **2001**, *4*, 69.

[25] Spatz, J.P.; Eibeck, P.; Mössmer, S.; Möller, M.; Kramarenko, E.Y.; Khalatur, P.G.; Potemkin, I.I.; Winkler, R.G.; Reineker, P. *Macromolecules* **2000**, *33*, 150.

[26] Eibeck, P.; Spatz, J.P.; Potemkin, I.I.; Kramarenko, E.Y.; Khokhlov, A.R.; Möller, M. *Polym. Prepr.* **1999**, *40*, 990.

[27] Böker, A.; Müller, A.H.E.; Krausch, G. *Macromolecules* **2001**, *34*, 7477.

[28] Henn, G.; Bucknall, D.G.; Stamm, M.; Vanhoorne, P.; Jerome, R. *Macromolecules* **1996**, *29*, 4305.

[29] Liu, Y.; Rafailovich, M.H.; Sokolov, J.; Schwarz, S.A.; Zhong, X.; Eisenberg, A.; Kramer, E.J.; Sauer, B.B.; Satija, S. *Phys. Rev. Lett.* **1994**, *73*, 440.

[30] Kerle, T.; Yerushalmi-Rozen, R.; Klein, J. *Europhys. Lett.* **1997**, *38*, 207.

83

Chapter 5

Large Scale Domain Alignment of a Block Copolymer from Solution using Electric Fields[1]

Abstract

We have aligned the microdomains of a polystyrene-*b*-poly(2-hydroxyethyl meth-acrylate)-*b*-poly(methyl methacrylate) (PS-*b*-PHEMA-*b*-PMMA) triblock copolymer during preparation from solution by virtue of an external electric DC field (1.8 kV/mm). Bulk samples cast in the presence of an electric field exhibit lamellar microdomains highly oriented parallel to the electric field vector, as shown by small-angle X-ray scattering (SAXS) and transmission electron microscopy (TEM).

5.1.   Introduction

The microphase separation of block copolymers has been studied extensively over the past two decades both experimentally and theoretically[2,3]. In the ordered state, these materials exhibit highly regular mesoscopic microdomain structures with characteristic length scales of the order of several tens of nanometers. Similar to polycrystalline materials, typically small grains of microdomains are formed, the size of which may be of the order of microns. As a consequence, although a single grain may have a highly anisotropic structure (e.g. in the case of cylindrical or lamellar structures), a bulk sample of a block copolymer typically exhibits isotropic materials properties. If macroscopic anisotropies are desirable, additional efforts have to be made to create macroscopic alignment of the microdomain structures. In the past, different techniques aiming towards macroscopic microdomain alignment have been devised. Most prominently, external mechanical fields have been successfully applied to orient block copolymer melts (e.g. Large Amplitude Oscillatory Shear (LAOS)[4 - 6] or extrusion[7]) and block copolymer solutions (e.g. roll-casting[8]).

In addition to mechanical fields, the potential of electric fields for microdomain alignment has attracted increasing interest in the recent past as it may also be of considerable technical interest[9]. It has been shown that both lamellar and cylindrical microdomain structures in polystyrene-*b*-poly(methyl methacrylate) (PS-*b*-PMMA) melts could be oriented macroscopically by virtue of a DC electric field [10 - 15]. Due to the differences in the dielectric constants ($\Delta\varepsilon$) of the blocks ($\varepsilon_{PS} \approx 2.4$, $\varepsilon_{PMMA} \approx 3.6$)[16], the microdomains tend to orient parallel to the electric field vector, thereby lowering the free energy of the system. The electric field - induced driving force is proportional to $(\Delta\varepsilon E)^2$ [11,15]. Cylindrical microdomains can in principle be aligned along the field vector resulting in a single monodomain (i.e. a block copolymer "single crystal"). In a lamellar microdomain structure, on the other hand, all lamellar orientations containing the electric field vector within the lamellar planes are energetically equivalent. Therefore, the electric field is expected to at best favor the sub-set of lamellar orientations with the lamellar normal pointing perpendicular to the field.

So far most experiments using electric fields have been conducted in the melt. Due to the high melt viscosities, they are limited with respect to the molecular weight of the copolymers and the size of the macroscopic regions to be oriented ($M_w \approx 74000$ g/mol for thin films of thickness 1 μm [17]; $M_w \approx 37000$ g/mol for samples of thickness 2 mm [10,11]). In addition, temperatures close to the decomposition temperature and electric field strengths of up to 25 kV/mm are required to achieve high degrees of orientation. These limitations render the orientation of higher molecular weight copolymers or copolymers of more complex

architectures (multiblock copolymers, star copolymers, etc.) rather difficult if not impossible, since their melt viscosities easily exceed the values faced in the investigations quoted above. Given the increasing interest in complex block copolymer structures, it is therefore desirable to explore alternative approaches, which circumvent the above limitations.

In the present contribution, we demonstrate the potential of an electric DC field for the microdomain alignment of a block copolymer *solution*[18,19]. The field is applied during solvent evaporation until final film formation and thereby leads to macroscopically oriented bulk specimens as well. The use of a solvent based procedure extends the potential of electric fields for block copolymer alignment to a much larger class of block copolymers. As an example, we apply the approach to an ABC triblock copolymer, where macroscopic melt alignment in electric fields is expected to be hardly possible. We note that the aligning force of an electric field is significantly smaller for block copolymer solutions than for melts due to an effective reduction of the difference in the dielectric constants of the blocks $\Delta\varepsilon$ by the solvent.

5.2. Experimental Section

A polystyrene-*b*-poly(2-hydroxyethyl methacrylate)-*b*-poly(methyl methacrylate) triblock copolymer was synthesized by sequential living anionic polymerization as described in detail elsewhere[20]. The polymer used in this study consists of 47 wt.-% polystyrene, 43 wt.-% poly(methyl methacrylate) (PMMA) and 10 wt.-% poly(2-hydroxyethyl methacrylate) (PHEMA) with a total number average molecular weight $M_n = 82000$ g/mol. GPC of the final block copolymer yields a polydispersity of $M_w/M_n = 1.04$.

5.2.1. Polymer Analysis

GPC measurements were performed using a set of 30 cm SDV-gel columns of 5 μm particle size having 10^5, 10^4, 10^3 and 10^2 Å pore size and dual detectors (RI and UV [$\lambda = 254$ nm]). The solvent was THF at room temperature with an elution rate of 1 mL/min. Narrowly distributed polystyrene samples were used as calibration standards.

^{1}H-NMR spectra were acquired on a 250 MHz Bruker AC 250 instrument using CDCl$_3$ as solvent and tetramethylsilane (TMS) as internal standard. The molecular weights of the PHEMA and PMMA blocks were calculated using the block copolymer composition determined by NMR and the polystyrene molecular weight obtained from GPC.

5.2.2.   Sample Preparation

The alignment experiments were performed in a cylindrical capacitor with aluminum electrodes (r = 5 mm, d = 1.1 mm; Figure 5-1) at room temperature. A DC voltage of 2 kV was applied resulting in an electric field strength of ~ 1.8 kV/mm. The voltage at the electrodes and the current were monitored during the course of the experiment indicating only a small leakage current (0.01 − 0.02 mA) during the first few seconds after the field was applied. Between 0.2 and 1.1 mm thick films were obtained by slowly evaporating the solvent from 30 vol.-% solutions of the block copolymer in chloroform.
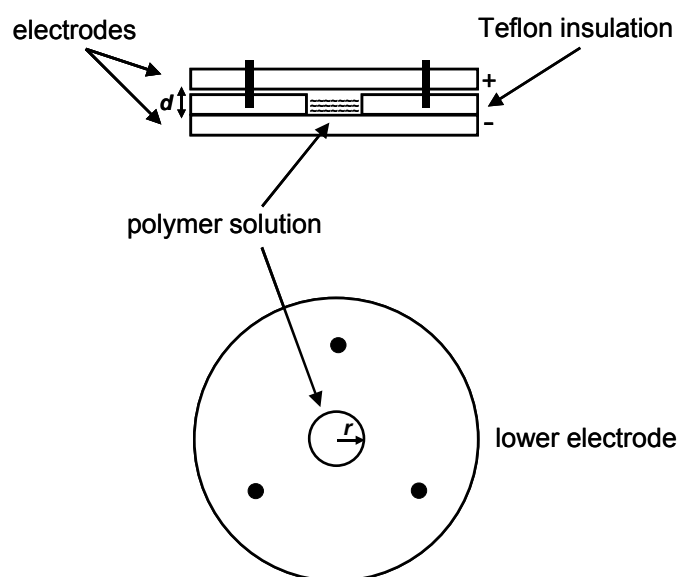

Figure 5-1:   *Capacitor setup used for sample preparation in the absence and in the presence of an electric field, respectively.*

5.2.3.   Small Angle X-ray Scattering (SAXS)

Cubic specimen of approximately 1 mm edge length were cut from the respective regions of interest of the as-cast film. SAXS measurements were performed using a Bruker-AXS Nanostar instrument with a sealed tube Cu K_α X-ray source (λ = 1.5418 Å) operated at 40 mA and 40 kV and a 2D Histar detector. The direction of the X-ray beam (approximate cross section: 100 μm/crossed Goebel mirrors) was perpendicular to the vector of the applied electric field. The scattering patterns were corrected for the beam stop and background prior to further evaluations.

In order to estimate the scattering contrast between PHEMA and PMMA we calculate the electron density of both possible methacrylic phases taking into account the different densities of ρ_{PHEMA} = 1.15 g/cm^3 [16] and ρ_{PMMA} = 1.19 g/cm^3 [16] and the molecular weights of 130 and 100 g/mol, respectively. The calculations yield an electron density of 0.64 mol/cm^3 for

PMMA and 0.62 mol/cm^3 for PHEMA. These values are similar and in both cases significantly higher than the 0.56 mol/cm^3 that we calculate for the polystyrene phase. Therefore we may conclude that there is no significant scattering contrast between the methacrylic phases compared to polystyrene.

5.2.4. Scanning Electron Microscopy (SEM)

SEM was performed using a LEO 1530 Gemini instrument equipped with a field emission cathode with a lateral resolution of approximately 2 nm. The acceleration voltage was 5 kV. The sample was prepared by freeze fracture. Prior to the measurements it was sputtered with gold.

5.2.5. Transmission Electron Microscopy (TEM)

Thin sections were cut from the as-cast films parallel to the electric field vector (far from any surface) using a Reichert-Jung Ultracut E microtome equipped with a diamond knife. In order to enhance the electron density contrast between polystyrene and the methacrylic blocks, the sections were exposed to RuO_4 vapor for 45 minutes, which leads to a preferential staining of the polystyrene block[21]. Bright field TEM was performed using a Zeiss electron microscope (CEM 902) operated at 80 kV in the bright field mode.

5.2.6. Calculation of order parameters

As will become clear from the experimental observations described below, domain alignment is induced by two competing external fields of different symmetry, i.e. the interfacial field between polymer solution and electrode surface and the electric field, respectively. To quantify the alignment, we calculate the order parameter P_2 by integrating the scattering intensity from $\varphi = 0°$ to $360°$:

$$P_2 = \frac{3\langle \cos^2 \varphi \rangle - 1}{2}$$

with

$$\langle \cos^2 \varphi \rangle = \frac{\int_0^{2\pi} d\varphi \left(I_q(\varphi) \cdot \cos^2(\varphi) \cdot |\sin(\varphi)| \right)}{\int_0^{2\pi} d\varphi \left(I_q(\varphi) \cdot |\sin(\varphi)| \right)}$$

Depending on the position of the maxima of the scattering intensity the calculation yields two different ranges of the order parameter. For lamellar alignment parallel to the electrodes (maximum at $\varphi = 0°$), P_2 ranges from 0 to 1 with $P_2 = 1$ corresponding to perfect lamellar alignment where all lamellar normals are oriented perpendicular to the surfaces, i.e. electrodes. For alignment of the lamellae along the field direction (maximum at $\varphi = 90°$), P_2 ranges from 0 to - 0.5 with $P_2 = - 0.5$ corresponding to the case where all lamellae are aligned parallel to the field, however, with the lamella normals being isotropically oriented in the plane of the electrodes. Depending on the type of alignment the maximum values describing perfect alignment are 1 and - 0.5, respectively.

5.3.   Results

5.3.1.   Films cast at zero electric field

In order to exclude any effect of solvent evaporation on the alignment process, films were cast in the setup shown in Figure 5-5-1, however in the absence of an external electric field. We observe a highly anisotropic SAXS pattern as shown in Figure 5-5-2a. The azimuthal angular dependence (φ) of the scattering intensity (Figure 5-5-2b) reveals a preferential alignment of the lamellae parallel to the electrodes. We attribute this finding to a strong affinity of the solution/electrode interface to one of the blocks, which leads to preferential orientation of the lamellae parallel to the electrodes during solvent evaporation. This phenomenon has already been observed by Annighöfer and Gronski for controlled solvent casting of lamellar polystyrene-*b*-polyisoprene diblock copolymers[22].

For the data presented in Figure 5-2 we calculate the order parameter of $P_2 = 0.43$. The lamellar spacing $d_{SAXS} = 45 \pm 2$ nm calculated from the first-order reflection in Figure 5-2c at $q^* = 0.14$ nm^{-1} ($d_{SAXS} = 2\pi/q^*$) fits well to the value $d_{TEM} = 40 \pm 2$ nm obtained from the TEM pictures (Figure 5-3a). Furthermore, Figure 5-3a shows a well-ordered lamellar microdomain alignment parallel to the electrode surfaces thereby corroborating the SAXS results.

5.3.2.   Films cast in the presence of an electric field

Film formation under the influence of an external electric field results in significant thickness undulations, which eventually lead to the formation of column-like protrusions that connect both electrodes. Recently, Schäffer *et al.* showed that electric fields can induce

instabilities in a liquid polymer film leading to the formation of polymer columns quite similar to the ones observed here[23,24].
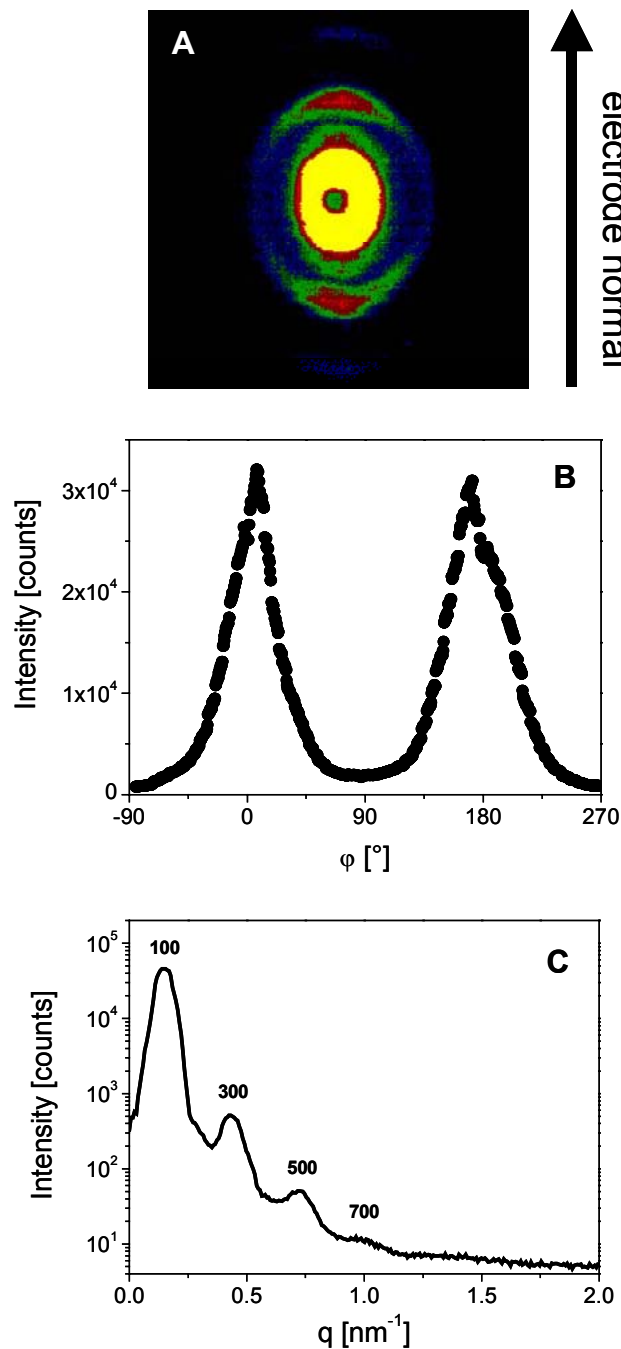

Figure 5-2: (A) 2D-SAXS pattern of a film cast under zero-field conditions. The lamellae are aligned parallel to the boundary surfaces (electrodes).
(B) azimuthal intensity distribution at $q* = 0.14$ nm^{-1} (corresponding to first order reflection).
(C) azimuthally integrated intensity as a function of scattering vector q.

Aside from the columns, we find areas with film thicknesses ranging between 0.2 and 0.7 mm. All these parts show a significant alignment of the lamellae parallel to the electric field. The most pronounced anisotropy, however, is found in the columnar protrusions on which we

89

will focus in the present study. Figure 5-4 shows a cross sectional SEM image of a typical column. The curvature of the boundaries is induced by the wetting of the electrode surfaces during evolution of the protrusion.

A representative SAXS pattern taken within one of the columns is shown in Figure 5-5a. It reveals an anisotropic azimuthal angular dependence of the scattering intensities (Figure 5-5b) shifted by 90° compared to the zero-field experiment. The Bragg reflections are identical to the ones observed in the zero-field experiment. The order parameter P_2 yields - 0.4. Thus, these results clearly indicate a predominant alignment of the lamellae parallel to the electric field vector. A representative TEM picture is shown in Figure 5-3b. There are regions of very uniform lamellae aligned parallel to the electric field vector throughout the whole picture. Interestingly, the orientation of these lamellae is not disturbed by the defect structures (e.g. disclinations). Furthermore, it appears that the trajectories of the disclination lines and other defects (coarse patterns similar to wood grain patterns) are aligned predominantly in the direction of the electric field as well. Especially the latter defects have been reported earlier for PS-*b*-PMMA block copolymers oriented in an electric field from the melt. These structures may arise from disclination lines cut shallowly parallel to their trajectories[25]. Investigations of the lamellar alignment at the film boundaries reveal the large influence of the electrode surface on the microdomain alignment as has already been observed for the zero-field experiment. Even with an applied electric field we find orientation of the lamellae parallel to the electrode surface for the first 10 to 40 lamellar layers as shown in Figure 5-6.

5.4.   Discussion

We start our discussion with a quantitative estimate of the energies involved in the process of domain ordering in our experiments. For this end we note that we have evidence that the PHEMA block is actually miscible with the PMMA block. This is indicated by differential scanning calorimetry (DSC), rheological and TEM experiments, where only a single methacrylic phase could be identified. TEM experiments involved the staining with phosphotungstic acid and long time exposure to ruthenium tetroxide vapor which is well known to lead not only to staining of the PS block but also should react with hydroxyl groups[21]. As both methods did not lead to definite results and DSC and rheological measurements only revealed two glass transition temperatures at 110 °C and 137 °C which are attributed to the PS and a methacrylic phase, respectively, we anticipate that PHEMA and PMMA may form a mixed phase.

cutting edge
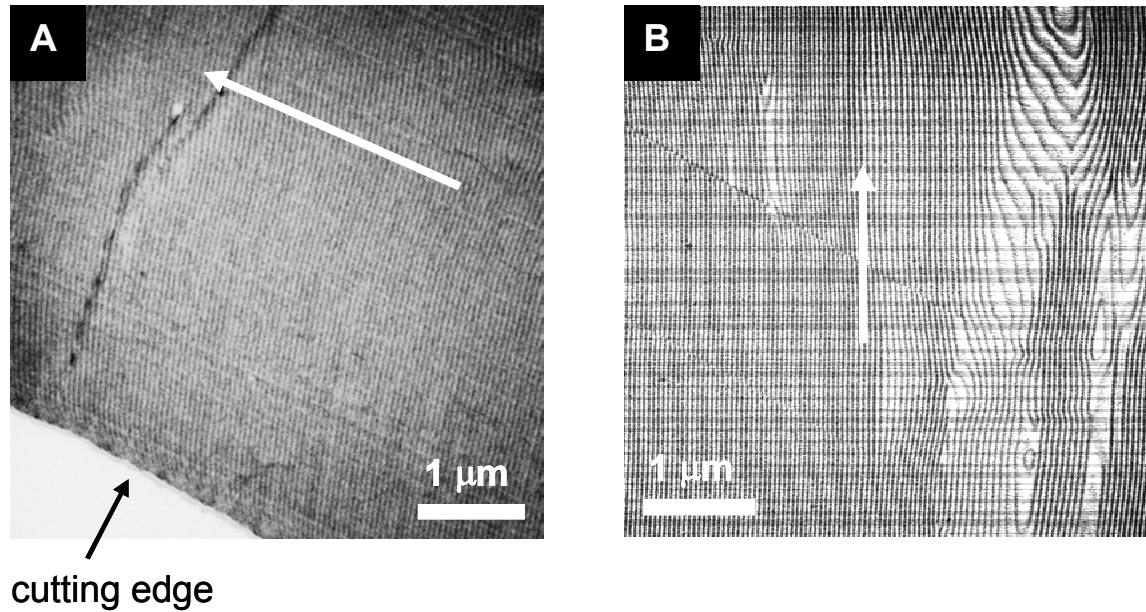
Figure 5-3:   TEM pictures of zero-field and alignment experiment.
(A) zero-field (The arrow indicates the direction perpendicular to the electrodes).
(B) E = 1.8 kV/mm (The arrow indicates the direction of the electric field vector). The image
was taken from one of the columns bridging between the electrodes.

This assumption leads us to treat the triblock copolymer as an AB diblock copolymer with the following composition: A: 47 wt.-% PS ($\varepsilon_A = 2.4$) and B: 53 wt.-% methacrylic blocks ($\varepsilon_B = 0.81 \varepsilon_{PMMA} + 0.19 \varepsilon_{PHEMA} = 4.6$; with $\varepsilon_{PMMA} = 3.6$ and $\varepsilon_{PHEMA} = 8.9$ [26]). As chloroform ($\varepsilon_{CHCl_3} \approx 4.8$) is a fairly non-selective solvent for the two main components, PS and PMMA, we expect a similar swelling behavior leading merely to a dilution effect with respect to the dielectric constants of each block. Therefore, with increasing solvent content in the films, the difference of the dielectric constants is reduced and the thermodynamic driving force for an alignment of the lamellae parallel to the field is expected to decrease[15]. As has been pointed out by Amundson *et al.*[11] with respect to melts of PS-*b*-PMMA block copolymers this force is already small, so that it is remarkable that its decrease still leaves a sufficient driving force to allow for preferential alignment of the microdomains.

To estimate the driving forces for domain alignment as a function of solvent concentration ϕ, we calculate the electric energy per unit area *W*, which is stored in the capacitor for the different situations sketched in Figure 5-7a. The model relies on two major assumptions: The dielectric constant of a mixture ε_{mix} of polymer ε_{pol} and solvent ε_{sol} is assumed to depend linearly on the solvent concentration ε

$$\varepsilon_{mix} = \phi\varepsilon_{sol} + (1-\phi)\varepsilon_{pol}$$

We further disregard any influence of the solvent on the partial molar volume of the polymer, i.e. the volumes of polymer V_{pol} and solvent V_{sol} simply add:

$$V_{mix} = V_{pol} + V_{sol}$$

Four basic geometries have been identified to describe the system, corresponding to a perpendicular ($W_{\perp,col}$, $W_{\perp,flat}$) and parallel ($W_{||,col}$, $W_{||,flat}$) alignment of the microdomains with respect to the electric field and to a formation of columns ($W_{\perp,col}$, $W_{||,col}$) and a flat film ($W_{\perp,flat}$, $W_{||,flat}$), respectively.

We calculate the energy W stored within the electric field of the capacitor according to

$$W = \frac{1}{2} \int \bar{E} \cdot \bar{D} \, dV$$

with $\bar{E}$ being the electric field and $\bar{D}$ the displacement field.
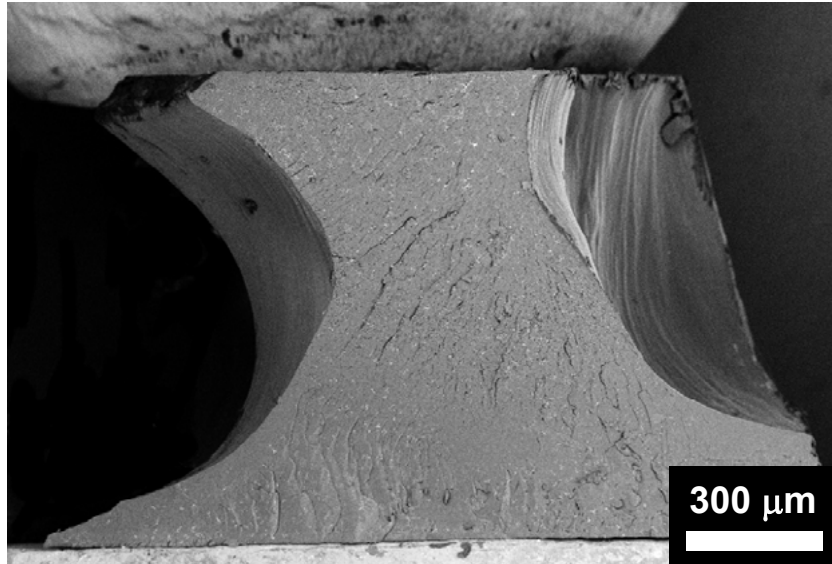

Figure 5-4:   *Cross sectional SEM image of a protrusion formed during exposure to a DC electric field (1.8 kV/mm).*

In contrast to the dielectric displacement $\bar{D}$, the electric field $\bar{E}$ along the z-direction of the capacitor is not uniform for the models, which incorporate a layered structure ($W_{\perp,flat}$ and $W_{\perp,col}$). This is due to the fact that the component of the electric field perpendicular to the interface between two materials is not continuous, but the one of the displacement field is: $\bar{D}_{\perp 1} = \bar{D}_{\perp 2}$ but $\bar{E}_{\perp 1} \neq \bar{E}_{\perp 2}$. Additionally $\bar{E}_i = \bar{D}_i / \varepsilon_i$ and the applied voltage $V = \int \bar{E} \, dz$, which means that as soon as air is present as a layer in the capacitor with the applied voltage V, the electric field in both polymer layers is reduced. This leads effectively to a reduced energy stored inside the capacitor and to a reduced alignment of the block copolymer in the thinner parts of the sample. We are well aware of the fact that our calculations neglect the

92

existence of interfacial boundary regions in concentrated polymer solutions. Therefore the results may represent an approximation to the upper limit of the real energetic situation.

Figure 5-7b shows the energy per unit area stored inside a capacitor filled with 15 vol.-% polymer A (ε_A = 2.4) and 15 vol.-% polymer B (ε_B = 4.6) as a function of solvent volume fraction (ε_{sol} = 4.8), corresponding to the four basic geometries, with a gap width of 1.1 mm and an applied voltage of 2 kV.
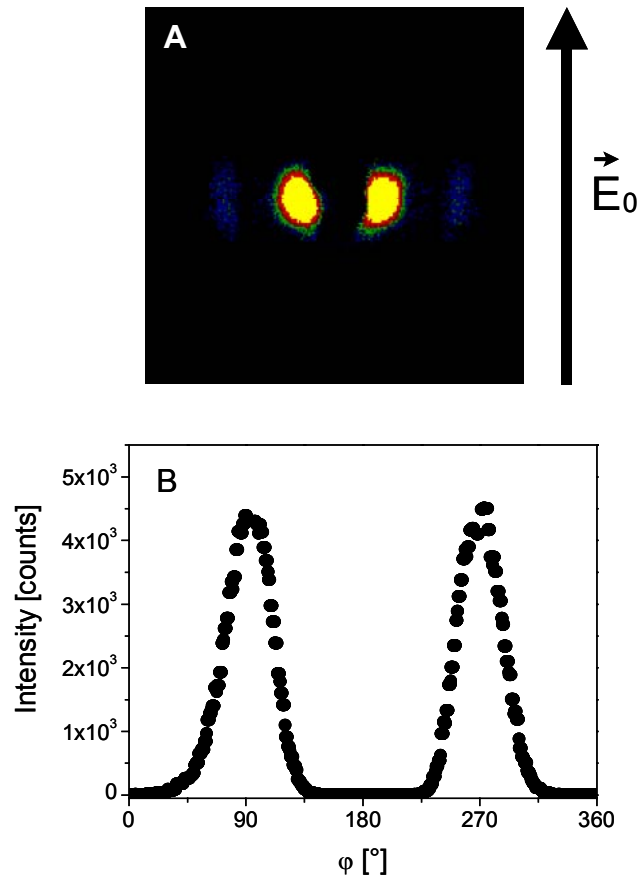

Figure 5-5:   (A) 2D-SAXS pattern of a film cast in the presence of a DC electric field (1.8 kV/mm).
                   The experiment has been performed within one of the columns bridging between the electrodes.
                   The lamellae are oriented preferentially along the field direction.
                   (B) azimuthal intensity distribution at first order reflection (P_2 = -0.4).

Curves $W_{\perp,col}$ and $W_{\perp,flat}$ as well as curves $W_{||,col}$ and $W_{||,flat}$ converge at a solvent concentration of 70 vol.-% (which is the starting concentration of our experiment), because at this point the capacitor is completely filled and the respective geometries are equivalent. For the major part of the plot, columns ($W_{\perp,col}$, $W_{||,col}$) store more energy than flat films ($W_{\perp,flat}$, $W_{||,flat}$) because the polymer/solvent mixture exhibits a higher dielectric constant as compared to air. Therefore column formation should be favored in agreement with the experimental finding. It has to be kept in mind though that column formation requires the formation of additional

surfaces, which leads to an energy penalty. Obviously, according to our results, the gain in energy during alignment of the lamellae parallel to the electric field vector is large enough to compensate for an additional surface energy cost. An approximation taking into account the dimensions of the observed protrusions, a mean surface energy of $\sim$ 30 mJ/m^2 (γ_{PS} = 40.7 mJ/m^2, γ_{PMMA} = 41.1 mJ/m^2, γ_{CHCl3} = 26.7 mJ/m^2)[16] and the gain in electric energy per unit area in the capacitor ($\sim$ 20 mJ/m^2 at 50 - 60 vol.-% solvent) leads to the following result: At a certain ratio of the radius R of a column to its height H ($R/H \sim 0.8$) the surface and electric energy contributions are equal. Given the fact that the columns observed in our experiment start to evolve at relatively high solvent concentrations, we have to consider a significant shrinkage in the lateral dimensions during film formation. However, the gain in electric energy for the aligned system is of the same order of magnitude as the surface energy cost. The observation that we still find material in between the protrusions can be explained by the fact that the overall process of film formation, i.e. drying of the polymer solution, occurs at a faster rate than the formation of the columns.
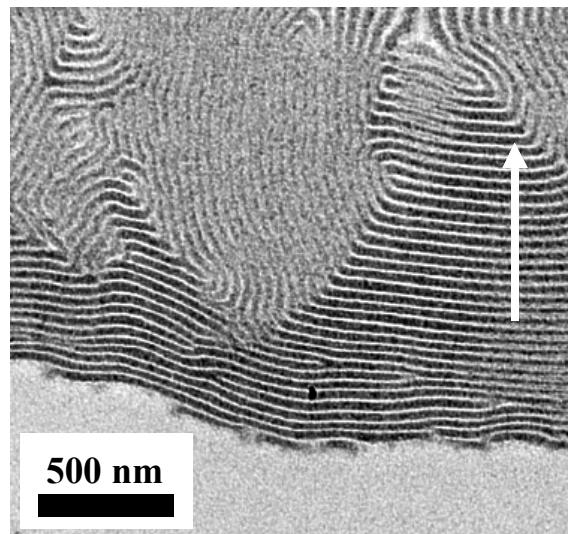

Figure 5-6:   *TEM picture of interfacial region between electric field aligned polymer film and electrode surface (Film embedded in epoxy resin. The arrow indicates the direction of the electric field vector).*

The electric energies for structures aligned parallel to the electric field are always larger than the ones for structures oriented perpendicular to the field, explaining the preferential alignment observed in the experiment. It is interesting to look at the energy difference between the microdomain orientations in the columns ($W_{\perp,col}$, $W_{||,col}$) and the one in the flat film ($W_{\perp,flat}$, $W_{||,flat}$), which is shown in the inset in Figure 5-7b. With decreasing solvent concentration this value is much higher for the columns. Therefore the microdomain ordering

inside the columns is expected to be better than inside the flat film regions in between the columns. In addition, for the case of the thinner films in between the columns we expect a larger influence of the electrode/polymer and the polymer/air interfaces, which would favor lamellar alignment parallel to the electrodes. These two effects are in competition and only if the electric field is large enough the microdomains will align parallel to the field[15]. Indeed, SAXS experiments performed in the flat areas in between the columns (Figure 5-8) show a lamellar alignment along the field direction, however, with a significantly smaller degree of order ($P_2 = -0.25$).
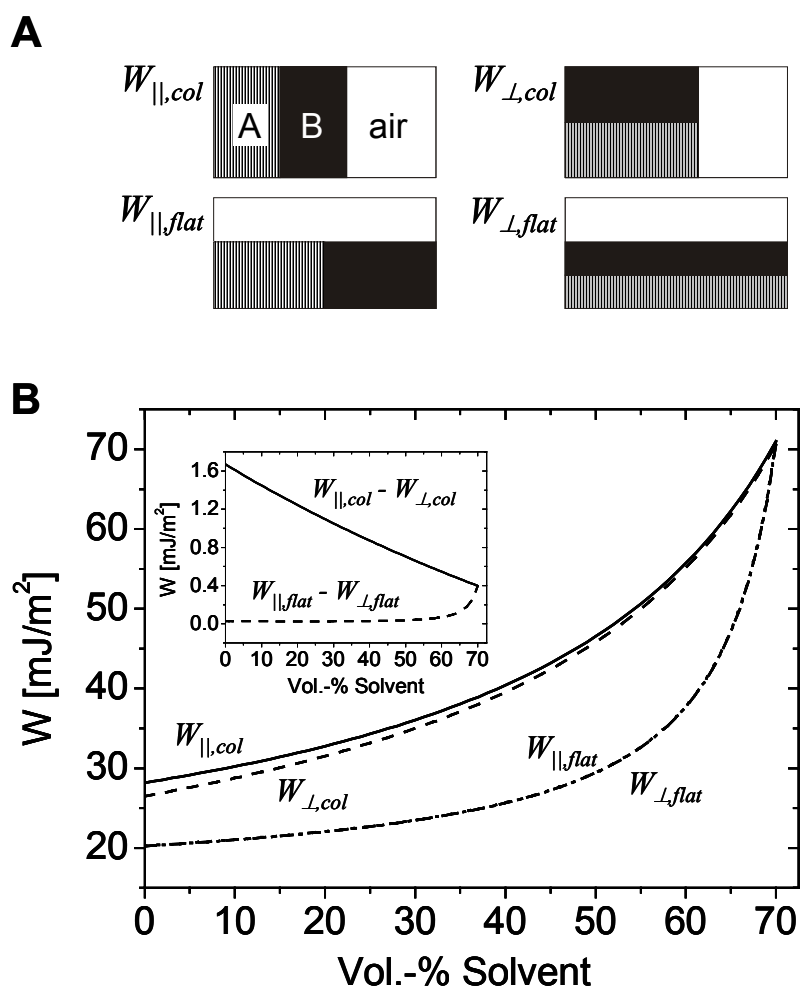

Figure 5-7:   (A) Different geometries used for the calculation of the electric energy W stored in a capacitor partially filled with polymers A and B. (B) Energy per area stored in the capacitor for the four geometries as a function of solvent concentration. The inset shows the energy difference between the two orientations for columns ($W_{\parallel,col} - W_{\perp,col}$) and for a flat film ($W_{\parallel,flat} - W_{\perp,flat}$), respectively.

There have been various assumptions concerning the mechanism of microdomain alignment, which are mostly based on defect movement, resulting in either mutual annihilation of equivalent defects (which are traverse to the electric field) or pinning of defect structures[11,25].

This would lead to clustering of defects and orientation along the electric field direction, which is consistent with our results as it explains why we do not reach "perfect" alignment of the lamellar microdomains. Nevertheless, the application of an external electric field to a block copolymer solution is capable of switching the in-plane alignment of the lamellae induced by the boundary surfaces to a significant orientation along the electric field direction. Investigations on the kinetics of this process are presently under way and will be presented in a separate publication[27].
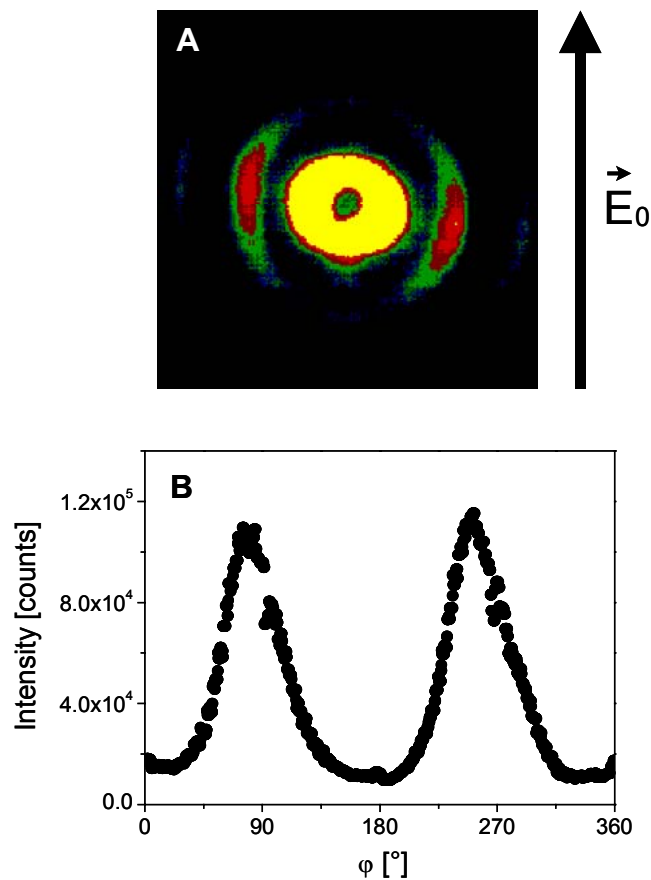

Figure 5-8:   (A) SAXS pattern of a sample taken from the flat areas in between the columns. The lamellae are oriented along the field direction (1.8 kV/mm), however the degree of order as calculated by the azimuthal angular dependence of the scattering intensity (B) is smaller than within the columns ($P_2 = -0.25$ compared to -0.4).

As the alignment of the microstructure takes place during solvent evaporation and along with a change of the macroscopic shape of the specimen (protrusions), we have to consider the potential effect of shear forces. Therefore, the following control experiment was performed: The distance between the electrodes was doubled and the same voltage as before was applied to the system (which results in half the electric field strength as before). While protrusions were formed as described above, no alignment of the microdomains along the

electric field was found under these conditions. We therefore exclude shear as the dominant driving force for domain alignment in our experiments.

Finally we note that although we can model our system as a diblock copolymer in our calculations, the incorporation of the PHEMA middle block seems to be essential for the ordering process to function. Similar experiments on PS-*b*-PMMA diblock copolymer solutions (not shown here) did *not* exhibit field induced domain alignment. Two reasons may be responsible for this observation: At first, the high dielectric constant of PHEMA ($\varepsilon_{PMMA} = 8.9$) significantly increases the driving force for ordering even at the rather small volume fraction realized in the present experiments. Moreover, microphase separation in PS-*b*-PMMA diblock copolymer solutions occurs only at polymer concentrations above 60 wt.-%, while the PHEMA containing triblock copolymers already microphase separate at polymer concentrations around 40 wt.-%. In the latter case, the viscosity of the phase separated solution is considerably smaller which helps the ordering process induced by the small electric force. Recent kinectic experiments indicate that there is a rather small concentration window in which microdomain ordering by electric fields can effectively be realized. This issue will be subject of a forthcoming publication[27]. The use of a PS-*b*-PHEMA diblock copolymer as a model system, however, is not suitable, as PHEMA exhibits a very strong surface interaction with the electrode material and its amphiphilic character leads to a selective solubility in all low dielectric constant solvents, which would further complicate the situation.

5.5.   Conclusions

We have shown that block copolymer solutions can be aligned in DC electric fields during solvent evaporation leading to highly anisotropic microdomain structures in the resulting films. In comparison to melt alignment, the method presented here is applicable to polymers with higher melt viscosities such as high molecular weight copolymers and copolymers of more complex architecture, which cannot be aligned in the melt by virtue of electric fields.

Furthermore, we were able to describe the observed behavior by a quantitative estimate of the electric energies involved in the alignment process. Our calculations predict the formation of column-like protrusions during solvent evaporation and explain the higher degree of orientation found in the columns as compared to the thinner parts of the films.

Future work will have to concentrate on a quantitative control of the solvent vapor pressure during orientation of the domains. There should exist an optimum degree of swelling around

the order-disorder-concentration, which combines a maximum chain mobility with a significant energetic difference between the different microdomain orientations. Keeping the system at the respective vapor pressure (i.e. concentration of the polymer solution) for a sufficient time should result in a significant improvement of the long-range order of the microdomains.

References

[1] The results of this chapter have already been published: A. Böker, A. Knoll, H. Elbs, V. Abetz, A.H.E. Müller, G. Krausch *Macromolecules*, **2002**, *35*, 1319-1325.

The contribution of A. Knoll consists of invaluable help with the calculations presented in Figure 5-7. In addition, I have benefitted from many helpful discussions with H. Elbs during start-up of this work.

[2] Bates, F.S.; Fredrickson, G.H.; *Ann. Rev. Phys. Chem.* **1990**, *41*, 525.

[3] Bates, F.S.; Frederickson, G.H.; *Physics Today* **1999**, *52*, 32.

[4] Wiesner, U.; *Macromol. Chem. Phys.* **1997**, *198*, 3319.

[5] Chen, Z.-R.; Kornfield, J.A.; Smith, S.D.; Grothaus, J.T.; Satkowski, M.M.; *Science* **1997**, *277*, 1248.

[6] Chen, Z.-R.; Kornfield, J.A.; *Polymer* **1998**, *39*, 4679.

[7] Keller, A.; Pedemonte, E.; Willmouth, F.M.; *Nature* **1970**, *225*, 538.

[8] Albalak, R.J.; Thomas, E.L.; *J. Polym. Sci., Polym. Phys. Ed.* **1993**, *31*, 37.

[9] Thurn-Albrecht, T.; Schotter, J.; Kastle, G.A.; Emley, N.; Shibauchi, T.; Krusin-Elbaum, L.; Guarini, K.; Black, C.T.; Tuominen, M.T.; Russell, T.P.; *Science* **2000**, *290*, 2126.

[10] Amundson, K.; Helfand, E.; Davis, D.D.; Quan, X.; Patel, S.S.; Smith, S.D.; *Macromolecules* **1991**, *24*, 6546.

[11] Amundson, K.; Helfand, E.; Quan, X.; Smith, S.D.; *Macromolecules* **1993**, *26*, 2698.

[12] Morkved, T.L.; Lu, M.; Urbas, A.M.; Ehrichs, E.E.; Jaeger, H.M.; Mansky, P.; Russell, T.P.; *Science* **1996**, *273*, 931.

[13] Morkved, T.L.; Lopez, V.A.; Hahm, J.; Sibener, S.J.; Jaeger, H.M.; *Polymer* **1998**, 39, 3871.

[14] Mansky, P.; DeRouchey, J.; Russell, T.P.; Mays, J.; Pitsikalis, M.; Morkved, T.L.; Jaeger, H.M.; *Macromolecules* **1998**, *31*, 4399.

[15] Thurn-Albrecht, T.; DeRouchey, J.; Russell, T.P.; Jaeger, H.M.; *Macromolecules* **2000**, *33*, 3250.

[16] Brandrup, J.; Immergut, E.H. *Polymer Handbook*; 3rd Ed.; Wiley Publisher: New York, **1991**.

[17] Thurn-Albrecht, T.; Steiner, R.; DeRouchey, J.; Stafford, C.M.; Huang, E.; Bal, M.; Tuominen, M.; Hawker, C.J.; Russell, T.P.; *Adv. Mat.* **2000**, *12*, 787.

[18] Le Meur, J.; Terrisse, J.; Schwab, C.; Goldzene, P.; *J. Phys., Colloq.* **1971**, *32*, C5a-301.

[19] Serpico, J.M.; Wnek, G.E.; Krause, S.; Smith, T.W.; Luca, D.J.; van Laeken, A.; *Macromolecules* **1992**, *25*, 6373.

[20] Böker, A.; Müller, A.H.E.; Krausch, G.; *Macromolecules* **2001**, *34*, 7477.

[21] C.C. Sawyer; D.T. Grubb; *Polymer Microscopy*, 2nd Ed.; Chapman & Hall: London, **1996**.

[22] Annighöfer, F.; Gronski, W.; *Makromol. Chem., Rapid Commun.* **1983**, *4*, 123.

[23] Schäffer, E.; Thurn-Albrecht, T.; Russell, T.P.; Steiner, U.; *Nature* **2000**, *403*, 874.

[24] Lin, Z.; Kerle, T.; Baker, S.M.; Hoagland, D.A.; Schäffer, E.; Steiner, U.; Russell, T.P.; *J. Chem. Phys.* **2001**, *14*, 2377.

[25] Amundson, K.; Helfand, E.; Quan, X.; Hudson, S.D.; Smith, S.D.; *Macromolecules* **1994**, *27*, 6559.

[26] Yamaguchi, R.; Sato, S.; *Jpn. J. Appl. Phys.* **1994**, *33*, 4007.

[27] Böker, A.; Elbs, H.; Hänsel, H.; Knoll, A; Zettl, H.; Urban, V.; Abetz, V.; Müller, A.H.E.; Krausch, G. in preparation.

Chapter 6

Microscopic Mechanisms of Electric Field Induced Alignment of Block Copolymer Microdomains[1]

Abstract

We investigate the microdomain orientation kinetics of concentrated block copolymer solutions exposed to a DC electric field by time-resolved synchrotron small-angle X-ray scattering (SAXS). As a model system, we use a lamellar polystyrene-*b*-polyisoprene block copolymer dissolved in toluene. Our results indicate two different microscopic mechanisms, i.e. domain boundary migration and grain rotation. The former dominates close to the order-disorder transition, while the latter prevails under more strongly segregated conditions. The orientation kinetics follows a single exponential behavior with characteristic time constants varying from a few seconds to some minutes depending on polymer concentration, temperature, electric field strength, and system size. From the experimental results we deduce optimum conditions for the preparation of highly anisotropic bulk polymer samples via solvent casting in the presence of an electric field.

6.1. Introduction

Block copolymers composed of incompatible components self-assemble into microphase separated domains usually leading to well-ordered structures on the mesoscale[2,3]. However, in the absence of external fields typically an isotropic grain structure is obtained characterized by a random distribution of microdomain orientations. It is well known from thin-film studies that external interfaces can align the block copolymer morphology, given that the interface selectively attracts one of the constituent blocks[4,5]. Usually, however, the influence of the substrate on the alignment decays quite rapidly, i.e. after a few long periods a more or less random orientation is observed as it is typical for the bulk state. In order to achieve large scale alignment throughout a macroscopically large bulk sample, different techniques have been devised in the past. Most prominently, external mechanical fields have been successfully applied to orient block copolymer melts and solutions, e.g. large amplitude oscillatory shear (LAOS)[6,7,8], extrusion[9] or roll-casting[10].

In addition to mechanical fields, the potential of *electric fields* for microdomain alignment has attracted increasing interest in the recent past as it may also have a considerable technological potential [11]. It has been shown that both lamellar and cylindrical microdomain structures in polystyrene-*b*-poly(methyl methacrylate) (PS-*b*-PMMA) thin films could be oriented by virtue of a DC electric field [12 - 18]. These *melt*-based electric field procedures suffer from severe limitations due to the high melt viscosities typical of high molecular weight copolymers or copolymers of more complex architectures. In order to overcome these limitations, one can try to align concentrated block copolymer solutions, where a non-selective solvent is used to induce sufficient mobility. Following earlier investigations by Le Meur *et al.*[19] we recently investigated the microdomain alignment of an ABC triblock copolymer during solvent casting in the presence of an external electric DC field[20]. After drying, bulk samples of the material exhibited lamellar microdomains highly oriented parallel to the electric field vector, as shown by small-angle X-ray scattering (SAXS) and transmission electron microscopy (TEM).

In the present paper, we describe real-time synchrotron radiation small-angle X-ray scattering (Synchrotron-SAXS) investigations aiming to follow the kinetics of electric field induced microdomain reorientation in concentrated block copolymer solutions and thus to elucidate the underlying microscopic mechanisms. As a model system, we investigate the orientation behavior of a lamellae-forming polystyrene-*b*-polyisoprene diblock copolymer dissolved in toluene. We discuss the influence of the polymer concentration, the electric field strength, the temperature, and the system size on the reorientation behavior. We identify two

different microscopic processes, *grain boundary migration* and *grain rotation,* which are found to dominate the reorientation process in different regimes of block copolymer concentration and temperature.

6.2. Experimental Section

6.2.1. Synthesis

A polystyrene-*b*-polyisoprene block copolymer (SI-80) with a total number-average molecular weight $M_n = 80$ kg/mol was synthesized by sequential living anionic polymerization as described in detail elsewhere[21]. The polymer used in this study consists of 52 wt.-% polystyrene and 48 wt.-% polyisoprene (92% 1,4-cis and 4% 1,2 and 3,4 microstructure). Gel permeation chromatography (GPC) of the final block copolymer yields a polydispersity $M_w/M_n = 1.02$. The block ratio and overall molecular weight were determined by ^{1}H-NMR using the integrated aromatic signals of the polystyrene block in combination with the GPC results of the corresponding polystyrene precursor.
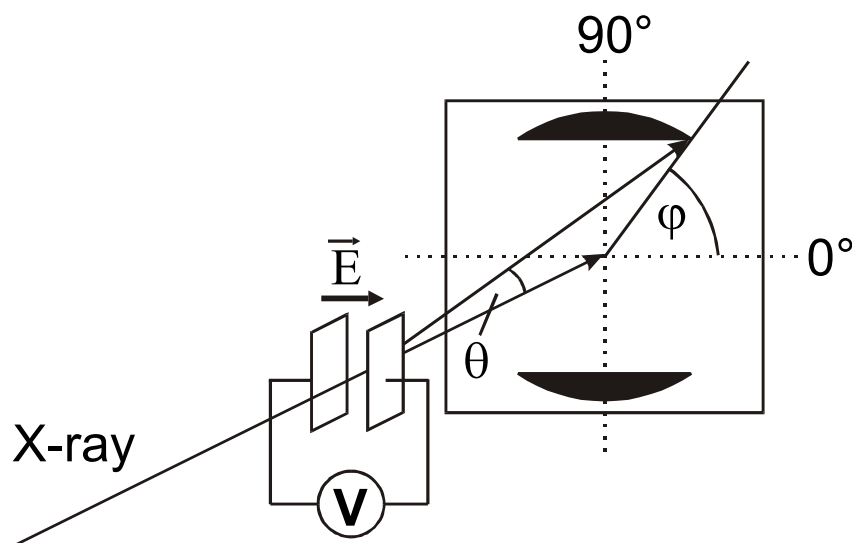

Figure 6-1:   Experimental setup for in-situ SAXS.

6.2.2. Sample Preparation

Toluene solutions of the block copolymer with concentrations ranging from 30 - 80 wt.-% were prepared. The alignment experiments were performed in a home built capacitor with gold electrodes (sample depth = 5 mm, electrode distance d = 0.5, 1, 2, 4 mm) at temperatures ranging from room temperature up to 80°C. A DC voltage between 0.5 kV and 6 kV was applied across the capacitor resulting in a homogeneous electric field pointing perpendicular

to the X-ray beam direction (Figure 6-1). Both the voltage at the electrodes and the current through the sample were monitored during the course of the experiment. No leakage currents were detected after the electric field was applied. The sample temperature was adjusted to within ±1 °C using Peltier elements.

6.2.3.   Viscosity Measurements

The solution viscosity, η, at 1 rad/sec was measured for different polymer concentrations using a Rheometrics Stress Rheometer SR-5000 with a plate-plate geometry (diameter: 25 mm). Time sweeps were performed and the final values are averages over at least three independent measurements.

6.2.4.   Synchrotron Small-Angle X-Ray Scattering (Synchrotron-SAXS)

Synchrotron-SAXS measurements were performed at the ID02A beamline at the European Synchrotron Radiation Facility (ESRF, Grenoble, France). The typical photon flux routinely obtained at the ID02A sample position is 10^{13} photons/sec, corresponding to twice the full width at half maximum beam size $(0.2 \text{ mm})^2$ and energy bandwidth $\Delta E/E = 2\text{x}10^{-4}$. The operating energy range was 12.5 keV, corresponding to a wavelength of 0.1 nm, at which the highest photon flux is obtained. The direction of the X-ray beam (cross section: 200 μm) was perpendicular to the direction of the applied electric field.

The detector system is housed in a 10 m evacuated flight tube. For most experiments an image intensified CCD detector was used, which can handle the full X-ray flux. The CCD is capable of acquiring up to 10 frames of 1024x1024 pixels per second and a sequence of 125 frames can be acquired with this time resolution. Prior to data analysis, background scattering was subtracted from the data and corrections were made for spatial distortions and for the detector efficiency.

6.2.5.   Transmission Electron Microscopy (TEM)

Some of the samples were dried in the presence of the electric field. Subsequently, thin sections were cut parallel to the electric field vector (far from any surface) using a Reichert-Jung Ultracut E microtome equipped with a diamond knife. In order to enhance the electron density contrast between polystyrene and polyisoprene, the sections were exposed to RuO_4

vapor for 45 minutes, which leads to a preferential staining of the polystyrene block[22]. Bright field TEM was performed using a Zeiss electron microscope (CEM 902) operated at 80 kV.

6.2.6.   Calculation of order parameters

As will become clear from the experimental observations described below, domain alignment is induced by two competing external fields of different symmetry, i.e. the interfacial field between polymer solution and the electrode surfaces and the electric field, respectively. To quantify the microdomain alignment, we calculate the order parameter P_2 by integrating the scattering intensity $I_q(\varphi)$ over the azimuthal angle φ from $\varphi = 0°$ to $360°$:

$$P_2 = \frac{3\langle\cos^2\varphi\rangle - 1}{2}$$

Equation 6-1

with

$$\langle\cos^2\varphi\rangle = \frac{\int_0^{2\pi} d\varphi\left(I_q(\varphi)\cdot\cos^2(\varphi)\cdot|\sin(\varphi)|\right)}{\int_0^{2\pi} d\varphi\left(I_q(\varphi)\cdot|\sin(\varphi)|\right)}$$

Equation 6-2

Depending on the type of alignment, two different ranges of the order parameter exist. For lamellar alignment parallel to the electrodes (maximum scattering intensity at $\varphi = 0°$), P_2 ranges from 0 to 1 with $P_2 = 1$ corresponding to perfect lamellar alignment parallel to the electrodes. For an alignment of the lamellae along the field direction (maximum scattering intensity at $\varphi = 90°$), P_2 ranges from 0 to -0.5 with $P_2 = -0.5$ corresponding to the case where all lamellae are aligned parallel to the field, however, with the lamella normals being isotropically oriented in the plane of the electrodes.

In order to quantify the orientation kinetics, the orientational order parameter P_2 was calculated for each single scattering pattern acquired during the course of the experiment. The behavior of P_2 as a function of time t could be fitted by a single exponential as described by:

$$P_2(t) = P_{2,\infty} + (P_{2,0} - P_{2,\infty})\, e^{-t/\tau}$$

Equation 6-3

with $P_{2,0}$ and $P_{2,\infty}$ being the limiting values of the order parameter before application of the electric field and at late times, respectively, and τ being the time constant.

The reminder of the paper is organized as follows. We shall first describe the structure formation in solution and its properties before we continue discussing the influence of an

external electric field on the domain orientation of solutions of different concentrations, at different electric field strengths, and at different temperatures. We will end the discussion by showing how our results can be used to generate well aligned block copolymer bulk samples.
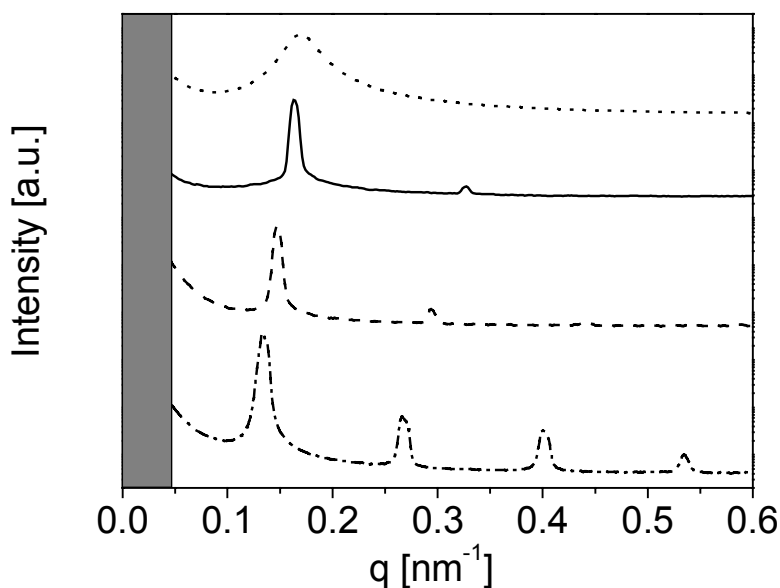

Figure 6-2:   *Scattering intensity profiles at various concentrations.*
                   34 wt.-% (·····), 35 wt.-% (—), 50 wt.-% (– –), 70 wt.-% (–··).

6.3.   Results

6.3.1.   Concentration Dependence of Structure Formation

Before we discuss the effects of external electric fields on the PS-*b*-PI block copolymer domains, we first concentrate on the microdomain structure formed in solution in the absence of an electric field. Toluene was chosen as it is a fairly non-selective solvent for PS and PI[23]. The Flory-Huggins interaction parameters between the two polymers and toluene are $\chi_{PS/Tol} = 0.44$ and $\chi_{PI/Tol} = 0.40$, respectively[24]. As anticipated from previous investigations on concentrated solutions of symmetric PS-*b*-PI block copolymers in toluene[25], we observe the evolution of a lamellar microstructure with increasing concentration as shown in Figure 6-2. Above a polymer concentration of $w_p = 34$ wt.-%, the system exhibits higher order Bragg peaks appearing at integer multiples of the first order maximum. The lamellar spacing $d_{100} = 2\pi/q_{100}^*$ increases with increasing polymer concentration, despite increasing *deswelling*, indicating that the segregation power continuously increases as the solvent content decreases (Figure 6-3). The dependence of the lamellar spacing d on the polymer volume fraction ϕ_p scales as $d \sim \phi_p^{0.30 \pm 0.01}$ for intermediate concentrations (see the double logarithmic plot in Figure 6-4). We also note, that the lamellar spacing of the bulk sample

106

($w_p = 100$ wt.-%) is much lower than expected by extrapolation. The above described observations are in agreement with previous investigations by Shibayama *et al.*[25].
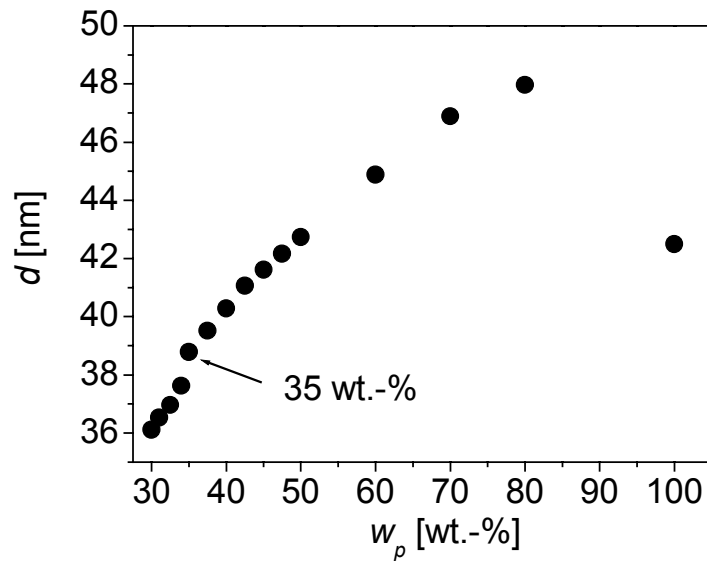

Figure 6-3:   *Concentration dependence of the lamellar spacing of PS-b-PI solutions in toluene ($d_{bulk} = 42.5$ nm).*

Above $w_p \approx 34$ wt.-% we observe a significant increase in scattering intensity. Moreover, we observe a distinct drop in d as the polymer concentration falls below 35 wt.-% (see arrow in Figure 6-3). In addition, optical birefringence, measured using crossed polarizers, disappears below $w_p \approx 35$ wt.-%, and no anisotropic scattering patterns were observed below $w_p \approx 35$ wt.-%, neither in the presence nor in the absence of the electric field (see below). We therefore locate the order-disorder transition at room temperature between 34 and 35 wt.-%.
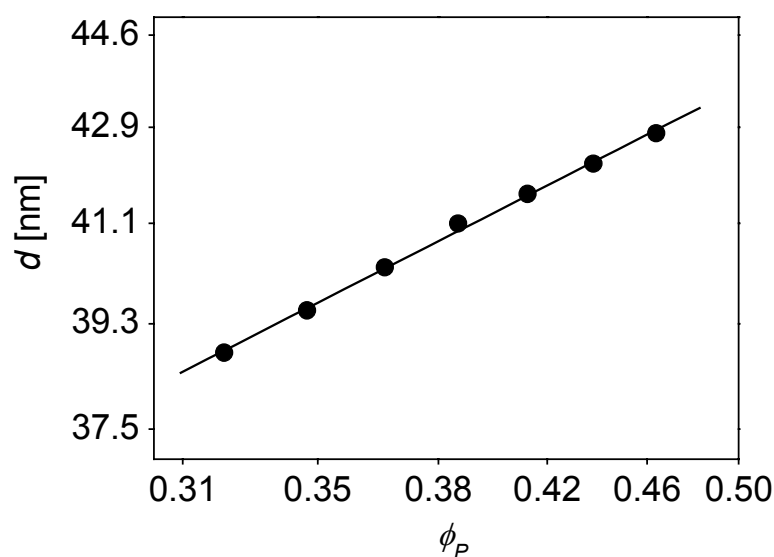

Figure 6-4:   *Double logarithmic plot of dependence of lamellar spacing on the volume fraction of polymer ϕ_P ($d \sim \phi_p^{0.30 \pm 0.01}$).*

107

6.3.2.   Reorientation Behavior of PS-*b*-PI in Toluene

Before we apply the electric field, all samples exhibit a distinctly anisotropic scattering pattern with maxima located at $\varphi = 0°$ and 180° (Figure 6-5A). This indicates an alignment of the lamellae parallel to the electrodes. Such an alignment can be caused both by preferential interaction of the PS with the Au surfaces[4] and by possible shear forces acting on the highly viscous solutions during filling of the capacitor with a syringe. In order to destroy any possible memory effect, we heated the solutions above the order disorder temperature. However, after cooling, still some alignment of the domains parallel to the electrodes prevailed, indicating the importance of the surface effects.
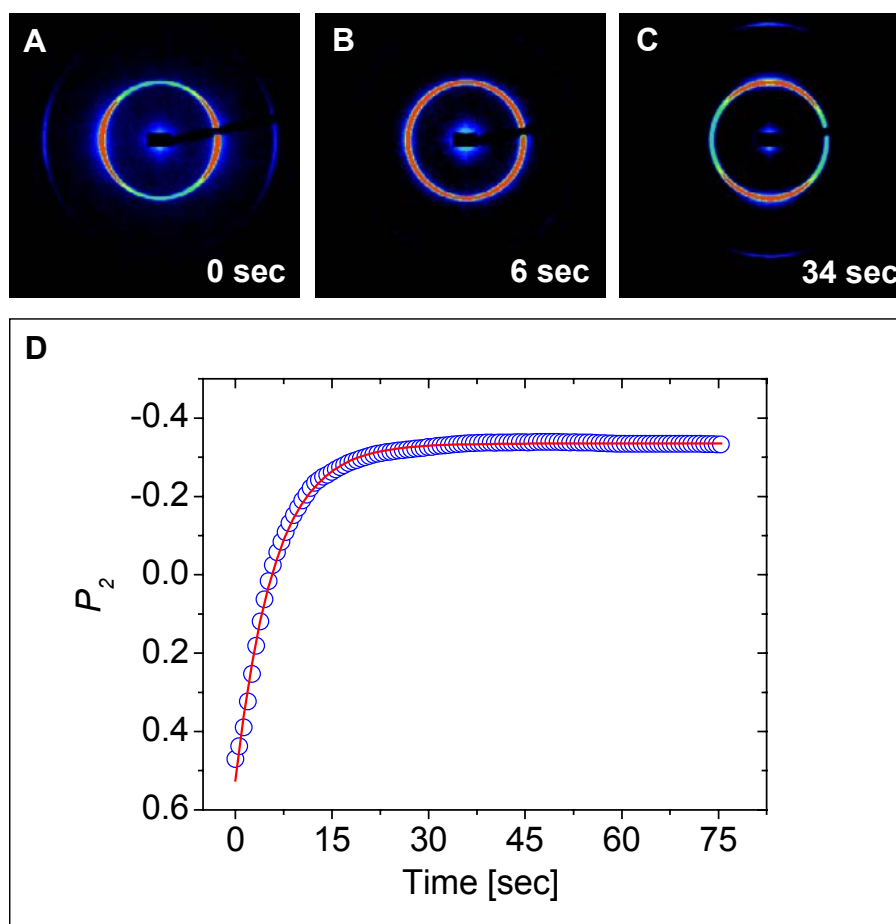

Figure 6-5:   *(A-C) Two-dimensional SAXS patterns of a 35 wt.-% solution of the SI-80 diblock copolymer in toluene taken at room temperature prior (A) and after application of an electric field (E = 1 kV/mm) (B, C). (D) Time dependence of the orientational order parameter P_2. The solid line is a least-squares fit to the data according to Equation 6-3 with $P_{2,0} = 0.52$, $P_{2,\infty} = -0.32$, and $\tau = 5$ sec.*

As soon as the electric field is applied (Figure 6-5B,C), the scattering pattern changes significantly. The peaks at $\varphi = 0°$ and 180° decrease and new scattering maxima at $\varphi = 90°$ and 270° grow with time. To quantify the kinetics of the orientation process, the orientational order parameter $P_2(t)$ was calculated from the 2D SAXS spectra as outlined above. Using a

single exponential fit, we can determine the time constant of the reorientation process (Figure 6-5D).

6.3.3.   Kinetics and Mechanism of Microphase Orientation

6.3.3.1.   Concentration dependence

We studied the reorientation kinetics as a function of polymer concentration, starting from $w_p = 30$ wt.-% and increasing w_p stepwise by 1 wt.-% up to 35 wt.-% and then by steps of 2.5 wt.-% to higher polymer concentrations. The electric field strength E was kept constant at $E = 1$ kV/mm at a capacitor spacing of 2 mm. The isotropic scattering pattern observed at polymer concentrations at and below $w_p = 34$ wt.-% did not change by the electric field. Above $w_p = 34$ wt.-%, the scattering patterns changed similar to the behavior shown in Figure 6-5 and time constants $\tau(w_p)$ were determined from the evolution of P_2 with time as shown in Figure 6-6. Above $w_p = 50$ wt.-%, however, the reorientation process became rather slow (time constant in the order of some 5 minutes) due to the high solution viscosities. We therefore limited our study to polymer concentrations between 34.5 and 50 wt.-%.
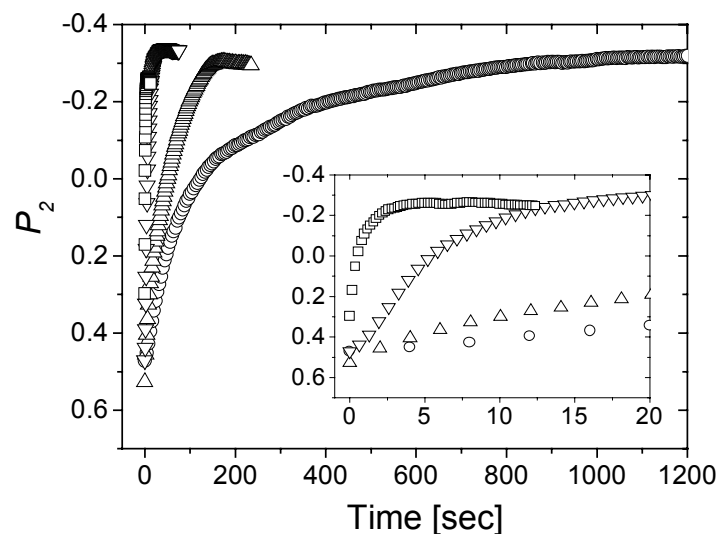

Figure 6-6:   Evolution of orientational order parameter P_2 with time for different concentrations at 2 kV/2 mm ($\square$ = 34.5 wt.-%, ∇ = 37.5 wt.-%, $\triangle$ = 42.5 wt.-%, $\bigcirc$ = 50 wt.-%).

The result of this procedure is shown in Figure 6-7. As anticipated from the solution viscosities, the time constant τ strongly increases with increasing polymer concentration. The results of the exponential fits are summarized in Table 6-1. The single exponential fit works quite well for all concentrations studied, as can be seen from the low χ^2 values. The time constants, τ, vary from the very fast process at 34.5 wt.-% ($\tau = 0.8$ sec) to more than 3 minutes ($\tau = 192$ sec) for the 50 wt.-% solution. In addition, within some 10% scatter P_2

109

reaches about the same limiting values $P_{2,\infty} = -0.3 \pm 0.03$ independent of polymer concentration. Therefore, we can conclude that the polymer concentration only influences the rate of orientation but not the final degree of orientation.
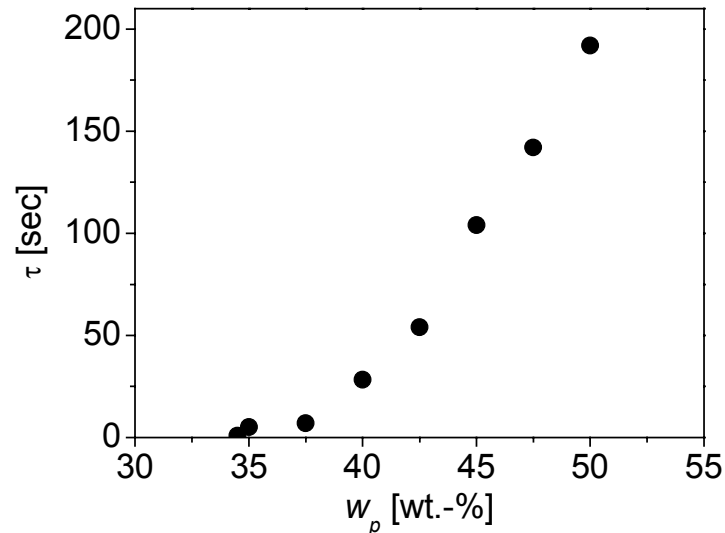

Figure 6-7:   *Concentration dependence of time constant τ.*

Interestingly, the microscopic mechanism of microdomain reorientation seems to change as the polymer concentration is increased.
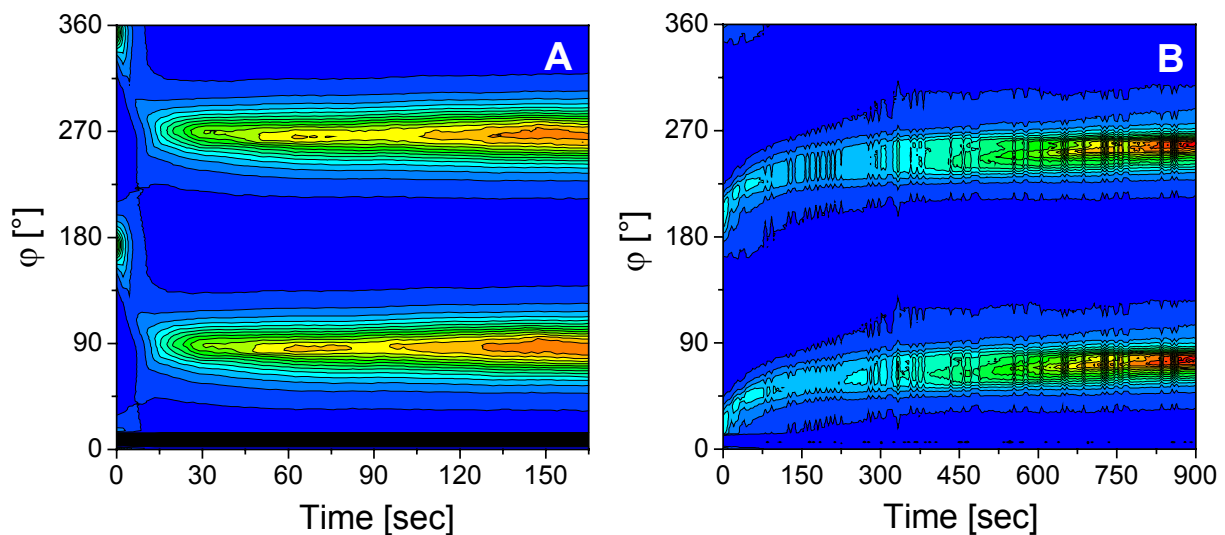

Figure 6-8:   *Azimuthal angular dependence of the scattering intensity for different concentrations at 2 kV/2 mm. (A) 35 wt.-%, (B) 50 wt.-%.*

In Figure 6-8, we compare the time dependence of the scattering patterns for the limiting polymer concentrations, $w_p = 35$ wt.-% and $w_p = 50$ wt.-%. For the low concentration (Figure 6-8A) the initial peaks at $\varphi = 0°$ and 180° almost vanish as the electric field is applied and new peaks are formed at $\varphi = 90°$ and 270°, the intensity of which grows with time. For high

110

polymer concentrations (Figure 6-8B) a distinctly different behavior is observed. The initial peaks are preserved and continuously shift from their original positions to their final positions at $\varphi = 90°$ and 270°, respectively. The intensity of the peaks does drop temporarily during the shift, however, a well-defined anisotropic scattering pattern is observed throughout the entire process. At intermediate concentrations (not shown), both behaviors are found to coexist.

Concentration [wt.-%]	τ [sec]	τ_{rot} [sec]	$P_{2,\infty}$	χ^2 [10^{-4}]	η [Pa sec]
34.5	0.8		-0.26	0.6	6.2
35	5.0	3.3	-0.32	1.4	31.5
37.5	7.0	5.1	-0.34	0.8	41.5
40	28.3	14.7	-0.33	1.3	51.7
42.5	54	20	-0.33	2.4	68.6
45	104	40	-0.34	3.2	80.5
47.5	142	82	-0.26	1.2	110
50	192	170	-0.31	5.6	118.5

Table 6-1:   *Time constants τ of the reorientation behavior at different polymer concentrations obtained from least-squares fits using Equation 6-3 (E = 2 kV/2 mm). In addition, the rotational time constant, τ_{rot}, was determined following the procedure outlined in the text.*

6.3.3.2.   Electric Field Dependence

In order to investigate the influence of the electric field strength on the orientation kinetics we varied the electric field between 0.25 kV/mm and 3 kV/mm. Again a 35 wt.-% solution was studied at room temperature. A selection of P_2 curves is shown in Figure 6-9.
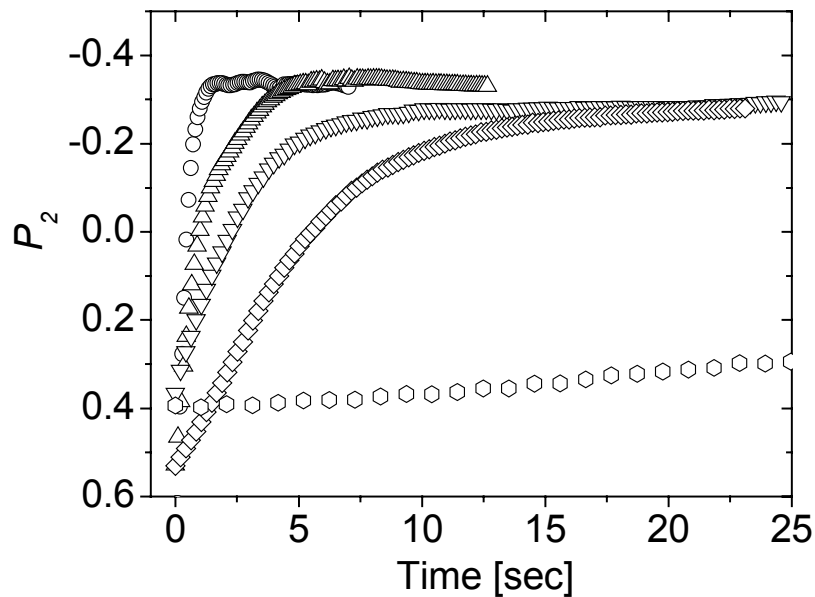

Figure 6-9:   *Evolution of orientational order parameter P_2 with time for 35 wt.-% solutions at different field strengths ($\bigcirc$ = 375 V/mm, $\diamondsuit$ = 1 kV/mm, $\triangledown$ = 1.25 kV/mm, $\triangle$ = 1.5 kV/mm, $\bigcirc$ = 3 kV/mm, electrode spacing: 2 mm).*

Voltage [kV/mm]	τ [sec]	$P_{2,\infty}$	χ^2 [10^{-4}]
0.25	(a)	(a)	(a)
0.375	100.1	-0.26	4.3
0.5	15.5	-0.32	2.3
0.75	8.3	-0.31	0.4
1	5.0	-0.32	1.4
1.25	2.5	-0.29	0.3
1.5	1.2	-0.34	1.8
1.75	0.90	-0.32	1.5
2	0.56	-0.29	4.2
2.25	0.48	-0.33	4
2.5	0.40	-0.35	3.8
3	0.34	-0.34	3.7

Table 6-2:   *Time constants of the reorientation behavior at different electric field strength obtained from least-squares fits using Equation 6-3 (w_p = 35 wt.-%, electrode spacing: 2 mm). (a) no electric field induced reorientation observed.*

The results of the fitting procedure are summarized in Table 6-2 and shown in Figure 6-10. The quality of the single exponential fits can be inferred from the low χ^2 values. Independent of the electric field strength, the limiting values $P_{2,\infty}$ always reach a value around $P_{2,\infty} = -0.3$ within a scatter of some 10%.
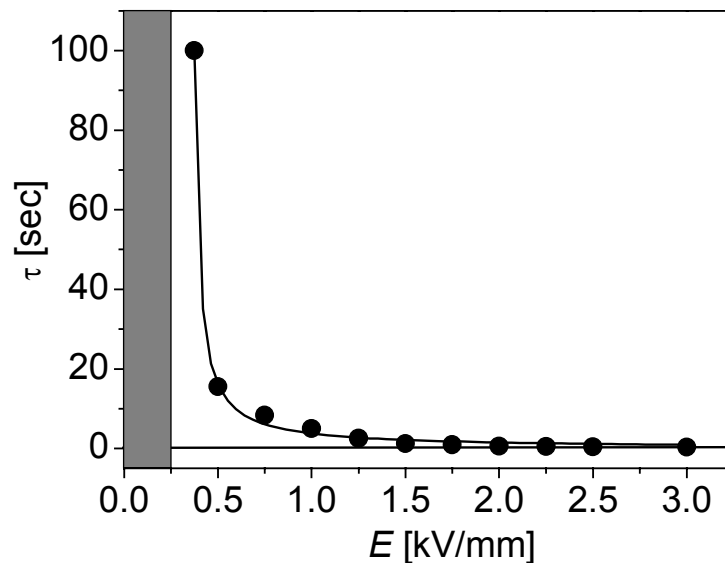

Figure 6-10:   *Electric field dependence of time constant for 35 wt.-% solutions (electrode spacing: 2 mm). The solid line represents a least-squares fit to the power law $\tau = \alpha(E - E_t)^a + \tau_\infty$ to the data points.*

The time constants τ range from 100 sec for low electric fields (0.375 kV/mm) to as low as 0.34 sec for the highest field strength (3 kV/mm). On the time scale of our experiment, we were not able to detect any reorientation for electric fields below 0.375 kV/mm. We may therefore conclude that there exists a threshold field strength E_t between 0.25 kV/mm and

0.375 kV/mm, below which no field induced reorientation is possible. Above E_t, the dependence of the time constant on the electric field reveals a power law dependence $\tau = \alpha(E - E_t)^a + \tau_\infty$. The data points are best fitted for $\alpha = 0.2$ sec $a = -1$, $E_t = 350$ V/mm and $\tau_\infty = 0$ sec (solid line in Figure 6-10).

6.3.3.3.   Temperature Dependence

In order to investigate the temperature dependence of the reorientation process, a 47.5 wt.-% solution was studied between 27.3°C and 80°C. The rather high polymer concentration was chosen to access a large temperature range before reaching the order-disorder transition temperature (T_{ODT}) of the solution.
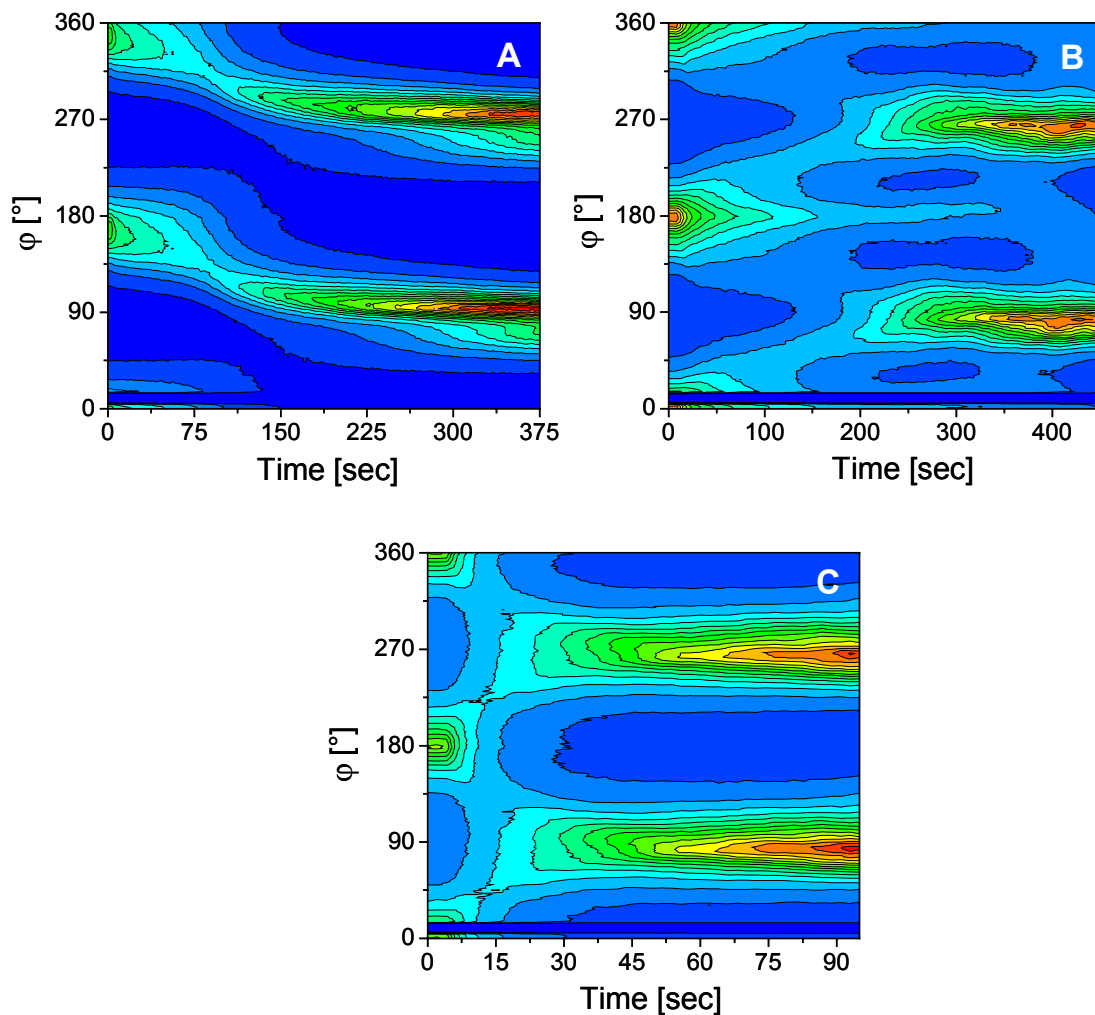

Figure 6-11:   *Azimuthal angular dependence of the scattering intensity for different temperatures at 2 kV/2 mm. (A) 27.3°C, (B) 51.5°C, (C) 80°C.*
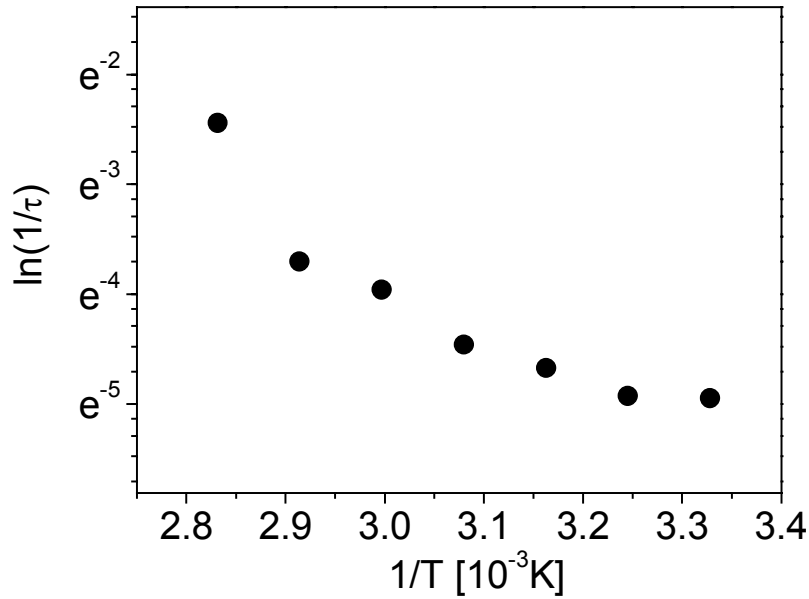
Figure 6-12:   *Arrhenius plot for the temperature dependence of the rate constant, 1/τ, for a 47.5 wt.-% solution in toluene.*

Similar to the behavior observed for low and high concentrations (Figure 6-8), a qualitatively different behavior is observed for low and high temperatures as well. At low temperatures the scattering pattern merely shifts into its new orientation (Figure 6-11A), while a destruction of the original peaks and the formation of new peaks at their final positions dominates at high temperatures (Figure 6-11C). Again, at intermediate temperatures, a superposition of both behaviors is observed (Figure 6-11B).

Temperature [K]	τ [sec]	$P_{2,\infty}$	χ^2 [10^{-4}]
300.15	141	-0.34	4
308.15	138	-0.28	0.6
316.15	106.9	-0.27	3
324.65	86.5	-0.28	3.8
333.65	52.5	-0.28	2.3
343.15	40.6	-0.27	2.5
353.15	11.5	-0.25	0.2

Table 6-3:   *Time constants of the reorientation behavior at different temperatures obtained from least-squares fits using Equation 6-3 (w_p = 47.5 wt.-%, E = 2 kV/2 mm).*

The results of a quantitative data evaluation are summarized in Table 6-3. At the lowest temperature (27°C) we measure a time constant of 141 sec, which gradually decreases down to 11.5 sec as the temperature is raised up to 80°C. The plateau values of the orientational order parameter $P_{2,\infty}$ seem to show a slight decrease from -0.34 to -0.25 with increasing temperature. An Arrhenius plot shows an upwards bent curve for higher temperatures (Figure

6-12). This behavior is typical for a process, which changes mechanism depending on the temperature. From the data, we can calculate two apparent activation energies, $E_{a,app}$, for the lower and higher temperature region, yielding 27 kJ/mol and 130 kJ/mol, respectively.

6.4. Discussion

6.4.1. Structure Formation in Solution

We start our discussion with the observed behavior in the absence of the electric field. As briefly indicated above, we locate the order disorder transition (w_{ODT}) at room temperature at a polymer concentration between 34 and 35 wt.-%. This assignment is based on various experimental observations. Most convincingly, we note the absence of birefringence at and below $w_p = 34$ wt.-%. It has been shown both experimentally and theoretically that phase separated (ordered) block copolymer materials consisting of randomly oriented lamellae are birefringent[26,27,28]. The lack of birefringence thus indicates the absence of randomly oriented lamellae. From the SAXS experiments, we find an increase in scattering intensity above $w_p = 34.5$ wt.-%, accompanied by a sharpening of the signal and the evolution of higher order Bragg peaks. Additional evidence is given by the fact that only starting from 34.5 wt.-% we observe an anisotropic scattering pattern in the absence of the electric field, which indicates some microdomain alignment induced either by shear (during filling of the sample chamber) or by preferential attraction of one block to the electrode surface. We note that the peak in the scattering profile at and below 34 wt.-% is due to composition fluctuations found commonly in the disordered state (correlation hole).

We may compare our result on the w_{ODT} to earlier measurements on similar systems (SI in toluene solution). Yao et al. determined the w_{ODT} of a symmetrical PS-b-PI block copolymer ($M_w = 84000$ g/mol) in toluene solution by dielectric measurements and found a critical concentration between 25 and 28 wt.-% at 273 K[29]. As our measurements have been conducted at room temperature (~ 298 K), it is reasonable that we find a somewhat higher concentration. Sakamoto et al. determined the w_{ODT} for a symmetrical SI block copolymer of higher molecular weight to be around 22 wt.-% and estimated the w_{ODT} for the Yao-system to be around 31 wt.-% at room temperature[30]. Both results compare well with our finding.

The lamellar spacing d was determined from the first order scattering maxima. It increases with increasing polymer concentration, indicating an increasing segregation power (or repulsive interactions) between the PS and PI chains as the polymer concentration increases.

The fact that the bulk lamellar spacing is significantly smaller than the extrapolated value from the solutions can be explained by the formation of a non-equilibrium structure during the solvent casting process. As the concentration of the solution increases, the T_g reaches room temperature and the viscosity of the whole system increases significantly. Therefore, the modulus of the whole system becomes high, so that deformation of grains requires a prolonged equilibration time, i.e. the displacement of the chemical junction points of the blocks, which is required for an increase in domain spacing, is hindered. This "frozen" domain structure is incapable of reaching an equilibrium at time scales smaller than the rate of solvent evaporation. Therefore, further evaporation of solvent results in a decrease of the spacing merely by a *deswelling* effect. Thus, in the high concentration regime the domain spacing is kinetically, but not thermodynamically controlled.

The dependence of *d* on polymer concentration in the intermediate concentration regime can be described by a scaling relation $d \sim \phi_P^{0.3}$. This behavior compares well with previous investigations by Shibayama *et al.*[25] who observed a $d \sim \phi_P^{1/3}$ dependence. In contrast, based on a theory by Noolandi and Hong[31], a $d \sim \phi_P^{1/6}$ relationship was predicted for the strong segregation limit[32]. Leibler and Frederickson predicted a $d \sim \phi_P^{-0.12}$ behavior for the weak segregation limit in block copolymer solutions[33]. In the light of these predictions, we may conclude that the positive exponent found in our experiments indicates that our system falls into the strong segregation limit. This assignment is corroborated by the observation that the polymer chains are significantly stretched in our system. This is found from a comparison of the lamellar half-width *d*/2 (some 19 nm and higher) to the unperturbed dimension of the block copolymer chains (approximately $2R_g \approx 9$ nm).

6.4.2.   Mechanism of Domain Alignment

One of the most important aspects for the understanding of the reorientation behavior of block copolymer microdomains in solution is the knowledge of the underlying mechanisms contributing to the rearrangement of domains. In contrast to in-situ birefringence[8,34], in-situ SANS[28,35] and ex-situ SAXS[36,37,38] measurements on block copolymer melts and solutions under shear, which lead to detailed insight into the respective mechanisms, so far only little is known about the microscopic processes during electric field alignment. Synchrotron-SAXS combines the advantages of birefringence (high time resolution) with the detailed and straightforward information about the microscopic order characteristic of scattering methods. Indeed, the SAXS data indicate two distinctly different mechanisms of microdomain reorientation. At low concentrations and high temperatures (Figure 6-8A, Figure 6-11C), a

destruction of the initial peaks is followed by a built-up of scattering intensity at the final peak positions. At high concentrations and low temperatures, on the other hand, the scattering pattern merely shifts into new peak positions with only a minor temporary loss in peak intensities.

These findings point to two different underlying mechanisms responsible for microdomain reorientation in the presence of the electric field. Close to the order/disorder transition (ODT), i.e. at low concentrations and high temperatures, microdomains aligned parallel to the electric field grow at the expense of those aligned parallel to the electrodes. Intermediate orientations, however, are not observed. This behavior matches the notion of the *migration of grain boundaries* (Figure 6-13A), which has previously been described for microdomain alignment under shear[37] and which was assumed to play a role in electric field experiments as well[12,13]. In this case one lamella grows at the expense of another with a significantly different orientation by motion of a tilt boundary (wall defect) between them, leading to a direct transfer of scattering intensity between widely separated azimuthal angles φ. This is indeed observed in Figure 6-8A and Figure 6-11C, where we find an almost complete decrease of the peak intensities (at $\varphi = 0°$, 180°) before new peaks start to evolve (at $\varphi = 90°$ and 270°).
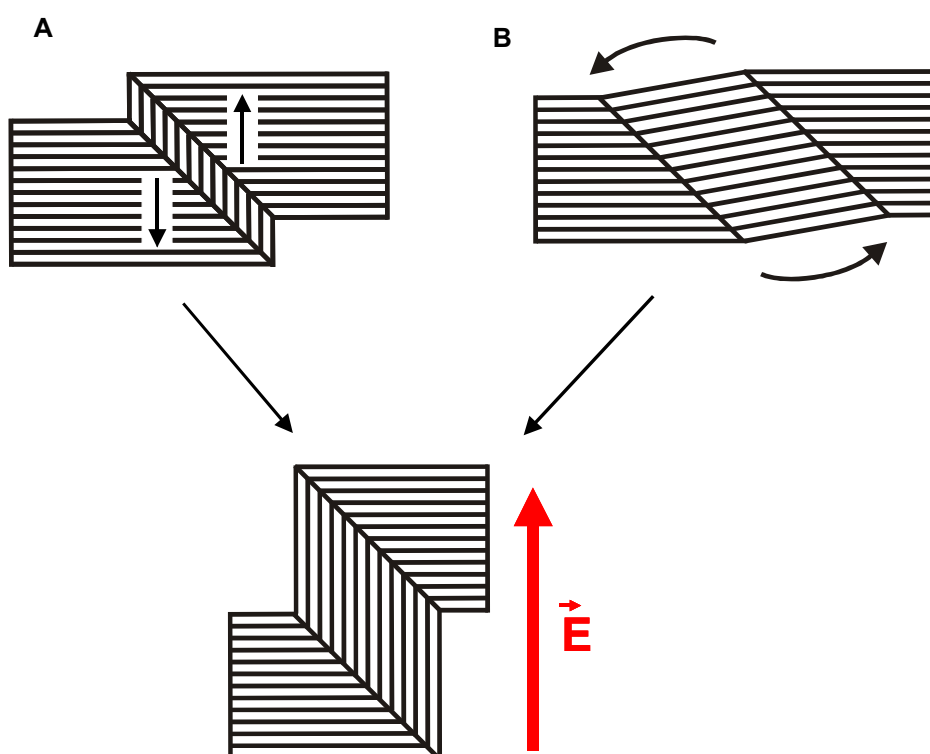

Figure 6-13:   *Schematic representation of proposed mechanisms: (A) migration of grain boundaries, (B) rotation of grains.*

Further away from the ODT, i.e. for high concentrations and low temperatures, the scattering pattern seems to be preserved and merely shifts into the new orientation. This

observation points to the *rotation of entire grains* as an alternative orientation process. In contrast to the migration of grain boundaries, microdomain orientations intermediate between the original and the final orientations are observed. At the same time no increase in isotropic scattering is found. Nevertheless, the peak intensity decreases temporarily and is recovered only after the final orientation is reached. This decrease indicates that the grains do not rotate about the X-ray beam direction, but rather about some other axis not fulfilling the Bragg law. We note that in contrast to mechanical shear fields, the electric field does not impose a preferred direction of domain rotation on the system. The fact that the final orientation parallel to the electric field vector is not fully reached within the experimental time frame is in agreement with the notion that the driving force for grain alignment almost vanishes as the aligned state is approached[13].
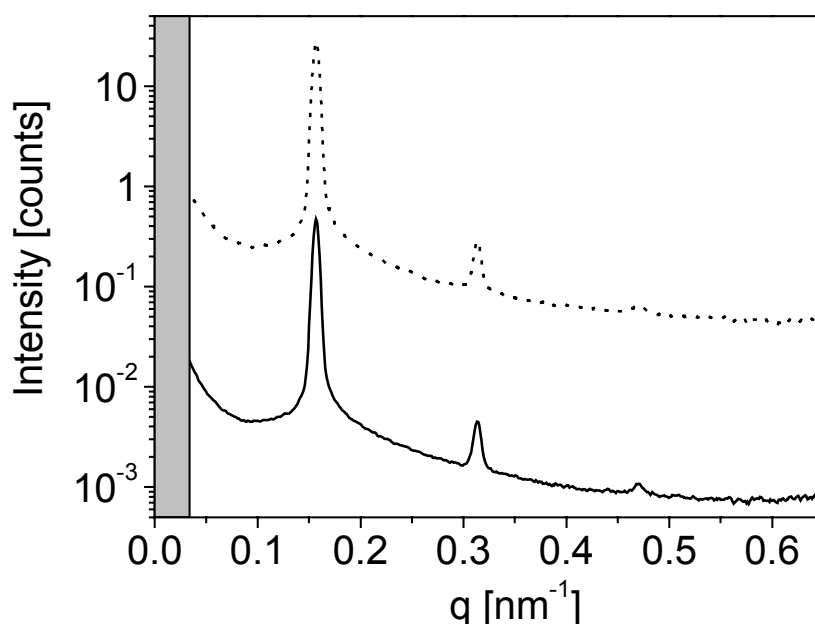

Figure 6-14:   *Scattering intensity profiles of a 37.5 wt.-% solution prior (••••) and during (──) application of an electric field of E = 1 kV/mm.*

We note that the observed behavior near ODT may also indicate what is typically referred to as the *dissolution/reformation* mechanism ("selective melting")[39,40]. This mechanism would involve partial dissolution of microdomains (at the size of several microns) which are perpendicular to the external field, followed by creation of domains parallel to the electric field. We do, however, not expect electric field induced mixing of PS and PI, since we were not able to detect any shifts in the ODT induced by the electric field. In addition, no peak broadening in the *q* dependence is observed during the reorientation process (Figure 6-14). We therefore tend to exclude the "melting" of entire microdomains as an important mechanism in our experiments. We note, however, that for migration of grain boundaries this

process may play a role *on a molecular level*, as in principle single chain motion is sufficient to stepwise change the orientation of large areas along a wall defect ("molecular scale reorientation" or "molecular scale dissolution/reformation").
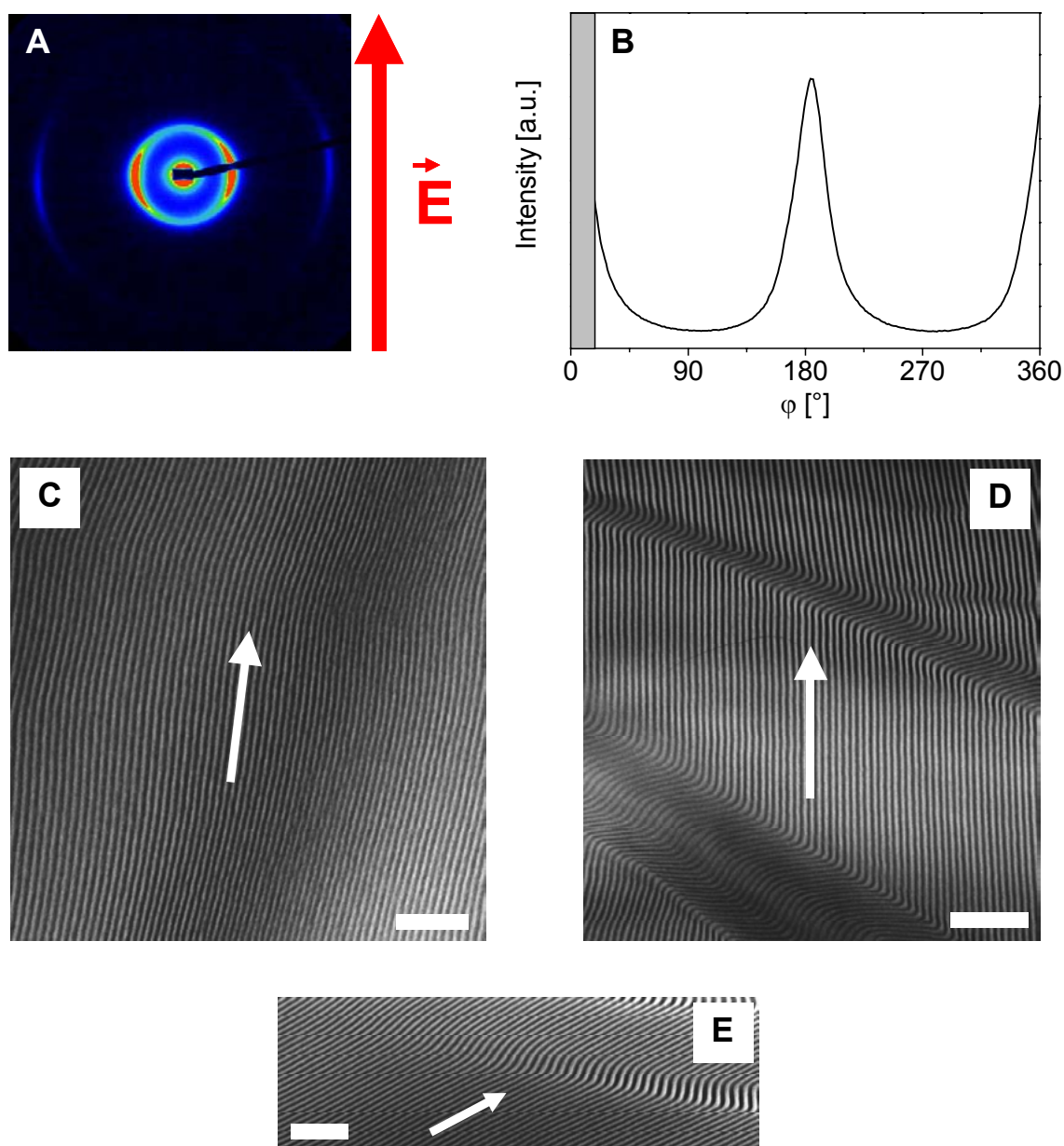

Figure 6-15:   *SAXS and TEM data of a bulk sample prepared from a 40 wt.-% solution of SI-80 in toluene dried under an applied electric field of 1 kV/mm. The arrows indicate the direction of the electric field vector. (A) 2D-SAXS pattern and (B) azimuthal intensity distribution at first order reflection (P_2 = -0.34). The TEM pictures show a defect free domain (C) and characteristic kink band defects (D/E). The scale bars represent 400 nm.*

Our mechanistic model is further corroborated by typical defects, so called "kink bands" (Figure 6-15D) , which are characteristic of the above described mechanisms and have been identified in similar processes during shear-induced lamellar reorientation[37]. Figure 6-15E shows the annihilation of a kink band by rotation of the defect structure.

We note that in most of our experiments both *migration of grain boundaries* and *grain rotation* seem to contribute to microdomain reorientation. One process dominates the other depending on the degree of segregation (i.e. in a certain concentration or temperature regime). An example for an intermediate regime is shown in Figure 6-11B, where we clearly observe the coexistence of both mechanisms. The decrease in intensity of the initial orientation is accompanied by the development of a shoulder which results in a new peak. This new signal shifts to the position of the final orientation ($\varphi = 90°$ and $270°$) and increases at the expense of the remaining intensities at the starting orientation ($\varphi = 0°$ and $180°$).
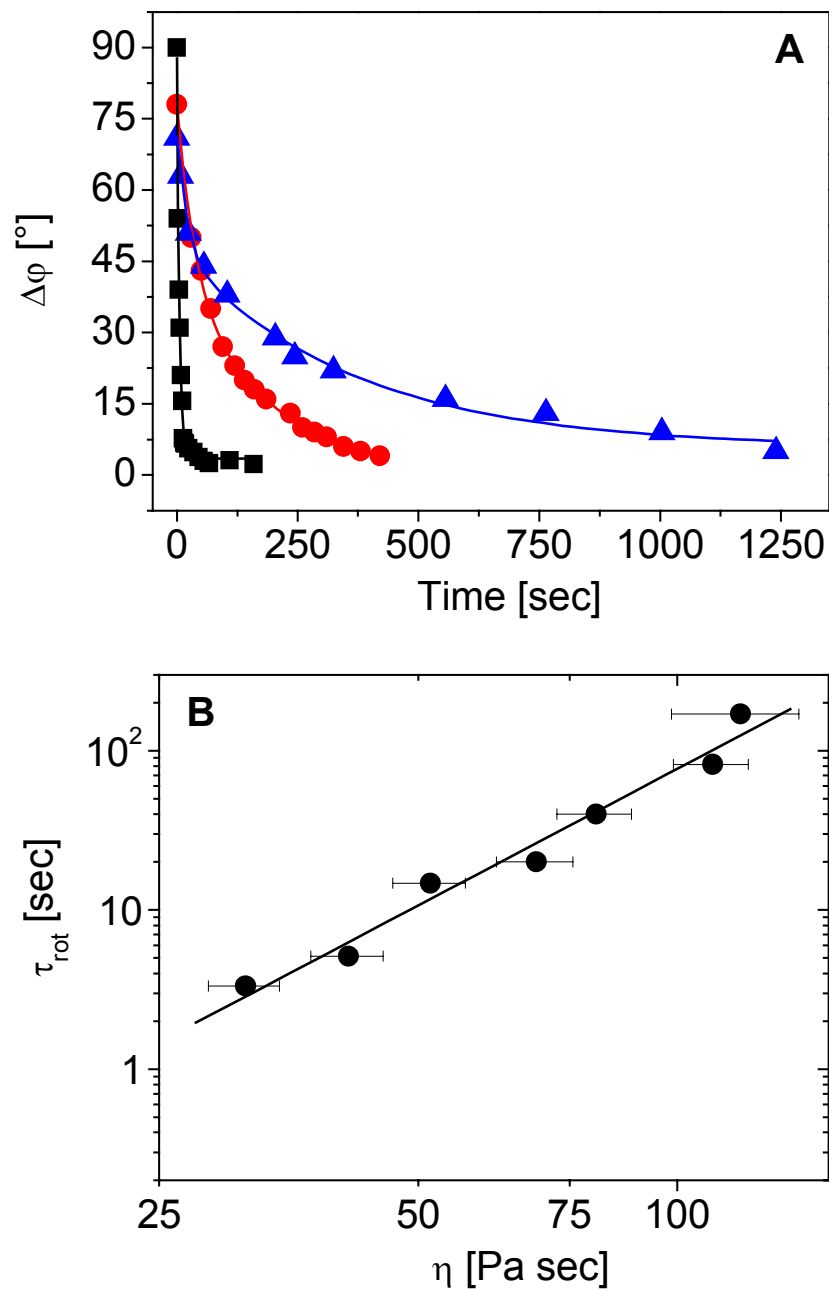

Figure 6-16:   *(A) Angular shift of rotational component at different concentrations (■ = 35 wt.-%, ● = 47.5 wt.-%, ▲ = 50 wt.-%) at a field strength of E = 1 kV/mm at T = 25 °C. The solid lines represent the least-squares fits to the data yielding the rotational time constant, τ_{rot}; (B) Double logarithmic plot of τ_{rot} versus solution viscosity, η ($\tau_{rot} \propto \eta^{2.85 \pm 0.22}$).*

In order to separately access the kinetics of the two different microscopic reordering mechanisms, we model the azimuthal scattering intensity around $\varphi = 180°$ by two Gaussians, one fixed at the initial peak position and the other being allowed to shift towards the final position as a function of time. We reveal the respective peak intensities and the position $\Delta\varphi$ of the maximum of the shifting peak from least-squares fits to the experimental data. The data for the position of the shifting peak, $\Delta\varphi$, versus time for different copolymer concentrations (not shown) can again be fitted by a single exponential yielding an effective rotational time constant, τ_{rot}. With these data we can establish a relation between the (microscopic) rotational time constant, τ_{rot}, and the (macroscopic) viscosity, η, of our block copolymer solutions (Table 6-1). A double logarithmic plot of τ_{rot} versus η (at 1 rad/s) (Figure 6-16B) yields a straight line with a slope of 2.85 ± 0.22 indicating a power law behavior $\tau_{rot} \propto \eta^{2.85 \pm 0.22}$.

If one considers the macroscopic viscosity dependence on the polymer concentration we find a typical behavior[41] as $\eta \propto c^{3.8}$. Obviously, the microscopic viscous properties of our system differ significantly from the macroscopic viscous response. Therefore, once the challenge of modeling the relationship between τ_{rot} and η has been resolved, the determination of the rotational time constant, τ_{rot}, might yield valuable insight into the microscopic properties of our system, i.e. information about viscous responses on the length scale of grain sizes ranging from a few to some hundred microns.

At this point we conclude that we are able to get detailed insight into the prevailing orientation mechanisms for lamellar domain alignment in block copolymer solutions by virtue of an external electric field. With increasing segregation power (i.e. increasing concentration/decreasing temperature, $\chi \propto \phi_P$, $\chi \propto 1/T$) we observe a transition from orientation by *migration of grain boundaries* to orientation by *grain rotation*. Intermediate conditions indicate the simultaneous action of both processes. In addition, we are able to separate both processes by a simple fitting procedure.

The transition from *grain rotation* to *migration of grain boundaries* when approaching ODT can be explained by the fact that at high concentrations and low temperatures, i.e. in a strongly segregated system, grain boundaries are thermodynamically unfavorable. Therefore, larger grains are formed which exceed a certain critical size, so that they can be rotated effectively by the electric field, which has already been anticipated for diblock copolymer melt systems[12]. At low concentrations and high temperatures, i.e. in a weakly segregated system, the energetic penalty for the creation of boundary interfaces is much lower. Furthermore, close to ODT, we also expect a high defect density and a high mobility of

defects. The vast majority of grains formed are obviously not large enough to be rotated by the electric field. Polarizing optical microscopy of block copolymer solutions of different concentration yields a broad distribution of grain sizes ranging from a few to some hundred microns (for example see Figure 6-17 which shows the evolution of birefringent domains during electric field-induced orientation of the lamellae). On the other hand, the mobility of defects such as grain boundaries (wall defects) is large, which allows the system to orient its domains parallel to the electric field by single chain based migration of grain boundaries.
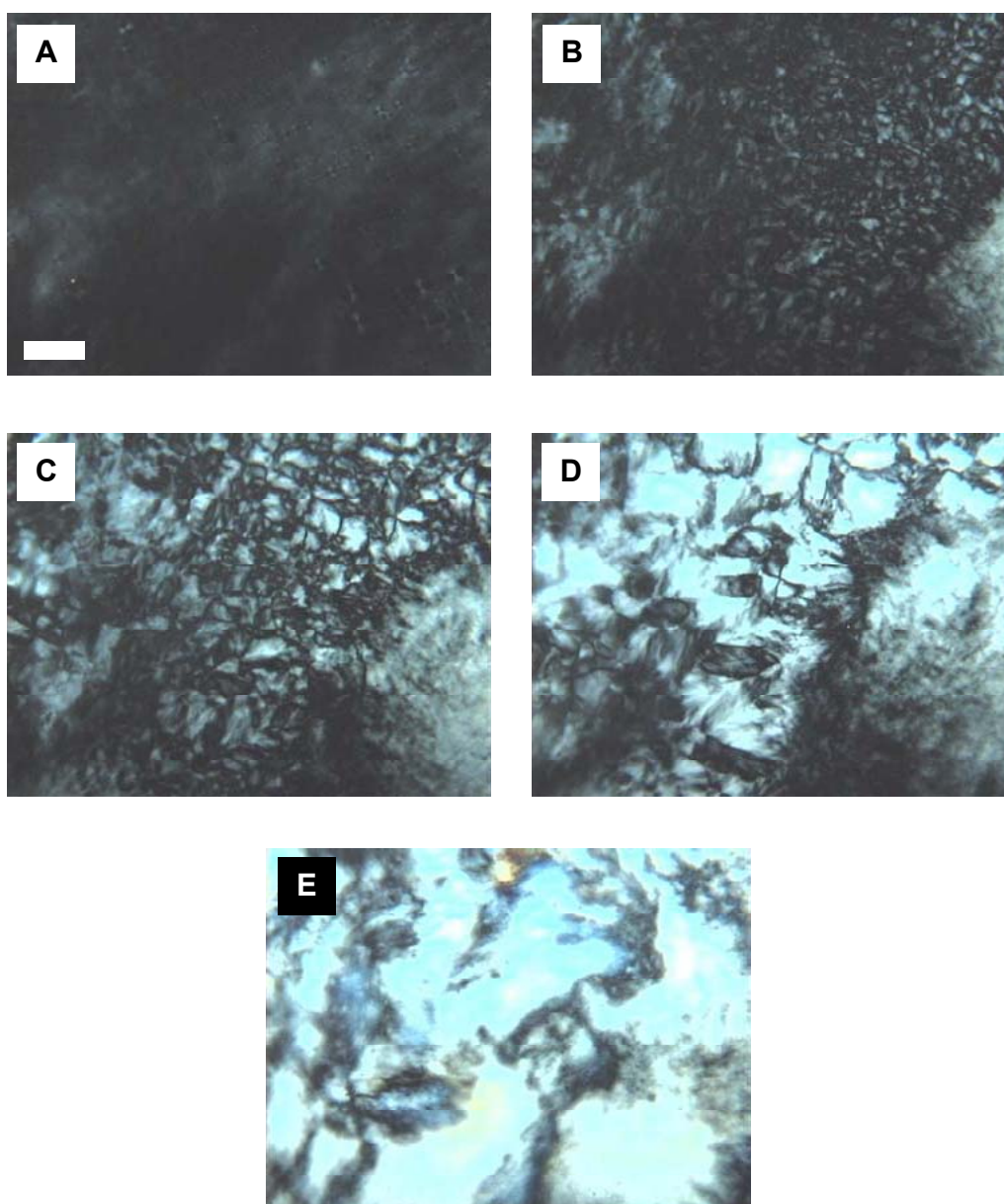
Figure 6-17:   *Polarizing optical micrographs of a 40 wt.-% solution of SI-80 in toluene between two ITO covered glass slides (d = 2mm) at 4 kV. (A) prior to electric field, (B) after 1 min, (C) 2 min, (D) 3 min and (E) 5 min. The viewing direction is parallel to the electric field vector. The scale bar represents 200 μm.*

6.4.3.   Kinetics of Microphase Orientation

For the effective preparation of highly anisotropic *melt* block copolymer samples via solvent casting in the presence of an external electric field, it is important to find an optimum set of parameters (e.g. degree of swelling of the block copolymer domains, electric field strength and temperature), which combines a maximum chain mobility (i.e. fast kinetics) with the highest possible polymer concentration. In short, the reorientation process should be faster than the rate of solvent evaporation during preparation of bulk samples from solution, i.e. it should be completed before the bulk structure "freezes".

6.4.3.1.   Concentration Dependence

With increasing polymer concentration the time constant τ increases as can be seen in Figure 6-7 and Table 6-1. Simultaneously we also observe an increase in viscosity of the respective systems. The viscosity only influences the kinetics but not the final degree of order $(P_{2,\infty})$, which is consistent with previous dielectric relaxation spectroscopy measurements on the realignment of a side-chain liquid crystalline polymer in its liquid-crystalline state induced by a DC electric field[42].

Furthermore, it is interesting to investigate the kinetics in the region of the order-disorder concentration. Below the w_{ODT} we do not observe any interaction of the polymer solution and the electric field. This can be explained by the fact that at this concentration the system is not yet microphase separated. Long range order is absent and only correlation hole scattering contributes to the SAXS pattern (Figure 6-2). As has been pointed out by Amundson in a recent review article[43], an organized state with long-range order is required for an anisotropic microstructure to be induced by the electric field. As soon as the order-disorder concentration (w_{ODT}) is reached, small grains are created from various nucleation centers and finally form a polydomain structure, which at low concentrations orients by migration of grain boundaries. From the mechanistic considerations in the previous section we already expect the reorientation process to be fast. Nevertheless, it is surprising to observe, that at 34.5 wt.-%, which is - within the error of measurement - in the region of w_{ODT}, the time constant is determined to be as low as $\tau = 800$ msec with the overall process completed after around 2.5 sec. These values are already comparable with the orientation times measured by Finkelmann and coworkers for various nematic liquid-crystalline side chain block copolymers exposed to a DC electric field, ranging from 200 msec to 5 sec at field strengths of 0.12-0.16 kV/mm[44].

In contrast to our system, where entire chains have to rearrange, in the case of the LC side chain polymers only the monomeric side groups have to realign in the electric field.

For the highest concentration we find a time constant of 192 sec with the overall process being finished within 20 minutes. As has been described earlier, even this process should be faster than the rate of solvent evaporation, so that all concentrations up to 50 wt.-% can in principle be used for the preparation of highly anisotropic bulk samples.

Using a home built capacitor which allows application of an electric DC field during film formation by solvent casting[20], we demonstrate the feasibility of such a process. The results of this *alignment-during-drying* process can be seen from the SAXS and TEM data of the resulting melt sample prepared from a 40 wt.-% solution dried under an applied electric field of 1 kV/mm (Figure 6-15A-C).

Electrode Spacing d [mm]	τ [sec]	$P_{2,\infty}$	χ^2 [10^{-4}]
0.5	61.1	-0.27	0.3
1	7.2	-0.37	0.9
2	5.0	-0.32	1.4
4	3.8	-0.33	0.2

Table 6-4:   *Time constants of the reorientation behavior at constant electric field strength and different electrode spacings obtained from least-squares fits using Equation 6-3 (E = 1 kV/mm, w_p = 35 wt.-%).*

Nevertheless, in all our experiments, we do not find degrees of orientation described by P_2 values larger than -0.35 for the block copolymer solutions and the melt sample, which are still significantly smaller than the expected value for perfect alignment parallel to the electric field vector (P_2 = -0.5). In the following, we will consider several possible explanations for these observations. First we have identified the movement of defects, i.e. wall defects (grain boundaries) as the main mechanism in samples close to ODT. It has been shown for electric field alignment of melt samples that other defects like disclination lines can reduce the mobility of grain boundaries significantly as the movement of a wall defects along a disclination line is associated with an energetic penalty which can even lead to final pinning of the boundary[12,18]. This finally leads to clustering of defects. Generally, the electric field-induced force on these clusters at field strengths used in this work is not sufficient to favor further defect annihilation. Moreover, the rotation of whole grains must be associated with a large scale reformation of the lamellar structure, thus creating new defects. In addition, as can be inferred from Equation 1-15, the electrodynamic driving force scales with $cos^2 \theta$, where θ is the tilt angle of the lamellar normal vector with respect to the electric field vector. This results in a reduction of the driving force to as low as 3% for lamellae slightly misaligned by

10° from a perfect orientation parallel to the electric field. In all cases, the application of electric fields of higher field strengths than have been accessible in this work, could improve the degree of alignment.

6.4.3.2.   Electric Field Dependence

The dependence of the time constant τ on the electric field strength exhibits a hyperbolic power law as described earlier. The asymptotic behavior at high electric fields (i.e. for a large force acting on the lamellae) indicates $\tau_\infty = 0$ sec for infinite field strength. This is expected in the absence of any electrorheological effects and limits in single chain diffusion, as the dominating process at 35 wt.-% is the migration of grain boundaries. The asymptotic behavior at low field strength indicates a threshold value E_t of some 0.35 kV/mm. This is in agreement with the experimental observation that at lower field strengths no effect of the electric field on the scattering pattern was observed. This threshold value can be explained by a competition of the electric field and the surface field generated by the gold electrodes. The latter exhibits an unexpected range, as has already been found by Annighöfer and Gronski for thick PS-*b*-PI block copolymer bulk samples cast from several aromatic solvents (including toluene) in the absence of an external electric field[5]. The threshold we determine differs from the one detected by Thurn-Albrecht *et al.*[17]. They defined the threshold field strength as the one needed for an alignment of the cylinders parallel to the electric field vector throughout the entire film. In our case, we always find 10 to 40 lamellar layers parallel to the boundary electrodes with a transition to lamellae perpendicular to the electrodes, as reported earlier (for example see Figure 5-6)[20]. Nevertheless, there is an indirect influence of the electrode surface on the threshold voltage in our case. As the formation of T-junctions for the transition from lamellae parallel to perpendicular to the boundary surfaces leads to an energetic penalty which has to be balanced by the electric field, we can define the threshold field strength as the voltage needed to overcome this energetic barrier. Therefore, a sufficient gain in energy is required, which can be derived from the overall size of the domains to be aligned parallel to the electric field vector. If the size of the domains which can be oriented is reduced by decreasing the electrode spacing, the threshold field strength will increase as the gain in energy (i.e. energy stored in the capacitor per area) decreases. This explains the dependence of the time constant τ on the electrode spacing as shown in Table 6-4 and Figure 6-18. Here, we measured the reorientation kinetics at constant field strength for different electrode spacings for a 35 wt.-% solution of SI-80 in toluene. We find a distinct jump in the time constant from 1 mm to 0.5 mm, indicating that below 1 mm the energetic cost decreasingly

can be balanced by the gain in energy from the aligned domains. Further reduction of the electrode spacing to the range of the electrode surface field might finally lead to a complete pinning of the starting orientation. This distinct dependence of the threshold field strength has recently been predicted by Tsori and Andelman[45] for a lamellar block copolymer system in the strong segregation limit. Nevertheless, we note that further experiments have to be conducted in order to exclude completely the possibility that due to the rather large domains size of up to 200 μm we have to consider a kinetic rather than a thermodynamic effect to explain our data.
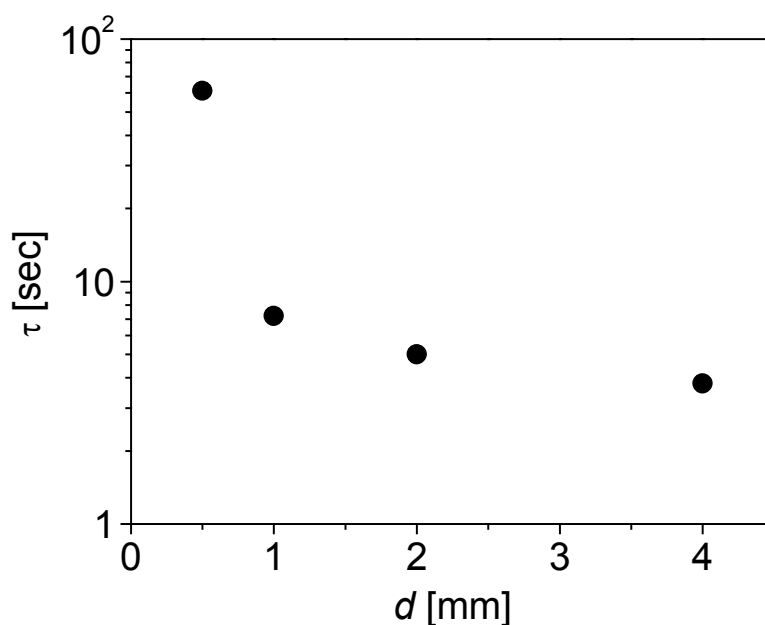
Figure 6-18:   Logarithmic dependence of the orientation kinetics on the electrode spacing for a 35 wt.-% solution of SI-80 in toluene at 1 kV/mm.

Amundson *et al.*[13] found an E^2 dependence of the rate constant for a limited range of field strengths (1, 1.5 and 1.75 kV/mm). In contrast, our data rather indicate a somewhat stronger dependence of the rate constant on the electric field strength. A double logarithmic plot of $1/\tau$ versus E yields a slope of 2.4 ± 0.1, i.e. $1/\tau \sim E^{2.4 \pm 0.1}$. As anticipated by Amundson *et al.* their range of electric field strength is not sufficient to draw a definite conclusion about the electric field strength dependence of the alignment kinetics. Moreover, we also agree with their assumption that the stronger dependence could indicate an activated process, such as nucleation of new defect structures, e.g. wall defects, which in turn would accelerate the orientation process by increasing the active centers for alignment in the sample, rearranging by migration of grain boundaries as this is the dominant mechanism for the 35 wt.-% used in this series.

6.4.3.3.   Temperature Dependence

The rate constant exhibits a non-linear behavior for an Arrhenius type plot as shown in Figure 6-12. This non-classical Arrhenius type behavior reveals that the observed shift in mechanism from grain rotation at low temperatures to migration of grain boundaries at higher temperatures goes along with a significant change in apparent activation energy. Due to an increase in temperature, many parameters like viscosity, interaction parameter and finally - with decreasing degree of phase separation - also the thermodynamic driving force for the electric field-induced alignment change. Therefore, we cannot give a definite explanation for the higher activation energy observed for the migration of grain boundaries. A possible explanation would have to take into account the interplay between decreasing viscosity, decreasing thermodynamic driving force and increasing composition fluctuations close to T_{ODT}. In addition, we note that the superposition of the above described two distinctly different mechanisms further complicates the kinetic behavior.

6.5.   Conclusion

We have identified two mechanisms governing the electric field alignment of a lamellar block copolymer from concentrated solutions. It was shown that depending on the segregation power ($\chi \propto \phi_P$, $\chi \propto 1/T$) a single mechanism dominates the orientation process, i.e. in a weakly segregated system (low concentration or high temperature) the *migration of boundaries* prevails, whereas a stronger phase separated system (high concentration or low temperature) predominantly exhibits *rotation of grains*.

Furthermore, the orientation kinetics slows down with increasing polymer *concentration*, which can be correlated to the respective solution viscosity and the mechanism of orientation. Additionally, we determined the influence of the *electric field strength* on the orientation kinetics, including a threshold value below which no electric field induced orientation could be achieved on the time scale of the experiment. The time constants of the fastest processes were in the range of 0.5 sec, reaching a final orientation described by order parameters of up to $P_2 = -0.35$. Finally, the variation of *temperature* lead us to control the governing mechanisms at a fixed polymer concentration.

In summary, we have demonstrated that electric field alignment of block copolymer domains from solution is a powerful tool to generate highly anisotropic bulk block copolymer samples. The large variety of parameters which we can control allows us to further improve

the preparation of macroscopically aligned melt samples via solvent casting in the presence of an electric field.

Acknowledgement

References

[1] A part of this work has been submitted to *Phys. Rev. Lett.* by A. Böker, H. Elbs, H. Hänsel, A. Knoll, S. Ludwigs, H. Zettl, V. Urban, V. Abetz, A.H.E. Müller, and G. Krausch.

Some of the coauthors (Elbs, Hänsel, Knoll, Ludwigs, Zettl, Abetz and Urban) have helped during the 72h beamtime at the ESRF with setup of the equipment and sample preparation. In addition the measurements were performed by different shifts round the clock in order to effectively use the allocated beamtime. Moreover, helpful discussions with H. Elbs, H. Hänsel, A. Knoll, H. Zettl, and V. Abetz about data evaluation and technical details are gratefully acknowledged. Additionally, H. Hänsel developed a LabView programm, which automated the calculation of the hundreds of P_2 values of each experiment.

[2] Bates, F.S.; Fredrickson, G.H. *Ann. Rev. Phys. Chem.* **1990**, *41*, 525.

[3] Bates, F.S.; Fredrickson, G.H. *Physics Today* **1999**, *52*, 32.

[4] Anastasiadis, S.H.; Russell, T.P.; Satija, S.K.; Majkrzak, C.F. *Phys. Rev. Lett.* **1989**, *62*, 1852.

[5] Annighöfer, F.; Gronski, W. *Makromol. Chem., Rapid Commun.* **1983**, *4*, 123.

[6] Wiesner, U. *Macromol. Chem. Phys.* **1997**, *198*, 3319.

[7] Chen, Z.-R.; Kornfield, J.A.; Smith, S.D.; Grothaus, J.T.; Satkowski, M.M. *Science* **1997**, *277*, 1248.

[8] Chen, Z.-R.; Kornfield, J.A. *Polymer* **1998**, *39*, 4679.

[9] Keller, A.; Pedemonte, E.; Willmouth, F.M. *Nature* **1970**, *225*, 538.

[10] Albalak, R.J.; Thomas, E.L. *J. Polym. Sci., Polym. Phys. Ed.* **1993**, *31*, 37.

[11] Thurn-Albrecht, T.; Schotter, J.; Kastle, G.A.; Emley, N.; Shibauchi, T.; Krusin-Elbaum, L.; Guarini, K.; Black, C.T.; Tuominen, M.T.; Russell, T.P. *Science* **2000**, *290*, 2126.

[12] Amundson, K.; Helfand, E.; Davis, D.D.; Quan, X.; Patel, S.S.; Smith, S.D. *Macromolecules* **1991**, *24*, 6546.

[13] Amundson, K.; Helfand, E.; Quan, X.; Smith, S.D. *Macromolecules* **1993**, *26*, 2698.

[14] Morkved, T.L.; Lu, M.; Urbas, A.M.; Ehrichs, E.E.; Jaeger, H.M.; Mansky, P.; Russell, T.P. *Science* **1996**, *273*, 931.

[15] Morkved, T.L.; Lopez, V.A.; Hahm, J.; Sibener, S.J.; Jaeger, H.M. *Polymer* **1998**, 39, 3871.

[16] Mansky, P.; DeRouchey, J.; Russell, T.P.; Mays, J.; Pitsikalis, M.; Morkved, T.L.; Jaeger, H.M. *Macromolecules* **1998**, *31*, 4399.

[17] Thurn-Albrecht, T.; DeRouchey, J.; Russell, T.P.; Jaeger, H.M. *Macromolecules* **2000**, *33*, 3250.

[18] Amundson, K.; Helfand, E.; Quan, X.; Hudson, S.D.; Smith, S.D. *Macromolecules* **1994**, *27*, 6559.

[19] Le Meur, J.; Terrisse, J.; Schwab, C.; Goldzene, P. *J. Phys., Colloq.* **1971**, *32*, C5a-301.

[20] Böker, A.; Knoll, A.; Elbs, H.; Abetz, V.; Müller, A.H.E.; Krausch, G. *Macromolecules* **2002**, *35*, 1319.

[21] Schmalz, H.; Böker, A.; Lange, R.; Krausch, G.; Abetz, V. *Macromolecules* **2001**, *34*, 8720.

[22] C.C. Sawyer; D.T. Grubb *Polymer Microscopy*, 2nd Ed.; Chapman & Hall: London, **1996**.

[23] Wang, W.; Hashimoto, T. *Polymer* **2000**, *41*, 4729.

[24] Noolandi, J.; Hong, K.M. *Ferroelectrics* **1980**, *30*, 117.

[25] Shibayama, M.; Hashimoto, T.; Hasegawa, H.; Kawai, H. *Macromolecules* **1983**, *16*, 1427.

[26] Amundson, K.; Helfand, E.; Patel, S.S.; Quan, X.; Smith, S.D. *Macromolecules* **1992**, *25*, 1953.

[27] Balsara, N.P.; Perahia, D.; Safinya, C.R.; Tirrell, M.; Lodge, T.P. *Macromolecules* **1992**, *25*, 3896.

[28] Balsara, N.P.; Hammouda, B.; Kesani, P.K.; Jonnalagadda, S.V.; Straty, G.C. *Macromolecules* **1994**, *27*, 2566.

[29] Yao, M.L.; Watanabe, H.; Adachi, K.; Kotaka, T. *Macromolecules* **1992**, *25*, 1699.

[30] Sakamoto, N.; Hashimoto, T.; Kido, R.; Adachi, K. *Macromolecules* **1996**, *29*, 8126.

[31] Hong, K.M.; Noolandi, J. *Macromolecules* **1981**, *14*, 736.

[32] Balsara, N.P.; Eastman, C.E.; Foster, M.D.; Lodge, T.P.; Tirrell, M. *Makromol. Chem., Makromol. Symp.* **1991**, *45*, 213.

[33] Fredrickson, G.H.; Leibler, L. *Macromolecules* **1989**, *22*, 1238.

[34] Chen, Z.R.; Issaian, A.M.; Kornfield, J.A.; Smith, S.D.; Grothaus, J.T.; Satkowski, M.M. *Macromolecules* **1997**, *30*, 7096.

[35] Balsara, N.P.; Hammouda, B. *Phys. Rev. Lett.* **1994**, *72*, 360.

[36] Winey, K.I.; Patel, S.S.; Larson, R.G.; Watanabe, H. *Macromolecules* **1993**, *26*, 2542.

[37] Polis, D.L.; Smith, S.D.; Terrill, N.J.; Ryan, A.J.; Morse, DC; Winey, K.I. *Macromolecules* **1999**, *32*, 4668.

[38] Zhang, Y.; Wiesner, U. *J. Chem. Phys.* **1995**, *103*, 4784.

[39] Morrison, F.A.; Winter, H.H. *Macromolecules* **1989**, *22*, 3533.

[40] Scott, D.B.; Waddon, A.J.; Lin, Y.G.; Karasz, F.E.; Winter, H.H. *Macromolecules* **1992**, *25*, 4175.

[41] D.S. Pearson, A. Mera, W.E. Rochefort *Polym. Prepr.* **1981**, *22*, 102.

[42] Kozak, A.; Simon, G.P.; Moscicki, J.K.; Williams, G. *Mol. Cryst. Liq. Cryst.* **1990**, *193*, 155.

[43] Amundson, K.R.: "Electric and magnetic field effects on polymeric systems exhibiting long-range orientational order" *Plast. Eng.* (N.Y.) **1998**, *45*, 1079.

[44] Finkelmann, H.; Naegele, D.; Ringsdorf, H. *Makromol. Chem.* **1979**, *180*, 803.

[45] Tsori, Y.; Andelman, D. *Macromolecules* **2002**, *35*, 5161.

Chapter 7

The Influence of Phase Separation and Dielectric Contrast on the Electric Field Induced Orientation of Lamellar AC and ABC Block Copolymer Solutions

Abstract

We investigate the reorientation kinetics of concentrated solutions of lamellar AC diblock and ABC triblock copolymers in the presence of an external DC electric field. The experiments were performed on polystyrene-*b*-poly(methyl methacrylate) and polystyrene-*b*-poly(2-hydroxyethyl methacrylate)-*b*-poly(methyl methacrylate) block copolymer solutions in tetrahydrofuran. In-situ synchrotron radiation small-angle X-ray scattering was used to monitor the reorientation process. For the ABC triblock copolymer, the orientation kinetics is well described by a single exponential with characteristic time constants varying between a few seconds and several minutes depending on the polymer concentration and the electric field strength. In addition, detailed insight into the dominant microscopic mechanisms is revealed. We identify a narrow concentration window, in which the interplay between chain mobility and gain in free energy in the electric field allows the preparation of highly anisotropic bulk polymer samples by exposure to an electric field. We compare the observations for the triblock copolymer with a lamellar polystyrene-*b*-poly(methyl methacrylate) diblock copolymer, were no electric field induced reorientation could be achieved.

7.1.   Introduction

In a recent work[1], we have demonstrated that electric field induced alignment can be applied successfully to block copolymer *solutions*, thereby effectively circumventing limitations associated with the high melt viscosities of high molecular weight copolymers or copolymers of more complex architectures (multiblock copolymers, star copolymers, etc.). Given the increasing interest in complex block copolymer structures, it is desirable to further explore such alternative approaches in detail. Therefore, we present in this work real-time Synchrotron-SAXS investigations on the kinetics and mechanisms of the reorientation of lamellar polystyrene-*b*-poly(2-hydroxyethyl methacrylate)-*b*-poly(methyl methacrylate) and polystyrene-*b*-poly(methyl methacrylate) block copolymers. Macroscopically aligned bulk samples of these polymers are of considerable technological interest as the methacrylic component can be decomposed by UV irradiation, yielding a crosslinked PS scaffold for application as a nanoporous membrane or a template for simple pattern transfer on nanometer scale[2].

7.2.   Experimental Section

7.2.1.   Synthesis

The polystyrene-*b*-poly(2-hydroxyethyl methacrylate)-*b*-poly(methyl methacrylate) (SHM) block copolymer was synthesized by sequential living anionic polymerization as described in detail elsewhere[3]. The polymer used in this study consists of 47 wt.-% polystyrene, 10 wt.-% poly(2-hydroxyethyl methacrylate) (PHEMA) and 43 wt.-% poly(methyl methacrylate) (PMMA) with a total number-average molecular weight M_n = 82,000 g/mol (we denote this material as $S_{47}H_{10}M_{43}^{82}$). GPC of the final block copolymer yields a polydispersity of M_w/M_n = 1.04. The block ratio and overall molecular weight were determined by ^{1}H-NMR using the integrated aromatic signals of the polystyrene block in combination with the GPC results of the corresponding polystyrene precursor. The diblock copolymer polystyrene-*b*-poly(methyl methacrylate) was synthesized and characterized analogously, yielding M_n = 100,000 g/mol and M_w/M_n = 1.03 with nearly symmetrical composition (49 wt.-% PS, 51 wt.-% PMMA, $S_{49}M_{51}^{100}$).

7.2.2.   Sample Preparation

Block copolymer solutions in THF with polymer concentrations from 30 to 70 wt.- % were used for the present study. The alignment experiments were performed in a home-built capacitor with gold electrodes (sample depth = 5 mm, electrode distance d = 1 – 2 mm; see Figure 6-1) at 25°C. A DC voltage between 0.5 and 6 kV was applied across the electrodes resulting in an electric field perpendicular to the X-ray beam direction. Both the voltage at the electrodes and the current were monitored during the course of the experiment indicating only a small leakage current (~ 0.01 mA) during the first few seconds after the field was applied. During this period, no lamellar reorientation was detected.

Oriented melt samples were produced via solvent casting using an open cylindrical capacitor with aluminum electrodes (r = 5 mm, d = 1.1 mm) at 25°C. The details of this setup have already been described elsewhere (see Figure 5-1)[1].

The experimental details for, TEM, viscosity and in-situ synchrotron SAXS measurements, as well as the evaluation of the SAXS data, including the calculation of the orientational order parameter and the quantification of the orientation kinetics have already been described in chapter 6.

The remainder of the paper is organized as follows. We shall first describe the structure formation in solution in the absence of the electric field before we continue discussing the influence of an external electric field on the domain orientation of solutions of different concentrations and at different electric field strengths. For reasons to become clear below, we first concentrate on the $S_{47}H_{10}M_{43}{}^{82}$ triblock copolymer before we compare the results to what was found for the $S_{49}M_{51}{}^{100}$ diblock copolymer.

7.3.   Results

7.3.1.   Concentration Dependence of the Microdomain Structure in Solution

We studied the microdomain structure of the SHM triblock copolymer in THF solution as a function of polymer concentration, starting from w_p = 30 wt.-% and increasing w_p stepwise by 2.5 wt.-% up to 50 wt.-% and by steps of 10 wt.-% to higher polymer concentrations. As shown in Figure 7-1, we find the formation of a narrow first-order reflection when increasing the concentration from 37.5 wt.-% to 40 wt.-%. We note that starting from 40 wt.-% the block copolymer solutions become birefringent (measured with a polarizing optical microscope, not

shown here). At higher concentrations we observe higher order scattering peaks which correspond to integer multiples of the first order signal, indicating the formation of lamellar microdomains in the solution. From these findings, we locate the order-disorder transition (ODT) at room temperature at around $w_{ODT} \approx 40$ wt.-%.
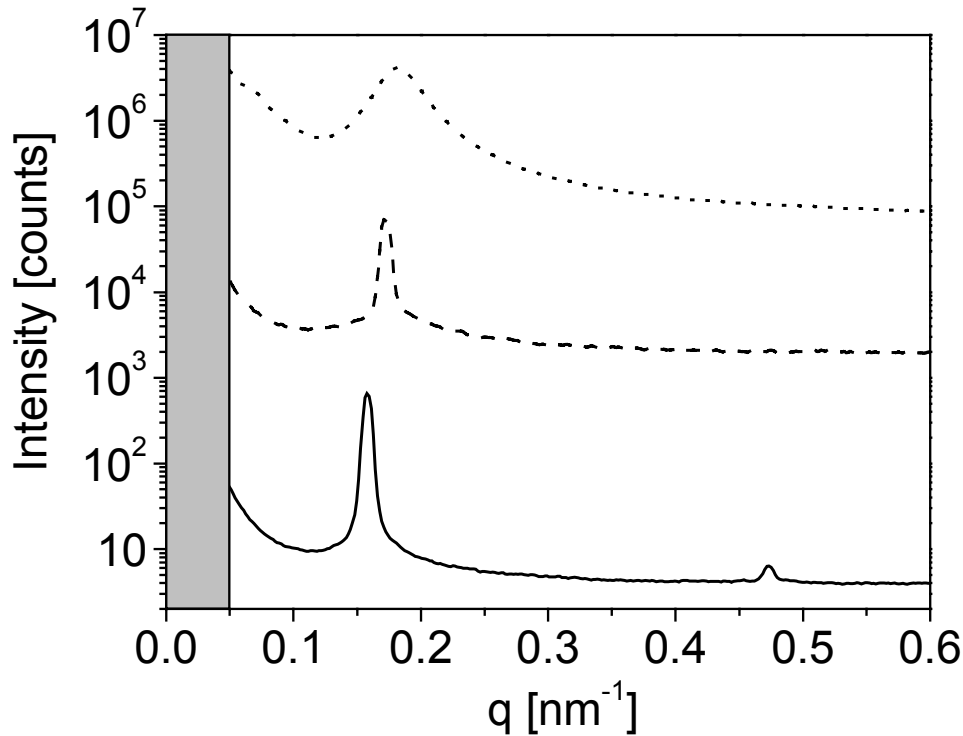

Figure 7-1:   *Scattering intensity profiles of $S_{47}H_{10}M_{43}^{82}$ solutions in THF at various concentrations. 37.5 wt.-% (·····), 40 wt.-% (- -), 47.5 wt.-% (—).*

We note that even harmonics seem suppressed in the SAXS patterns. This may be attributed to a minimum in the structure factor, which would be expected for a *symmetrical* block copolymer. As indicate above, we do not expect PHEMA and PMMA to exhibit a sufficient scattering contrast, so that these two phases may indeed not be distinguished in the SAXS experiment.

In addition, as shown in Figure 7-2, we find a continuous increase of the lamellar spacing, $d_{100} = 2\pi/q_{100}$, with increasing polymer concentration, indicating that the segregation power continuously increases as the solvent content decreases. At higher concentrations, the spacing gradually approaches the lamellar spacing of the bulk sample. The dependence of the lamellar spacing, d, on the polymer volume fraction, ϕ_p, scales as $d \sim \phi_p^{0.5}$ for intermediate concentrations. This can be seen in the double logarithmic plot in Figure 7-3.
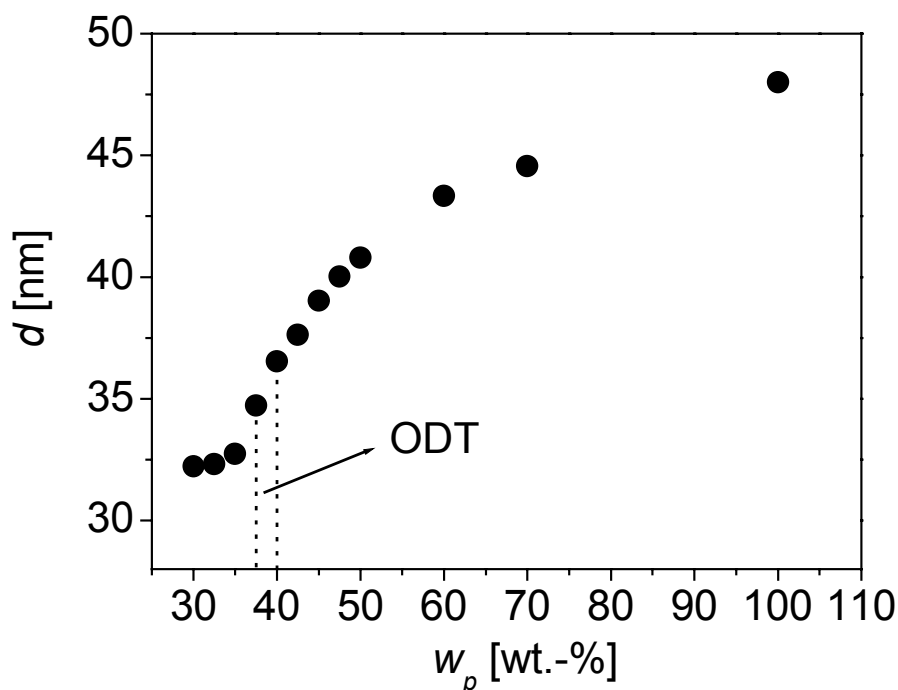
Figure 7-2:   Concentration dependence of the lamellar spacing (d_{100}).

7.3.2.   Reorientation Behavior of PS-*b*-PHEMA-*b*-PMMA

After sample preparation and prior to electric field exposure, all phase-separated solutions exhibit a distinctly anisotropic scattering pattern with maxima located at $\varphi = 0°$ and $180°$, respectively (Figure 7-4A). This pattern indicates alignment of the lamellae parallel to the electrodes. Such an alignment can be caused both by preferential interaction of PS with the gold surfaces and by possible shear forces acting on the highly viscous solutions during filling of the capacitor with a syringe. In order to destroy any possible memory effect, we heated the solutions above the order-disorder temperature. However, after cooling, still some alignment of the domains parallel to the electrodes prevailed, indicating the importance of the surface effects[4].

As soon as the electric field is applied, the scattering pattern changes significantly. The peaks at $\varphi = 0°$ and $180°$ decrease and new scattering maxima at $\varphi = 90°$ and $270°$ grow with time (Figure 7-4A-C). In order to quantify the kinetics of the orientation process, $P_2(t)$ was calculated from the 2D SAXS patterns as described above. Using a single exponential fit, we can determine the time constant τ of the reorientation process (see Equation 6-3).

The evolution of the orientational order parameter, $P_2(t)$, is shown in Figure 7-5 for 40 wt.-% and 45 wt.-% solutions of SHM in THF. The solid lines represent least squares fits to the data. For the 45 wt.-% solution only little alignment was achieved on application of

136

1 kV/mm. Therefore, after some 400 sec, the electric field strength was increased to 2 kV/mm.
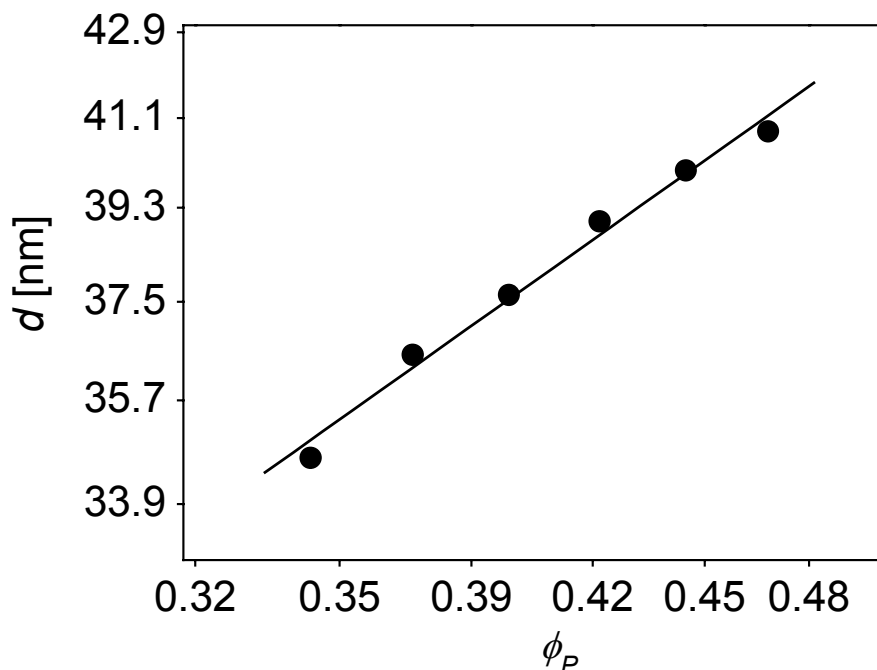

Figure 7-3:   *Double logarithmic plot of dependence of lamellar spacing on the volume fraction of polymer ϕ_P for intermediate concentrations ($d \sim \phi_P^{0.5}$).*

7.3.3.   Kinetics of Microphase Orientation

7.3.3.1.   Concentration dependence

The kinetics of the alignment of the microdomains formed in our triblock copolymer system was followed within a narrow concentration window between 40 wt.-% (where phase separation sets in) and 50 wt.-%. As anticipated from the increasing solution viscosities, the time constant, τ, strongly increases with increasing polymer concentration. As can be seen from Figure 7-5 and Table 7-1, the time constants for the reorientation process at 1kV/mm in a 1 mm capacitor are in the range of some minutes (1.5 minutes and nearly 6 minutes for 40 and 45 wt.-%, respectively). At concentrations above 45 wt.-% no electric field induced orientation could be detected. Moreover, at 45 wt.-% (Figure 7-5B) the process is slowed down significantly at an incomplete degree of alignment ($P_2 = 0.28$), which can only be overcome by increasing the field strength.
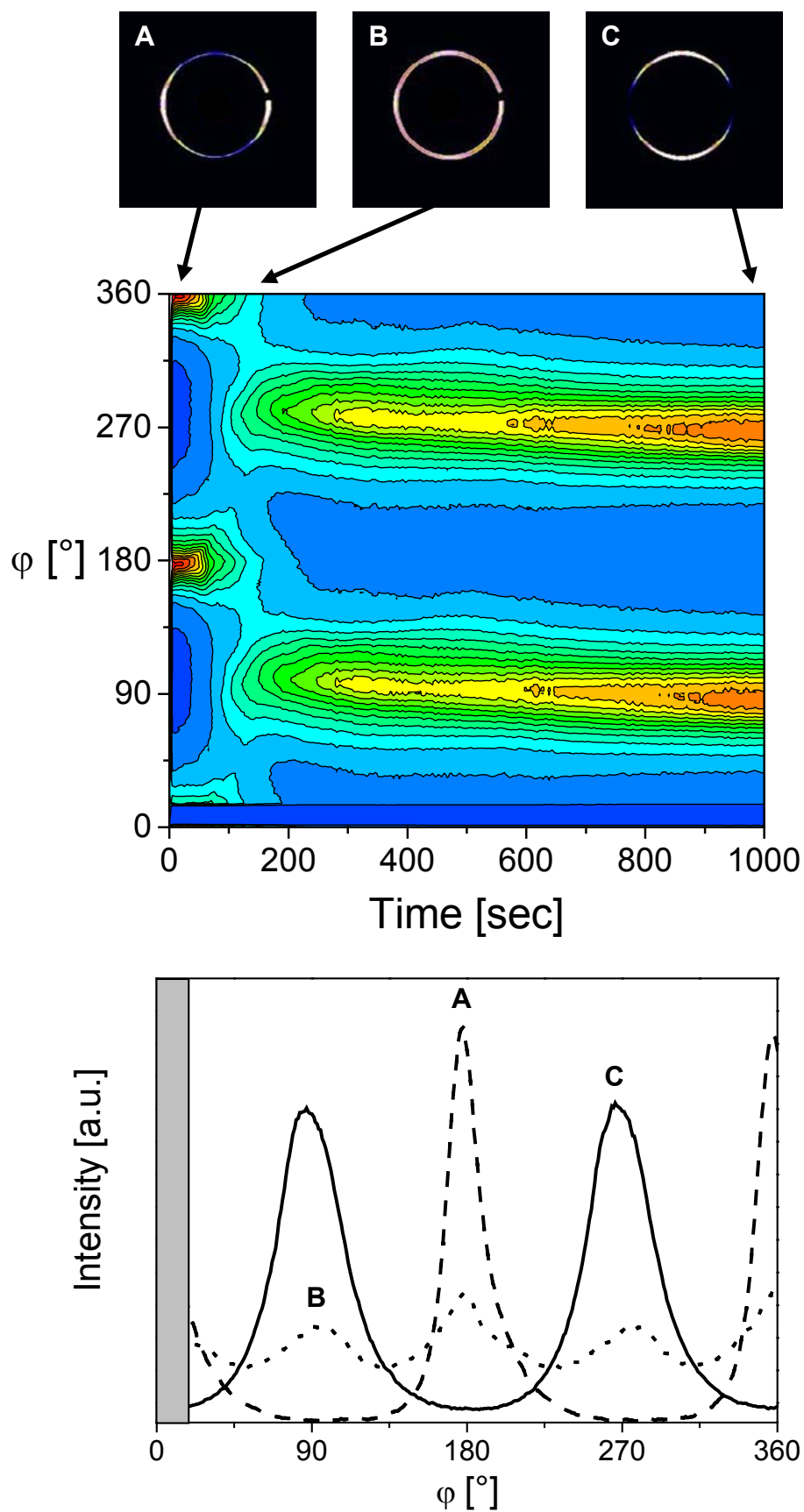
*Figure 7-4:   Scattering profiles and azimuthal angular dependence of the scattering intensity of a 40 wt.-%
solution of $S_{47}H_{10}M_{43}{}^{82}$ in THF at 1 kV/mm; (A) t = 0 sec, (B) t = 100 sec, (C) t = 985 sec*

The results of the exponential fits are summarized in Table 7-1. The single exponential fit works quite well for all concentrations studied, as can be seen from the low χ^2 values. At a sufficiently high electric field strength, P_2 reaches about the same limiting values $P_{2,\infty}$ = -0.25 ± 0.02 independent of concentration. Therefore, we may assume that the polymer concentration only influences the rate of orientation rather than the final degree of alignment.

Within the narrow concentration window accessible for electric field induced alignment we observe the superposition of two different microscopic reorientation mechanisms[5]. As can be seen in Figure 7-4, the initial peaks at $\varphi = 0°$ and 180° almost vanish as the electric field is applied and new peaks are formed at $\varphi = 90°$ and 270°, the intensity of which grows with time. Simultaneously, we observe small peaks, which shift into their new positions (from 180° to 90° and from 360° to 270°). This is seen best in the azimuthal contour plot in Figure 7-4.

Concentration [wt.-%]	Voltage [kV/mm]	τ [sec]	$P_{2,\infty}$	χ^2 [10^{-4}]
40	1	89	-0.26	3.8
45	1	348	0.28	0.5
45	2	151	-0.23	1.4
45	3	157	-0.27	0.6

Table 7-1:   *Time constants τ of the reorientation behavior at different polymer concentrations and different electric field strength obtained from least squares fits using Equation 6-3. (1 mm electrode distance)*

7.3.3.2.   **Electric Field Strength Dependence**

In order to investigate the influence of the electric field strength on the orientation kinetics we varied the electric field between 0.25 kV/mm and 3 kV/mm. In this case a 40 wt.-% solution of the triblock copolymer was studied at room temperature in a 2 mm capacitor in order to exclude dominant surface effects. A selection of P_2 vs. *t* curves is shown in Figure 7-6. The results of the fitting procedure are summarized in Table 7-2 and shown in Figure 7-7. The quality of the single exponential fits can be inferred from the low χ^2 values. Except for $E = 0.375$ kV/mm ($P_{2,\infty}$ = -0.08), the limiting values, $P_{2,\infty}$, always reach a value around $P_{2,\infty}$ = -0.2 ± 0.03. With increasing field strength, there is a slight tendency towards higher plateau values (-0.17.....-0.22). The time constants, τ, range from 545 sec for low electric fields (0.375 kV/mm) to as low as 0.64 sec for the highest field strength (3 kV/mm). On the time scale of our experiment, we were not able to detect any reorientation for electric fields below 0.25 kV/mm. We may therefore conclude that there exists a threshold field strength

$E_t = 0.25 \ldots 0.375$ kV/mm, below which no field induced reorientation is possible. Above E_t, the time constant scales with the electric field strength in a hyperbolic power law dependence $\tau = \alpha(E - E_t)^a + \tau_\infty$. The data points are best fitted for $\alpha = 0.10$ sec, $a = -1.47$, $E_t = 310$ V/mm and $\tau_\infty = 0$ sec (solid line in Figure 7-7).
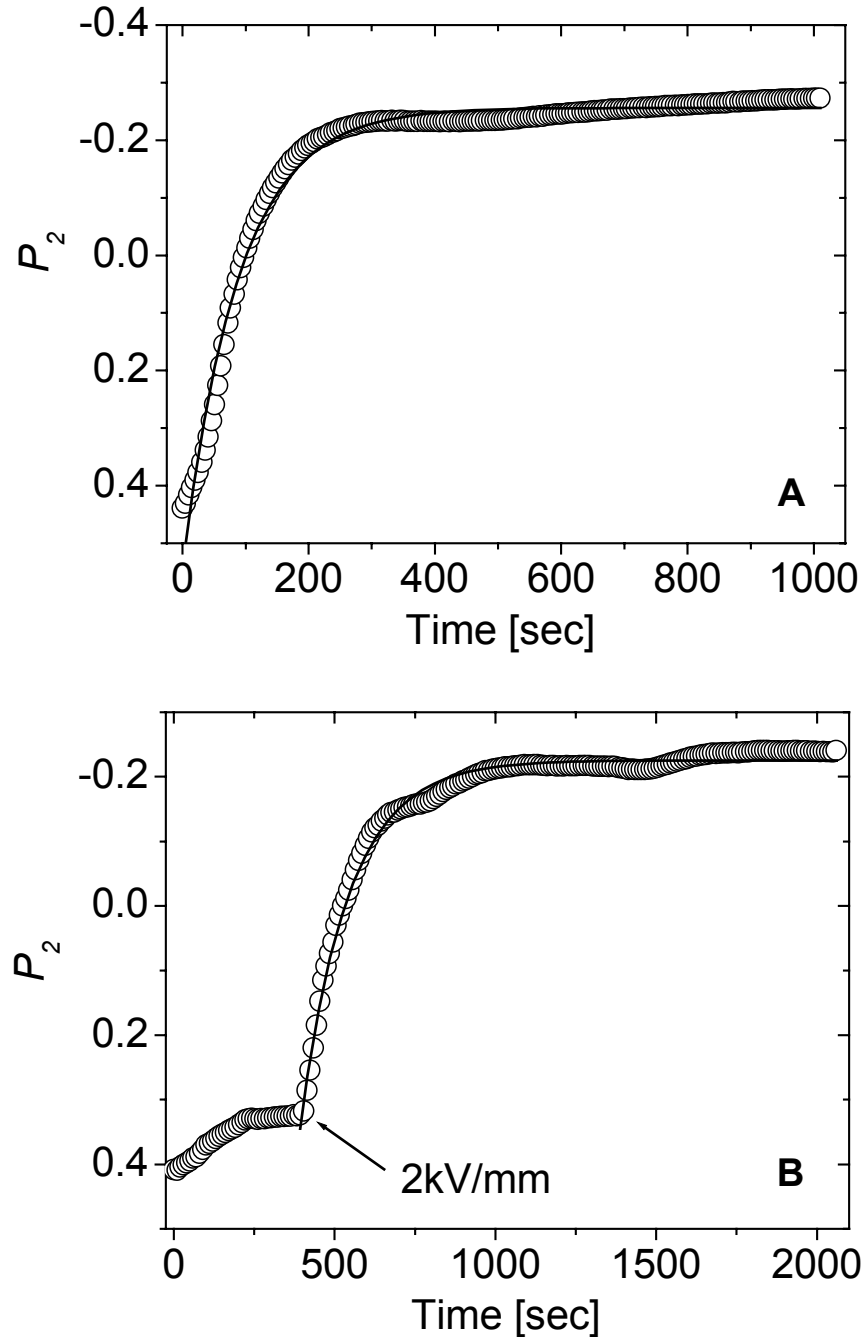

Figure 7-5:   Evolution of orientational order parameter P_2 with time (for orientation parallel to the electric field vector): (A) 40 wt.-% solution of $S_{47}H_{10}M_{43}^{82}$ in THF at 1 kV/mm, (B) 45 wt.-% solution of $S_{47}H_{10}M_{43}^{82}$ in THF at 1 kV/mm and 2 kV/mm. The solid lines represent least squares fits to the data according to Equation 6-3.
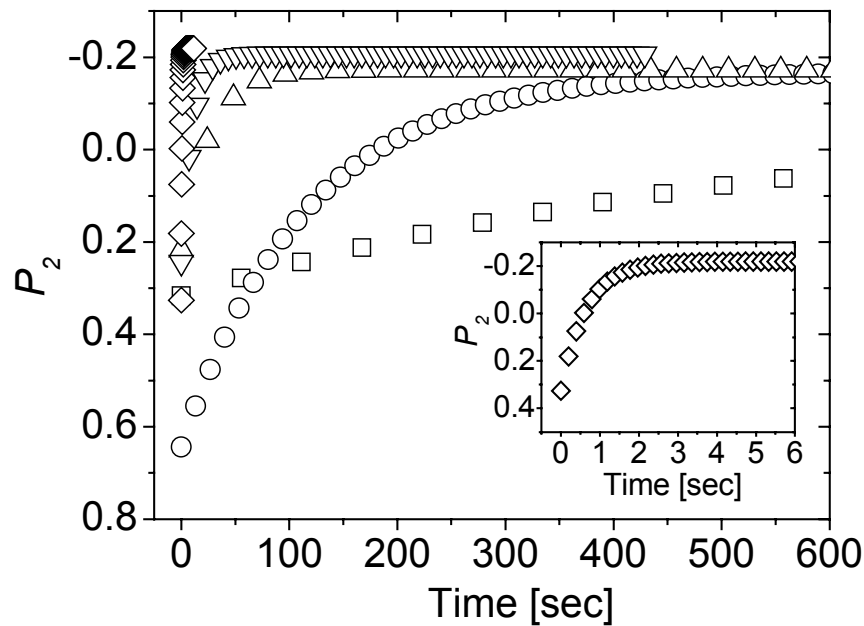
Figure 7-6:   Evolution of orientational order parameter P_2 with time for 40 wt.-% solutions at different field strengths   ($\Box$ = 375 V/mm, τ = 545 sec; $\bigcirc$ = 500 V/mm, τ = 116 sec; $\triangle$ = 1 kV/mm, τ = 18.7 sec; ∇ = 1.5 kV/mm, τ = 10.3 sec; $\Diamond$ = 3 kV/mm, τ = 0.64 sec). Electrode spacing: 2 mm.

Voltage[kV/mm]	τ [sec]	$P_{2,\infty}$	χ^2 [10^{-4}]
0.25	(a)	(a)	(a)
0.375	545	-0.08	5.0
0.5	116.2	-0.17	4.1
0.75	32	-0.16	5.5
1	18.7	-0.17	4.8
1.25	12.7	-0.20	2.5
1.5	10.3	-0.21	2.6
1.75	5.6	-0.21	3.2
2	2.9	-0.20	4.8
2.25	2	-0.21	3.9
2.5	1.3	-0.21	3.1
3	0.64	-0.22	2.9

Table 7-2:   Time constants τ of the reorientation behavior at different field strength obtained from least squares fits using Equation 6-3. (w_p = 40 wt.-%, 2 mm electrode distance). (a) no electric field induced reorientation observed.

In addition to the 40 wt.-% solution, a 45 wt.-% solution was measured at 1, 2, and 3 kV/mm. Due to the higher solution viscosity, the system exhibits a much slower kinetic behavior. In addition, an increase in field strength from 2 to 3kV/mm does not lead to a

141

significant change in the time constant τ as shown in Table 7-1. Here, we may assume that the rate of reorientation in such a high viscosity solution is already significantly limited by chain diffusion.
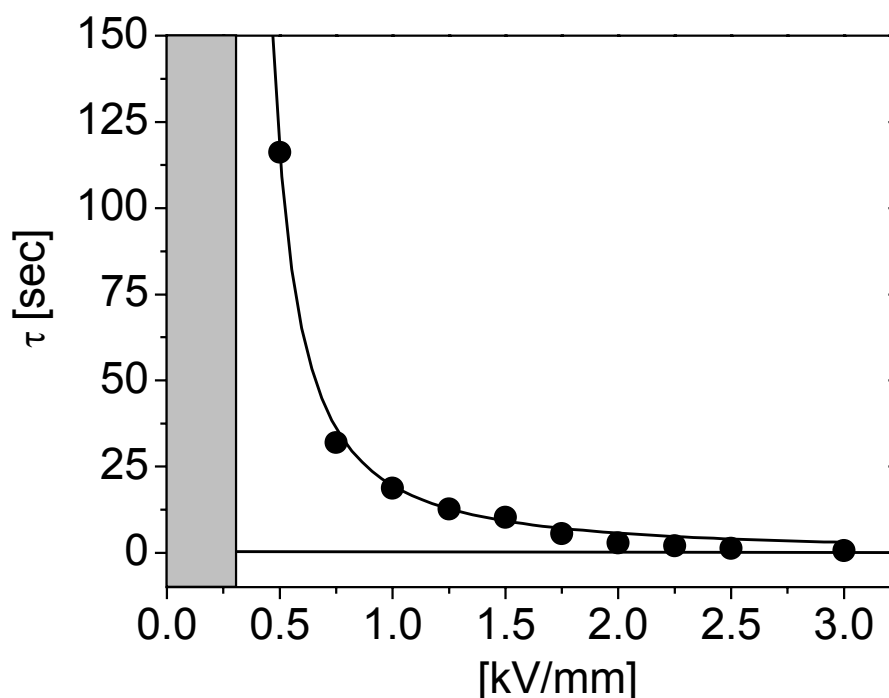

Figure 7-7:   *Electric Field dependence of time constant τ for 40 wt.-% solutions. The solid line represents a least squares fit of the power law $\tau = \alpha(E - E_t)^a + \tau_\infty$ to the data points yielding $\alpha = 0.10$ sec $a = -1.47$, $E_t = 310$ V/mm and $\tau_\infty = 0$ sec.*

7.3.3.3.   Kinetic Behavior of PS-*b*-PMMA Diblock Copolymer

Similar experiments were conducted on solutions of the $S_{49}M_{51}^{100}$ diblock copolymer. Although the total molecular weight of this polymer is slightly larger than for the $S_{47}H_{10}M_{43}^{82}$ triblock copolymer, the absence of the PHEMA middle block leads to an increased compatibility and thereby to a higher order-disorder concentration. The w_{ODT} was localized between 50 and 60 wt.-%. Therefore the viscosity of the microphase-separated solutions is significantly higher in the diblock copolymer case as compared to the triblock system. Indeed, above w_{ODT} no reorientation of the microdomains could be realized even at electric field strength as high as 5 kV/mm. As shown in Figure 7-8, a 50 wt.-% solution which, in the absence of the electric field, only exhibited scattering due to composition fluctuations found commonly in the disordered state (correlation hole), could be deformed parallel to the electric field vector at 5 kV/mm. It appears that above w_{ODT} the force implied on the lamellae by the electric field in not sufficient to lead to reorientation[1]. We note that the introduction of even a short block of the high dielectric constant material PHEMA ($\varepsilon_{PHEMA} = 8.9$)[6], both enhances

phase separation and increases the effective dielectric contrast sufficiently to enable electric field induced microdomain alignment in solution.
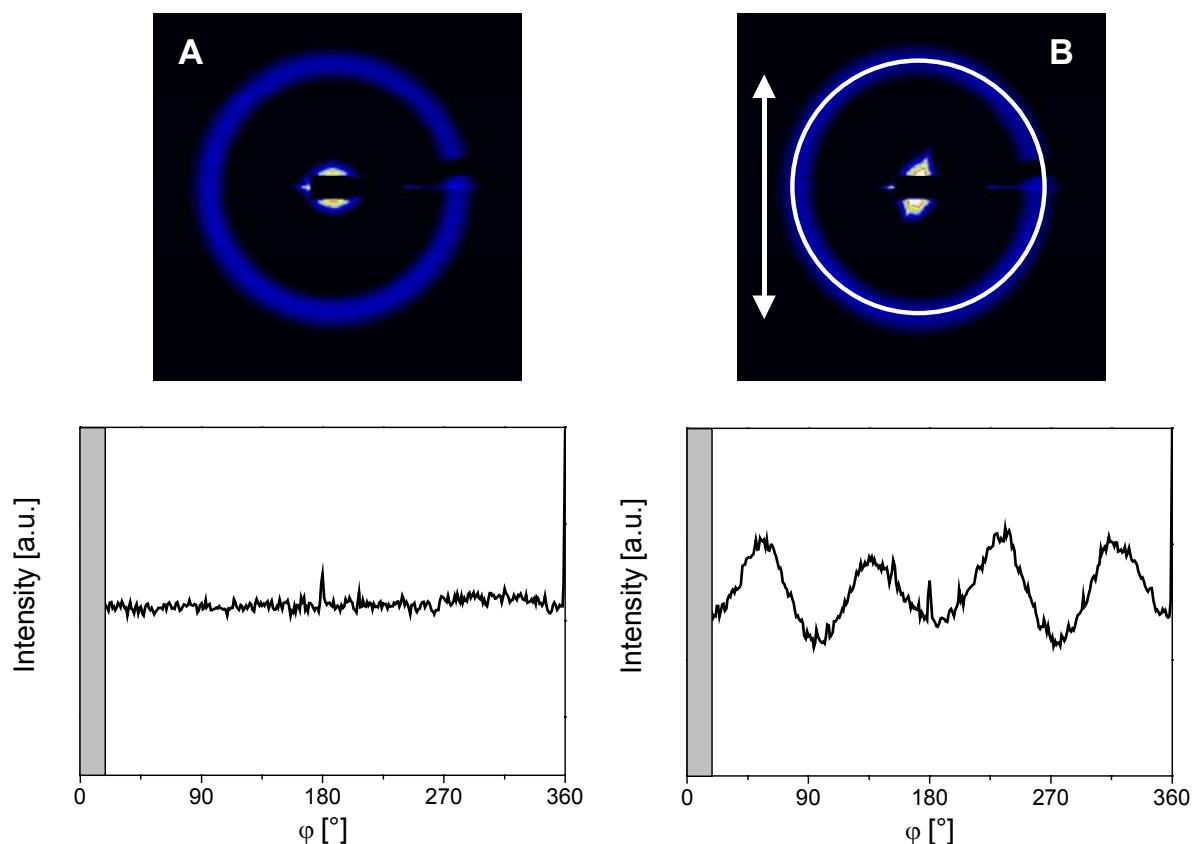

Figure 7-8:   *2D SAXS patterns and respective azimuthal angular dependence of scattering intensity of a 50 wt.-% solution of $S_{49}M_{51}^{100}$ in THF. (A) Before and (B) after application of an electric field of strength E = 5 kV/mm.*

7.4.   Discussion

7.4.1.   Structure Formation in Solution

We start our discussion with the observed behavior of the triblock copolymer solutions in the absence of the electric field. As briefly indicated above, we locate the order-disorder transition (ODT) at room temperature at a polymer concentration between 37.5 and 40 wt.-%. This assignment is based on various experimental observations. Most convincingly, we note the absence of birefringence below $w_p = 40$ wt.-%. It has been shown both experimentally and theoretically that microphase-separated (ordered) block copolymer materials consisting of randomly oriented lamellae are birefringent[7,8,9]. We therefore take the absence of birefringence as an indication that no microphase separation has occurred yet. From the SAXS experiments, we find an increase in scattering intensity above $w_p = 37.5$ wt.-%, accompanied by a sharpening of the first order Bragg peak and the evolution of higher orders

143

Bragg peaks with increasing concentration. Additional evidence is given by the fact that only starting from 40 wt.-% we observe an anisotropic scattering pattern in the absence of the electric field, which indicates some microdomain alignment induced either by shear (during filling of the sample chamber) or by preferential attraction of one block to the electrode surface. We note that the broad peak in the scattering profile at and below 37.5 wt.-% is due to correlation hole scattering.

The lamellar spacing, d, increases with increasing polymer concentration, indicating an increasing segregation power (or repulsive interactions) between the PS and PHEMA/PMMA chains as the polymer concentration increases. The dependence of d on polymer concentration can be described by a scaling relation $d \sim \phi_P^{0.5}$. Based on calculations by Noolandi and Hong[10] a $d \sim \phi_P^{1/6}$ relationship was predicted for the strong segregation limit in block copolymer solutions[11]. Shibayama *et al.*[12] found a $d \sim \phi_P^{1/3}$ dependence for PS-*b*-PI in toluene in the strong segregation limit. Leibler and Frederickson predicted a $d \sim \phi_P^{-0.12}$ behavior for the weak segregation limit in block copolymer solutions[13]. From these predictions, we may conclude that the positive exponent found in our experiments indicates that our system falls into the strong rather than into the weak segregation limit.

7.4.2.   Mechanism of Domain Alignment

Synchrotron-SAXS is an excellent tool to microscopically investigate the reorientation process as it combines the advantages of birefringence (high time resolution) with the detailed and straightforward information about the microscopic order characteristic of scattering methods.

The change in the azimuthal angular dependence of the scattering pattern as shown in Figure 7-4A-C, i.e. increase of scattering signals parallel to the electric field vector ($\varphi = 90°/270$) and simultaneous decrease of the peaks parallel to the electrodes ($\varphi = 0°/360°$) reveals the prevailing mechanism characteristic for all processes described here. This behavior matches the description of the migration of grain boundaries, as described earlier for electric field- and shear-induced orientation of lamellae[5,14]. In this case one lamella grows at the expense of another one with a significantly different orientation by motion of a tilt boundary (wall defect) between them, leading to a direct transfer of scattering intensity between widely separated azimuthal angles φ.

Additionally, the small component exhibiting a shift towards the final position at $\varphi = 90°$ and 270° indicates the rotation of entire grains. Details of this mechanism have already been identified and described for similar experiments on highly concentrated lamellar PS-*b*-PI

solutions in toluene[5]. Both mechanisms coexist in all our experiments, but within the rather narrow concentration window accessible in our experiment (w_p = 40……45 wt.-%), grain boundary migration appears to be the dominating microscopic process.

7.4.3.   Kinetics of Microphase Orientation

For the effective preparation of highly anisotropic *melt* block copolymer samples by virtue of an external electric field, it is important to find an optimum set of parameters (e.g. degree of swelling of the block copolymer domains, electric field strength and temperature), which combines a maximum chain mobility (i.e. fast kinetics) with the highest possible polymer concentration. In short, the reorientation process should be faster than the rate of solvent evaporation during preparation of bulk samples from solution, i.e. it should be completed before the bulk structure "freezes".

7.4.3.1.   Concentration Dependence

When increasing the polymer concentration from 40 to 45 wt.-% the time constant, τ, increases significantly as can be seen in Figure 7-5 and Table 7-1. This can be attributed to an increase in viscosity of the respective system. For a sufficiently high electric field strength the viscosity only influences the kinetics but not the final degree of order ($P_{2,\infty}$), which is consistent with previous dielectric relaxation spectroscopy measurements on the realignment of a side-chain liquid crystalline polymer in its liquid-crystalline state induced by a DC electric field[15].

For w_p = 45 wt.-% we find a time constant of around 150 sec with the overall process being finished within 10 minutes at field strengths of 2-3 kV/mm. As has been described earlier, even this process should be faster than the rate of solvent evaporation, so that all concentrations up to 45 wt.-% could be used for bulk sample preparation.

Using a home-built capacitor which allows application of an electric DC field during film formation by solvent casting[1], we demonstrate the feasibility of such a process. Figure 7-9 shows SAXS data of a melt sample prepared from a 40 wt.-% solution dried in the presence of an electric field of 2 kV/mm. From the azimuthal angular dependence of the scattering intensity at the first order reflexion, we calculate P_2 = -0.4.
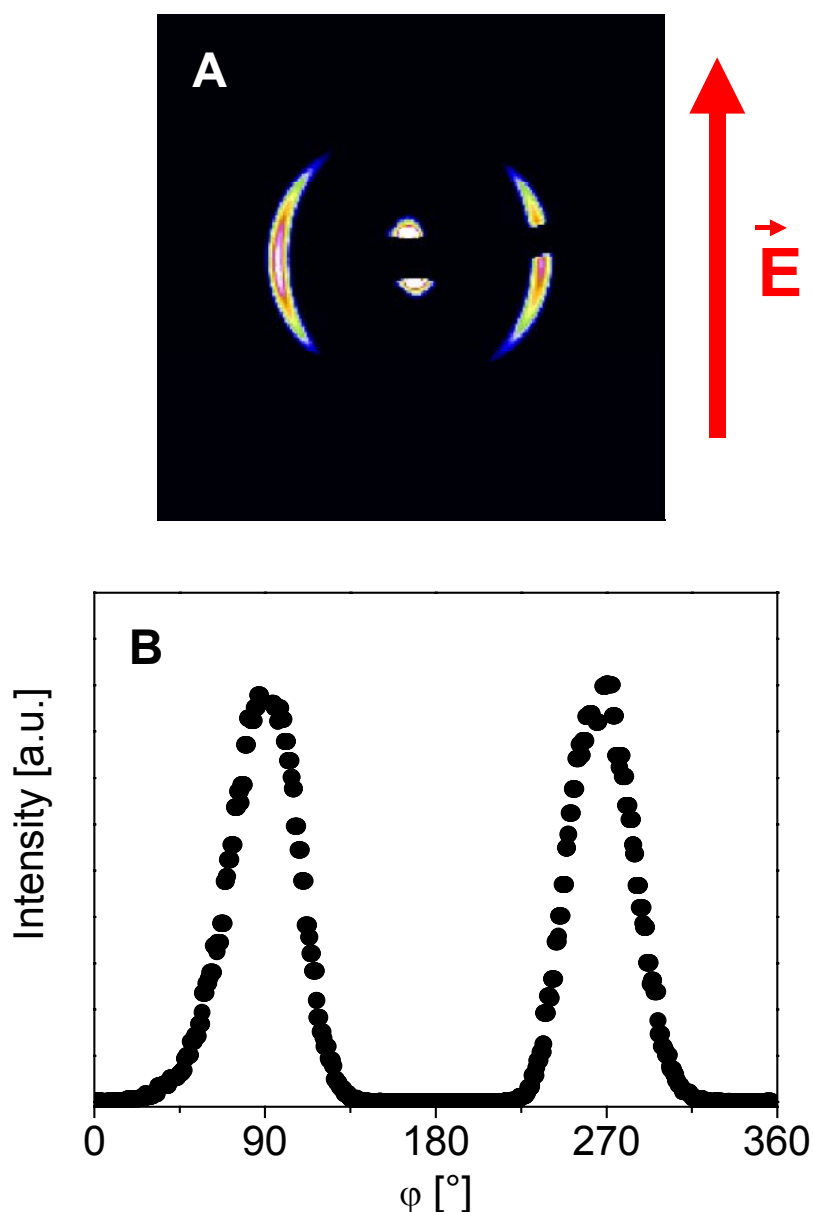
Figure 7-9:   *SAXS data of a SHM bulk sample prepared from a 40 wt.-% solution dried under an applied electric field of 1 kV/mm. (A) 2D-SAXS pattern and (B) azimuthal intensity distribution at first-order reflection (P_2 = -0.4).[1]*

As has already been described in chapter 6 for the PS-*b*-PI block copolymer in toluene solution, we only reach for the PS-*b*-PHEMA-*b*-PMMA dissolved in THF degrees of orientation described by P_2 values of around -0.25 for the block copolymer solutions and -0.4 for the respective melt sample. In principle, we assume the same reasons which have already been considered in chapter 6 to apply to the SHM system. Mainly, pinning of wall defects by disclination lines and the reduction of the electric driving force as the lamellae approach the final orientation parallel to the electric field vector, prevent the system from reaching a better degree of orientation on the time scale of the experiment at the given intermediate field strengths. In addition, we can not exclude electrohydrodynamic destabilization of the lamellar

pattern induced by nanomolar amounts of lithium salts from the synthesis of the block copolymer (even though we do not detect any leakage current in the late stages of the experiments). Such charges might cause convective vortices between the electrodes leading to an isotropisation of the lamellar orientations. Similar processes are well known for nematic liquid crystals[16].

7.4.3.2.   Electric Field Dependence

We assume that the 45 wt.-% sample shows a lower limit in the time constant due to a viscosity-induced chain diffusion limit at increasing field strength, we investigated the 40 wt.-% solutions of the $S_{47}H_{10}M_{43}{}^{82}$ block copolymer. The dependence of the time constant on the field strengths exhibits a hyperbolic power law $\tau = \alpha(E - E_t)^a + \tau_\infty$. The asymptotic behavior at high electric field strength (i.e. for a large force acting on the lamellae) indicates $\tau_\infty = 0$ sec for infinite field strength. This is expected in the absence of any electrorheological effects and limits in single chain diffusion, as the dominating process at $w_p = 40$ wt.-% is the migration of grain boundaries. The asymptotic behavior at low field indicates a threshold field strength, $E_t = 310$ V/mm. This is in agreement with the experimental observation that at lower field strengths no effect of the electric field on the scattering pattern was observed.

This threshold value can be explained by a competition between the electric field and the surface field generated by the gold electrodes. The latter exhibits a rather wide range, as has already been found by Anastasiadis *et al.* for PS-*b*-PMMA block copolymer films without an external field[4]. In a recent theoretical work, Tsori and Andelman[17] have described the different threshold fields expected for a strongly phase separated system. As we always find some 10 lamellar layers parallel to the polymer-electrode interface with a transition to lamellae perpendicular to the electrodes as reported earlier[1], we conclude that our system exhibits a mixed orientation as considered by Tsori and Andelman. In this state, the system has to compensate a positive energy penalty associated with the formation of T-junctions for the transition from lamellae parallel to perpendicular to the boundary surfaces, which mainly depends on the dielectric contrast of the block copolymer system and the sample thickness. This penalty has to be balanced by the electric field. Therefore, in accordance with Tsori and Andelman, we can define the threshold field strength as the voltage needed to overcome this energetic barrier. Thus, a sufficient gain in energy is required, which can be derived from the overall size of the domains (given by the sample thickness) to be aligned parallel to the electric field vector and the dielectric contrast in the system.

Further experiments will be dealing with the influence of the sample thickness, the magnitude of the surface fields and dielectric contrast of the block copolymer system on the threshold field strength[5]. We note that, in contrast to investigations by Thurn-Albrecht et al.[18], the threshold field identified in our study yields the electric field strength required for a transition from lamellae parallel to the electrodes to a mixed morphology with a parallel and predominantly perpendicular lamellar orientation. The threshold field determined by Thurn-Albrecht et al. is the one required for a second transition from a mixed to a fully perpendicular alignment.

In contrast, to investigations by Amundson et al.[19] a double logarithmic plot of $1/\tau$ versus E yields a slope of 2.8 ± 0.2 for our data, i.e. $1/\tau \sim E^{2.8 \pm 0.2}$, which significantly differs from the expected E^2 dependence (see Equation 1-17). We do agree with their assumption that the stronger dependence could indicate an activated process, such as nucleation of new defect structures, e.g. wall defects, which in turn would accelerate the orientation process by increasing the active centers for alignment in the sample, rearranging by migration of grain boundaries as this is the governing mechanism for all samples used in this series.

7.4.4.   Comparison of the Diblock ($S_{49}M_{51}{}^{100}$) and the Triblock ($S_{47}H_{10}M_{43}{}^{82}$) System

In the following we will consider electrostatic and thermodynamic arguments explaining the advantages associated with the introduction of a PHEMA middle block with a high dielectric constant in a PS-b-PMMA diblock polymer.

We aim to estimate the electrostatic energy difference between the different microdomain orientations. As the SAXS measurements in Figure 7-1 indicate that the PHEMA and PMMA blocks form a mixed phase, we will treat the $S_{47}H_{10}M_{43}{}^{82}$ copolymer as an AB diblock copolymer with the following composition: A: 47 wt.-% PS ($\varepsilon_A = 2.4$) and B: 53 wt.-% methacrylic blocks ($\varepsilon_B = 0.81\,\varepsilon_{PMMA} + 0.19\,\varepsilon_{PHEMA} = 4.6$; with $\varepsilon_{PMMA} = 3.6$ and $\varepsilon_{PHEMA} = 8.9$). The resulting dielectric contrast amounts to $\Delta\varepsilon = 2.2$. The $S_{49}M_{51}{}^{100}$ diblock copolymer on the other hand is calculated with 49 wt.-% PS ($\varepsilon_A = 2.4$) and 51 wt.-% PMMA ($\varepsilon_{PMMA} = 3.6$) leading to a dielectric contrast of only $\Delta\varepsilon = 1.2$. As THF ($\varepsilon_{THF} \approx 7.8$) and chloroform ($\varepsilon_{CHCl_3} \approx 4.8$) are fairly non-selective solvents for the two main components, PS and PMMA, we expect a similar swelling behavior leading merely to a dilution effect with respect to the dielectric constants of each block. Therefore, with increasing solvent content in the films, the

difference of the dielectric constants is reduced to $\Delta\varepsilon_{eff} = w_p \, \Delta\varepsilon$ and the thermodynamic driving force for an alignment of the lamellae parallel to the field is expected to decrease accordingly.
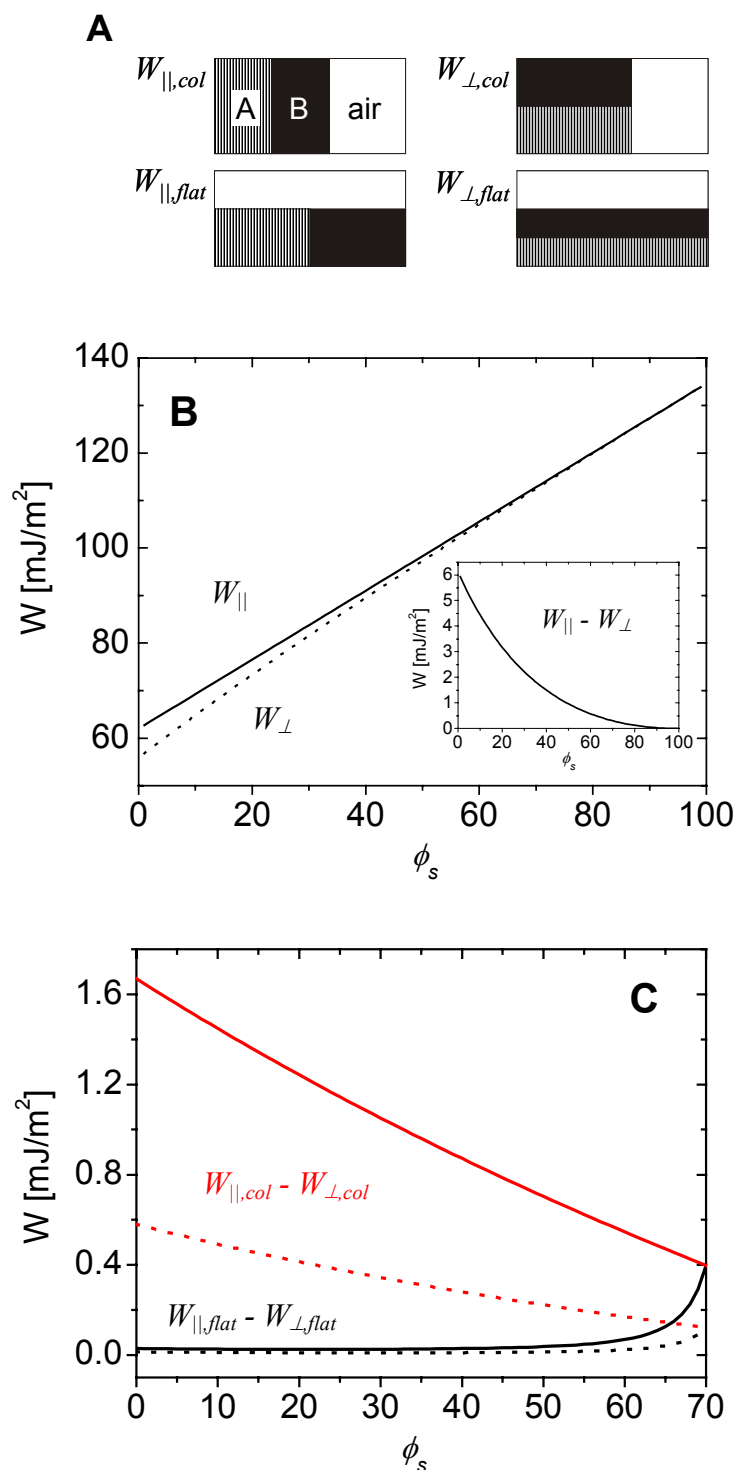

Figure 7-10: (A) Four basic geometries of lamellar orientation. Calculated differences in energy stored in the capacitor between lamellar alignment parallel and perpendicular to the electric field vector in dependence of solvent volume fraction; (B) SHM solution in THF in closed capacitor, (C) open capacitor which allows for solvent evaporation with SHM (——) and with SM block copolymer (....) in CHCl₃.

In order to estimate the driving forces for domain alignment as a function of the volume fraction of solvent, ϕ_s, we calculate the electric energy per unit area, W, which is stored in a capacitor for the different situations sketched in Figure 7-10A. The details of the model calculation are given elsewhere[1]. Furthermore, we distinguish between an open capacitor (solvent: $CHCl_3$) which allows for solvent evaporation (layer of air in the system) and a closed system (solvent: THF) as used for the in-situ SAXS studies.

Film formation in the open capacitor under the influence of an external electric field may result in significant thickness undulations which eventually lead to the formation of column-like protrusions that connect both electrodes. Recently, Schäffer et al. showed that electric fields can induce electrohydrodynamic instabilities in a liquid polymer film leading to the formation of polymer columns quite similar to the ones observed here[20,21]. Aside from the columns, we find areas with film thicknesses ranging between 0.2 and 0.7 mm. All these parts show a significant alignment of the lamellae parallel to the electric field. The most pronounced anisotropy, however, is found within the columnar protrusions[1].

Therefore, for our calculations, we have chosen four basic geometries to describe the system, corresponding to a perpendicular ($W_{\perp,col}$, $W_{\perp,flat}$) and parallel ($W_{\parallel,col}$, $W_{\parallel,flat}$) alignment of the microdomains with respect to the electric field and to a formation of columns ($W_{\perp,col}$, $W_{\parallel,col}$) and a flat film ($W_{\perp,flat}$, $W_{\parallel,flat}$) in the open capacitor, respectively. In the case of the closed capacitor, the two perpendicular ($W_{\perp,col}$, $W_{\perp,flat} = W_\perp$) and two parallel ($W_{\parallel,col}$, $W_{\parallel,flat} = W_\parallel$) cases are equivalent.

We calculate the energy, W, stored within the electric field of the capacitor as

$$W = \frac{1}{2} \int \vec{E} \cdot \vec{D} dV$$

with $\vec{E}$ being the electric field and $\vec{D}$ the displacement field.

In contrast to the dielectric displacement, $\vec{D}$, the electric field, $\vec{E}$, along the z-direction of the capacitor is not uniform for the models, which incorporate a layered structure ($W_{\perp,flat}$ and $W_{\perp,col}$). This is due to the fact that the component of the electric field perpendicular to the interface between two materials is not continuous, but the one of the displacement field is: $\vec{D}_{\perp 1} = \vec{D}_{\perp 2}$ but $\vec{E}_{\perp 1} \neq \vec{E}_{\perp 2}$. Additionally, $\vec{E}_i = \vec{D}_i/\varepsilon_i$ and the applied voltage $V = \int \vec{E} dz$, which means that as soon as air is present as a layer in the capacitor with the applied voltage V, the electric field in both polymer layers is reduced.

Figure 7-10B shows the energy per unit area stored inside a closed capacitor filled with different solutions of our model AB block copolymer in THF with $\varepsilon_A = 2.4$ and $\varepsilon_B = 4.6$ (resembling $S_{47}H_{10}M_{43}{}^{82}$) as a function of THF volume fraction ($\varepsilon_{THF} = 7.8$) at a field

strength of 2 kV/mm. The inset depicts the difference in energy between the orientations parallel and perpendicular to the electric field vector. Compared to an open capacitor the system stores at least 2 times more energy at given solvent concentration[1].

Figure 7-10C shows the energy per unit area stored inside a capacitor filled with 15 vol.-% polymer A ($\varepsilon_A = 2.4$) and 15 vol.-% polymer B ($\varepsilon_B = 4.6$ with PHEMA and $\varepsilon_B = 3.6$ without PHEMA) as a function of $CHCl_3$ volume fraction ($\varepsilon_{CHCl_3} = 4.8$), corresponding to the four basic geometries, at a field strength of 2 kV/mm. Curves $W_{\perp,col}$ and $W_{\perp,flat}$ as well as curves $W_{||,col}$ and $W_{||,flat}$ converge at a solvent volume fraction of 70 vol.-% (which is the starting concentration of our experiment), because at this point the capacitor is completely filled and the respective geometries are equivalent. Besides the fact that for the SHM as well as the SM system the difference in energy between the two orientations in column ($W_{\perp,col}$, $W_{||,col}$) is larger than for flat films ($W_{\perp,flat}$, $W_{||,flat}$), the energetic difference is more than 3 times higher for the SHM than for the SM system.

When we compare the two situations described above, we find that: (i) the closed system stores more energy per unit area, and (ii) the difference in energy between the two orientations is always higher in the closed capacitor, especially for higher concentrations. Therefore, from our experimental findings, we may conclude that, if the electric field induced orientation of a block copolymer does not work in the closed capacitor, it will neither function in the open system, as the energetic difference is always larger for the closed capacitor set-up. This is even more appropriate as the higher dielectric constant solvent THF was used for the calculation of the closed capacitor, which reduces the dielectric contrast of the blocks even more than the lower dielectric constant solvent $CHCl_3$. Therefore, the incorporation of the high dielectric constant PHEMA middle block into the SM diblock copolymer is the key to creating a well-performing methacrylate-based block copolymer system for electric field induced alignment from *solution*.

Moreover, the PHEMA block enhances the microphase separation in the block copolymer solutions compared to the PS-*b*-PMMA system which only phase-separates at polymer concentrations above 60 wt.-%, while the PHEMA containing block copolymer already microphase separates at polymer concentrations between 37.5 and 40 wt.-%. Therefore, in the latter case, the viscosity of the phase-separated solution is considerably smaller, which promotes the ordering process induced by the small electric force. On the other hand, a lower polymer concentration also reduces the effective field strength and driving force in the capacitor as shown in Figure 7-10.

To this point, we can not decide definitely, if in this case enhanced phase separation or the

increased dielectric contrast between the block is more important for the electric field-induced ordering process to function. Further experiments to elucidate the influence of a high dielectric contrast in a block copolymer will be described in chapter 8.

7.5. Conclusion

Using Synchrotron-SAXS we have identified migration of grain boundaries as the governing mechanism of the electric field induced microdomain alignment of a PS-*b*-PHEMA-*b*-PMMA block copolymer in solution. In addition, the time-resolved SAXS measurements allowed us to study the kinetic behavior of the PS-*b*-PHEMA-*b*-PMMA system compared to the PS-*b*-PMMA diblock copolymer. The interplay of enhanced phase separation and contribution to a high dielectric contrast between the phases by the incorporation of the PHEMA block results in a functioning electric field driven ordering process. Furthermore, we have identified a rather small concentration window between 40 and 45 wt.-% in which microdomain ordering by electric fields can be effectively realized. The variation of the electric field strength revealed a threshold value, below which no electric field induced orientation can be achieved. In summary, the maximum final orientation reached in solution could be described by order parameters of up to $P_2 = -0.27$. The time constants of the fastest processes were in the range of $\tau = 0.6$ sec. Finally, after complete solvent evaporation, bulk samples exhibited order parameters of up to $P_2 = -0.4$.

We have demonstrated that electric field alignment of block copolymer domains from solution provides a useful tool to generate anisotropic bulk block copolymer samples by controlling a large variety of parameters like block copolymer composition, polymer concentration, and electric field strength.

References

[1] Böker, A.; Knoll, A.; Elbs, H.; Abetz, V.; Müller, A.H.E.; Krausch, G. *Macromolecules* **2002**, *35*, 1319.

[2] Thurn-Albrecht, T.; Schotter, J.; Kastle, G.A.; Emley, N.; Shibauchi, T.; Krusin-Elbaum, L.; Guarini, K.; Black, C.T.; Tuominen, M.T.; Russell, T.P. *Science* **2000**, *290*, 2126.

[3] Böker, A.; Müller, A.H.E.; Krausch, G. *Macromolecules* **2001**, *34*, 7477.

[4] Anastasiadis, S.H.; Russell, T.P.; Satija, S.K.; Majkrzak, C.F. *Phys. Rev. Lett.* **1989**, *62*, 1852.

[5] Böker, A.; Elbs, H.; Hänsel, H.; Knoll, A.; Ludwigs, S.; Zettl, H.; Urban, V.; Abetz, V.; Müller, A.H.E.; Krausch, G. in preparation.

[6] Yamaguchi, R.; Sato, S.; *Jpn. J. Appl. Phys.* **1994**, *33*, 4007.

[7] Amundson, K.; Helfand, E.; Patel, S.S.; Quan, X.; Smith, S.D. *Macromolecules* **1992**, *25*, 1953.

[8] Balsara, N.P.; Perahia, D.; Safinya, C.R.; Tirrell, M.; Lodge, T.P. *Macromolecules* **1992**, *25*, 3896.

[9] Balsara, N.P.; Hammouda, B.; Kesani, P.K.; Jonnalagadda, S.V.; Straty, G.C. *Macromolecules* **1994**, *27*, 2566.

[10] Hong, K.M.; Noolandi, J. *Macromolecules* **1981**, *14*, 736.

[11] Balsara, N.P.; Eastman, C.E.; Foster, M.D.; Lodge, T.P.; Tirrell, M. *Makromol. Chem., Makromol. Symp.* **1991**, *45*, 213.

[12] Shibayama, M.; Hashimoto, T.; Hasegawa, H.; Kawai, H. *Macromolecules* **1983**, *16*, 1427.

[13] Frederickson, G.H.; Leibler, L. *Macromolecules* **1989**, *22*, 1238.

[14] Polis, D.L.; Smith, S.D.; Terrill, N.J.; Ryan, A.J.; Morse, D.C.; Winey, K.I. *Macromolecules* **1999**, *32*, 4668.

[15] Kozak, A.; Simon, G.P.; Moscicki, J.K.; Williams, G. *Mol. Cryst. Liq. Cryst.* **1990**, *193*, 155.

[16] Kramer, L.; Pesch, W., in "*Pattern Formation in Liquid Crystals*", A. Buka, L. Kramer, ed., Springer-Verlag, New York, **1995**.

[17] Tsori, Y.; Andelman, D. *Macromolecules* **2002**, *35*, 5161.

[18] Thurn-Albrecht, T.; DeRouchey, J.; Russell, T.P.; Jaeger, H.M.; *Macromolecules* **2000**, *33*, 3250.

[19] Amundson, K.; Helfand, E.; Davis, D.D.; Quan, X.; Patel, S.S.; Smith, S.D.; *Macromolecules* **1991**, *24*, 6546.

[20] Schäffer, E.; Thurn-Albrecht, T.; Russell, T.P.; Steiner, U.; *Nature* **2000**, *403*, 874.

[21] Lin, Z.; Kerle, T.; Baker, S.M.; Hoagland, D.A.; Schäffer, E.; Steiner, U.; Russell, T.P.;
J. Chem. Phys. **2001**, *14*, 2377.

Chapter 8

Electric Field Induced Alignment of High Molecular Weight AB and ABC Block Copolymers with High Dielectric Contrast

Abstract

We investigate the microdomain orientation kinetics of concentrated block copolymer solutions exposed to a DC electric field by time-resolved synchrotron small-angle X-ray scattering (SAXS). The feasibility of the electric field-induced ordering process is demonstrated for polystyrene-*b*-poly(2-vinyl pyridine), polystyrene-*b*-poly(*tert*-butyl methacrylate) and polystyrene-*b*-poly(2-vinyl pyridine)-*b*-poly(*tert*-butyl methacrylate) block copolymers dissolved in tetrahydrofuran. The orientation kinetics follow a single exponential time behavior with characteristic time constants varying from a few seconds to some minutes depending on polymer concentration, electric field strength and block copolymer architecture. Moreover, we systematically compare the above described block copolymers to polystyrene-*b*-polyisoprene and polystyrene-*b*-poly(methyl methacrylate)-based systems with respect to their microstructure, dielectric contrast and the surface tension, i.e. interaction with the electrode surfaces.

8.1.   Introduction

In the previous chapters we have discussed the influence of block copolymer composition and solution properties on the electric field-induced alignment of lamellar microdomains from solution. In the following chapter we will extend these investigations to block copolymers with a higher dielectric contrast, e.g. polystyrene-*b*-poly(2-vinyl pyridine) ($\varepsilon_{PS} = 2.4$, $\varepsilon_{P2VP} = 7.5$), higher molecular weight and more complex microstructures. Thus aiming towards demonstrating the wide range of applicability of the process of electric field alignment of microstructures from concentrated solutions.

8.2.   Experimental Section

8.2.1.   Synthesis

Polystyrene-*b*-poly(2-vinyl pyridine), polystyrene-*b*-poly(*tert*-butyl methacrylate), and polystyrene-*b*-poly(2-vinyl pyridine)-*b*-poly(*tert*-butyl methacrylate) block copolymers were synthesized by sequential living anionic polymerization as described in detail elsewhere[1,2]. The polymers used in this study have the following compositions: $S_{50}V_{50}^{78}$, $S_{50}T_{50}^{100}$, $S_{27}V_{35}T_{38}^{84}$ and $S_{16}V_{21}T_{63}^{138}$. (The subscripts denote the weight fractions of the respective blocks and the superscript gives the number-average molecular weight in kg/mol). Gel permeation chromatography (GPC) of the final block copolymers yielded polydispersities, M_w/M_n, of 1.05, 1.03, 1.04, and 1.03, respectively. The block ratios and overall molecular weights were determined by ^{1}H-NMR using the integrated aromatic signals of the polystyrene block in combination with the GPC results of the corresponding polystyrene precursor. Structural analysis of the bulk structures reveals that all systems except $S_{16}V_{21}T_{63}^{138}$ exhibit a lamellar morphology. $S_{16}V_{21}T_{63}^{138}$ forms a hexagonal array of core-shell cylinders with a PS core surrounded by a P2VP shell embedded within a P*t*BMA matrix[2].

8.2.2.   Sample Preparation

Block copolymer solutions in THF with concentrations ranging from 30 to 50 wt.- % were used for the present study. The alignment experiments were performed in a home-built capacitor with gold electrodes (sample depth = 5 mm, electrode distance: $1 - 2$ mm) at room temperature. A DC voltage between 0.25 and 5 kV was applied resulting in a homogeneous electric field pointing perpendicular to the X-ray beam direction. Both the voltage at the

electrodes and the current were monitored during the course of the experiment indicating only a small leakage current (~ 0.01 mA) during the first few seconds after the field was applied.

8.3.   Results and Discussion

8.3.1.   Polystyrene-*b*-poly(2-vinyl pyridine) $S_{50}V_{50}^{78}$

8.3.1.1.   Concentration Dependence of the Microdomain Structure in Solution

We studied the evolution of structure of the $S_{50}V_{50}^{78}$ diblock copolymer in THF solution in the absence of the electric field as a function of polymer concentration, starting from $w_p = 30$ wt.-% and increasing w_p stepwise by 2.5 wt.-% up to 50 wt.-%.
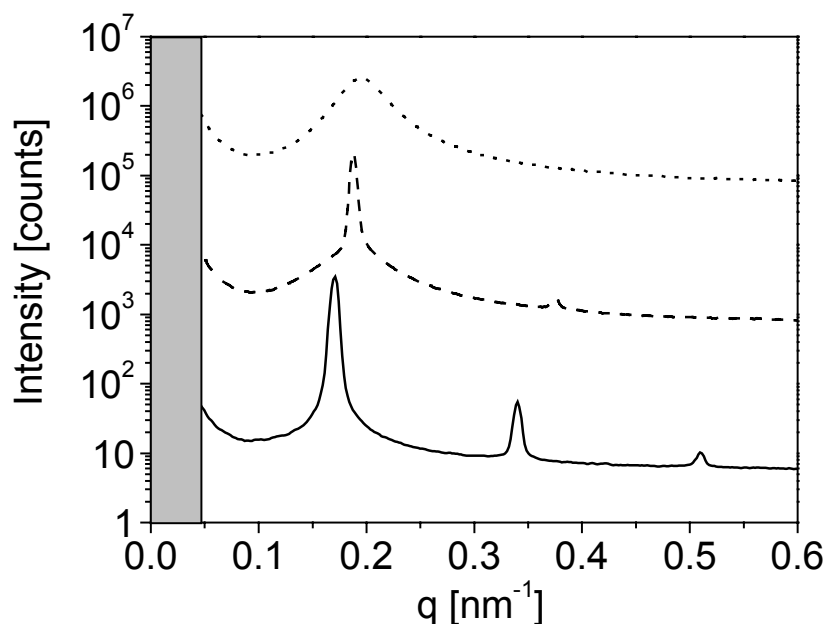
Figure 8-1:   *Scattering intensity profiles of $S_{50}V_{50}^{78}$ solutions in THF at various concentrations.*
35 wt.-% ($\cdots$), 37.5 wt.-% (--), 50 wt.-% (—).

As shown in Figure 8-1 we find the formation of a narrow first order reflection when increasing the concentration from 35 wt.-% to 37.5 wt.-%. Starting from 37.5 wt.-%, the block copolymer solutions become birefringent (not shown here) and we observe higher order scattering peaks which correspond to integer multiples of the first order signal. The latter indicates the formation of lamellar microdomains in the solution. In addition, as shown in Figure 8-2, we find a continuous increase of the lamellar spacing $d_{100} = 2\pi/q_{100}$ with

157

increasing polymer concentration, indicating an increasing segregation power (or repulsive interactions) between the PS and P2VP chains as the polymer concentration increases. We anticipate that at higher concentrations, the spacing gradually approaches the melt lamellar spacing of 43 nm. The dependence of the lamellar spacing d on the polymer volume fraction ϕ_p scales as $d \sim \phi_p^{0.21 \pm 0.02}$ for intermediate concentrations as can be seen from the double logarithmic plot in Figure 8-3. Similar to the systems described in chapter 6 and 7, we may conclude from the predictions made by Shibayama et al.[3] and Leibler and Frederickson[4] for block copolymer solutions in the strong and weak segregation limit, respectively, that the positive exponent found in our experiments indicates that the PS-*b*-P2VP chains in our solutions are strongly segregated.

From the experimental observations described above, we locate the order-disorder transition (ODT) at room temperature at a polymer concentration between 35 and 37.5 wt.-%. This assignment is further corroborated by the absence of birefringence at and below $w_p = 35$ wt.-%. It has been shown both experimentally and theoretically that phase-separated (ordered) block copolymer materials consisting of randomly oriented lamellae are birefringent[5,6,7]. Therefore, the lack of birefringence indicates the absence of randomly oriented lamellae. From the SAXS experiments, we find an increase in scattering intensity at and above $w_p = 37.5$ wt.-%, accompanied by a sharpening of the signal and the evolution of higher order Bragg peaks with increasing concentration (Figure 8-1). Additional evidence is given by the fact that only starting from 37.5 wt.-% we observe an anisotropic scattering pattern in the absence of the electric field, which indicates some microdomain alignment induced either by shear (during filling of the sample chamber) or by preferential attraction of one block to the electrode surface. We note that the broad peak in the scattering profile at and below 35 wt.-% is due to composition fluctuations found commonly in the disordered state (correlation hole).

8.3.1.2.   Reorientation Behavior

After filling the samples into the capacitor, all phase-separated solutions exhibit a distinctly anisotropic scattering pattern with maxima located at $\varphi = 0°$ and $180°$, respectively (Figure 8-4). This finding indicates an alignment of the lamellae parallel to the electrodes, which may be caused both by preferential interaction of the PS with the Au surfaces and by possible shear forces acting on the highly viscous solutions during filling of the capacitor with a syringe. In order to destroy any possible alignment induced by the preparation process, we heated the solutions above the order-disorder transition temperature. However, after cooling,

still some alignment of the domains parallel to the electrodes prevailed, indicating the importance of the surface effects[8].
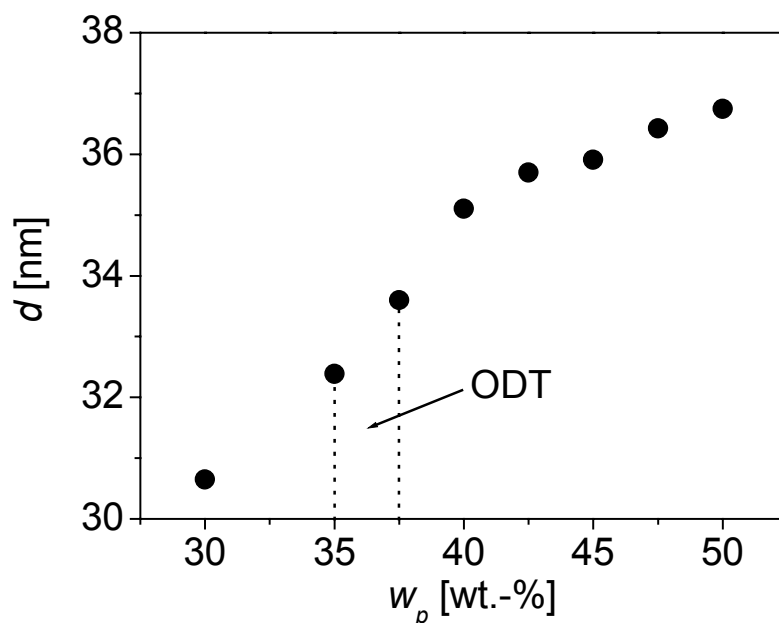

Figure 8-2:   *Concentration dependence of the lamellar spacing for $S_{50}V_{50}{}^{78}$ solutions in THF (d_{bulk} = 43 nm).*

As soon as the electric field is applied, the scattering pattern changes significantly. The peaks at $\varphi = 0°$ and $180°$ decrease and new scattering maxima at $\varphi = 90°$ and $270°$ grow with time (Figure 8-4). To quantify the kinetics of the orientation process, $P_2(t)$ was calculated from the 2D SAXS patterns as described above. Using a single exponential fit, we can determine the time constant τ of the reorientation process.

Concentration [wt.-%]	τ [sec]	$P_{2,\infty}$	χ^2 [10^{-4}]	η [Pa sec]
35	(a)	(a)	(a)	8
37.5	0.28	-0.15	2.0	66
40	0.84	-0.19	1.1	107
47.5	5.6	-0.27	1.3	258
50	6.4	-0.28	1.5	269

Table 8-1:   *Time constants τ of the reorientation behavior of $S_{50}V_{50}{}^{78}$ at different polymer concentrations obtained from least squares fits according to Equation 6-3 (E = 2 kV/mm, 1 mm electrode distance). (a) system not phase separated*

159

As a typical example for the high time resolution of the SAXS experiment, the time evolution of the orientational order parameter $P_2(t)$ is shown in Figure 8-5 for a 40 wt.-% solution of $S_{50}V_{50}^{78}$ in THF at 4 kV/2 mm. The least-squares fit to the data yields $P_{2,0} = 0.26$, $P_{2,\infty} = -0.22$, and $\tau = 0.86$ sec. The results of the least-squares fits for different concentrations and electric field strength are summarized in Tables 8-1 and 8-2, respectively.
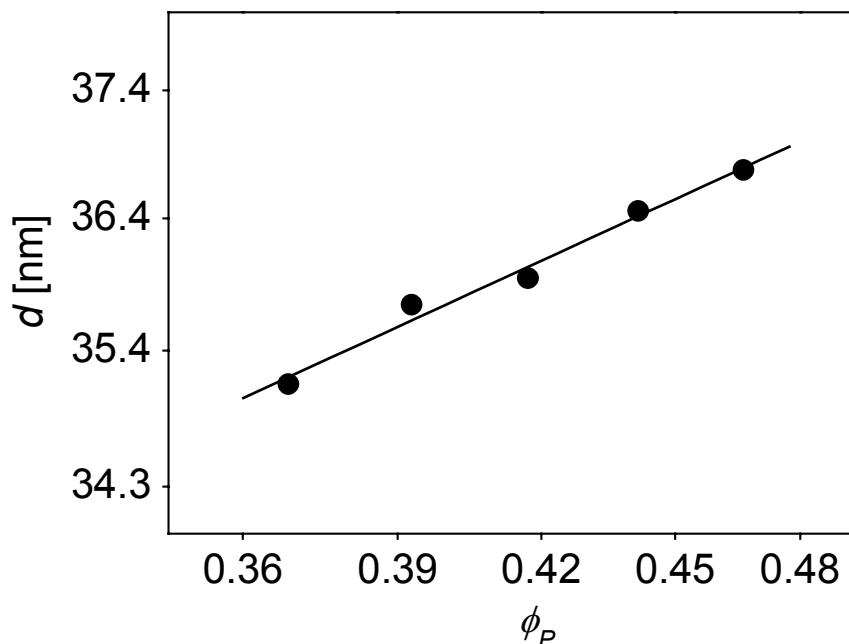
Figure 8-3:   *Double logarithmic plot of dependence of lamellar spacing on the volume fraction of polymer ϕ_P for intermediate concentrations of $S_{50}V_{50}^{78}$ in THF ($d \sim \phi_P^{0.21 \pm 0.02}$).*

Mechanism of Domain Alignment. The change in the azimuthal angular dependence of the scattering pattern as described above, reveals the prevailing mechanism characteristic for all processes described here. This behavior is expected for the migration of grain boundaries, as observed earlier for electric field- and shear-induced orientation of lamellae[10,9]. In this case one lamella grows at the expense of another with a significantly different orientation by motion of a tilt boundary (wall defect) between them, leading to a direct transfer of scattering intensity between widely separated azimuthal angles φ.

In detail, after complete destruction of the initial peaks at $\varphi = 0°$ and 180°, two small new signals are generated around $\varphi = 90°$ and 270° (Figure 8-4, signal after 5.6 sec), which eventually shift towards the final positions. After merging they grow with time. This observation indicates that aside from grain boundary migration a rotation of entire grains is involved in the orientation mechanism, too. Within the rather narrow concentration window where electric field induced reorientation can be achieved ($w_p = 37.5\ldots\ldots.50$ wt.-%), both

160

mechanisms coexist, but the overall process is dominated by the migration of grain boundaries.
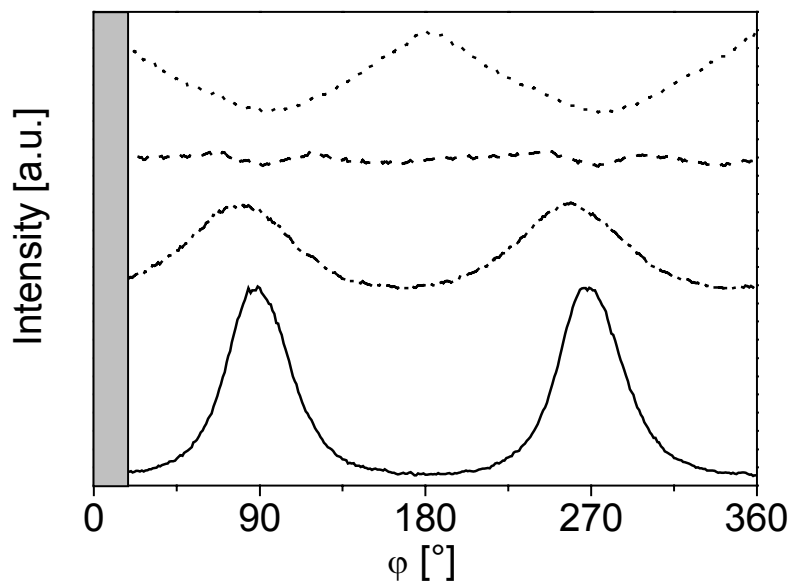
Figure 8-4:   *Azimuthal angular dependence of the scattering intensity for a 40 wt.-% $S_{50}V_{50}^{78}$ solution in THF exposed to an electric field of $E = 1$ kV/mm: 0 sec (·····), 5.6 sec (⁻⁻), 16.4 sec (⁻··⁻), 50.6 sec (⎯).*

8.3.1.3.   Kinetics of Microphase Orientation

Concentration Dependence. The kinetics of the alignment of the microdomains formed in the $S_{50}V_{50}^{78}$ block copolymer system was measured in a 1 mm capacitor at $E = 2$ kV/mm for a narrow concentration window from 37.5 wt.-% (where phase separation sets in) to 50 wt.-%. As anticipated from the increasing solution viscosities, the time constants, τ, increase with increasing polymer concentration. Nevertheless, they are still rather small and range from 0.28 sec for 37.5 wt.-% to 6.4 sec for 50 wt.-%. The results of the exponential fits according to Equation 6-3 are summarized in Table 8-1. The single exponential fit works quite well for all concentrations studied, as can be seen from the low χ^2 values.

We find that depending on the concentration, i.e. the degree of phase separation, the limiting value of the orientational order parameter $P_{2,\infty}$ shows a clear tendency to higher values, starting from $P_{2,\infty} = $ -0.15 low polymer concentrations and eventually reaching -0.28 at the highest polymer concentration studied. Obviously, in contrast to earlier investigations on polystyrene-*b*-poly(2-hydroxyethyl methacrylate)-*b*-poly(methyl methacrylate) (SHM) and polystyrene-*b*-polyisoprene (SI) block copolymers as described in chapters 6 and 7 [10], the polymer concentration not only influences the rate of orientation but also the final degree of alignment ($P_{2,\infty}$). In the following we will compare the SHM system already described in

chapter 7 with the SV system as the only parameter changed is the dielectric contrast of the block copolymers ($\varepsilon_{PS} = 2.4$, $\varepsilon_{PHEMA/PMMA} = 4.6$, $\varepsilon_{P2VP} = 7.5$). As shown in Tables 7-1 and 7-2, the SHM system exhibits maximum final degrees of alignment ranging from -0.22 to -0.27, which is very similar to the values obtained for the SV system. In this case, the higher dielectric contrast between the blocks does not seem to have an influence on the final degree of orientation. We may anticipate that similar factors as described in chapter 7, i.e. pinning of wall defects and electrohydrodynamic destabilization of the lamellar pattern lead to a limit in the maximum degree of alignment.
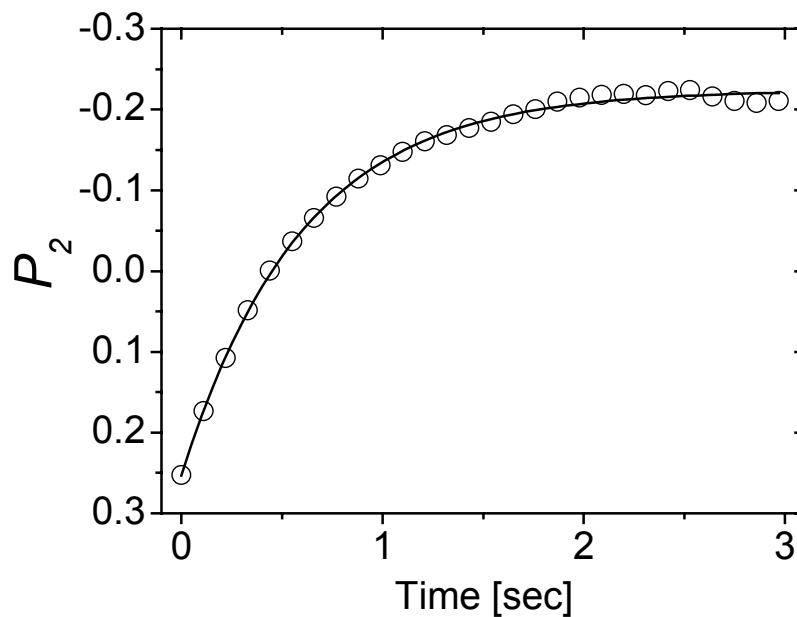
Figure 8-5:   *Evolution of the orientational order parameter P_2 for a 40 wt.-% solution of a $S_{50}V_{50}{}^{78}$ diblock copolymer in THF (E = 4 kV/2 mm) The solid line is a least squares fit to the data according to Equation 6-3 with $P_{2,0} = 0.26$, $P_{2,\infty} = -0.22$, and $\tau = 0.86$ sec.*

On the other hand, if we compare the kinetics of the alignment processes, we find that for the concentration range studied, the SV system is about one order of magnitude faster than the SHM block copolymer in THF solution. Unfortunately, this can not only be assigned to the higher dielectric contrast as the solution viscosity for the SHM system is significantly larger than for the SV system ($\eta_{SHM, 40\ wt.-\%} = 1550$ Pa sec, $\eta_{SV, 40\ wt.-\%} = 107$ Pa sec). In this case it is obvious that the interplay between lower solution viscosity and higher dielectric contrast leads to the better performance of the PS-*b*-P2VP block copolymer solutions in THF. Even the highly concentrated sample with $w_p = 50$ wt.-% exhibits a time constant of a few seconds with the overall process being finished within a minute at a field strength of 2 kV/mm. As has been described earlier, this process should be faster than the rate of solvent evaporation, so that all

concentrations up to 50 wt.-% could be used for macroscopic alignment of melt samples via solvent casting.

Using a home-built capacitor which allows application of an electric DC field during film formation by solvent casting, we demonstrate the feasibility of such a process. An example is shown in Figure 8-6, where we display SAXS data of a melt sample prepared from a 37.5 wt.-% solution cast in the presence of an electric field of 2 kV/mm.
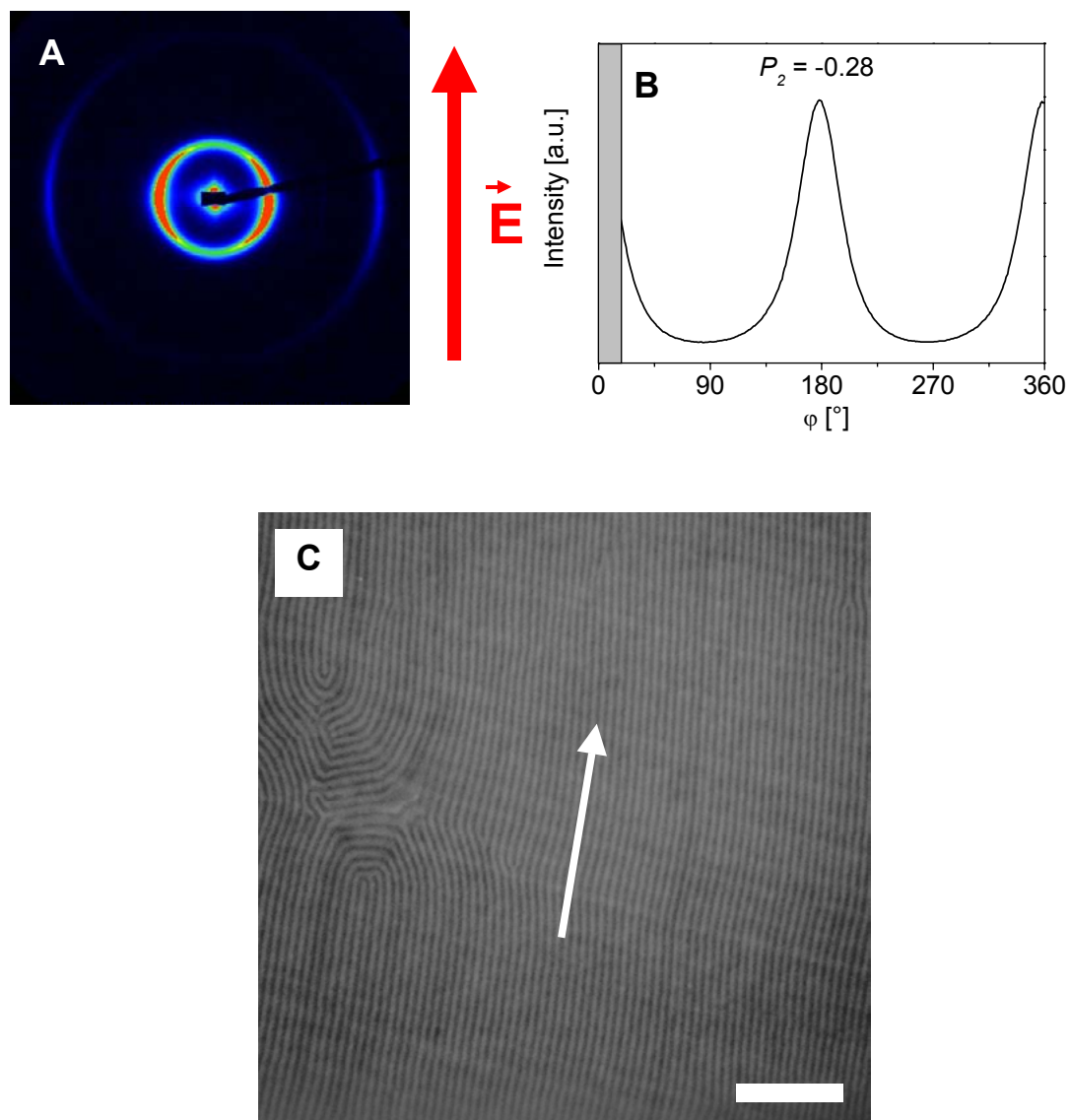

Figure 8-6:   *SAXS and TEM data of a $S_{50}V_{50}^{78}$ melt sample prepared from a 37.5 wt.-% solution cast in the presence of an electric field of 2 kV/mm. (A) 2D-SAXS pattern and (B) azimuthal intensity distribution at first order reflection. (C) TEM micrograph (stained with iodine). The arrow indicates the direction of the electric field vector. The scale bar represents 500 nm.*

Electric Field Strength Dependence. In order to investigate the influence of the electric field strength on the orientation kinetics we varied the electric field strength from 0.125 kV/mm to 2.5 kV/mm. In this case a 40 wt.-% solution of the $S_{50}V_{50}^{78}$ block copolymer was studied at room temperature in a 2 mm capacitor in order to minimize potential surface effects.
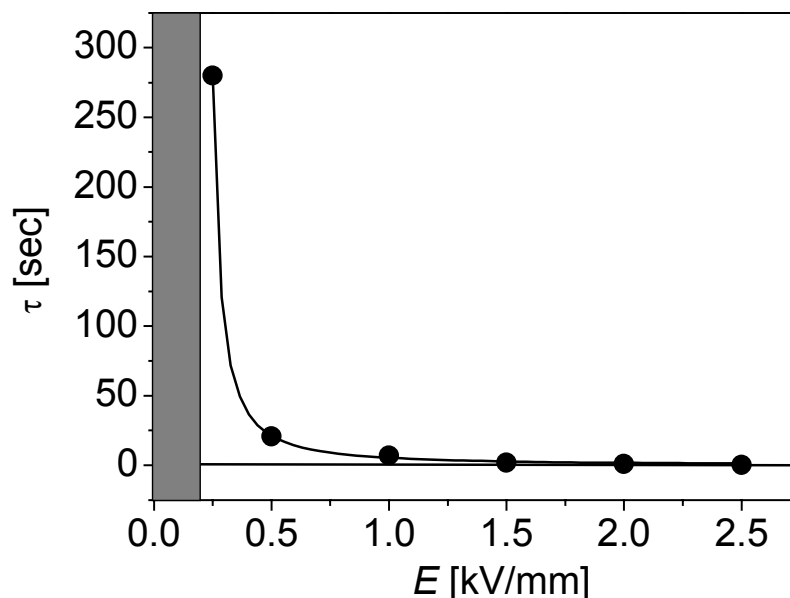
Figure 8-7:   *Electric Field dependence of time constant τ for 40 wt.-% solutions of a $S_{50}V_{50}^{78}$ diblock copolymer in THF. Electrode distance: 2mm. The solid line represents a least squares fit of the power law $\tau = \alpha(E - E_t)^a + \tau_\infty$ to the data yielding $\alpha = 0.19$ sec, $a = -1.4$, $E_t = 200$ V/mm, and $\tau_\infty = 0$ sec.*

Voltage [kV/mm]	τ [sec]	$P_{2,\infty}$	χ^2 [10^{-4}]
0.125	(a)	(a)	(a)
0.25	280	-0.19	1.8
0.5	20.9	-0.22	3.2
1	7.1	-0.24	1.3
1.5	2	-0.24	2.7
2	0.86	-0.22	3.0
2.5	0.24	-0.20	3.4

Table 8-2:   *Time constants τ of the reorientation behavior of $S_{50}V_{50}^{78}$ at different field strength obtained from least squares fits according to Equation 6-3 (w_p = 40 wt.-%, electrode distance: 2mm). (a) no electric field induced orientation detected*

The results of the least squares fits according to Equation 6-3 are summarized in Table 8-2 and shown in Figure 8-7. The quality of the single exponential fits can be inferred from the low χ^2 values. The limiting values $P_{2,\infty}$ always reach a value around $P_{2,\infty} = -0.22 \pm 0.03$. Increasing the field strength, does not seem to have an effect on the plateau values. The time constants τ range from 280 sec for low electric fields (0.250 kV/mm) to as low as 0.24 sec for the highest field strength (2.5 kV/mm). On the time scale of our experiment, we were not able to detect any reorientation for electric fields below 0.125 kV/mm. Therefore, we conclude that there exists a threshold field strength E_t below which no field induced reorientation is possible. Above E_t, the time constant scales with the electric field strength in a hyperbolic power law dependence $\tau = \alpha(E - E_t)^a + \tau_\infty$. The data points are best fitted for $\alpha = 0.19$ sec, $a = -1.4$ and $E_t = 200$ V/mm (solid line in Figure 8-7).

The asymptotic behavior at high electric fields (i.e. for a large force acting on the lamellae) indicates $\tau_\infty = 0$ sec for infinite field strength. This is expected in the absence of any electrorheological effects and limits in single chain diffusion, as the dominating process at $w_p = 40$ wt.-% is the migration of grain boundaries.

If we consider the dependence of the rate constant, $1/\tau$, we find for our system a cubic exponent. This is a significantly stronger dependence than expected theoretically as derived from Equation 1-17 ($1/\tau \sim E^2$)[11]. As can be seen in chapters 6 and 7, this has been found for all diblock copolymer systems under investigation in this work.

Polymer	E_t [kV/mm]	$\Delta\varepsilon$
PS-*b*-PI	350	0.2
PS-*b*-PHEMA-*b*-PMMA	310	2.2
PS-*b*-P2VP	200	5.1

Table 8-3:   *Threshold field strengths and dielectric contrast of different diblock copolymers.*

Another property common to all diblock copolymer samples is the low threshold field strength which ranges between 200 and 350 V/mm and decreases with increasing polarity of the second block. In the sequence PS-*b*-PI/PS-*b*-PHEMA-*b*-PMMA/PS-*b*-P2VP, the asymmetry in the surface tension between the blocks increases and therefore the interaction with the electrode surface field becomes stronger, i.e. one of the blocks interacts with the surface increasingly stronger than the other block and the surface field strength increases. In a recent theoretical work, Tsori and Andelman[12] have predicted that the threshold field strength

for a transition from an alignment of the lamellae parallel to the electrodes to a mixed morphology only depends on the dielectric contrast between the blocks, i.e. a larger dielectric contrast is expected to decreases the threshold field. This prediction is corroborated by our experimental results as the threshold field strength for our systems decreases with increasing dielectric contrast as shown in Table 8-3. This agreement is even more surprising as intuitively one would have expected the polarity of the second block of our systems to lead to an increase in the threshold field strength due to a stronger surface field.

8.3.2. Polystyrene-*b-p*oly(*tert*-butyl methacrylate) $S_{50}T_{50}{}^{100}$

In the following we will consider the different kinetic behaviors of the various block copolymer systems consisting of PS, P2VP and P*t*BMA.

Similar experiments as described above for the $S_{50}V_{50}{}^{78}$ block copolymer system were also conducted for the $S_{50}T_{50}{}^{100}$ diblock copolymer and for the triblock copolymers $S_{27}V_{35}T_{38}{}^{84}$ and $S_{16}V_{21}T_{63}{}^{138}$. For $S_{50}T_{50}{}^{100}$ solutions in THF we find a weakly established lamellar phase starting at a polymer concentration of about 40 wt.-%. Even the 50 wt.-% solution exhibits large concentration fluctuation scattering around the beam stop as can be seen in Figure 8-8A. Nevertheless, we identify weak first and second order maxima. Due to the larger interaction-parameter χ_{ST} as compared to χ_{SM}, the solutions phase separate at lower concentrations than the respective PS-*b*-PMMA system, which has been described in chapter 7. As this also results in a lower solution viscosity at the order-disorder transition, the electric field induced force on the lamellae is sufficient to induce a reorientation very similar to the processes already discussed[10].

If we compare the diblock copolymers $S_{50}V_{50}{}^{78}$ and $S_{50}T_{50}{}^{100}$, we find that at a polymer concentration of 40 wt.-% the $S_{50}T_{50}{}^{100}$ system is by far not as strongly phase separated as the $S_{50}V_{50}{}^{78}$ block copolymer. Obviously, the effective interaction-parameter χ_{ST} in THF solution is smaller than χ_{SV}. For a 40 wt.-% solution the concentration fluctuations associated with the disordered regions are even more pronounced. From Figure 8-8B we can see the time evolution of the orientational order parameter for the first order reflexion. Due to the weak phase separation, we observe a sigmoidal curve, which is characteristic for a non-cooperative process. As the system is not yet fully phase-separated, there are only small grains of ordered regions in a disordered matrix. Therefore, direct interaction between the grains during the reorientation process is inhibited, leading to the observed non-cooperative induction period at

166

early stages of reorientation. A fit to the empirical function $P_2(t) = \dfrac{P_{2,0} - P_{2,\infty}}{1 + e^{(t-t_0)/\tau}} + P_{2,\infty}$ yields a

time constant $\tau = 9.7$ sec and a plateau value $P_{2,\infty} = -0.14$.
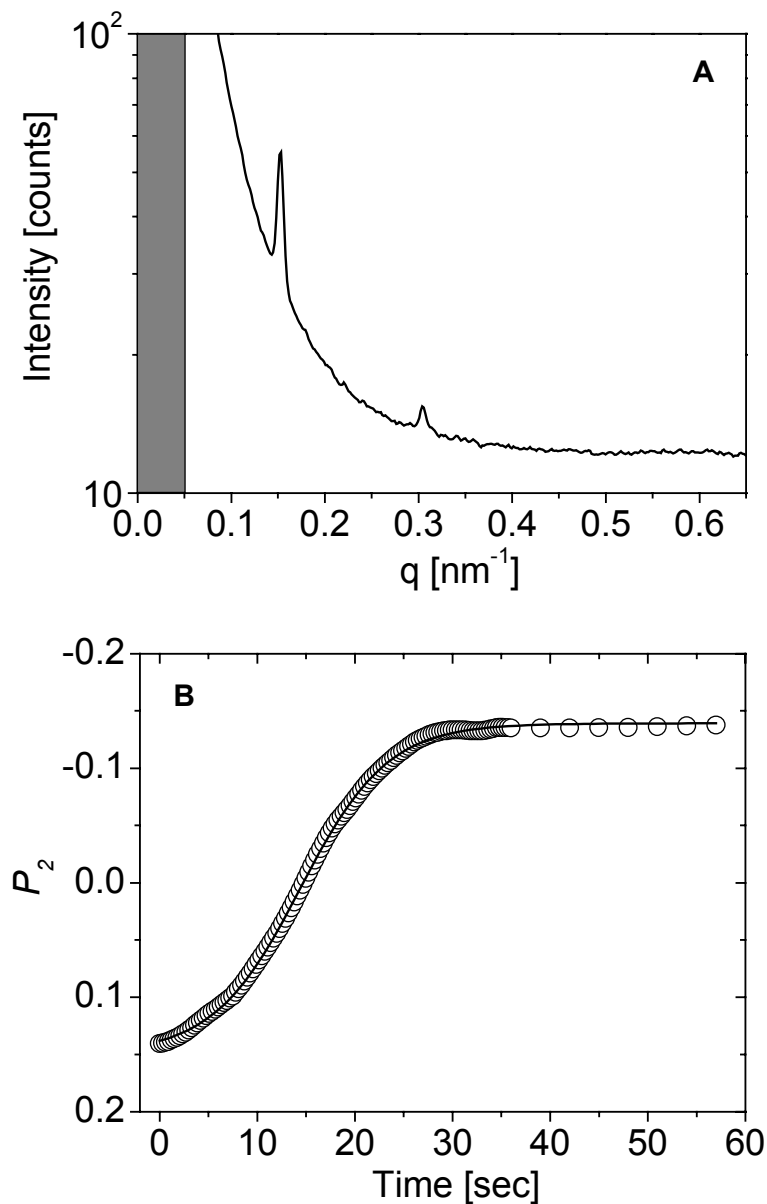
Figure 8-8:   *(A) Scattering intensity profile of a 50 wt.-% solution of $S_{50}T_{50}^{100}$ in THF. (B) Evolution of*
        orientational order parameter with time for a 40 wt.-% solution of $S_{50}T_{50}^{100}$ in THF at
        2 kV/mm: $\tau = 9.7$ sec, $P_{2,\infty} = -0.14$.

As we are dealing with a very weakly phase-separated system, the final degree of orientation is low as anticipated from the concentration dependence of $P_{2,\infty}$ for the $S_{50}V_{50}^{78}$ block copolymers as shown in Table 8-1. Furthermore, the $S_{50}V_{50}^{78}$ system exhibits a much faster reorientation behavior than $S_{50}T_{50}^{100}$, which can be explained by a combination of the different degrees of phase separation and the difference in the dielectric constants. With

ε_{P2VP} = 7.5 the dielectric constant of P2VP nearly twice as large as the respective value of PtBMA which is expected to be around 3.4 [13], similar to PMMA. In addition, as has been described by Amundson *et al.*, since the formation of grains of a certain size is required for an effective coupling between the microdomains and the electric field, the weak phase separation of $S_{50}T_{50}^{100}$ might lead to a reduction of the effective driving force for the overall orientation process.

Nevertheless, it has been demonstrated that THF solutions of PS-*b*-P2VP as well as a PS-*b*-PtBMA can be aligned by virtue of an external electric field. This result finally lead us to investigate the orientation behavior of more complex triblock copolymers composed of the above described diblock copolymer components.
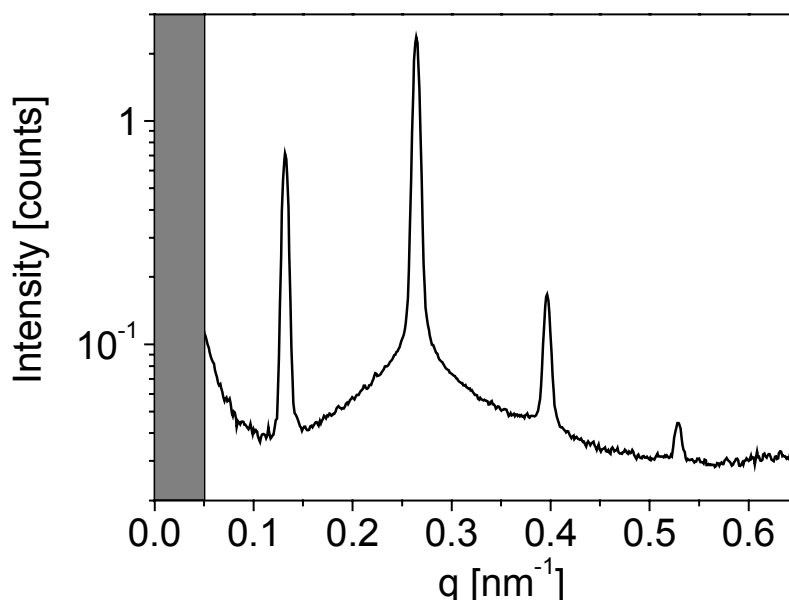
Figure 8-9:   *Scattering intensity profile of a 40 wt.-% solution of $S_{27}V_{35}T_{38}^{84}$ in THF.*

8.3.3.   Polystyrene-*b*-poly(2-vinyl pyridine)-*b*-poly(*tert*-butyl methacrylate) $S_{27}V_{35}T_{38}^{84}$ and $S_{16}V_{21}T_{63}^{138}$

In order to demonstrate the feasibility of our solvent-based orientation method for higher molecular weight polymers and more complex block copolymer systems, which can not be aligned by conventional melt-based processes, we additionally investigated a lamellar ($S_{27}V_{35}T_{38}^{84}$) and a core-shell cylindrical ($S_{16}V_{21}T_{63}^{138}$) PS-*b*-P2VP-*b*-PtBMA triblock copolymer of 84,000 g/mol and 138,000 g/mol molecular weight, respectively.
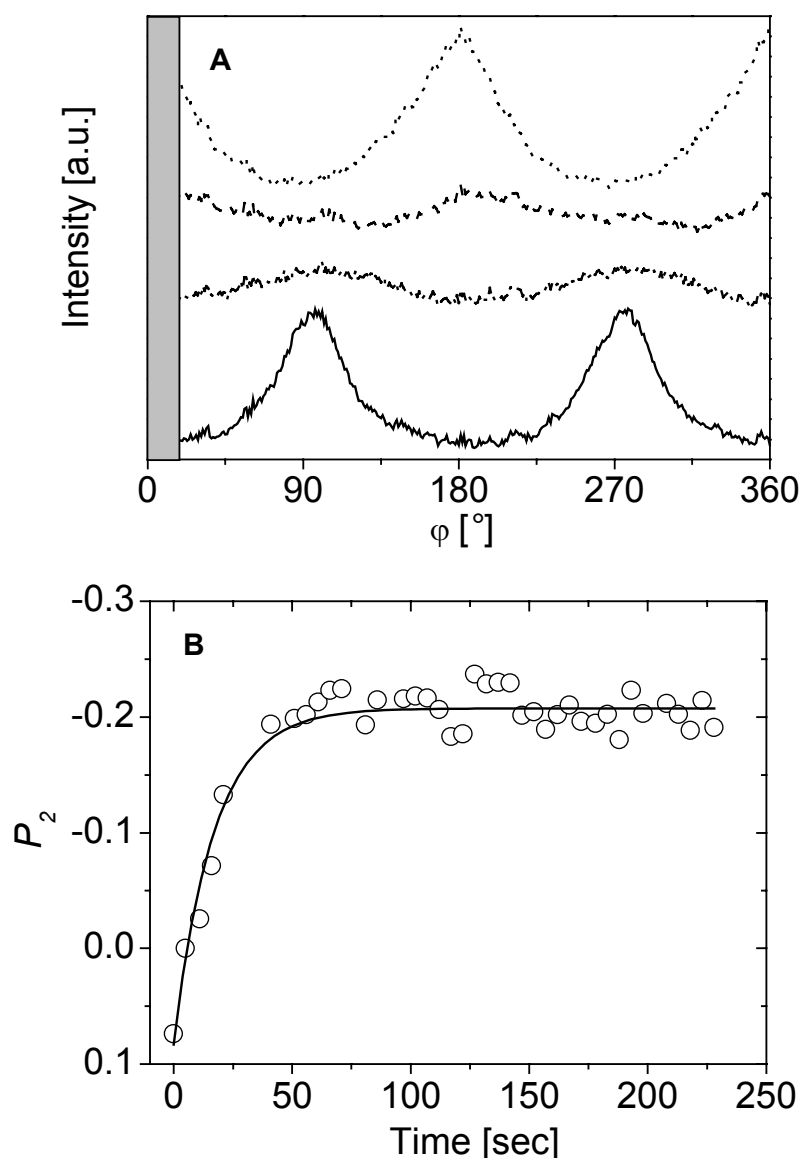
Figure 8-10: (A) Azimuthal angular dependence of the scattering intensity for a 40 wt.-% solution of $S_{27}V_{35}T_{38}{}^{84}$ in THF at 2 kV/2 mm: 0 sec (····), 5 sec (– –), 10 sec (···), 85 sec (—). (B) Time evolution of P_2 for the same system, $\tau = 17.7$ sec, $P_{2,\infty} = -0.21$.

$S_{27}V_{35}T_{38}{}^{84}$ phase-separates at concentrations above 37.5 wt.-% in THF. In Figure 8-9 we show the scattering intensity profile of a 40 wt.-% solution of $S_{27}V_{35}T_{38}{}^{84}$ in THF. Clearly several higher order scattering maxima at integer multiples of the first order Bragg peak can be identified. After filling the capacitor we also find lamellae predominantly aligned parallel to the electrode surfaces. Once the electric field is switched on, the scattering pattern changes significantly. As can be seen from the azimuthal angular dependence of the scattering intensity in Figure 8-10A, the initial peaks at $\varphi = 0°$ and 180° disappear within the first 5 seconds of the experiment and new peaks at $\varphi = 90°$ and 270° grow with time. This indicates the migration of grain boundaries as the dominating mechanism, which has previously been

169

observed for lamellar diblock copolymer solutions[10]. The evolution of the orientational order parameter with time for the above described process is shown in Figure 8-10B. The solid line represents a least-squares fit to the data according to Equation 6-3 yielding a time constant $\tau = 17.7$ sec and a plateau value $P_{2,\infty} = -0.21$. As anticipated from the measurements dealing with the respective diblock systems, the electric field induced orientation of $S_{27}V_{35}T_{38}{}^{84}$ is a fast and well-controlled process, which can be described by a single exponential.
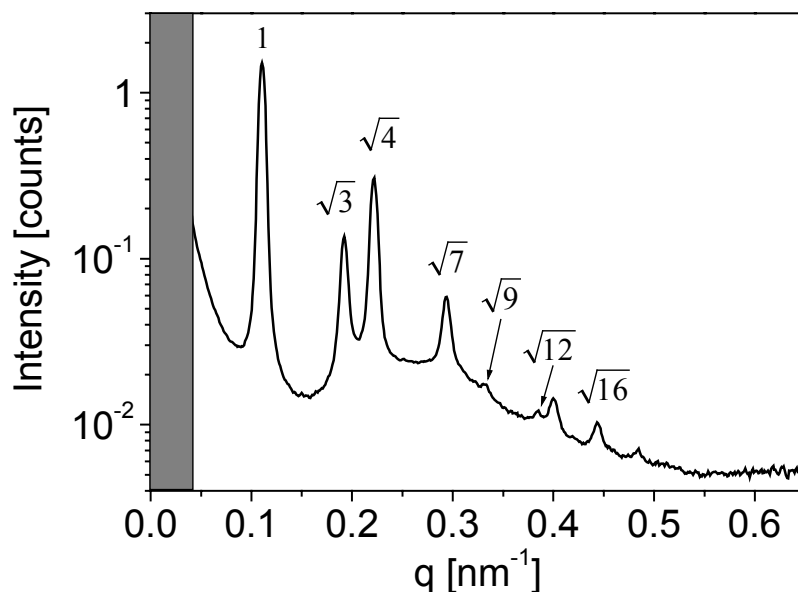
Figure 8-11:   Scattering intensity profile of a 40 wt.-% solution of $S_{16}V_{21}T_{63}{}^{138}$ in THF.

Figure 8-11 shows the SAXS pattern of a 40 wt.-% solution of $S_{16}V_{21}T_{63}{}^{138}$ in THF. From the relative peak positions at 1, $\sqrt{3}$, 2, $\sqrt{7}$, 3, and $\sqrt{12}$ we infer a hexagonally ordered cylindrical morphology. For the alignment experiments we start with orientation of the cylinders parallel to the electrodes, so that a hexagonal scattering pattern is observed (Figure 8-12A). The initial peaks of the hexagonal pattern merge to form new signals at $\varphi = 90°$ and 270° (Figure 8-12B/C). Therefore, we can identify the migration of grain boundaries as the governing process. The reorientation of the cylindrical microdomains is significantly slower than the reorientation of the lamellae in $S_{27}V_{35}T_{38}{}^{84}$. The least-squares fit to the calculated P_2 values according to Equation 6-3 gives a time constant of $\tau = 480$ sec and a plateau value $P_{2,\infty} = -0.23$ (solid line in Figure 8-12D).
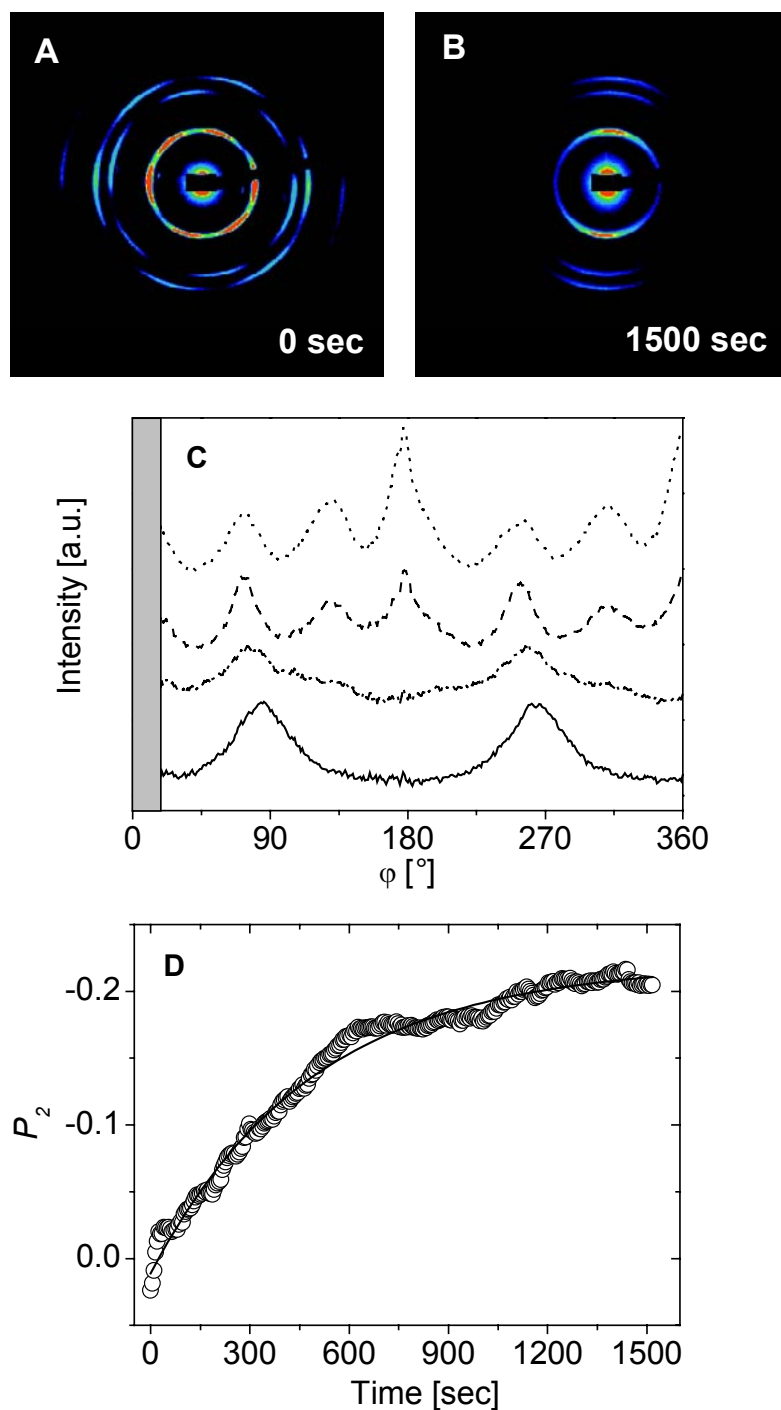
Figure 8-12:   *2D SAXS pattern of a 40 wt.-% solution of $S_{16}V_{21}T_{63}^{138}$ in THF (A) prior to and (B) after application of the electric field. (C) Azimuthal angular dependence of the scattering intensity for a 40 wt.-% solution of $S_{16}V_{21}T_{63}^{138}$ in THF at 2 kV/2 mm: 0 sec (⋯), 45 sec (--), 330 sec (-⋅-), 1500 sec (—). (D) Time evolution of orientational order parameter P_2 for the same system: τ = 480 sec, $P_{2,\infty}$ = -0.23.*

On one hand, we may assume that the slow kinetic behavior is due to the higher solution viscosity of the higher molecular weight block copolymer solution at constant concentration. In addition, there is an electrostatic argument, as the electric field induced driving force also

depends on the volume fraction of the dielectric bodies in the solution. As the cylindrical microdomains exhibit an asymmetry where PS and P2VP represent the minority component embedded within a PtBMA matrix, the driving force for reorientation should be significantly smaller than for the lamellar case. Nevertheless, time permitting the cylinders will also align predominantly parallel to the electric field vector.

8.4.   Conclusion

Using Synchrotron-SAXS we have identified migration of grain boundaries as the governing mechanism of the electric field induced microdomain alignment of a PS-b-P2VP block copolymer in solution. In addition, we found a concentration range from 37.5 wt.-% up to 50 wt.-%, in which reorientation of the lamellar microdomains can be realized on the time scale of a few seconds. The variation of the electric field strength revealed a threshold value ($E_t = 200$ V/mm), below which no electric field induced orientation can be achieved. In summary, the maximum final orientation reached in solution could be described by order parameters of up to $P_2 = -0.28$. The time constants of the fastest processes were in the range of 0.3 sec.

In addition, the time resolved SAXS measurements allowed us to study the kinetic behavior of a PS-b-PtBMA, which - in contrast to PS-b-PMMA - showed electric field-induced orientation of the microdomains due to a larger interaction parameter χ_{ST} compared to χ_{SM} leading to a phase-separated solution at lower viscosities. Furthermore, we could show that the even more complex lamellar and core-shell cylindrical PS-b-P2VP-b-PtBMA high molecular weight triblock copolymer systems could be oriented by virtue of an electric field from solution.

We have demonstrated that our solvent-based method for electric field-induced alignment of block copolymer microdomains can be applied successfully to a large variety of block copolymer compositions and microstructures, even at molecular weights too high for melt-based procedures.

Acknowledgement

References

[1] Giebeler, E.; Stadler, R. *Macromol. Chem. Phys.* **1997**, *198*, 3815.

[2] Ludwigs, S.; Böker, A.; Abetz, V.; Müller, A.H.E.; Krausch, G. *Polym. Prepr.* **2002** in print.

[3] Shibayama, M.; Hashimoto, T.; Hasegawa, H.; Kawai, H. *Macromolecules* **1983**, *16*, 1427.

[4] Frederickson, G.H.; Leibler, L. *Macromolecules* **1989**, *22*, 1238.

[5] Amundson, K.; Helfand, E.; Patel, S.S.; Quan, X.; Smith, S.D. *Macromolecules* **1992**, *25*, 1953.

[6] Balsara, N.P.; Perahia, D.; Safinya, C.R.; Tirrell, M.; Lodge, T.P. *Macromolecules* **1992**, *25*, 3896.

[7] Balsara, N.P.; Hammouda, B.; Kesani, P.K.; Jonnalagadda, S.V.; Straty, G.C. *Macromolecules* **1994**, *27*, 2566.

[8] Anastasiadis, S.H.; Russell, T.P.; Satija, S.K.; Majkrzak, C.F. *Phys. Rev. Lett.* **1989**, *62*, 1852.

[9] Polis, D.L.; Smith, S.D.; Terrill, N.J.; Ryan, A.J.; Morse, DC; Winey, K.I. *Macromolecules* **1999**, *32*, 4668.

[10] Böker, A.; Elbs, H.; Hänsel, H.; Knoll, A.; Ludwigs, S.; Zettl, H.; Urban, V.; Abetz, V.; Müller, A.H.E.; Krausch, G. in preparation.

[11] Amundson, K.; Helfand, E.; Quan, X.; Smith, S.D. *Macromolecules* **1993**, *26*, 2698.

[12] Tsori, Y.; Andelman, D. *Macromolecules* **2002**, *35*, 5161.

[13] Polak, A.J.; Sundahl, R.C. . *Polymer* **1989**, *30*, 1314.

Chapter 9

Summary

The influence of external fields on the microdomain structure of block copolymers has been studied. Both *surface fields* and *electric fields* have been considered.

The first part describes the synthesis and characterization of ABC triblock copolymers aiming towards the generation of tailor-made substances for the controlled patterning of surfaces on nanometer scale. It is demonstrated that thin and ultrathin films of polystyrene-*b*-poly(2-vinyl-pyridine)-*b*-poly(methyl methacrylate) and polystyrene-*b*-poly(2-hydroxyethyl methacrylate)-*b*-poly(methyl methacrylate) block copolymers on silicon wafers reveal regular surface patterns with worm-, stripe- or island-like morphologies. The characteristic spacings can be controlled via the molecular weight of the different blocks of the respective copolymers and the film thickness.

Thin films (~ 20 nm thickness) prepared by dip-coating from a polymer solution were found to exhibit a phase-separated worm-like surface morphology that presumably only consists of PS and PMMA microdomains with a characteristic lateral length scale similar to the bulk period L_0. The generation of such a striped surface pattern can be explained by complete coverage of the silicon oxide surface by PHEMA or P2VP, resulting in a thin film structure that consists of a homogeneous layer of the middle block adsorbed at the substrate covered with a laterally microphase-separated surface layer of PS and PMMA microdomains. The proposed model for this morphology is in agreement with recent self-consistent field calculations.

In the case of the *ultrathin films* (thickness < 7 nm), our results demonstrate that adsorption of a block copolymer as an ultrathin film leads to a periodic surface domain structure (stripes), where both polar blocks (B and C) adsorb to the surface. Due to significant stretching of the adsorbed blocks the spacings between the domains are large for the rather

low molecular weight block copolymers. The lateral dimensions correlate well with the molecular dimensions of the A and B/C blocks according to recently derived scaling laws.

In the second part of this thesis *external electric fields* are used to create macroscopically oriented bulk samples. In order to circumvent limitations associated with the application of external fields to *melts* of high molecular weight block copolymers and multiblock copolymers of complex architecture, a new *solvent-based* procedure is introduced, i.e. the block copolymer microdomains are aligned by application of an electric field ($E \sim 1 - 2$ kV/mm) during solvent casting of bulk samples.

In order to elucidate the dominating parameters and governing mechanisms, the microdomain orientation kinetics of concentrated block copolymer solutions exposed to a DC electric field is investigated by time-resolved synchrotron small-angle X-ray scattering (SAXS) at the ID02A beamline at the European Synchrotron Radiation Facility (ESRF) in Grenoble, France. As a first model system, a lamellar polystyrene-*b*-polyisoprene block copolymer dissolved in toluene is used. The orientation kinetics follows a single exponential behavior with characteristic time constants varying from a few seconds to some minutes depending on polymer concentration, temperature, electric field strength, and system size.

Furthermore, two mechanisms governing the electric field alignment of a lamellar block copolymer from concentrated solutions are identified. It is shown that depending on the segregation power ($\chi \propto \phi_P$, $\chi \propto 1/T$) a single mechanism dominates the orientation process, i.e. in a weakly segregated system (low concentration or high temperature) the *migration of boundaries* prevails, whereas a stronger phase separated system (high concentration or low temperature) predominantly exhibits *rotation of grains*.

In addition, the orientation kinetics slows down with increasing polymer *concentration*, which can be correlated to the respective solution viscosity and the mechanism of orientation. Moreover, the influence of the *electric field strength* on the orientation kinetics is determined, including a threshold value below which no electric field induced orientation could be achieved on the time scale of the experiment. The time constants of the fastest processes were in the range of 0.5 sec, reaching a final orientation described by order parameters of up to $P_2 = -0.35$. Finally, the variation of *temperature* yields control of the governing mechanisms at a fixed polymer concentration.

In additional studies, the dielectric contrast of the block copolymer components was varied systematically (PS-*b*-PI, PS-*b*-PMMA, PS-*b*-P*t*BMA, PS-*b*-PHEMA-*b*-PMMA, PS-*b*-P2VP). It is found that a high dielectric contrast leads to faster alignment kinetics (e.g. the time

constants of the fastest processes for a PS-*b*-P2VP diblock system in THF are in the range of 0.3 sec) and reduces the threshold field strength (around 200 V/mm for PS-*b*-P2VP).

Furthermore, it could be shown that the interplay between degree of phase-separation, solution viscosity and dielectric contrast is crucial to decide if a given polymer/solvent system can be used for electric field-induced microdomain alignment. For example, it was found that PS-*b*-P*t*BMA shows electric field-induced orientation of the microdomains while PS-*b*-PMMA does not. This can be explained by the larger interaction parameter χ_{ST} compared to χ_{SM} leading to a phase-separated solution at lower viscosities. In a similar way, the introduction of a high dielectric constant middle block (PHEMA) into a PS-*b*-PMMA, which additionally enhances phase separation, is shown to be the key to creating a well-performing methacrylate-based block copolymer system for electric field induced alignment from solution.

Finally, we could show that the even more complex lamellar and core-shell cylindrical PS-*b*-P2VP-*b*-P*t*BMA high molecular weight triblock copolymer systems could be oriented by virtue of an electric field from solution.

In summary, it was demonstrated that electric field alignment of block copolymer domains from solution is a powerful tool to generate highly anisotropic bulk block copolymer samples. The large variety of parameters which we can control allows us to further improve the preparation of macroscopically aligned melt samples via solvent casting in the presence of an electric field.

Zusammenfassung

In der vorliegenden Arbeit wurde der Einfluß von äußeren Feldern auf die Mikrodomänenstruktur von Blockcopolymeren untersucht. Dabei wurden sowohl *Oberflächenfelder* als auch *elektrische Felder* betrachtet.

Im ersten Teil wird die Synthese und Charakterisierung von ABC Dreiblockcopolymeren zur kontrollierten lateralen Strukturierung von Oberflächen auf Nanometerskala beschrieben. Es wird gezeigt, daß dünne und ultradünne Filme aus Polystyrol-*b*-Poly(2-Vinylpyridin)-*b*-Polymethylmethacrylat und Polystyrol-*b*-Poly(2-Hydroxyethylmethacrylat)-*b*-Polymethylmethacrylat auf Siliziumoberflächen regelmäßige Oberflächenstrukturen in Form von Streifen oder Inseln ergeben. Die charakteristischen Abstände der Strukturen können mittels der Filmdicke und dem Molekulargewicht der jeweiligen Blöcke gesteuert werden.

Durch Tauchbeschichten aus einer verdünnten Polymerlösung hergestellte *dünne Filme* (ca. 20 nm dick) zeigen eine wurmartige Oberflächenmorphologie, die ausschließlich aus Polystyrol- und Polymethylmethacrylatmikrodomänen besteht. Die charakteristische Wiederholungseinheit der Oberflächenstrukturen ist mit den Längenskalen der Volumenstruktur identisch. Die Entstehung einer solchen Oberflächenmorphologie kann durch die vollständige Adsorption des PHEMA- bzw. P2VP-Mittelblockes an die Siliziumoxidoberfläche bei gleichzeitiger lateraler Entmischung der Außenblöcke erklärt werden. Das hier vorgestellte Modell deckt sich mit jüngsten SCF-Rechnungen.

Im Fall der *ultradünnen Filme* (Filmdicke kleiner als 7 nm) zeigen die Ergebnisse, daß die Adsorption der beiden polaren Blöcke B und C an die Substratoberfläche zu einer gestreiften Oberflächenstruktur führt. Aufgrund der deutlichen Streckung der adsorbierten Blöcke erhält man verhältnismäßig große Domänenabstande, die sehr gut mittels kürzlich etablierter Skalengesetze anhand der molekularen Dimensionen beschrieben werden können.

Im zweiten Teil dieser Arbeit wurden *externe elektrische Felder* zur Herstellung von makroskopisch ausgerichteten Volumenproben verwendet. Um Beschränkungen zu umgehen, die üblicherweise mit der Ausrichtung von Mikrodomänen hochmolekularer Blockco-polymere oder von Blockcopolymeren mit komplexem Aufbau aus der Schmelze verbunden sind, wird eine neue Methode zur Ausrichtung aus Lösung vorgestellt. Dabei werden die Mikrodomänen einer Blockcopolymerlösung während des Eintrocknens mit einem elektrischen Feld ($E \sim 1 - 2$ kV/mm) parallel zu den elektrischen Feldlinien orientiert.

Um die Parameter und Mechanismen zu ergründen, die den Orientierungsprozess im elektrischen Feld dominieren, sind die Kinetiken der Mikrodomänenorientierung in konzentrierten Blockcopolymerlösungen unter Einfluß eines elektrischen Feldes mit Hilfe von in-situ Röntgenkleinwinkelstreuung an der europäischen Synchrotronstrahlquelle (ESRF) in Grenoble vermessen worden. Als erstes Modellsystem wurde ein Polystyrol-*b*-Polyisopren Blockcopolymer in Toluollösung verwendet. Die Ausrichtungskinetik kann mit einer Exponentialfunktion erster Ordnung beschrieben werden. Man erhält in Abhängigkeit von der Polymerkonzentration, der Temperatur, der elektrischen Feldstärke, sowie dem Elektroden-abstand unterschiedliche Zeitkonstanten von ein paar Sekunden bis zu wenigen Minuten.

Darüber hinaus wurden zwei Mechanismen identifiziert, die den Orientierungsvorgang bestimmen. Es kann gezeigt werden, daß die Stärke der Phasenseparation ($\chi \propto \phi_P$, $\chi \propto 1/T$) in einer Blockcopolymerlösung über den dominierenden Mechanismus entscheidet. In einem schwach phasenseparierten System (niedrige Konzentration oder hohe Temperatur) herrscht die *Wanderung von Korngrenzen* vor. In einer stark phasenseparierten Probe (hohe Konzentration oder niedrige Temperatur) findet man bevorzugt die *Rotation von einzelnen Körnern*.

Außerdem nimmt die Orientierungsgeschwindigkeit mit zunehmender Polymerkonzen-tration ab, welches mit der steigenden Lösungsviskosität (trotz zunehmender Phasen-separation und ansteigender elektrostatischer Triebkraft für den Orientierungsprozeß) und dem Mechanismus des Prozesses korreliert werden kann.

Darüber hinaus wurde der Einfluß der elektrischen Feldstärke auf die Ausrichtungskinetik untersucht. Dabei konnten, je nach Polymersystem, unterschiedliche Grenzfeldstärken bestimmt werden. Unterhalb einer solchen Grenzfeldstärke konnte keine Orientierung der Mikrodomänen durch das elektrische Feld erzielt werden.

Die schnellsten Prozesse lassen sich mit Zeitkonstanten im Bereich von 0.5 Sekunden beschreiben. Die höchste erreichte Ausrichtung ergibt einen Wert von −0.35 für den Ordnungsparameter P_2. Schließlich konnte gezeigt werden, daß durch Kontrolle der

Temperatur bei konstanter Konzentration, der dominierende Mechanismus der Mikro-domänenausrichtung eingestellt werden kann.

In zusätzlichen Studien wurden die Dielektrizitätskonstanten der einzelnen Polymerblöcke systematisch variiert (PS-*b*-PI, PS-*b*-PMMA, PS-*b*-P*t*BMA, PS-*b*-PHEMA-*b*-PMMA, PS-*b*-P2VP). Dabei wurde festgestellt, daß die Orientierungsgeschwindigkeit mit erhöhtem dielektrischen Kontrast zwischen den Blöcken ansteigt und die Grenzfeldstärke abnimmt (der schnellste Prozeß für eine THF-Lösung von PS-*b*-P2VP verläuft mit einer Zeitkonstante von 0.3 Sekunden und eine Grenzfeldstärke von nur 200 V/mm).

Darüber hinaus konnte gezeigt werden, daß das Zusammenspiel von Phasenseparation, Lösungsviskosität und dielektrischem Kontrast entscheidet, ob ein gegebenes Polymer/Lösungsmittel-System für die Ausrichtung der Mikrodomänen im elektrischen Feld verwendet werden kann. So wurde z.B. festgestellt, daß PS-*b*-P*t*BMA in THF ein geeignetes System darstellt, wohingegen PS-*b*-PMMA ungeeignet ist. In diesem Fall führt der größere Wechselwirkungsparameter χ_{ST} zur Phasenseparation in Lösung bei niedrigeren Viskositäten als bei PS-*b*-PMMA. In ähnlicher Weise führt die Einführung eines Mittelblockes mit hoher Dielektrizitätskonstante, der außerdem die Phasenseparation fördert, zu einem Blockco-polymersystem auf Methacrylatbasis, dessen Mikrodomänen sich leicht im elektrischen Feld ausrichten lassen.

Schließlich war es auch möglich, zylindrische Kern-Schale und lamellare Morphologien hochmolekularer PS-*b*-P2VP-*b*-P*t*BMA Dreiblockcopolymere unter dem Einfluß eines elektrischen Feldes aus Lösung zu orientieren.

Zusammenfassend kann man sagen, daß die Ausrichtung von Blockcopolymerdomänen aus Lösung im elektrischen Feld ein vielversprechendes Verfahren zur Herstellung makroskopisch orientierter Volumenproben darstellt. Die Kontrolle der oben genannten Parameter, aufgrund der in dieser Arbeit beschriebenen Untersuchungen, erlaubt eine deutliche Verbesserung dieses Prozesses.

10.   List of Publications

During the course of this thesis the following papers have been published:

A. Böker, A.H.E. Müller, G. Krausch[*]
"Nanoscopic Surface Patterns from Functional ABC Triblock Copolymers"
Macromolecules **2001**, *34*, 7477.

A. Böker, A. Knoll, H. Elbs, V. Abetz, A.H.E. Müller, G. Krausch[*]
"Large Scale Domain Alignment of a Block Copolymers from Solution using Electric Fields"
Macromolecules **2002**, *35*, 1319.

A. Böker, H. Elbs, H. Hänsel, A. Knoll, S. Ludwigs, H. Zettl, V. Urban, V. Abetz, A.H.E. Müller, and G. Krausch[*]
"Microscopic Mechanisms of Electric Field Induced Alignment of Block Copolymer Microdomains**"**
Phys. Rev. Lett. **2002**, submitted.

A. Böker, T. Herweg, K. Reihs[*]
" Selective Alteration of Polymer Surfaces by Thermal Cleavage of Fluorinated Side Chains"
Macromolecules **2002**, *35*, 4929.

R. Erhardt, A. Böker, H. Zettl, H. Kaya, W. Pyckhout-Hintzen, G. Krausch, V. Abetz[*], A.H.E. Müller[*]
"Janus Micelles"
Macromolecules **2001**, *34*, 1069.

H. Mori, A. Böker, G. Krausch, A.H.E. Müller[*]
"Surface-grafted Hyperbranched Polymer Films via Self-condensing Atom Transfer Radical Polymerization from Silicon Surfaces"
Macromolecules **2001**, *34*, 6871.

G. Cheng, A. Böker, M. Zhang, G. Krausch, A.H.E. Müller[*]
"Cylindrical Core-Shell Brushes via a "Grafting From' Process Using ATRP"
Macromolecules **2001**, *34*, 6883.

H. Schmalz, A. Böker, R. Lange, G. Krausch, V. Abetz[*]
"Synthesis and Properties of ABA and ABC Triblock Copolymers with Glassy (A), Elastomeric (B), and Crystalline (C) Blocks"
Macromolecules **2001**, *34*, 8720.

A. Böker, A.H.E. Müller, G. Krausch[*]
"Functional ABC triblock copolymers for controlled surface patterns on nanometer scale";
Polym. Mater. Sci. Eng. **2001**, *84*, 312.

A. Böker, H. Elbs, H. Hänsel, A. Knoll, S. Ludwigs, H. Zettl, V. Urban, V. Abetz, A.H.E. Müller, and G. Krausch[*]
"Macroscopic Alignment of Concentrated Block Copolymer Solutions in Electric Fields**"**
Polym. Prepr. **2002** in print.

S. Ludwigs, A. Böker, V. Abetz, A.H.E. Müller and G. Krausch[*]
"Self-Assembly of Polystyrene-*b*-poly(2-vinylpyridine)-*b*-poly(*tert*-butyl methacrylate)
(SVT) Triblock Copolymers in Bulk and in Thin Films"
Polym. Prepr. **2002** in print.

A.H.E. Müller[*], G. Cheng, A. Böker, G. Krausch
"Unimolecular amphipolar nanocylinders via a 'grafting from' process using ATRP"
Polym. Mater. Sci. Eng. **2001**, *84*, 91.

R. Erhardt, A. Böker, H. Zettl, H. Kaya, W. Pyckhout-Hintzen, G. Krausch, V. Abetz[*], A.H.E.
Müller[*]
"Superstructures of Janus Micelles"
Polym. Mater. Sci. Eng. **2001**, *84*, 102.

H. Mori, A. Böker, G. Krausch, A.H.E. Müller[*]
"Hyperbranched (meth)acrylates grafted onto silicon"
Polym. Mater. Sci. Eng. **2001**, *84*, 933.

H. Schmalz, A. Böker, R. Lange, V. Abetz[*]
"ABC Triblock Copolymers with Crystalline End Blocks and their Use as Thermoplastic
Elastomers"
Polym. Mater. Sci. Eng. **2001**, *85*, 478.

Presentations at international meetings:

DPG, Potsdam, März 2000, Poster presentation:
"Synthese und Charakterisierung von funktionellen mikrophasenseparierten ABC
Dreiblockcopolymeren zur Erzeugung lateral strukturierter Oberflächen"

IUPAC World Polymer Congress, Warschau, Juli 2000, Poster presentation:
"Synthesis and Characterization of Functional ABC Triblock Copolymers for Controlled
Surface Patterns on Nanometer Scale"

ACS, San Diego, April 2001, Oral presentation:
"Nanoscopic Surface Patterns from Functional ABC Triblock Copolymers"

DPG, Regensburg, März 2002, Oral presentation:
"Orientation Kinetics of Block Copolymer Solutions under the Influence of an Electric Field"

APS, Indianapolis, April 2002, Poster presentation:
"Electric Field Induced Macroscopic Alignment of Concentrated Block Copolymer Solutions"

Danksagung

Diese Arbeit wäre ohne die Unterstützung, die ich von vielen Seiten erhalten habe, nicht möglich gewesen. Besonders bedanken möchte ich mich bei:

Erklärung

Die vorliegende Arbeit wurde von mir selbstständig verfasst und ich habe dabei keine anderen als die angegebenen Hilfsmittel und Quellen benutzt.

Ferner habe ich nicht versucht, anderweitig mit oder ohne Erfolg eine Dissertation einzureichen oder mich der Doktorprüfung zu unterziehen.

Bayreuth, den 18.7.2002

(Alexander Böker)